

Locomotion of Serial Multiply-Actuated Tumbling Robots

**A DISSERTATION
SUBMITTED TO THE FACULTY OF THE GRADUATE SCHOOL
OF THE UNIVERSITY OF MINNESOTA
BY**

Brett Robert Hemes

**IN PARTIAL FULFILLMENT OF THE REQUIREMENTS
FOR THE DEGREE OF
Doctor of Philosophy**

Nikolaos Papanikolopoulos

June, 2011

© Brett Robert Hemes 2011
ALL RIGHTS RESERVED

Acknowledgements

Foremost, I wish to thank my advisor Nikolaos Papanikolopoulos for his continuing encouragement and support throughout my studies. He gave me the courage to dream big and to not fear failure; without him this thesis would not be possible.

Additionally, I would like to thank all of my labmates from the Center for Distributed Robotics; from these, I extend special thanks to Mike Belsky, Sam Kristoff, Duc Fehr, Alex Kossett, Hyeun Jeong Min, and Dario Canelon-Suarez for all of their valuable help and insight. Also to my good friends not yet mentioned: Joey Cross, Jonathan Kwan, Chris Lin, Nicolas Zea, Sarah Bales, Ben Duplechin, Seppie Sevcik, and Brett Waybrant.

Finally, I owe my deepest gratitude to my wife and best friend Ameara Mansour and to the rest of my family for all of their support abundant love.

Abstract

Mobile robots that are able to move about and effectively negotiate their environment are attractive for a wide variety of applications. Such applications include surveillance, inspection, and mobile sensing where robots often present cost-effective alternatives to human labor. Other applications include those that are potentially hazardous to humans; examples of these include search and rescue, monitoring and maintenance of toxic environments, and planetary exploration.

A vast majority of research into mobile robots has been limited to structured environments such as research labs, indoor office environments, industrial settings, maintained roads, etc. As the number of mobile robot applications grows, so does the need for such systems to be able to operate in unstructured (general) environments. Such environments often exhibit a wide variety of terrain including uneven surfaces and significant terrain irregularities. In some cases hazardous areas can be tactically avoided with careful path planning, but in general this is not always possible and obstacles must be negotiated directly. For these applications it is imperative that the robot exhibits a sufficient level of mobility to be able to perform required tasks.

In addition to mobility requirements, many mobile robot applications are further constrained by limitations on physical size and/or cost. It is often the case that small (inexpensive) robots are preferable if not required. In general, however, it is the case that miniature mobile robots sacrifice mobility in exchange for their small size. Additionally, the increased design complexity of miniature systems often increases both design and manufacturing cost. In this thesis we present a relatively new and unexplored form of robotic locomotion called tumbling which addresses many of the aforementioned existing limitations of miniature mobile robots; the thesis is comprised of three main parts.

In the first, tumbling and tumbling robots are defined and discussed in detail as well as other useful notation. Additionally, we present a classification of tumbling robots along with a catalog of existing designs to establish the state of the art. This treatment marks the first of its kind and establishes the first formal definitions with respect to tumbling locomotion for mobile robots. In the second, we examine terrainability of the class of serial multiply actuated tumbling robots by looking at the underlying principles

of tumbling interactions with several idealized obstacles. Specifically, we derive configuration equations that relate terrainability to the parameters of an idealized tumbling robot. The results are supported through experimentation using the Adelopod, a physical tumbling robot developed as part of this thesis, over a variety of repeatable terrains. Finally, we conclude by examining the maneuverability for the class of serial multiply actuated tumbling robots and begin to address motion planning for such devices. We present results of several planning algorithms as well as a method for deriving useful distance metrics for significant planning speedup and increased path quality. Results of applying such metrics are presented.

Contents

Acknowledgements	i
Abstract	ii
List of Tables	viii
List of Figures	ix
1 Introduction	1
1.1 Motivation	2
1.2 Thesis Statement	3
1.3 Approach	4
2 Background	5
2.1 Design for Mobility	5
2.2 Tumbling	5
2.3 Mobility Analysis	6
2.3.1 Mobility of Mobile Robots	6
2.3.2 Focus on Rigor and Repeatability	8
2.4 Stability	9
2.5 Motion Planning with Differential Constraints	11
2.6 Minimalistic Manipulation	12
3 Tumbling and Robotic Tumbling Locomotion	14
3.1 Discrete Tumbles	14

3.2	Major Tumbles and the Definition of Tumbling Robots	19
3.3	Classification of Tumbling Robots	24
3.4	Tumbling Designs by Classification	28
3.4.1	Serial / Singly-Actuated Tumbling Robots	28
3.4.2	Serial / Multiply-Actuated Tumbling Robots	31
3.4.3	Composite-Bodied / Singly-Actuated Tumbling Robots	32
3.4.4	Composite-Bodied / Multiply-Actuated Tumbling Robots	33
3.4.5	Catalog of Existing Designs	34
3.5	Characteristics of Tumbling Robots	37
3.5.1	Benefits of Unrestricted Terrain-body Interactions	37
3.5.2	Issues with Tumbling	41
3.5.3	Numerous Support Sets and Hybrid Representations	43
3.6	P2AT: A Planar 2-Armed Tumbling Robot	47
3.6.1	Physical Description	47
3.6.2	Behavioral Description	49
3.6.3	Hybrid System Representation	52
4	The Adelopod Tumbling Robot	57
4.1	Morphology, Hardware, and Actuation	58
4.1.1	Arm Kinematics	60
4.1.2	Low-cost High-torque Gearmotors with Positional Feedback	61
4.1.3	Structural Assembly	62
4.1.4	Shell Design	65
4.2	Electrical	68
4.3	The Adelopod-T: A Hybrid Treaded-Tumbling Robot	69
4.4	Other Variants	72
5	Terrainability of Serial Tumbling Locomotion	73
5.1	Robot Designs for Mobility	73
5.2	Terrainability Analysis of Serial Tumbling Robots	75
5.2.1	Planar Framework	76
5.2.2	Step Climbing	79
5.2.3	Ditch Crossing	100

5.2.4	Overhangs	101
5.2.5	Composite Obstacles	102
5.3	Experimental Adelopod Performance Analysis	102
5.3.1	Robot Test Platforms	103
5.3.2	Terrain Selection	104
5.3.3	Forward Locomotion	108
5.3.4	Complex Terrain	115
5.3.5	Hybrid Tumble-tread Locomotion	119
5.3.6	Idealized Step Climbing	121
5.4	Final Thoughts	122

6 Maneuverability and Motion Planning of Serial Multiply-actuated Tumbling **130**

6.1	Motion Planning Formulation	130
6.2	Motion Primitives for Tumbling	133
6.2.1	Discretization	134
6.2.2	Configuration Graph	136
6.2.3	Displacement	138
6.2.4	Gaits	141
6.2.5	Planning	142
6.2.6	Final Thoughts on Motion Primitives for Tumbling	143
6.3	Support Set Planning	144
6.3.1	Tumble Calculations	145
6.3.2	Dynamics Propagation and Planning	148
6.4	Path Planning with RRTs	149
6.5	Maneuverability of Serial Multiply-Actuated Tumbling Robots	153
6.5.1	P2AT	154
6.5.2	Adelopod	158
6.5.3	Adelopod-T	162
6.6	Maneuverability Analysis with Isochronal Surfaces	163
6.7	Experimental Analysis of the Adelopod Maneuverability	165
6.8	Distance Metrics for Serial Multiply-actuated Tumbling	172

6.8.1	Metric Results Applied to RRT's	172
6.9	Final Thoughts on Maneuverability and Planning	179
7	Summary	180
7.1	Contributions	181
7.2	Future Work Directions	182
	References	184
	Appendix A. Adelopod SPI Interface	198
A.1	Notation	198
A.2	Command Set	199
	Appendix B. Adelopod Mechanical Drawings	210
	Appendix C. Adelopod Schematics	217
	Appendix D. Adelopod Printed Circuit Board Layout	228
	Appendix E. Adelopod RRT Metric Evaluation: Example Trees	239

List of Tables

3.1	Table of Existing Tumbling Robot Designs	34
4.1	Left arm link parameters of the Adelopod robot.	60
4.2	Adelopod Gearmotor Specifications	63
4.3	Summary of Adelopod Specifications	70
4.4	Summary of Adelopod-T Specifications	72
5.1	Experimental Results of Optimal Model Parameter Search	97
5.2	Test Platform Characteristic Summary	104
5.3	Forward Locomotion Experimental Statistics	109
5.4	Forward Locomotion Average Velocity Statistics	113
5.5	Adelopod Complex Terrain Statistics	118
5.6	Complex Terrain Statistics: Adelopod-T	120
5.7	Experimental results for maximum step height with measured friction.	122
6.1	Arm-body configuration parameters for the Adelopod robot.	136
6.2	Experimental results for displacements of 5 configuration transitions.	140
6.3	Table of Best Fit Parameters for Equation (6.35)	169
6.4	Parameters for RRT Metric Evaluation	174
A.1	SPI notational conventions	199
A.2	Values of dataSpec12	203

List of Figures

3.1	Figure demonstrating static stability of the Adelopod robot.	17
3.2	Depiction of a tumbling robot approaching and climbing a single step. . .	18
3.3	Consecutive frames from a video of the Adelopod while tumbling.	20
3.4	Example body connection graphs with primary body assignments.	25
3.5	Classification of ground-based tumbling robot designs.	26
3.6	Adelopod recovering from / tumbling away from an uncontrolled decent. . .	39
3.7	Aiming of rigidly attached directional sensors.	41
3.8	The P2AT, a planar 2-armed idealized tumbling robot.	48
3.9	Equivalent mechanisms of the P2AT.	51
3.10	Hybrid automaton representation of the P2AT.	53
3.11	Guards and transitions for the P2AT hybrid system representation.	55
4.1	The Adelopod tumbling robot.	58
4.2	Kinematic frame assignments of the Adelopod.	59
4.3	Depiction of Adelopod arm motion (workspace).	61
4.4	Details of Adelopod gearmotors.	63
4.5	Adelopod required machined parts.	64
4.6	Adelopod CAD models with shoulder actuation.	66
4.7	Photo of low-friction servo centering pads.	67
4.8	Example exterior shells.	67
4.9	System schematic for the Adelopod tumbling robot.	69
4.10	The Adelopod-T: a hybrid tumbling-crawling robot.	71
4.11	Adelopod-T interior showing crawler tread details.	71
4.12	The Aquapod: an amphibious Adelopod.	72
5.1	Considered morphologies for terrainability analysis.	77

5.2	Idealized obstacles with their parametrizations.	78
5.3	Example step reach of spoked wheel-legs.	82
5.4	Geometric maximum step reach for the n -spoked wheel-legs.	83
5.5	Schematic drawing of ideal and unstructured contacts.	84
5.6	Consecutive frames of the Adelopod climbing a step.	86
5.7	Quasi-static step climbing of tumbling and wheel-tail models.	87
5.8	Contour plot of the surface of Figure 5.14(i).	90
5.9	Quasi-static step climbing of singly-actuated tumbling robot.	92
5.10	Plot of μ_2 vs. μ_3 for idealized tumbling and wheel-tail models.	93
5.11	Frictional requirements of idealized and non-idealized tumbling models.	94
5.12	Considerations of step climbing for non-idealized tumbling robot.	96
5.13	Visual representation of optimal models for step climbing.	97
5.14	Minimum required coefficients of friction at body (wheel)-step interface.	99
5.15	Schematic diagram of idealized ditch crossing.	101
5.16	Geometric maximum step-ditch reach for the n -spoked wheel-legs.	103
5.17	Experimental hardware platform configurations.	105
5.18	Experimental terrains with Adelopod posed for size reference.	106
5.19	Pinching failure exhibited by the Adelopod on thick grass.	110
5.20	Tracks left in sand by experimental test platforms.	112
5.21	Adelopod specific resistances with legged robot comparisons.	116
5.22	Complex terrain experimental setup.	117
5.23	Example stepfield failure.	119
5.24	Adelopod forward locomotion velocity and energetic results.	124
5.25	Wheel-tail forward locomotion velocity and energetic results.	125
5.26	Stepfields used for terrainability evaluation.	127
5.27	Angled arm Adelopod complex terrain velocity and energetic results.	128
5.28	Straight arm Adelopod complex terrain velocity and energetic results.	128
5.29	Current consumption versus runtime for Adelopod over complex terrain.	129
6.1	Sample configurations with corresponding chart icons.	135
6.2	Configuration graph derived from discretizations of Section 6.2.1.	137
6.3	Graphical depiction of ${}^G P_{k+1}$ with ${}^G P_k = (0, 0)^T$ and $\phi_k = \pi/2$	141
6.4	Gaits derived from motion primitives.	142

6.5	Proposed modular schema for control of serial multiply-actuated tumbling.	145
6.6	Plots of stability versus arm configuration for $C = \{v_d, v_e, v_n\}$.	147
6.7	Rapidly exploring random tree search of the robots state space.	150
6.8	Example RRTs generated for the Adelopod over various terrain.	152
6.9	Depiction of the P2AT configuration with local controllability.	158
6.10	Depiction of sweeping motions resulting from arm angles.	160
6.11	Ruggedized Adelopod turning in sand with arm sweeping.	161
6.12	Two example support set manipulation sequences of the Adelopod.	163
6.13	Observed minimum cost of displacement vs. arm angle/friction.	168
6.14	Modeled cost versus heading for fixed values of ρ .	170
6.15	Resultant fits from least squares fit from model of Equation...	171
6.16	Models for isochronal metrics for three different horizons.	174
6.17	RRT planner results comparing weighted Euclidean and isochronal metrics.	178
A.1	Formats of the Adelopod SPI instructions.	199
B.1	Servo Mount	211
B.2	Servo Hinge	212
B.3	Arm Mounting Pins	213
B.4	Arm Mounting Pins	214
B.5	PCB Dimensions 1 of 2	215
B.6	PCB Dimensions 2 of 2	216
C.1	Schematic: Top PCB (sheet 1 of 6).	218
C.2	Schematic: Top PCB (sheet 2 of 6).	219
C.3	Schematic: Top PCB (sheet 3 of 6).	220
C.4	Schematic: Top PCB (sheet 4 of 6).	221
C.5	Schematic: Top PCB (sheet 5 of 6).	222
C.6	Schematic: Top PCB (sheet 6 of 6).	223
C.7	Schematic: Bottom PCB (sheet 1 of 4).	224
C.8	Schematic: Bottom PCB (sheet 2 of 4).	225
C.9	Schematic: Bottom PCB (sheet 3 of 4).	226
C.10	Schematic: Bottom PCB (sheet 4 of 4).	227
D.1	Layout: Top PCB top documentation	229
D.2	Layout: Top PCB top traces	230

D.3	Layout: Top PCB supply and ground layers	231
D.4	Layout: Top PCB bottom traces	232
D.5	Layout: Top PCB bottom documentation	233
D.6	Layout: Bottom PCB top documentation	234
D.7	Layout: Bottom PCB top traces	235
D.8	Layout: Bottom PCB supply and ground layers	236
D.9	Layout: Bottom PCB bottom traces	237
D.10	Layout: Bottom PCB bottom documentation	238
E.1	Weighted Euclidian pseudo-metric d_{we} example RRTs for $r = 0.448$ m. . .	240
E.2	Isochronal pseudo-metric $d_{iso_{r448}}$ example RRTs for $r = 0.448$ m.	241
E.3	Weighted Euclidian pseudo-metric d_{we} example RRTs for $r = 1.5$ m. . .	242
E.4	Isochronal pseudo-metric $d_{iso_{r448}}$ example RRTs for $r = 1.5$ m.	243

Chapter 1

Introduction

Mobile robots that are able to move about and effectively negotiate their environment are attractive for a wide variety of applications. Such applications include surveillance, inspection, and mobile sensing where robots often present cost-effective alternatives to human labor. Other applications include those that are potentially hazardous to humans; examples of these include search and rescue, monitoring and maintenance of toxic environments, and planetary exploration.

The vast majority of research into mobile robots has been limited to structured environments such as research labs, indoor office environments, industrial settings, maintained roads, etc. As the number of mobile robot applications grows, so does the need for such systems to be able to operate in unstructured (general) environments. Such environments often exhibit a wide variety of terrain including uneven surfaces and significant terrain irregularities. In some cases hazardous areas can be tactically avoided with careful path planning, but in general this is not always possible and obstacles must be negotiated directly. For these applications it is imperative that the robot exhibits a sufficient level of mobility to be able to perform required tasks.

In addition to mobility requirements, many mobile robot applications are further constrained by limitations on physical size and/or cost. It is often the case that small (inexpensive) robots are preferable if not required. In general, however, it is the case that miniature mobile robots sacrifice mobility in exchange for their small size. Additionally, the increased design complexity of miniature systems often increases both design and manufacturing costs. These issues have spawned large areas of research dedicated to

developing and utilizing new methods of locomotion for mobile robots that exhibit increased mobility on smaller scales. Aside from the numerous advances in wheeled and legged robots, there has been a significant push to discover more interesting forms of robotic locomotion (e.g., wheel-leg robots, jumping robots, snake-like robots, tensegrity robots, etc.).

1.1 Motivation

In this thesis we present a relatively new and unexplored form of robotic locomotion called tumbling which aims to address some of the aforementioned existing limitations of miniature mobile robots. Tumbling robots, which we will formally define in the next chapter, are robots that exhibit net body rotations while moving about. Additionally, while not required, nearly all tumbling robots allow (and benefit from) contact between their body and the terrain. Such terrain-body interactions along with the characteristic net body rotations give rise to some surprising capabilities unique to tumbling systems. Most interesting is their capability to provide increased mobility on surprisingly small scales along with their inherent hardware simplicity that enables minimalistic design (and therefore decreased system cost).

In order to compare the mobility of robotic systems some form of normalization is required to make up for the intrinsic differences between them. In terms of miniature mobile robots, a natural normalization is their size (e.g., profile or volume). System performance by this metric is some measure of its achievable mobility-to-size ratio. With regard to mobility-to-size, tumbling robots often excel due to the utilization of their bodies in achieving locomotion. Traditionally terrain-body contacts (i.e., collisions) are avoided in robotics but it turns out that their utilization can be quite beneficial. In the context of tumbling robots, the extra interactions provide extra options for overcoming terrain irregularities, effectively increasing the space of possible trajectories. Additionally, when combined with the characteristic net body rotations, the body itself can be used to actively push/pull the robot over or through the terrain. Thus, tumbling can be viewed as a more efficient utilization of the robot's exterior, providing a distinct advantage over other traditional forms of robot locomotion.

In addition to heightened mobility, tumbling also is attractive due to its conservative hardware requirements. Depending on the design goals and/or application, various types of tumbling robots can vary greatly in their hardware complexity (i.e., number of moving parts, actuators, etc.). However, the allowance of terrain-body interactions along with utilization of the body in producing propulsion results in systems with very few (if any) immobile configurations. This often remains true even for underactuated tumbling systems, thus tumbling presents a lower bound of minimum hardware complexity such that sufficient mobility can be achieved with remarkably few moving parts and actuators when desired or necessary. In this regard, forms of tumbling can be considered minimalistic approaches to robotic locomotion that exhibit all of the benefits of minimalistic design (i.e., increased economy, reliability, ease of manufacturing, etc.) while preserving the ability to traverse many real-world terrains of significant complexity.

1.2 Thesis Statement

There has been little work addressing tumbling for robot locomotion. The work that does exist, lacks precision and fails to offer any formal analysis regarding the advantages of robotic tumbling locomotion. This issue is further compounded by the fact that tumbling locomotion is relatively nonintuitive and therefore its merit as a means of locomotion is not immediately obvious. Additionally, issues involving the design, evaluation, and planning for such systems are possible. The purpose of this work is to begin to address these issues and make clear the benefits and issues surrounding tumbling as a means of robotic locomotion. The goal is to promote tumbling as a feasible method of locomotion for future mobile robot designs and establish a framework in which the development, discussion, and evaluation of such systems is possible.

In response to the need to improve the current state of the art, this work aims to prove the the following thesis:

Tumbling is a largely unexplored method of robotic locomotion that has the potential to enable increased mobility relative to other forms of robotic locomotion with respect to the robot's size and/or complexity.

1.3 Approach

The approach of this thesis to explore the merit of tumbling as a means of robotic locomotion is to:

- Develop definitions and identify basic principles regarding tumbling locomotion for mobile robots.
- Assemble a catalog of existing tumbling robots to establish the state of the art. Robots are included based on the definitions we develop in this thesis.
- Present a preliminary assessment regarding the mobility of tumbling systems as motivation for their study. Focus is on general designs that capture underlying mechanisms of locomotion while avoiding the inherent complexity of final design instantiations.
- Detail the design of several preliminary tumbling systems and directly evaluate their performance. In doing so we establish benchmarks for future comparisons of tumbling robots/locomotion.
- Begin to address the issues of motion planning applied to serial multiply-actuated tumbling, a class of (generally) underactuated tumbling robots.

Chapter 2

Background

2.1 Design for Mobility

Generally, a land-based robotic platform’s mobility, or ability to traverse terrain, is proportional to its overall size. This limitation is obvious in conventional wheeled and tracked platforms where bigger robots almost always outperform smaller robots. There has been significant work in developing new methods of robotic propulsion that take a step away from conventional designs, providing increased mobility on smaller scales. Examples include modular robots [1], wheel-leg robots [2, 3], jumping robots [4, 5], snake-like robots [6], tensegrity robots [7], and tumbling robots [8, 9].

2.2 Tumbling

Tumbling robots, as described in our work, constitute a largely unexplored area of robotic locomotion (one possible reason for this is the fact that tumbling is not readily seen in nature and is therefore non-intuitive to human beings). In the literature, the first mention of a dedicated tumbling robot occurs in [10] where the authors briefly discuss Turbot 2, a two-armed tumbling robot that exhibits phototaxis in generally lit environments. Although the exact details of the control circuit are not mentioned, the authors describe the general Turbot control topology as two chaotic oscillators (one for each arm) weakly coupled by a single analog neuron. Video of Turbot 2 in motion can be found in [8]. Another tumbling robot is presented in [11]; this particular instantiation

uses a simple state machine based on relative values from two pairs of photosensors along with motor stall detection. The robot activates one motor at a time based on which of the six possible states it is currently in, resulting in positive phototaxis. The above methods succeed in producing directed tumbling motion, however they require significant expertise to apply, lack the plasticity required by complex tasks, and fail to generalize to other tumbling platforms.

Another interesting tumbling robot is the TETwalker [9]. The TETwalker is a tetrahedral robot that achieves motion by controlling its center of gravity. This is achieved by changing the lengths of its struts (edges of the tetrahedron). By moving the center of gravity outside of the robot's stability margin, a tumble is achieved. Although the current hardware realization results in a discrete tumbling motion, future works plan to add actuation (significantly increasing the hardware complexity) that will allow the robot to morph over the terrain, absorbing the irregular features as it moves.

2.3 Mobility Analysis

Before the advent of robotics, work related to the study of mobility was centered around the design of off-road vehicles for both civilian transportation and military use. Central to this area of interest is the field of terramechanics, the study of soil interaction of large vehicles. Bekker, in his thorough work [12, 13, 14], characterizes the performance of wheeled and tracked vehicles over various soil conditions. In his discussion, Bekker presents various metrics regarding vehicle-soil interaction including drawbar pull, geometric steps and ditches, wheel/track sinkage, etc. While these ideas are common to mobile robots for rough terrain, their application is somewhat limited due to their general applicability only to large/heavy vehicles. Additional work in this area includes [15].

2.3.1 Mobility of Mobile Robots

Mobility plays a crucial role in the field of mobile robots. Some of the first works to specifically address mobility for mobile robots came from the study of walking robots. In the works [16, 17], Waldron and McGhee stress the importance of robot design on performance. In these two works, the authors begin to establish a framework for

characterizing locomotion capabilities of various types of mobile robots. Presented are ideas pertaining to the use terrain's power spectral density and idealized obstacles to quantify performance. In terms of idealized obstacles, the authors discuss various geometric measures but ultimately stress the usefulness of two parameter obstacles where multiple idealized features are combined to make a more sophisticated yet still easily parameterizable terrain feature. Many of these performance characterizations were applied to the design and evaluation of the adaptive suspension vehicle [18, 19] where computer aided design was used to design legs for optimal obstacle crossing ability.

In [20], Hirose et al. identify various characteristics of various methods for producing mobile robot locomotion for lunar rovers. This work is interesting in that begins to raise questions regarding the relative merit of different types of locomotion.

A rather comprehensive list of mobility measures appear in the master's thesis of Lietzau [21] addressing mars rover performance. Topics addressed include traction (static, dynamic, drawbar pull, etc.), turning radius, tipping/slipping, slope performance (max angle and slippage), obstacle crossings (cliffs, crevices, steps, spikes, and side/center ramps), and energy consumption.

Gennery in [22] developed measures of height, slope, and roughness for lunar rovers using binocular camera data. Values are calculated by performing a weighted least squares fit of planes to equally spaced points in the data (height and slope are direct results of the fit while roughness is measured in terms of the fit's residual). Weights are determined from the covariance of the measurements and the distance of points from the center of the fit.

In [23], Seraji introduced the Fuzzy Traversability Index to quantify the traversability (the ease of traversal by mobile robots) in terms of linguistic variables represented by fuzzy sets. Terrain characteristics considered include slope, roughness, and hardness. Slope membership is calculated using the methods of [22] however roughness is redefined linguistically based on the average size and density of rocks in the area of consideration. Hardness is also defined linguistically based on the result of shooting small puffs air into the terrain and measuring the resulting displacement. Seraji later extended his work in [24] to include both local and global traversability indices.

2.3.2 Focus on Rigor and Repeatability

While many works acknowledge the importance of mobility, many lack comparable results. On particular work that stresses the importance of comparable results is [2]. In this work the authors test their robot, RHex over a wide variety terrains such as carpet, grass, gravel, and an obstacle course among others where focus is placed on rigor and repeatability. Additionally, the authors address issues with results pertaining to energetic analysis of mobile robots. Specifically, the authors promote the use of metrics such as specific resistance [25] reported for the entire energy usage of the robot. In [26] we see a similar approach where the authors run two well established mobile robots over a test-bed.

Another work to address the general lack of repeatability in mobility evaluations is [27]. Here the authors introduce stepfields, a repeatable terrain based on an obstacle course used to test the RHex mobile robot platform in [2]. A stepfield pallet consist of a grid of square wooden posts of various heights that form a reconfigurable and repeatable testbed for mobile robots. The authors present standards for three different scales of pallets to accommodate different size classes of robots. Additionally, the authors propose various pallet configurations and rules for generating random stepfields for use in experiments or competitions. A previous work by the same group, [28], define the metrics coverability and crossability which quantify the difficulty encountered by robots traversing rough terrain. These metrics, combined with stepfields, allow designers the ability to quantify the performance of a given robot, however the properties of the robot are not directly included in the metrics, therefore direct comparisons of non-similar robots is difficult.

Apostolopoulos, in [29, 30] identifies and addresses the often ad-hoc nature of robot design through the development of new metrics along with a framework for improved configuration of wheeled mobile robots (synthesis and analysis of wheeled rovers to predict performance). The work is focused on study of parametric configuration equations which express the quantitative relationships between the robot configuration, task requirements, and robot performance. The framework combines computation, simulation, and design to aid in producing optimal configurations in the performance indices of trafficability, maneuverability, and terrainability. This work is revolutionary in that it presents specific methods that focus on producing generalized methods applicable

to the configuration synthesis and performance evaluation of general wheeled mobile robots.

An open issue of mobility analysis and perhaps the most interesting with respect to our work is that of normalization. The above mentioned metrics enable performance measures over various (repeatable) terrains, however, the results of such metrics vary greatly with respect to the tested robot’s characteristics (e.g., size, mass, morphology, etc.). Without any form of normalization, comparisons between robots are For our work, where we are concerned with the potential of a type of locomotion instead of actual performance of a particular instantiation, some form of normalization is necessary. Noteworthy work that directly address this issue include that of [31, 32]. In these works, Thueer quantifies relative performance of various suspension configurations for wheeled rovers where normalization is achieved through clever design that allows for testing various robot configurations while maintaining equivalent mass and volume characteristics.

2.4 Stability

Over the past few decades there has been a significant amount of work in developing gaits for walking robots. Included in the literature are a multitude of different stability measures that we believe to be useful in developing methods of control for tumbling robots. We are most interested in the stability margins developed for legged robots with greater than two legs, as these measures require little or no modification when applied to tumbling robots. In this section we provide a brief overview of some of the more applicable legged stability measures. For a more complete discussion along with an in depth comparison, we direct readers to [33, 34].

The first stability margin for quadruped robots, the *static stability margin*, was proposed in [35]. The static stability margin is defined to be the shortest distance between the boundary of the support polygon created by the feet in contact with the ground and the robot’s center of gravity projected vertically onto the polygon. This measure is applicable to static robots on a smooth horizontal surface, however it was later extended in [36] to handle uneven terrain by projecting the feet contact points vertically onto a horizontal plane. In this same work the authors define the *support state longitudinal stability margin* which simplifies calculations by only taking distances

to the support polygon along the direction of travel. The simplified support state longitudinal stability margin was found to be misleading under certain crab angles (angle between longitudinal axis of robot and direction of motion) in [37]. Instead they proposed the use of the *body-longitudinal (or lateral) stability margin* which measures stability along the longitudinal and lateral axes of the robot. This was shown to more accurately approximate the static stability margin (true stability margin under quasi-static motion on even terrain) for quasi-static motion regardless of the crab angle.

Despite being able to handle uneven terrain, the improved static stability margin of [36] does not actually take the degree of terrain unevenness into account. This was addressed by the authors of [38] who defined the *energy stability margin* in terms of the minimum energy required to tip the robot about any two feet in support. Finally, [39] proposes the *normalized energy stability margin* as the energy stability margin of [38] normalized by the mass of the robot. This prevents the robot’s mass from affecting the stability measure.

All of the above mentioned stability margins are based on static assumptions and fail to take dynamics into account. Although most of our proposed work is for quasi-static motion over even terrain, we believe that some of the dynamic stability margins may prove useful in both static and dynamic cases. In addition to being required when removing static assumptions, the dynamic stability margins provide alternate formulations of stability that are also applicable in static conditions which may lead to more convenient tumble control calculations (minimizations).

In [40] the authors define stability margins in terms of moments about the edges of the support polygons. Specifically, the authors define the *dynamic stability margin* as the minimum resultant moment about the boundaries of the support polygon normalized by the gravitational force on the system. The work [41] takes a geometric approach and define the *force-angle stability margin* as the minimum angle between the net force (excluding the ground reaction forces) on the center of mass and the normals of the tip-over axes (edges of the support polygon). In [42, 43] the authors propose stability margins based on the zero moment point from biped literature. These stability margins are analogous to those of [35, 36] with the difference that the center of gravity is projected along the resultant force acting on the robot, thus it also suffers in the presence of uneven terrain.

It was shown in [33] that all of the aforementioned stability margins are inaccurate in the presence of inertial and manipulation effects. This shortcoming was addressed in [44] where the authors extended the work of [45] to come up with the *normalized dynamic energy stability margin*. This margin was shown to be exact in the presence of robot dynamics and manipulation forces.

2.5 Motion Planning with Differential Constraints

Nonholonomic constraints significantly complicate the motion planning problem by inducing constraints on the tangent bundle of the configuration space. Therefore arbitrary paths in the configuration space are not necessarily realizable by the system (i.e., holonomic planning methods are not directly applicable). As a result, nonholonomic motion planning is often considered as two separate problems referred to as the decision problem and the complete problem. The decision problem concerns itself only with the existence of feasible paths while the complete problem is that of actually finding such paths [46].

An important concept from nonholonomic control theory closely related to the decision problem is the notion of controllability. A system is said to be small time locally controllable from a configuration q if the set of configurations reachable from q before some time τ contain a neighborhood of q for all $\tau > 0$. This desirable property has been shown to be linked to the control Lie algebra of the system. By the Lie algebra rank condition (LARC), a nonholonomic robot is small time locally accessible from q if and only if the control Lie algebra of the system at q has full rank; if the system is symmetric small time local controllability is also implied (see [47, 48]). Algorithms exist for checking the LARC in [46, 49].

One of the first works where nonholonomic control ideas were applied specifically to mobile robots was that of [50]. In this paper, the author presents a constructive proof of controllability for a car-like robot in the plane. The proof assumes a kinematic model equivalent to car-like systems and therefore fails to generalize to other mobile robot configurations. The work was later extended in [51] to n -body car-like systems comprised of a robot pulling $n - 1$ trailers. Additionally, in [50] Laumond presents a planner based on a two-phase approach where the first phase is computed off-line and brings the robot close to the goal configuration while the second phase generates trajectories from

pre-defined maneuvers based on the results of the controllability analysis. Specifically the maneuvers consist of translating sideways (parallel parking motion) and turning in place. Despite the success of the work the proof of controllability is specifically for a car-like robot and fails to generalize to other mobile robots. Additionally the resulting trajectories are far from optimal, as they include many time consuming maneuvers.

The work [52] addressed the generality shortcoming of [50] and presented the first general nonholonomic planner for controllable systems without drift. The planner assumes a suitable holonomic path is provided and then finds control sequences based on the P. Hall basis construction of the control vector fields that moves the robot along the path. The planner was shown to be exact for nilpotent systems and can achieve solutions to arbitrary accuracy through iteration for non-nilpotent systems. The work [53] removes the assumption that a holonomic path is given and present a planner for n-body car-like robots in the presence of obstacles. The planner uses Dijkstra's algorithm to search a discretization of the free configuration space. The resulting algorithm is asymptotically complete for car-like robots and asymptotically optimal in the number of reversals for n-body car-like robots. Despite the attractive guarantees, the algorithm has time/space complexity that is exponential in the number of bodies and is therefore not practical for a large number of trailers.

Up until this point, all of the reported works have been based on controllability of nonholonomic systems. A separate approach in [54] exploits properties of chained form systems and uses sinusoidal inputs to steer the system. The main idea is that for chained form systems one can find sinusoidal inputs that effect successive subsets of the state variables.

2.6 Minimalistic Manipulation

Tumbling robots are interesting in that they generally violate many (if not all) of the assumptions of above section's works. A related area of study more along the lines of tumbling robots is that of graspless manipulation and more specifically rolling polyhedral bodies. Instead of avoiding nonholonomy this branch of research looks at nonholonomic phenomena as a desirable property in designing minimalistic systems (e.g., low degree of freedom dexterous manipulators). This idea is very similar to those that have inspired

our research into tumbling locomotion and we believe that with some modifications it might be possible to incorporate tumbling robots into the developed theory.

Some of the earlier works to look at grasps manipulation include [55, 56]. In [55], the authors motivate such manipulation and classify the manipulation options as pushing, tumbling, and pivoting. In [56] an actual planner is presented that manipulates polyhedra in unknown configurations to reduce uncertainty of the final configuration. Works that address a motion planning problem similar to the one we are interested in include [57, 58, 59, 60]. In these works, the authors consider polyhedra rolling on the plane. Issues such as reachability and steering are addressed. In [61] the authors presented a generalized notion of nonholonomy that allows for discrete and hybrid systems. Two different types of nonholonomic behavior are identified for such systems and are defined as internal and external behaviors respectively. Such a framework might prove useful in our analysis of tumbling locomotion where the major difference is that we have replaced external manipulation with tumbles induced through self-deformation. Whether or not these tools will prove useful is unknown to the authors at this point.

Chapter 3

Tumbling and Robotic Tumbling Locomotion

Tumbling robots are ground-based mobile robots that utilize tumbling motions while ambulating and exhibit a variety of benefits that make them attractive candidates for mobile robot tasks. The goal of this chapter is to make precise what exactly is meant by the terms “*tumbling*” and “*tumbling robot*.” In doing so, this chapter establishes the first formal definitions regarding tumbling for mobile robots along with some additional useful terminology regarding tumbling. With the established definitions and terminology it is possible to accurately characterize tumbling locomotion and robots while distinguishing them from other existing forms of locomotion and robots. Various types of tumbling robots are identified and discussed along with their respective characteristics. Additionally, this chapter introduces a planar toy example of tumbling analogous to some existing real-world tumbling systems that serves to both demonstrate the basic principles of tumbling and provide a base for research into the topics of motion planning and control for tumbling robots.

3.1 Discrete Tumbles

With respect to mobile robots, the term tumbling originates from the appearance of the first known dedicated tumbling robots, turbots [10, 8], while in motion. While ambulating, these robots utilize unstable states in which the robot effectively *falls* forward

through the environment, behaving as an inverted pendulum. The end result of this process is some linear and rotational displacement (ambulation). We call such motions discrete tumbles due to the fact that they have an identifiable beginning and end.

Definition 3.1 *A **discrete tumble** is a sequence of unstable states in which the system accelerates with gravity about the **tumble axis** formed by its contact points with the terrain. The tumble is said to begin at the moment the system becomes unstable and ends either when stability is regained or the tumble axis changes, in which a new tumble begins immediately.*

Central to the above definition is the notion of stability. Borrowing from works pertaining to legged systems, a number of useful stability measures exist with which it is possible to quantify the stability of the system at any instant (see Chapter 2 for a review of common choices). As an example, if the system is assumed to be quasi-static, we can apply the intuitive static stability margin of McGhee and Frank, defined as follows:

Definition 3.2 *The **static stability margin** is equal to the shortest distance from the vertical projection of the center of gravity to any point on the boundary of the support pattern. If the pattern is statically stable, the stability margin is positive. Otherwise, it is negative [35].*

Here the support pattern is defined as (modified from [35, 36]):

Definition 3.3 *The **support pattern** associated with a given state is the convex hull (minimum area convex polygon) of the point set in a horizontal plane which contains the vertical projection of all points of contact between the robot and terrain.*

In addition to the above definitions, it is also useful to be able to refer to the supporting points in contact with the terrain separate from their vertical projections; these points make up the support set.

Definition 3.4 *The **support set** associated with a given state is the set of all points on the robot in contact with the terrain.*

The above tumbling stability concepts are illustrated in Figure 3.1 where a two-armed static-body tumbling robot is shown in a stable position where the terrain is

simply the xy -plane. The support set C is defined by the three vertices in contact with the ground v_d , v_e , and v_n . Vertex v_n is a discrete contact while vertices v_d and v_e define an edge of the robot's body in contact with the ground. From this we can express C as the collection of points as follows:

$$C = \{v_n, \overline{v_e v_d}\} = \{v_n, av_d + (1 - a)v_e \mid a \in [0, 1]\}. \quad (3.1)$$

The support pattern \mathcal{P} is the convex hull (minimum area convex polygon) of the support set projected into a horizontal plane. Because the terrain in this example is itself a horizontal plane, the projections of points in C are equivalent to the points themselves; therefore the support pattern is simply the convex hull of the support set,

$$\mathcal{P} = \mathcal{CH}(C_{\text{proj}}), \quad (3.2)$$

where \mathcal{CH} denotes the convex hull formally defined as

$$\mathcal{CH}(\mathcal{X}) \equiv \left\{ \sum_{i=1}^k a_i x_i \mid x_i \in \mathcal{X}, a_i \in \mathbb{R}, \sum_{i=1}^k a_i = 1, i = 1, 2, \dots \right\}. \quad (3.3)$$

The support pattern \mathcal{P} is depicted in the figure by the shaded triangle with the black outline. Stability can be calculated for each edge of the support pattern's boundary, depicted by the dashed lines from the projected center of mass, p_{proj} , to edges of the support pattern boundary. The static stability margin of the configuration shown is calculated as

$$s = \min_{p \in \partial \mathcal{P}} (\|p_{\text{proj}} - p\|), \quad (3.4)$$

where $\partial \mathcal{P}$ is the boundary of \mathcal{P} . Assuming quasi-static motion, a discrete tumble will occur at the instant that p_{proj} leaves \mathcal{P} (i.e., $s < 0$). As an example, as ϕ_4 rotates the right arm in the direction of the ground, the body of the robot will react by rotating about the edge $\overline{v_e v_d}$, causing p_{proj} to approach and eventually cross edge $\overline{v_e v_d}$ thus initiating a tumble. In cases where the quasi-static assumption is not applicable (i.e., in the presence of significant inertial or external forces) a dynamic measure of stability such as the normalized dynamic energy stability margin [62] can be used.

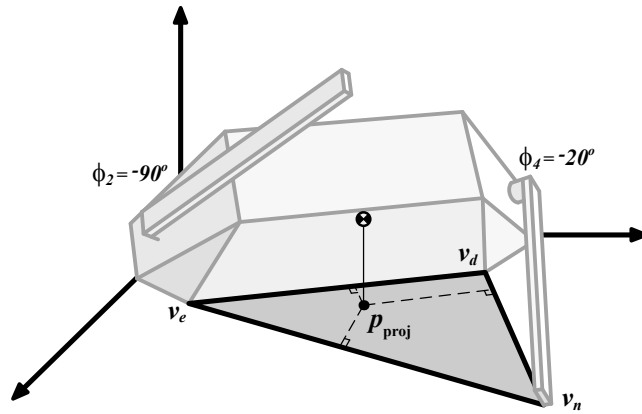


Figure 3.1: Figure demonstrating static stability of the Adelopod robot. Stability measures to each edge of the support pattern are depicted by dashed lines from the projected center of mass, p_{proj} , to the respective edge.

From an energy standpoint, a discrete tumble is the conversion of potential energy into kinetic energy as the robot accelerates with gravity through the tumble. On severely sloped terrain it is possible to have a large number of consecutive discrete tumbles where potential energy is converted with altitude. On flatter terrains, however, a tumble often leaves the robot in a low energy state far from any feasible tumbling states. From such states it is necessary for the robot to accumulate additional potential energy through actuation before another discrete tumble is possible. In general, locomotion using discrete tumbles requires alternating between stable energy building states and unstable tumbling states.

Locomotion over extended distances is possible by repeatedly inducing discrete tumbles. As an example Figures 3.2(a)-(c) depict a planar single-armed rectangular robot tumbling up to and over a single step. The entire sequence is broken into three parts for clarity: the approach, initiation, and climb. Each subfigure contains noteworthy snapshots of the robot's configuration along with the resulting trajectory of the robot's center of mass; discrete tumble states are denoted by dashed trajectory curves. This sample tumbling sequence demonstrates the various methods of manipulating the support set including stable energy building states (solid trajectory curves), discrete tumbles (dashed trajectory curves), and stable addition of contact points. The stable addition of contact points occurs when the robot rotates the arm back into contact with the terrain

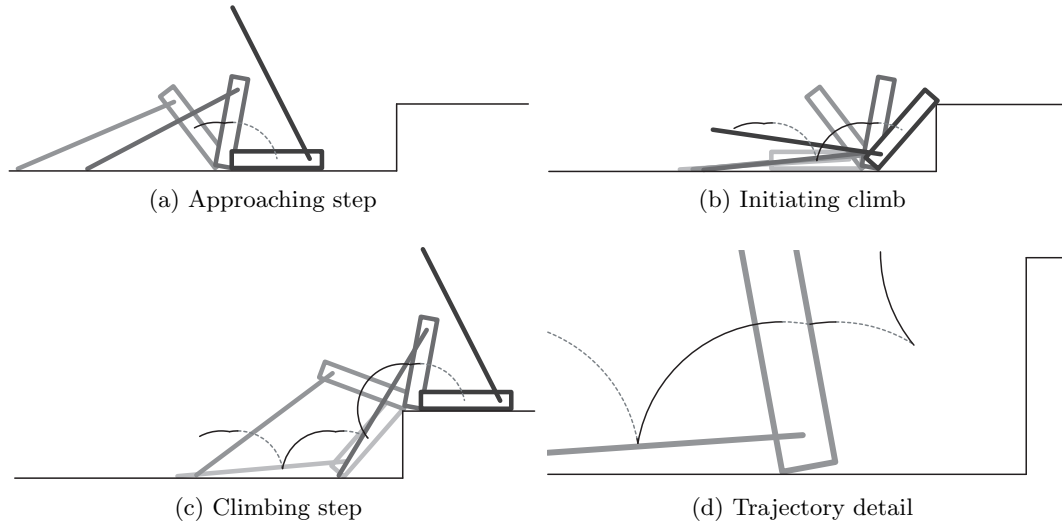


Figure 3.2: (a)-(c) Depiction of a single-armed tumbling robot approaching and climbing a single step. Sequential configurations are distinguished by varying shades of gray with darker lines depicting newer configurations. Also shown is the trajectory of the robot's center of mass up to the most recent configuration: solid curves denote stable transitions while dashed curves denote tumbling transitions. (d) Detail of tumble trajectory showing tumbles resulting from the robot's thickness.

immediately following a discrete tumble (e.g., between the final configuration snapshot of Figure 3.2(a) and the first configuration snapshot of Figure 3.2(b)). Although not shown, it is also desirable in more complicated tumbling systems to utilize the stable removal of a contact point.

Figure 3.2(d) shows an enlarged view of the trajectory with the robot just in front of the step. Here it is possible to see an instance of a small discrete tumble resulting from the robot's thickness not visible in Figures 3.2(a)-(c). The size of such tumbles are dependent on the body mass, body geometry, and arm mass. The figure depicts the trajectory with a massless arm, however with significant arm mass and/or a thin body it is possible for these tumbles to not exist, resulting in a stable transitions of the support set.

3.2 Major Tumbles and the Definition of Tumbling Robots

The most straightforward way to define a tumbling robot is simply as any robot that tumbles in order to move about. This classification sufficiently captures many tumbling robots, however it excludes some special cases and is simultaneously overly broad for the purpose of this work. For instance, one can easily argue that some current forms of robotic locomotion could (incorrectly) be considered tumbling robots; one such example is the class of bipedal robots. A bipedal robot can be considered to alternate between single and double support phases where a statically unstable single support phase, by our definition, is a tumble. Additionally, it is interesting to note that in the presence of compliant terrain (i.e., sand, thick grass, etc.) a tumbling robot that normally utilizes discrete tumbles may never become unstable. In these situations it is possible for the terrain to conform to the shape of the robot, resulting in a smooth rolling body motion and preventing any would-be discrete tumbles. This introduces the awkward situation where the definition of tumbling robots would be dependent on the terrain.

A more suitable definition can be formulated by identifying the defining characteristic of a tumbling robot not as discrete tumbling but rather the end over end body motion exhibited while ambulating. By this observation we arrive at our definition of a tumbling robot that we will use throughout the remainder of this thesis.

Definition 3.5 *A **tumbling robot** is a robot that ambulates by the strategic manipulation of its support set achieved primarily through major tumbles.*

Here the end over end body motion is captured by the utilization of major tumbles:

Definition 3.6 *A **major tumble** starting from any reference state consists of a full revolution of the robot's primary body about one or more axes that results in some non-zero positional displacement in the world.*

An example major tumble exists in Figure 3.2 starting with the last (darkest) configuration of Figure 3.2(a) and ending with the last (darkest) configuration of Figure 3.2(c). Figure 3.3 extends the previous planar scenario by demonstrating tumbling in \mathbb{R}^3 . In this figure we show eight stills taken from a video of an experimental tumbling robot tumbling over some tire tracks left in soil at a construction site. In this particular

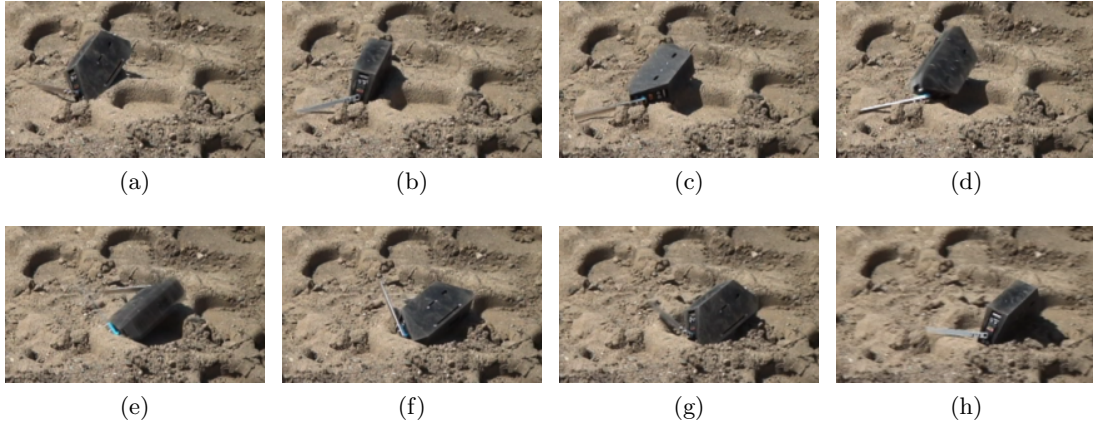


Figure 3.3: Consecutive frames captured at 1/3 second intervals from a video of the Adelopod tumbling through deep tire tracks from a construction vehicle.

example the end over end motion of the primary body (black trapezoidal prism) is apparent as the robot progresses over the terrain. Specifically, two major tumbles can be seen starting with the states of Figures 3.3(a),(b) and ending with the states of Figures 3.3(g),(h) respectively.

Compared with discrete tumbles, major tumbles are less useful when describing actual tumbling trajectories. This is due largely in part to their dependence on a reference state along with the fact that there exist an infinite number of possible reference states for any trajectory of non-zero length. The main purpose of this definition is to capture the defining characteristic of tumbling locomotion which we have identified as the aforementioned end over end motion of the robot’s primary body. It is interesting to note that, within our defined scope, we encompass the notion of continuous tumbles which allows for some very interesting types of tumbling robots that we will discuss later in Sections 3.3 and 3.4.

The final issue to address is what exactly is meant by the term “*body*” (primary or otherwise). For all practical purposes we assume that robots are collections of physical bodies connected by joints that interact with the world through some form of actuation. At this point we make no restrictions on the physical bodies or joints (i.e., bodies can be rigid or flexible; joints can be active or passive). In addition to the physical bodies that make up the robot, we introduce the notion of a primary body on which our definitions

of tumbling and tumbling robots are based (see Definitions 3.5 and 3.6). It is important here to make clear the difference between the two. A *physical body* from which the robot is comprised is taken to be “a material thing, an object; something that has physical existence and extension in space” (OED, n., V.17.b [63]). The *primary body*, on the other hand, is taken loosely to mean the “main, central, or principal part, as distinguished from subordinate or less important parts; the part round which others are grouped, or to which they are attached as appendages, etc. Freq. with *of*” (OED, n., II.5 [64]). Each robot is assumed to have a single physical body that is designated as the primary body. Finally, in addition to physical and primary bodies, it is also beneficial to introduce the notion of a composite body. Composite bodies, informally, are groups of bodies that work together to achieve actuation. Formally, we define composite bodies as follows:

Definition 3.7 *A **composite body** is a closed kinematic chain of physical bodies connected only by bounded joints. Multiple closed chains that share a common physical body are considered a single composite body.*

Due to the overwhelmingly extensive variety of mobile robots, the formulation of a precise definition for the primary body applicable to all cases is quite difficult. In simple cases, the primary body is easily identified as the central physical body from which power, control, and actuation originate (e.g., in wheeled, treaded, and legged robots). However, this assignment quickly breaks down as more interesting robots are considered. In systems with multiple power sources, distributed control, and/or modular hardware the identification of a single physical body as the primary body becomes less clear or even impossible. Take for instance snake-like robots and morphing robots with parallel structure; in these systems the robot is comprised of many physical bodies and joints that operate as a whole with no single module “more important” than another. Fortunately, as we shall see, the resulting tumbling/non-tumbling classification of the majority of such systems is not dependent on the choice of the primary body.

In fact, all of the primary body assignment issues we have discovered that affect our tumbling definitions arise in robots that utilize physical bodies actuated by unbounded revolute joints (e.g., wheeled robots, treaded robots, etc.). In these cases, it is possible to change the tumbling classification by reassigning the primary body. For example,

identifying a wheel of a car-like robot as the primary body results in the robot, by our definitions, being classified (improperly) as a tumbling robot. Assigning the primary body as the car's chassis, however, results in a (correct) non-tumbling classification. Fortunately, these problematic systems are the same in which the primary body is often evident (i.e., a central body from which power, control, and actuation originate exists) and/or they are easily identified as established non-tumbling robots. For cases in which this is not so, we have found that an intelligent/convenient selection of generalized coordinates (i.e., one that results in the simplest equations of motion) almost always leads naturally to a meaningful identification of the primary body as that to which the base reference frame is attached. For the aforementioned car-like example, attaching the base reference frame to the car's chassis results in much more elegant equations of motion when compared to an assignment in which the base frame is attached to a wheel.

In an effort to eliminate the above issues, we make the observation that the transmission of data and power through unbounded revolute joints is quite uncommon, especially in mobile robotic systems. Such setups require additional hardware that in general increases the size and complexity of the resulting system and, from an engineering perspective, are avoided unless absolutely required by the specific design application. With this in mind, we are able to, for the purpose of this thesis, make the assumption that all data and power transmission between physical bodies occurs only through bounded joints. Under this assumption it is then possible to present a procedure for assigning the primary body that results in unique tumbling/non-tumbling classifications. The procedure is presented below and is assumed throughout the entirety of this thesis unless otherwise noted.

Procedure 3.1 (Primary Body Assignment)

1. If such exists, the primary body is assigned to the central physical body from which power and centralized high-level control are generated.
2. If the above does not exist or is not apparent, then the primary body is assigned as follows:
 - (a) Construct a graph representation of the robot where physical bodies are represented as vertices and joints as edges.

- (b) Remove any edges from the graph that represent unbounded revolute joints on the robot.
- (c) Assign the primary body to a physical body in the connected component that contains the power and high-level control.

The connected component of step 2(c) is guaranteed to exist due to the previous assumption that no data or power are passed through unbounded revolute joints (those that were removed from the graph in step 2(b)). Additionally, because the connected component of step 2(c) contains no unbounded revolute joints, the resulting tumbling/non-tumbling classification of the robot is independent of the primary body assignment. Therefore, we suggest an assignment that is most meaningful or convenient (e.g., with respect to the chosen set of generalized coordinates and the resulting equations of motion).

In Figure 3.4 we show the results of applying Procedure 3.1 to two example robots. The first example (Figures 3.4(a)-(c)) is of the Adelopod-T, a tumbling robot with the addition of crawler treads that wrap around central physical body of the robot. For the sake of this example we assume that the primary body assignment is not evident and thus proceed with step 2 of the assignment procedure. The resulting graph of step 2(a) contains nine physical bodies (the central physical body, two arms, four tread rollers, and the two crawler treads) and is shown in Figure 3.4(b). Here we can see that the structure is tree-like with all bodies emanating from the central physical body through unbounded revolute joints (denoted by R^* where the $*$ designates an unbounded joint). The dashed lines between the rollers and crawler treads represent virtual links that illustrate the rotational dependence between the rollers and treads (i.e., each system of two rollers and one tread has $3 - 2 = 1$ degree of freedom). These virtual links do not count when identifying connected components or composite bodies. Removing the unbounded links as in step 2(b) leads to the graph of Figure 3.4(c) where the connected components are identified by the gray rectangular regions. Finally, the primary body is assigned to the primary connected component that contains the power and high-level control. In this case, the primary connected component is a single body shown circled in Figure 3.4(c). Figures 3.4(d)-(f) show the output for another interesting leg-crawler hybrid robot called TITAN X [65]. This particular robot is a four legged robot with three degrees of freedom per leg and additional crawler treads on the second link of each

leg. The primary body procedure is again straightforward with the difference that there are multiple physical bodies in the primary connected component (see Figure 3.4(f)) and thus the primary body assignment is not unique. Per our above recommendations, we have chosen the most central physical body that also carries the power and high-level control as the primary body in this case.

3.3 Classification of Tumbling Robots

Classifications can be useful on a number of levels. With respect to mobile robots, taxonomies are useful for discussion, organization, and can be used to show relations between various designs. Many of these taxonomies are created to accompany a new robot design and are intended to show where the new design fits in relation to existing ones. In this respect taxonomies can be used as a visual indication to the novelty of proposed designs.

Common taxonomy divisions of land-based robots include wheeled, tracked, walking, jumping, etc. In these taxonomies tumbling robots often fall under the catch-all category *other* and are thus of little use regarding tumbling. Despite this trend, there are a couple existing classification schemes that are worth mentioning. The first is the taxonomy by Bartlett et al. in [66] used to motivate design choices for a new design for a lunar rover. This taxonomy is interesting in that it is the only instance we have found that specifically includes tumbling as a class of mobile robots. Tumbling appears twice in the classification (once under continuous, non-wheeled robots and again under discrete, walking, parallel robots) but is not addressed in the text.

Another interesting and noteworthy taxonomy can be found in the thesis of Mark Yim [67]. This particular taxonomy does not classify types of mobile robots but instead classifies their gaits. This particular choice of classification is in direct response to the deficiency of the common catch-all *other* category when discussing interesting and non-traditional forms of locomotion. While technically a taxonomy of robot gaits, our definition of tumbling robots fits within Yim's classification if the robot's body itself is considered a generalized foot (G-foot). With this modification tumbling robots produce roll-legged gaits. Specifically, tumbling falls under two classifications, Roll-Discrete-Big (RDB) and Roll-Continuous-Big (RCB). Here the roll-legged classification is very

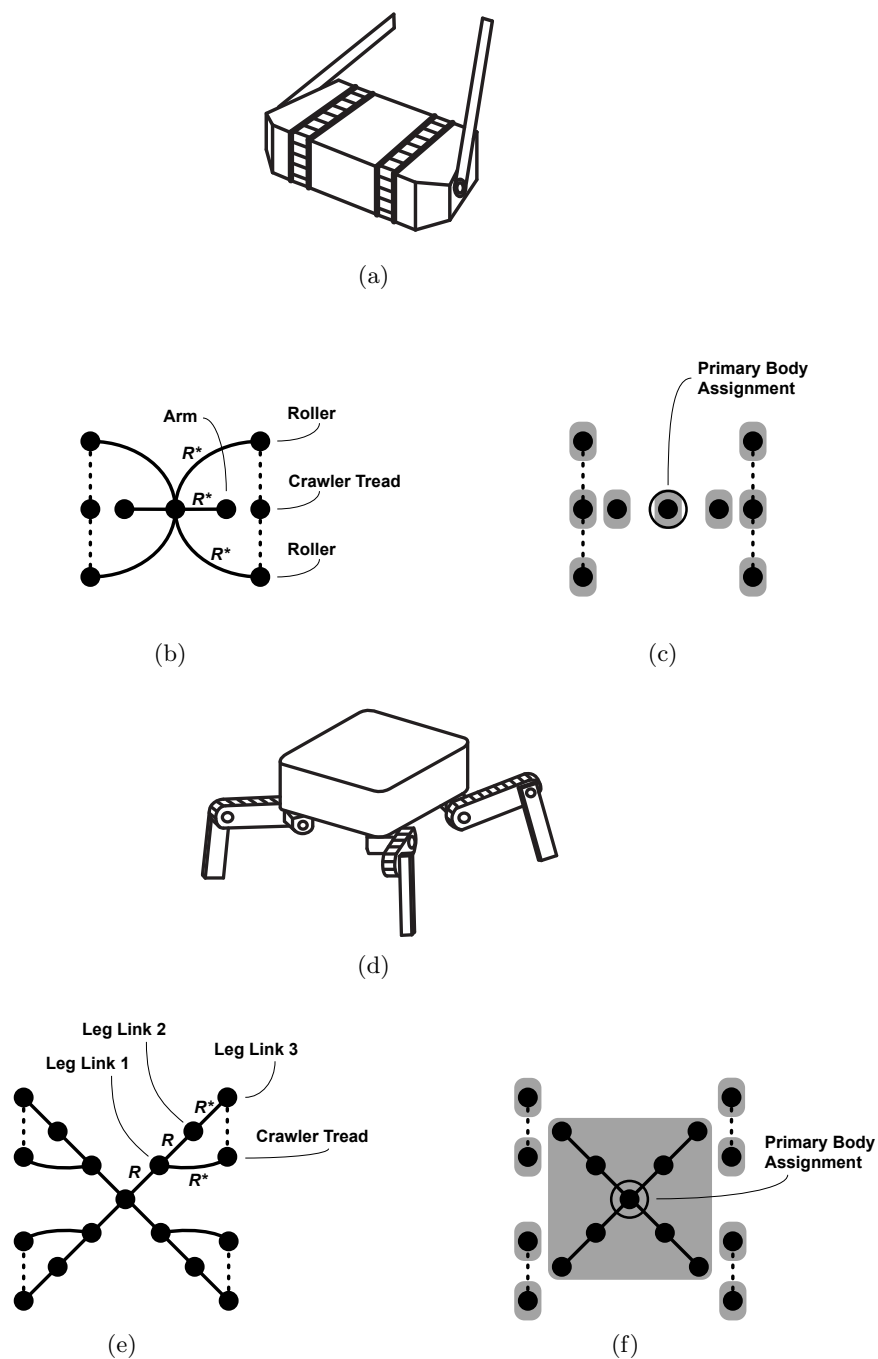


Figure 3.4: Example graph construction and resulting primary body assignments for the (a) Adelopod-T (see Section 4.3) and the (d) TITAN X [65].

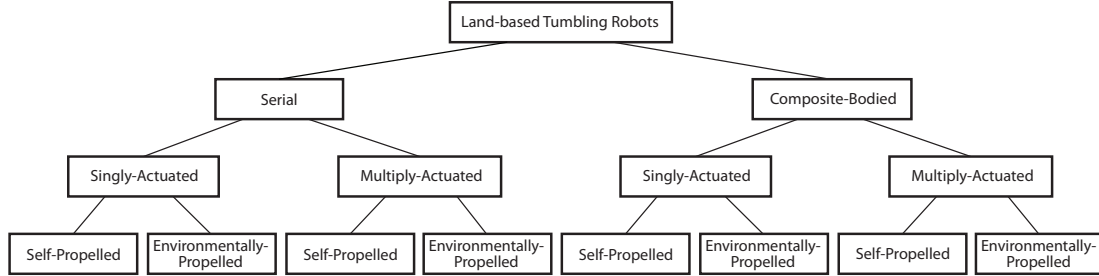


Figure 3.5: Classification of ground-based tumbling robot designs.

similar to our required net body rotations of Definition 3.5, however it is overly broad in that it doesn't differentiate between leg rotations and body rotations (i.e., all tumbling robots produce roll-legged gaits, but not all roll-legged robots are tumbling robots).

Here we present a classification of tumbling robots based on their methods of actuation. Assuming that a particular robot, by Definition 3.5, is a tumbling robot, it can be classified by the taxonomy of Figure 3.5. Such a taxonomy can easily be added to many existing taxonomies of mobile robots as a separate branch parallel to the common wheeled, tracked, walking, and jumping branches, however, its main purpose with respect to this thesis is to guide our discussion on the various types of tumbling robots and help make clear their fundamental differences. The taxonomy of Figure 3.5 groups tumbling robots based on up to three characteristics that we feel capture the fundamental differences of tumbling robot designs. The three classifying characteristics are as follows: serial versus composite-bodied, singly versus multiply-actuated, and self versus environmentally-propelled. For Figure 3.5 we have chosen the branch ordering in such a way that classifications of adjacent leaf nodes are similar by nature. Below we define each classification characteristic while Section 3.4 provides examples of each classification along with a catalog of existing tumbling robots.

Serial / Composite

The first characteristic we use in our classification of tumbling robots is based on the configuration of the robot's actuators and is analogous to the differentiation between serial and parallel manipulators.

Definition 3.8 *Any tumbling robot that utilizes a composite body in achieving locomotion is classified as a **composite-body** tumbling robot. All other tumbling robots are classified as **serial** tumbling robots.*

Serial mobile robots in general make up the largest of the two groups. Typically a serial tumbling robot consists of a primary body to which some number of appendages/manipulators are attached; wheeled and legged robots are prevalent examples of common non-tumbling mobile robots that fall within this category. In terms of tumbling robots, serial designs usually consist of one or more lever-arms connected to a main body by unbounded revolute joints. The lever-arms can be used to manipulate the robot's center of mass or produce external forces to produce tumbles. Composite-body tumbling designs, in contrast, often use the closed kinematic loops as the main structural component of the robot itself, resulting in an actuated body capable of conforming to terrain irregularities. Such configurations often sacrifice hardware simplicity in exchange for extreme mobility. Composite-body tumbling robots can often be considered a class of morphing robots.

Single Body / Multiple Body Actuation

The second classifying characteristic separates designs based on the location of generated forces used for tumbling.

Definition 3.9 *Any tumbling robot that utilizes a single body (physical or composite) in contact with the terrain to generate locomotion is classified as a **singly-actuated** tumbling robot. All other tumbling robots are classified as **multiply-actuated** tumbling robots.*

Singly-actuated tumbling robots make up a very interesting class of tumbling robots where the actuation occurs at the primary (composite) body or within the robot itself. The advantages of such systems include a small possible form-factors and the ability to easily isolate the internals of the robot from the environment.

Self-Propelled / Environmentally-Propelled

This classifier is used to distinguish between robots that produce their own locomotion and those that depend on external (environmental) forces for motion generation. Example energy sources for environmentally-propelled robots include gravity and fluid (e.g., wind/water) currents.

Definition 3.10 *Tumbling robots capable of generating tumbles over smooth level terrain without the aid of external (environmental) forces are classified as **self-propelled**. All other tumbling robots are classified as **environmentally-propelled**.*

3.4 Tumbling Designs by Classification

In this section we describe in detail the four major branches of Figure 3.5 defined by the serial/composite-bodied and single/multiply-actuated classifications. For each branch we discuss some general characteristics and present existing tumbling designs that fit within the classification.

3.4.1 Serial / Singly-Actuated Tumbling Robots

In this section we discuss serial-bodied singly-actuated tumbling robots. This class consists of all tumbling robots that contain no closed kinematic chains of actuators and have only one *driving body* (physical or composite body in contact with the terrain). Because this class is limited to a single driving body, actuation is generally achieved indirectly through some internal means. In this respect, the class of serial singly-actuated tumbling robots lends itself to self-contained systems that have the benefit of being completely isolated from any environmental factors.

This particular class of tumbling robots serves as a good starting point for our discussion in that it encompasses a surprising portion of existing literature in robotics. It turns out that much of the work pertaining to spherical rolling robots fits nicely within our framework defined in Section 3.2. Spherical rolling robots generally consist of a rigid sphere containing various sensors and actuation mechanisms where locomotion is achieved through some form of internal mass manipulation. Advantages of spherical

rolling robots include the ability to completely isolate the internals from any environmental factors, low risk of entanglement (due to smooth external body shape), and the ability to (theoretically) move in any direction.¹ For a review of existing spherical rolling robots we direct readers to [68] and [69].

While it is exciting that our definitions encapsulate a rather well-studied class of existing robots, there are some caveats pertaining to the tumbling/non-tumbling classification of spherical rolling robots. The main issue is that the tumbling/non-tumbling classification of spherical rolling robots is somewhat sensitive to the chosen method of actuation. In [68], the author identifies seven major propulsion types for spherical rolling robots as follows: sprung central member, car driven, mobile masses, hemispherical wheels, gyroscopic stabilization, ballast mass fixed axis, and ballast mass moving axis. Of these, it turns out that only the mobile mass method and in some cases gyroscopic stabilization result in tumbling robots via our classification scheme. All of the other methods involve some internal physical body separate from the spherical shell that remains upright (and thus exhibit no net rotations) with respect to the world. This is an interesting artifact of our definitions where robots that behave similarly (from a high-level viewpoint) can have varying classifications. The main difference is that spherical rolling robots traditionally are classified based on their external appearance while our definitions of tumbling focus on the internal behavior of the primary body. In general, inclusion in one class (spherical rolling or serial singly-actuated tumbling) implies nothing with respect to inclusion in the other.

Example spherical rolling robots that do fit our tumbling definitions include the Spherobot [70] and the August/Glory rolling robot of [71, 72]. In both robots, four masses are actuated along rods that travel outward radially from a central core and connect rigidly to the external spherical shell. The core, rods, and shell are all rigid and thus make up the primary body. By adjusting the relative linear position of each mass along the rods, the desired rotational forces resulting in motion of the sphere can be achieved. The motion and planning for these particular robots is similar to the well-studied ball and plate problem in nonholonomic motion planning and is addressed in detail with respect to the Spherobot in [73, 74].

¹Being able to simultaneously move in any direction is not possible by all spherical rolling robots and is limited depending on the implementation of the physical drive mechanism.

One other existing robot design that is worth discussing is the Torquer Rover [75]. This particular robot is a polyhedral hopping robot designed for use in micro gravity environments such as asteroids or comets. The robot ambulates through a series of hops that are induced by quick primary body rotations. The body rotations responsible for locomotion are controlled by internal spinning masses called torquers; specifically, angular accelerations of the torquers are converted through inertial effects to the primary body which ultimately result in primary body rotations. The goal of the Torquer Rover is to use rapid body angular accelerations/velocities to induce ballistic trajectories to “hop” through the environment; such is easily achievable in micro gravity. One could argue that this particular robot is a jumping robot, however, we have included it based on the tumbling motions used to generate the hops (jumps). Additionally, with controlled inputs, such a robot could ambulate by tumbling without ever leaving the terrain surface.

This class turns out to be the only one in which we are aware of any existing environmentally-propelled tumbling robots. As mentioned previously, environmentally-propelled tumbling robots are those that rely on some external force such as wind or gravity to ambulate. One key example of such robots is the JPL Tumbleweed [76, 77]. This particular robot is comprised of a large inflatable body of spherical shape which houses all power and sensing. Ambulation is achieved in the presence of wind due to the drag of the body resulting in motion in the general direction of the local atmospheric currents. In its most basic form the robot has no direct influence on its direction and is at the mercy of the wind. Later modifications suggest the addition of a controllable mass that was shown to effect the trajectory [78]. This robot is very similar to the above spherical rolling robots and can be considered a passive version of such.

Other environmentally-propelled examples of tumbling can be found in the research areas pertaining to the study of rolling polyhedra and minimalistic manipulation (see [55, 57, 58, 60, 61]). While not specifically about physical self-contained robots, a surprising number of parallels can be drawn between these works and environmentally-propelled (passive) tumbling.

3.4.2 Serial / Multiply-Actuated Tumbling Robots

Serial-bodied multiply-actuated tumbling robots have the allowance of multiple bodies in contact with the terrain. This relaxes the constraints and includes designs with external mechanisms for producing propulsion. The utilization of multiple actuated bodies in general sacrifices the ability to completely seal the robot from the environment and also increases the risk of entanglement. The external force generation allowed by multiple actuation bodies, however, enables the robots to climb significantly larger obstacles when compared with similarly sized singly-actuated tumbling robots. In addition to increased mobility, this class of robots is well suited to minimalistic locomotion solutions where tumbling is utilized to make up for the resulting underactuation that accompanies minimal hardware complexity.

Belonging to this class are the earliest known dedicated tumbling robots, turbots. Turbots came about as a part of research into biomorphic machines, autonomous machines designed to express survivalist behaviors [10]. The project focused on combining simple adaptive control circuits (nervous networks [10, 8, 79, 80, 81]) with simple hardware to produce robust platforms. The project's underlying themes of minimalism and robustness resulted in small robots that could be produced from only a handful of cheap electrical components. As a result, numerous design combinations of control and hardware were tested (over 70 in all), resulting in the discovery of turbots. Several variations of the turbot are mentioned by the authors in [10] and examples of their motion can be found in [8]. Known turbots include Turbot 1.0, Turbot 1.4 (Liam/Sith), Turbot 2.0, Turbot 2.1, and Tiny Turbot, each with various control circuits and/or hardware configurations. Unfortunately, however, no specific design details or performance analyses were ever published. Through the examination of various figures and photos we have found that all of the turbot designs utilize two single degree of freedom arms (rigid in Turbot 1.0, 2.0, and 2.1; compliant in Turbot 1.4) with the exception of the Tiny Turbots which use multiple wheel-legs to tumble.

Another serial-bodied multiply-actuated tumbling robot is the Adelopod, a research platform designed as part of this thesis to aid in the study of tumbling locomotion [82, 83]. Inspired by the aforementioned turbots, the Adelopod uses two arms that rotate about a primary rigid body to produce tumbles. As a research platform, the Adelopod was designed such that it is reconfigurable, allowing the effects various features with

respect to tumbling performance to be examined. The robot supports a wide variety of arms (e.g., rigid and compliant), sensors, and body configurations while also including optional shoulder actuation enabling the plane in which the arm rotate to be controlled. The second degree of freedom in the arms can be used actively for locomotion purposes or can be set to a particular position to test the effect of various arm offset angles. In addition to the Adelopod we have designed and built the Adelopod-T, a hybrid tumbling robot with crawler treads that wrap around the body. With this configuration the robot can switch modes between differential drive, tumbling, and a combination of the two depending on the particular terrain encountered. To the author's knowledge, this is the first instance of such a robot. Both the Adelopod and Adelopod-T are described in detail in Chapter 4.

One final robot we would like to mention within this class is the Aquapod [84], another variation of the Adelopod platform. This particular robot is the result of a study into the use of tumbling robots for environmental monitoring of swamps and marshlands. In addition to two arms used for tumbling, the robot is equipped with an active ballast system allowing for buoyancy control.

We are currently unaware of any serial multiply-actuated environmentally-propelled tumbling robots in existence. Such designs are hard to imagine due to the fact that any additional driving bodies (required to be multiply-actuated) can usually be used to produce tumbles. Despite this issue, tumbling robots in this category are theoretically possible, however their practicality is unclear. Examples might include tumbling robots similar to the above Tumbleweed with the addition of passive appendages that emanate from the primary body that exist to influence the robots motion as it tumbles with the wind.

3.4.3 Composite-Bodied / Singly-Actuated Tumbling Robots

Composite-bodied tumbling robots make up a very interesting class of tumbling robots where closed kinematic chains are utilized for tumbling. In the case of singly-actuated composite-bodied tumbling robots the composite body is often the driving body which allows for the robot to change its shape and conform to the terrain while ambulating.

The seminal example of composite-bodied singly-actuated tumbling is the TET-walker [9]. This robot consists of parallel prismatic actuators that form a tetrahedral

structure. Locomotion is achieved by strategically manipulating the various prismatic struts to alter the robots shape and center of mass. Several designs have been proposed that vary in the number of tetrahedrons in the structure including the 1Tet, 4Tet, 6Tet, 12Tet, etc. The smaller tets are somewhat limited in their configurations but as the number of tetrahedrons grows the robot is able to better adapt to the terrain, conforming to any irregularities as it tumbles. Simulated videos of the 4Tet and the more advanced 12Tet can be found in [85] and [86] respectively. Tumbling robots such as the TETwalker abandon the usual minimalistic approach of tumbling and instead sacrifice hardware simplicity in exchange for extreme mobility. As one can imagine, however, control of such devices can get quite complicated; preliminary planning results are presented in [87, 88, 89, 90].

Parallel to the rigid TETwalkers is an area of tumbling that utilizes soft composite bodies. The most prevalent example of such is the iRobot ChemBot [91, 92], a robot similar in structure to the TETwalker. This robot is spherical in shape and made of many soft silicone cells connected in parallel. For locomotion, the robot utilizes jamming skin enabled locomotion to achieve tumbles; by selectively jamming and unjamming cells while simultaneously controlling its internal volume, the robot is able to control its shape and center of mass to induce tumbles. Other soft designs worth mentioning are the circular/spherical morphing robots of [93, 94, 95] (robots comprised of circular bands that are deformed by controllable tension elements internal to the robot) and the Wormsphere [96], a large sphere for planetary exploration that induces tumbles by altering its support pattern through the selective inflation/deflation of air pockets on the exterior of the robot.

3.4.4 Composite-Bodied / Multiply-Actuated Tumbling Robots

This class is another where we are unaware of any existing designs. This class requires a composite body but allows multiple bodies to contact the terrain. This class would include any hybrid approaches to tumbling that utilized morphing (such as the TETwalker) along with some extra external manipulation (such as the arms of the Adelepod). With this in mind, we foresee this class being much more likely to produce practical designs when compared with the environmentally-propelled classes within serial multiply-actuated and composite-bodied singly-actuated classifications.

3.4.5 Catalog of Existing Designs

Here we present a catalog of tumbling robots known to exist in rough chronological order based on the first known publications to mention their design. Our findings are presented in Table 3.1 where each entry includes the name (or descriptive name if no official name is given), year, relevant citations, a short description, and a visual representation of the robot.

Table 3.1: Table of Existing Tumbling Robot Designs

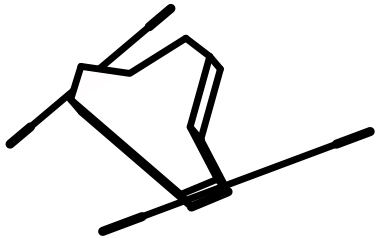
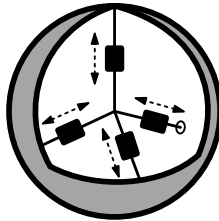
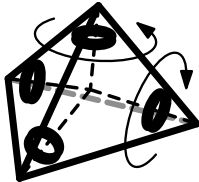
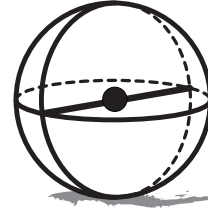
<p>Turbots - 1995 (Serial-Multiple-Self) [10, 8, 11]</p> <p>The first dedicated tumbling robots. This group of robots tumble by rotating arms about their primary body through unbounded revolute joints. Many variations were built including Turbot 1.0, Turbot 1.4 (Liam/Sith), Turbot 2.0, Turbot 2.1, and Tiny Turbot. Designs vary in control circuitry, body shape, and arm flexibility. Designs are focused on both hardware and control simplicity. Many versions are solar powered.</p>	
<p>Spherobot - 1999 (Serial-Singly-Self) [70]</p> <p>August/Glory - 2002 (Serial-Singly-Self) [71, 72]</p> <p>Spherical rolling robots that exhibit tumbles through center of mass manipulation. The center of mass is controlled by four reciprocating masses connected to the inside of the primary body by prismatic joints extending radially outward from the center of the robot. The Spherobot has additional feet that can be deployed to prevent tumbles while collecting data from an onboard periscope-like camera.</p>	
<p>Torquer Rovers - 1999 (Serial-Singly-Self) [75]</p> <p>A series of rovers designed for micro-gravity environments. Tumbles are achieved by accelerating internal masses that spin about fixed axes. Various designs are proposed that differ in rover shape and number/placement of the spinning masses. With significant mass acceleration and/or the presence of micro-gravity, ballistic trajectories (hops) can be achieved.</p>	

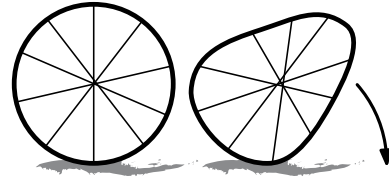
Table 3.1: (continued)

NASA/JPL Tumbleweed Rover - 2003 (?-Singly-Environmental) [76, 77]

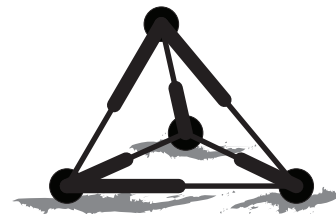
A completely passive (environmentally-propelled) tumbling robot designed to explore large areas with little power. This design utilizes body drag in the presence of wind to achieve tumbles. This particular rover has no actuation (and thus no directional control) so the serial/composite-bodied classification is not applicable, however, later works suggested design modifications with internal mass control (e.g., [78]) to bias the passive tumbles; this would result in a serial-singly-environmental classification.

**Deformable Spherical Robots - 2004** (Composite-Singly-Self) [93, 94, 95]

Robots constructed from numerous spring rings in both circular (planar) and spherical configurations. Tumbles are achieved through the deformation of the primary body by internal controllable tension elements (i.e., shape memory alloy). In addition to tumbling, these robots are also capable of jumping by relaxing the tension elements from a deformed state. This allows the body to rapidly return to its resting circular/spherical shape and results in significant vertical accelerations (jumps).

**TETwalkers (4Tet, 12Tet) - 2004** (Composite-Singly-Self) [9, 87, 88, 89, 90]

A series of robots constructed from various numbers of actuated tetrahedrons arranged to share faces. Each edge of the tetrahedrons is prismatically actuated, resulting in numerous closed kinematic chains. Tumbles are achieved through body deformations controlled by strategically varying edge lengths. Robots are identified by the number of tetrahedrons included in the design; 1-tets, 4-tets, 6-tets, and 12-tets have been proposed.

**Wormsphere - 2004** (Composite-Singly-Self) [96]

A rover designed to explore Mars that achieves tumbles through the control of deformable air vessels covering the exterior of the robot. By selectively inflating and deflating individual air vessels in contact with the terrain, the robot can produce primary body rotations resulting in directed motion.

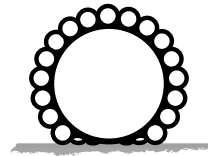
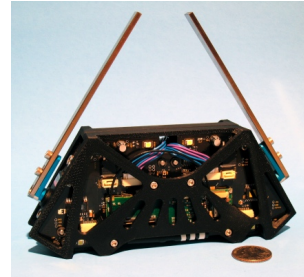


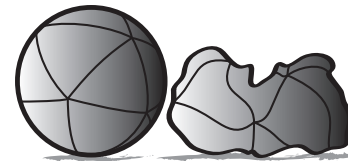
Table 3.1: (continued)

Adelopod - 2008 (Serial-Multiple-Self) [83]

A small tumbling robot similar to turbots that ambulates by inducing body tumbles through the use of two rigid arms that rotate about the body. This particular tumbling robot allows for an optional degree of freedom (bounded joint) on each arm that allows independent control of the planes in which each arm rotates. This extra actuation can be used directly to induce (previously unachievable) tumbles and/or to enable the execution of gradual turning trajectories over consecutive forward tumbles.

**iRobot ChemBot - 2009** (Composite-Singly-Self) [92, 91]

A soft (compliant) tumbling robot based around the theory of jamming skin enabled locomotion. The robot achieves tumbles through controlled body deformations made possible by selectively jamming and unjamming primary body cells while simultaneously controlling internal pressure. Internal pressure forces alter the shape only of unjammed cells while the jammed cells retain their shape. This robot can be viewed as a soft parallel to the above TETwalker.

**Aquapod - 2010** (Serial-Multiple-Self/Environmental) [84]

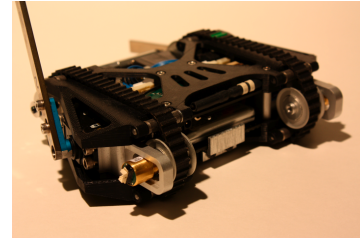
A tumbling robot inspired by the Adelopod designed to explore rivers and marshes while monitoring water quality. This particular tumbling robot uses its two rigid arms to tumble on dry land and is equipped with an active ballast system to control buoyancy while in water, thus allowing samples to be collected from various depths. The robot is classified as both self and environmentally-propelled due to the fact that tumbles are not controllable while suspended in water (tumbles are however controllable on the floor of the water body).



Table 3.1: (continued)

Adelopod-T - 2011 (Serial-Multiple-Self) [97]

An adaptation of the Adelopod that replaces the shoulder actuation with two independently controlled crawler treads that wrap around the central physical body. This design allows for multi-modal locomotion including tumbling, differential drive, and simultaneous tumbling-crawling. In addition to improving mobility, the addition of crawler treads also significantly relax the path planning and control requirements of the system.



3.5 Characteristics of Tumbling Robots

As we have shown, tumbling robots come in a variety of shapes and forms, however, there are a couple of characteristics that are common among most of the variations. In this section we provide an overview of these general characteristics along with some specific to certain classes of tumbling robots where necessary. Interestingly, many of the characteristics we address stem from the single fact that the majority of tumbling designs make use of unrestricted interactions between the terrain and physical bodies of the robot (including the primary body); the central idea is that extra mobility and stability are gained by fully utilizing collisions with obstacles. Traditionally, such unrestricted collisions (especially between the primary body and the terrain) are avoided. In tumbling systems however, the leveraging of such interactions when paired with net body rotations allow tumbling robots to achieve a surprising variety of benefits including high mobility, inherent robustness, small size, and minimal hardware.

3.5.1 Benefits of Unrestricted Terrain-body Interactions

Generally, for most robot platforms there are some physical bodies within the system that are not allowed to come into contact with the terrain due to the possibility of damage to the robot. Such contacts are referred to as collisions and are avoided in any planning or control software of the robot. Even in traditional robotic systems that do not take damage from such contacts, a majority of the possible terrain-body contacts are not utilized to produce locomotion. This is evident in off-road (ruggedized) wheeled,

legged, and tracked robots where terrain-body collisions are not necessarily detrimental to the robot but are still avoided due to the risk of hang-up failures resulting in immobile configurations due to the robot's (often primary) body getting stuck on the terrain.

In contrast to the above, tumbling robots are designed in such a way that, assuming bounded velocities, any possible terrain-body contact will not damage the system. In this respect we say that tumbling designs allow unrestricted terrain-body interactions. In addition to allowing such interactions, tumbling robots are often designed specifically to utilize these unrestricted contacts to produce or aid in achieving locomotion. Unrestricted terrain-body interactions often help overcome any underactuation of the robot while simultaneously enabling higher mobility-to-size ratios. Additionally, the design principle of full terrain-body contact utilization greatly reduces and often eliminates the set of immobile configurations of the robot. In this respect, tumbling robots generally exhibit some notion of inherent stability not present in many other forms of robotic locomotion. The following characteristics of tumbling robots stem from terrain-body interactions:

Increased Mobility

The unrestricted terrain-body interactions of tumbling robots provide extra options for overcoming terrain irregularities, effectively increasing the space of possible (and hopefully successful) trajectories. Additionally, when combined with tumbling's characteristic net body rotations, the primary body itself can be used to actively push/pull the robot over or through the terrain. Thus, tumbling can be viewed as a more efficient utilization of the robot's exterior, providing a distinct advantage over other traditional forms of robot locomotion. This characteristic is one of the main motivating factors of tumbling locomotion and is readily apparent in serial multiply-actuated tumbling robots such as the Adelopod and in composite-bodied tumbling robots such as the TETwalker. For their size, these classes of tumbling robots can negotiate surprisingly complex terrain. We address this specific characteristic in detail later in Chapter 5.



Figure 3.6: Frames captured of the Adelopod recovering from and tumbling away from an uncontrolled decent down a steep embankment.

Inherent Robustness

The allowance of unrestricted terrain-body interactions along with utilization of the body in producing propulsion results in systems with very few (if any) immobile configurations when free from obstacles. As an example, Figure 3.6 shows superimposed frames from a video showing an Adelopod tumbling robot start an uncontrolled series of tumbles down a steep decent. The fall is uncontrolled but the resulting motion (that would prove detrimental to many types of robots) is the same end over end motion experienced during a normal tumble, thus no damage is incurred (frames 1-5). Due to the allowance of unrestricted ground-body interactions, the robot is guaranteed to come to rest in a mobile configuration pending any entanglement with the terrain. This is observed from captured frames 6 to 11 where the robot recovers and tumbles away from the base of the slope.

There are some obstacles that can be quite problematic for tumbling such as thick brush, deep holes, etc., however such obstacles are usually problematic for all miniature mobile robots. In general, the extra utilization of interesting terrain-body configurations and resulting robustness gives tumbling an advantage over other traditional forms of locomotion.

Minimalistic Hardware

In addition to increased mobility and inherent robustness, tumbling is also attractive due to its conservative hardware requirements. Depending on the design goals and/or application, various types of tumbling robots can vary greatly in their hardware complexity (i.e., number of moving parts, actuators, etc.). However, with the unrestricted terrain-body contacts and resulting increase in robustness, tumbling robots can often operate with fewer actuators than system degrees of freedom. In these cases the robot is underactuated and is limited in the motions it can execute from any given configuration. However, unlike many traditional forms of robot locomotion, tumbling robots are not forced to remain upright or prevent any form of collisions with the terrain. This effectively relaxes the constraints on the allowed trajectories, helping to relieve the impact of any motion constraints due to underactuation on the system's performance. This desirable characteristic allows tumbling robots to be designed minimally (i.e., less actuators and moving parts) when necessary/desirable while preserving sufficient mobility. Thus tumbling presents a lower bound of minimum hardware complexity such that sufficient mobility can be achieved with remarkably few moving parts and actuators when desired or necessary. In this regard, forms of tumbling can be considered minimalistic approaches to robotic locomotion that exhibit all of the benefits of minimalistic design (i.e., increased economy, reliability, ease of manufacturing, etc.) while preserving the ability to traverse interesting terrains.

Another interesting benefit of tumbling that furthers its minimalism is the fact that tumbling very rarely requires additional actuators to aim any onboard directional sensors. Due to the intrinsic net body rotations of tumbling, sensors fixed rigidly to the robot's body can be aimed with the same actuators that are used to generate locomotion. Figure 3.7 shows an example of both a MegaScout (wheel-tail robot) [98] and an Adelopod (tumbling robot) where each robot has two actuators for achieving locomotion. A rigidly mounted sensor on the MegaScout is limited by the terrain surface (e.g., a forward facing sensor can only be aimed tangent to the terrain surface) while the Adelopod, in general, can point the sensor in any direction. This method does come with some limitations, the major one being that tracking and locomotion are coupled and in general can not be achieved simultaneously. Additionally any adjustments made to the sensor result in some positional displacement of the robot. If the robot is underactuated



Figure 3.7: Figure depicting the ability of tumbling robots to aim rigidly attached directional sensors using the same actuators employed to generate locomotion. Sensor direction is represented by the red arrows. (a) shows a MegaScout with its sensor constrained to \mathbb{R}^2 while the Adelopod of (b) can point its sensor along vectors in \mathbb{R}^3 .

(which is often the case if minimalism is desired) sometimes small corrections in sensor direction result in large displacements in the inputs. Despite these drawbacks, the ability to eliminate extra complexity is an attractive characteristic for miniature mobile robotics if low cost is desirable.

Minimalistic tumbling designs are common in the class of serial tumbling robots while generally composite-bodied designs sacrifice this characteristic in exchange for extreme mobility (e.g., the TETwalker). Example minimalistic designs include almost all spherical tumbling designs (especially the environmentally-propelled designs such as the JPL Tumbleweed), the serial multiply-actuated turbots, and the Adelopod.

3.5.2 Issues with Tumbling

So far we have cast many of tumbling's characteristics in a positive light. As with many design choices, tumbling is very much a science of tradeoffs; the same terrain-body interactions that enable the aforementioned desirable characteristics are responsible for many of the difficulties surrounding tumbling systems. The main issues with tumbling are the difficulties in accurate planning and control due to the modeling of terrain interactions. Additional issues involving directional sensing, power efficiency, and vibration / large accelerations due to impacts also exist.

Modeling

Central to any planning or control algorithm is a model of the system; in terms of mobile robots we are concerned with the motion model. Accurate motion models are desirable for both predicting system behavior given a set of inputs (forward problem) and finding feasible input trajectories that bring the robot from some initial state to a goal state (backward problem). Models vary greatly depending on the application and required accuracy. In general, models can be kinematic (first-order velocity-based models) or dynamic (higher-order acceleration-based models). Kinematic models are attractive due to their simplicity and are chosen whenever possible. Often times such models can avoid unnecessary complexity and provide insightful descriptions of a system's behavior. Furthermore, if a system is *well behaved*, kinematic models can even be sufficient for use directly in planning and control tasks. In many real-world systems, however, issues such as inertial effects and friction require the use of more accurate higher-order dynamic models that take forces and accelerations into account. With respect to tumbling robots, model selection is constrained by the utilization of discrete tumbles along with the presence of sliding contacts.

During a discrete tumble (see Definition 3.1) the robot accelerates with gravity about the tumble axis and thus (due to the presence of accelerations) requires a dynamic model to accurately describe the resulting motion. Because of this, many tumbling robots can not directly be modeled as kinematic systems. It is possible however to formulate sufficient models where tumbles are treated separately from non-tumbling stable states. Such a hybrid kinematic-dynamic approach results in kinematic models where applicable (e.g., stable states) with tumbles handled dynamically when they occur. It is also possible to treat tumbles abstractly as jumps in the system state. Here statically stable states can again be modeled as kinematic where applicable while tumbles are resolved as instantaneous (discontinuous) jumps in the robot's state. The states immediately before and after the jump represent the robot right before and right after the tumble. Obviously some accuracy is lost with such methods, but the resulting purely kinematic model can be useful in some simple cases.

More restraining than discrete tumbles are sliding contacts with the terrain common in multiply-actuated and some composite-bodied tumbling robots. These classes of tumbling robots allow for multiple physical bodies in contact with the terrain at any given

time. If a robot is sufficiently actuated such contacts can be controlled independently allowing for locomotion without slip (e.g., fully actuated legged robots). As mentioned previously, a significant portion of tumbling robots are designed with minimalism in mind and are purposefully left underactuated. This combination of underactuation and multiple terrain contacts often results in sliding contacts. Unless assumptions can be made (e.g., low friction contacts assumed to be frictionless), modeling systems with sliding contacts requires that frictional forces be taken into account. This adds significantly to the models complexity and presents issues regarding the unilateral nature of terrain contacts and discontinuities inherent to Coulomb's law of friction. Other issues pertaining to the modeling of tumbling robots include those due to the presence of multiple frictional contacts for a single or chain of bodies. A variety of formulations exist for the problem as well as numerical techniques for obtaining solutions for the cases of rigid physical bodies (e.g. [99, 100, 101, 102]); depending on the required amount of accuracy, these techniques allow for the simulation of rigid tumbling robots in two [103] and three dimensions [104, 105]. We wish to note, however, that the resulting solution methods / simulations are relatively time-consuming and limited by the accuracy of the terrain model. This can be problematic when searching large spaces for trajectories (motion planning) under real-time constraints as well as when executing open-loop motion plans from the model where the error quickly becomes apparent (tumbling robots are especially prone to this due to the complex nature and number of frictional contacts). We discuss these issues further in Chapter 6.

3.5.3 Numerous Support Sets and Hybrid Representations

While many mobile robots move through the manipulation of their support set, few of them have as many possible support sets as tumbling robots do. With the exception of serial singly-actuated tumbling robots, the utilization of unrestricted terrain-body interactions provides a multitude of possible support sets. This is in stark contrast to wheeled and legged robots that have a comparably small number of possibilities. Due to underactuation tumbling robots often have a limited set of reachable states for a particular support set and are usually subject to numerous nonholonomic constraints and, therefore, appropriate transitions of the support set must be made to achieve directed motion. The support set can change through a stable addition or removal of a

contact or through a (unstable) discrete tumble. Strategic manipulation of the support pattern is a central issue to tumbling locomotion and is the focus of Chapter 6, where we examine the issues surrounding tumbling with emphasis on the particular (often underactuated) class of serial multiply-actuated tumbling robots.

With respect to modeling, the large number of support sets as well as the dependence of the system's behavior on the current support set leads to a natural representation of tumbling as a hybrid system. Hybrid systems combine differential equations with the idea of finite automata to create representations capable of modeling systems that exhibit both continuous and discrete dynamics. Within this model, discrete states represent all possible support sets while each support set gets its own set of differential equations that describe the continuous motion of the system while in the corresponding discrete support set. Several formulations of hybrid systems exist depending on the area of application; with respect to tumbling robots, we are most interested in the hybrid automaton definition taken from [106]:

Definition 3.11 A *hybrid automaton* is described by a septuple

$(L, X, A, W, E, Inv, Act)$ where the symbols have the following meanings.

- L is a finite set, called the set of *discrete states* or *locations*. They are the *vertices* of a graph.
- X is the continuous state space of the hybrid automaton in which the continuous state variables x take their values. For our purposes $X \subset \mathbb{R}^n$ or X is an n -dimensional manifold.
- A is a finite set of symbols which serve to label the edges.
- $W = \mathbb{R}^q$ is the continuous communication space in which the continuous external variables w take their values.
- E is a finite set of edges called transitions (or *events*). Every edge is defined by a five-tuple $(l, a, Guard_{l'}, Jump_{l'}, l')$ where $l, l' \in L$, $a \in A$, $Guard_{l'}$ is a subset of X and $Jump_{l'}$ is a relation defined by a subset of $X \times X$. The transition from the discrete state l to l' is *enabled* when the continuous state x is in $Guard_{l'}$, while during the transition the continuous state x jumps to a value x' given by the relation $(x, x') \in Jump_{l'}$.
- Inv is a mapping from the locations L to the set of subsets of X , that is $Inv(l) \subset X$

for all $l \in L$. Whenever the system is at location l , the continuous state x must satisfy $x \in Inv(l)$. The subset $Inv(l)$ for $l \in L$ is called the *location invariant* of location l .

- *Act* is a mapping that assigns to each location $l \in L$ a set of differential-algebraic equations F_l , relating the continuous external variables w :

$$F_l(x, \dot{x}, w) = 0. \quad (3.5)$$

The solutions of these differential-algebraic equations are called the *activities* of the location. [106]

Let V be the set of all points that make up the exterior of the robot. For our purposes, elements of L correspond to the feasible support sets that make up a subset of the powerset $P(V)$ of V . For any real-world physical robot, V is infinite, resulting in L being infinite as well. This is in contrast to Definition 3.11 but does not pose any theoretical issues for our purposes. When modeling a real-world tumbling robot as a hybrid automaton, however, allowing V to be infinite can lead to unrealizable representations; in these cases it might be necessary/desirable to let V be a finite approximation of the robot's exterior.

The set of location invariants Inv corresponds to subsets of x in which the contact constraints for a particular $l \in L$ are satisfied. These constraints take the form

$$h(v_i, x) = 0, \quad v_i \in V_l \quad (3.6)$$

$$h(v_i, x) > 0, \quad \text{otherwise} \quad (3.7)$$

where V_l represents the support set corresponding to the location l and the function h returns the shortest distance between the terrain and point v_i for the robot in state x . Definition 3.5 allows for both autonomous (internally induced via x) and controlled (externally induced via discrete variables in w) switches. For the tumbling systems we study controlled switches have no physical meaning and are ignored, therefore the guards $Guard_{ll}$ simply correspond to the subsets of x such that any constraint of Equations (3.6) or (3.7) is not satisfied. In this manner, the union of guards for a location l makes up the set complement in X of $Inv(l)$, resulting in immediate autonomous

switches as soon as a guard is satisfied. In other words, if a contact point is added or removed, the hybrid automaton makes a unique discrete transition from l to l' in which the new set of contact constraints is satisfied.

Large Changes in Orientation

The last characteristic we discuss follows directly from Definition 3.5, which states that tumbling robots move primarily through the use of net body rotations. Even moving small distances, it is not uncommon for tumbling robots to exhibit multiple net revolutions about one or more body axes. This is in stark contrast with conventional forms of robots which often require a limited range of orientations to remain functional.

The characteristic changes in orientation serve as the primary method of producing locomotion (and are thus necessary) however, they can be somewhat inconvenient when it comes to sensing. Many exteroceptive sensors are directional by nature and, if mounted rigidly to a tumbling system, exhibit constant directional changes as the robot ambulates. Examples of such sensors include contact, range (e.g., lasers, ultrasonic, etc.), and vision (cameras) sensors. Earlier we mentioned that this characteristic can be used to reduce system complexity by eliminating extra actuators for aiming sensors while stationary, however while ambulating, the net body rotations often inhibit a single sensor from maintaining a view of its target as the robot tumbles. If such continuous tracking during ambulation is necessary there exist a number of workarounds for many sensors common to mobile robots. As examples, omnidirectional lenses or multiple cameras can be used to effectively increase the viewing angle and reduce the effect of interrupted data while tumbling (downward facing cameras). Alternatively, if multiple cameras are not feasible, a single camera can be used to collect images over consecutive tumbles which can then be stitched together to create a usable (although slow to update) image. Global positioning sensors are another directional example where the antennas generally require some form of line-of-sight to open sky. In practice this turns out not to be an issue due to the usually low required (or available) frequency of positional data, allowing measurements to be taken when possible/convenient as the robot ambulates. Care must be taken, however, to preserve any satellite locks while the sensor's antenna is occluded. Proprioceptive sensors generally do not exhibit such issues aside from requiring occasional geometric transformations to interpret and/or compare

data.

3.6 P2AT: A Planar 2-Armed Tumbling Robot

In this section we present a planar toy example of a tumbling robot. The purpose of this example is two-fold and is included to provide the reader with additional insight into tumbling while also serving as model for later methods regarding maneuverability in Chapter 6. The Planar 2-Armed Tumbling Robot (P2AT), shown in Figure 3.8, is a serial multiply-actuated self-propelled tumbling robot constrained to the xy -plane that ambulates by rotating its arms about its body using two unbounded revolute joints. In this respect, the P2AT is a planar example of tumbling robots similar to the aforementioned turbots and Adelopod.

3.6.1 Physical Description

The P2AT is characterized by the set of points $\{v_1, v_2, v_3, v_4\}$ that exist in the planar workspace $\mathcal{W} = \mathbb{R}^2$. The robot's frame A is centered at point Gv_1 with the x -axis Ax along Av_2 . The points v_1 and v_2 are referred to as body points and have mass $m_{\text{body}} > 0$. The points v_3 and v_4 are referred to as arm points and have mass $m_{\text{arm}} = 0$. The set of all points that make up the robot are represented by the set V ; the robot can be treated abstractly as the set of discrete points (e.g., $V = \{v_1, v_2, v_3, v_4\}$) or can be given some notion of length/area. Unless otherwise noted, we take V to be

$$V = \{v_1 + \alpha(v_i - v_1) \mid \alpha \in (0, 1), i = 2, 3, 4\}, \quad (3.8)$$

where the robot is represented as a set of line segments radiating outward from v_1 .

The system is subject to the following holonomic constraints imposed by l_2 , l_3 , and l_4 (the lengths of vectors Av_2 , Av_3 , and Av_4 respectively):

$$\sqrt{(v_{ix}^2 - v_{1x}^2) + (v_{iy}^2 - v_{1y}^2)} - l_i = 0, \quad i = 2, 3, 4, \quad (3.9)$$

which result in the system having a total of 5 degrees of freedom. As a choice of generalized coordinates we let v_{1x} and v_{1y} denote the respective global x and y coordinates of point v_1 , and thus the origin of the robot's frame A . The rotation of the robot is

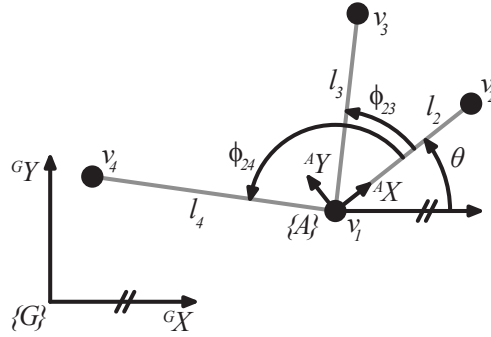


Figure 3.8: The P2AT, a planar 2-armed idealized tumbling robot.

represented by θ and is equal to the angle between ${}^A X$ and ${}^G X$, the x -axis of the global frame. ϕ_{23} and ϕ_{24} are the arm angles of the robot where ϕ_{ij} is defined to be the angle between vectors ${}^A v_i$ and ${}^A v_j$. A configuration is then represented by

$$q = (v_{1x}, v_{1y}, \theta, \phi_{23}, \phi_{24})^T \in \mathcal{Q}, \quad (3.10)$$

Where \mathcal{Q} is the configuration space

$$\mathcal{Q} = \mathbb{R}^2 \times S^1 \times T^2 = SE(2) \times T^2, \quad (3.11)$$

with T^2 the 2-dimensional torus and $SE(2)$ the two-dimensional special Euclidian group.

The terrain and obstacles (\mathcal{O}_i with $i \in \mathbb{N}$) are represented as a closed regions of \mathcal{W} . Due to the physical nature of obstacles, we do not allow any penetrations of obstacles by the robot. That is,

$$V \cap \left(\bigcup_i \text{int}(\mathcal{O}_i) \right) = \emptyset, \quad (3.12)$$

where $\text{int}(\mathcal{O}_i)$ denotes the interior of \mathcal{O}_i . While penetrations are not allowed, collisions are. Let the set C be the support set (points in contact with an obstacle/terrain),

$$C = V \cap \left(\bigcup_i \partial \mathcal{O}_i \right), \quad (3.13)$$

where $\partial \mathcal{O}_i$ denotes the boundary of \mathcal{O}_i .

3.6.2 Behavioral Description

Being a toy example, we have a significant amount of freedom in specifying the behavior of the P2AT. While there are a number of ways to proceed, we have chosen to present here behavior conducive to a kinematic definition of the P2AT robot. Despite tumbling being an inherently dynamic process, the following kinematic description preserves many of the characteristics we wish to discuss without introducing unnecessary complexity. Fully dynamic and kinematic-dynamic hybrid descriptions are straightforward to derive and follow naturally from the following description.

The kinematic P2AT system has the following properties:

1. Inputs $u = (\dot{\phi}_{23}, \dot{\phi}_{24})^T \in \mathbb{R}^2$ are quasi-static.
2. Tumbles occur when the static stability margin s becomes negative.
3. Tumbles and free-falls resolve instantly.
4. In configurations with multiple contacts ($|C| \geq 2$) the system behaves like a crank-slider four-bar mechanism.

Properties 1 and 3 eliminate any system dynamics induced by accelerations or high velocities. Tumbles are inherently dynamic, therefore to keep our system kinematic we treat free-fall and tumble states as instantaneous jumps in the system's configuration. Free-falls (states with $|C| = 0$) are resolved by decreasing v_{1y} by the smallest value that results in a non-empty set of contact points C . Tumbles ($|C| \geq 1$ and $s < 0$) are resolved by rotating the robot about the vertex in C closest to the projected center of mass toward the center of mass until $|C| \geq 2$ (the first new collision occurs).

Property 2 requires that tumbles occur when the stability of the system vanishes (i.e., $s < 0$). For the chosen system description, we use the static stability margin previously defined in Definition 3.2. In our planar case, polygons of Definition 3.2 are taken as line segments and planes as lines.

Property 4 defines the behavior of the system in stable states to be that of a crank-slider four-bar mechanism (see Figure 3.9(a)). Under this assumption, one contact point is assumed to *stick* to the surface and act as the hinge while all other contacts are free to slide. This allows the removal of any dynamics resulting from frictional forces acting at the contacts and is analogous to assuming infinite friction at the hinge of the crank contact and zero friction everywhere else (slider). Several choices can be made

in assigning which contacts stick and which slide. In a real-world analogous system, assuming all contacts have identical coefficients of friction, the point that sticks will in general be the one with the largest ground reaction force. In this example, we make the assumption that $\mu_2 \gg \mu_3 \gg \mu_4$ where the μ 's are the coefficients of friction for the body and two arms respectively. This assumption leads to the contact of the shortest arm sticking while on relatively smooth/flat terrain (i.e., contact points assumed exhibit similar height with normals near vertical). Any applications with terrain that violates this assumption will be made clear and we will resort to a model where the hinge is assigned by the relative calculated frictional forces.

From the above properties, assuming either a convex terrain surface and/or $V = \{v_1, v_2, v_3, v_4\}$ is discrete, we get the following kinematic expressions for the robot where v_i is the hinge contact and v_j is the slider contact:

$$f_{1,2}(q, u) = \dot{q} = \left(0, 0, 0, \dot{\phi}_{23}, \dot{\phi}_{24} \right)^T, \quad (3.14)$$

$$f_{1,j}(q, u) = \dot{q} = \left(0, 0, -\dot{\phi}_{2j}, \dot{\phi}_{23}, \dot{\phi}_{24} \right)^T, \quad (3.15)$$

$$f_{i,j}(q, u) = \dot{q} = \begin{pmatrix} \frac{d\psi}{d\phi_{ij}}(\dot{\phi}_{2j} - \dot{\phi}_{2i})l_i \sin(\theta + \phi_{2i}) \\ -\frac{d\psi}{d\phi_{ij}}(\dot{\phi}_{2j} - \dot{\phi}_{2i})l_i \cos(\theta + \phi_{2i}) \\ \frac{d\psi}{d\phi_{ij}}(\dot{\phi}_{2j} - \dot{\phi}_{2i}) - \dot{\phi}_{2i} \\ \dot{\phi}_{23} \\ \dot{\phi}_{24} \end{pmatrix}, \quad (3.16)$$

where

$$\phi_{ij} = \phi_{2j} - \phi_{2i}, \quad (3.17)$$

$$\phi_{ii} \equiv 0, \quad (3.18)$$

and $d\psi/d\phi_{ij}$ expresses the change in the crank angle with respect to ϕ_{ij} ; the symbols are depicted graphically in Figure 3.9(b). Cases where neither of the assumptions that the terrain is convex or V discrete hold, it is possible to have a contact where a continuous portion of V lies tangent to the terrain/obstacle (see Figure 3.9(c)); these will be referred to as type A contacts (as in the convention of [107]) in contrast to the previous type B contacts of a discrete point on the robot in contact with a continuous portion of the

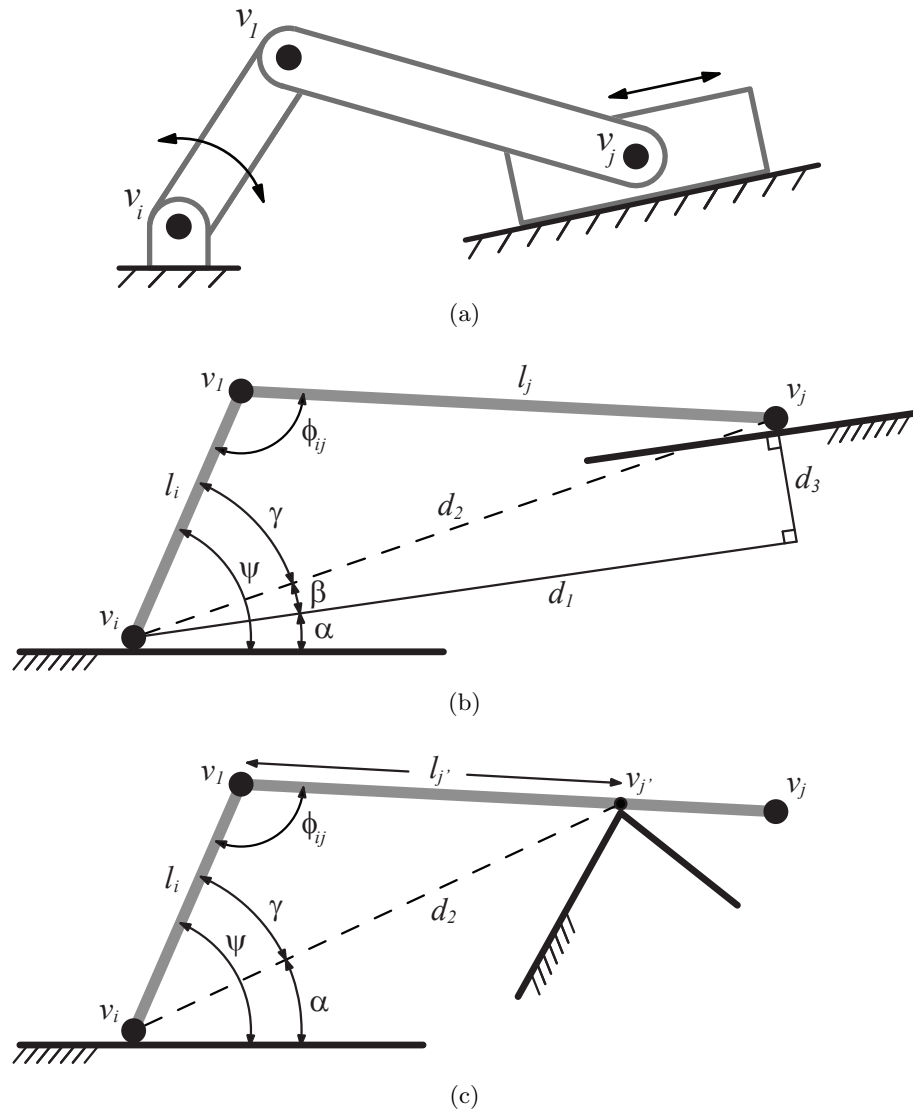


Figure 3.9: Equivalent systems for the P2AT with conditions $s \geq 0$, $|C| \geq 2$, and v_i acting as the hinge. Shown for type B contacts in (a)-(b) and type A contacts in (c).

terrain. These type A contacts result in an inversion of the crank-slider mechanism model where the robot arm now represents the coupler and the terrain functions as the slider of the mechanism. Equations (3.14)-(3.16) hold for both type A and type B contacts with only $d\psi/d\phi_{ij}$ changing; $d\psi/d\phi_{ij}$ for both types of contact are as follows:

$$\frac{d\psi}{d\phi_{ij}} = \begin{cases} \frac{-l_i \cos \phi_{ij}}{d_2 \cos \frac{l_i \sin \phi_{ij}}{d_2}} - 1, & \text{type A,} \\ \frac{l_j (\sin(\psi + \phi_{ij}) \tan \alpha + \cos(\psi + \phi_{ij}))}{l_j \cos(\psi + \phi_{ij}) + l_i (\cos \psi + \sin \psi \tan \alpha) - l_j \sin(\psi + \phi_{ij}) \tan \alpha}, & \text{type B.} \end{cases} \quad (3.19)$$

3.6.3 Hybrid System Representation

In Section 3.5.3 we motivated the use of hybrid systems for modeling tumbling robots that exhibit discrete changes in their support sets. Here we show a hybrid system representation of the P2AT that combines Equations (3.14)-(3.16) with a finite automaton that captures the discrete changes in the support set.

From the behavioral description of Section 3.6.2, there are three possible transitions between stable states; free-falls, tumbles, and the stable addition/removal of contact points. All of these transitions are captured by the set of edges E in the hybrid automaton. A compact graph representation of the hybrid automaton is shown in Figure 3.10 where we have combined all of the states into a single generalized location (vertex) with the discrete transitions (edges) looping back into itself. The depicted generalized location contains activities chosen appropriately from Equations (3.14)-(3.16) depending on the points in C corresponding to the represented location (e.g., the location l_{34} for the support set $C = \{v_3, v_4\}$ contains the activities defined by Equation (3.16) with $i = 3, j = 4$ or $i = 4, j = 3$ depending on which contact acts as the hinge). Such a representation is very convenient in that it captures all possible support sets.

At this point, all that is left to specify are the location invariants and the guards. For any given location there are four types of guards that become active when either a new point comes into contact, a point in C_l breaks contact, the stability becomes

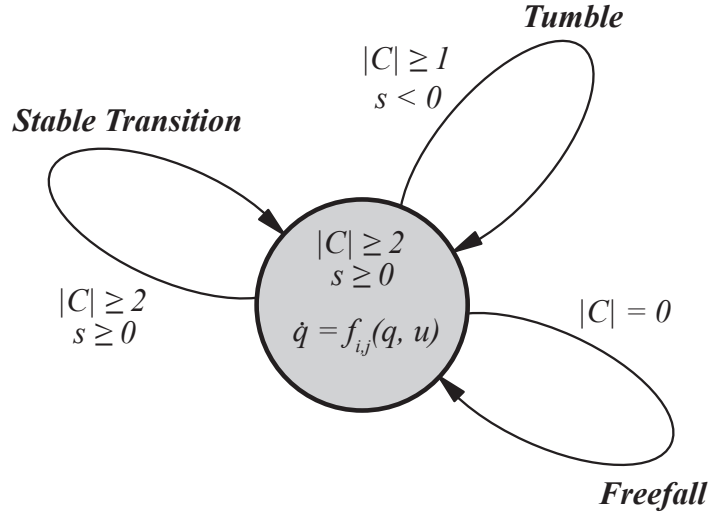


Figure 3.10: Hybrid automaton representation of the P2AT.

negative, or the hinge contact changes within C_l . The first three guards take the forms

$$\{h_i(x) = 0, v_i \notin C_l, \forall i\} \subset X \quad (3.20)$$

$$\{h_i(x) > 0, v_i \in C_l, \forall i\} \subset X \quad (3.21)$$

$$\{s_l(x) < 0\} \subset X \quad (3.22)$$

respectively, where h_i is a function that returns shortest distance between the point v_i and the terrain/obstacles \mathcal{O} . The final (fourth) guard is optional in our case depending on the method chosen to define the hinge contact in property 4 of the behavioral description. If the contact of the shortest arm is assumed to stick this guard overlaps with Equations (3.20) and (3.21). More sophisticated methods would require the sticking/slipping to influence locations in addition to support set (such as the aforementioned possibility of selecting contact with largest normal force or maximum friction $N_i\mu_i$). Interestingly, the hinge contact identification is an artifact resulting from our desire to have a kinematic model; with a dynamic model, the stick/slip conditions can be handled directly by the activities of the location. Because our system does not exhibit any

controlled switches, the location invariants are as follows:

$$Inv(l) = \{h_i(x) > 0, v_i \notin C_l, \forall i\} \cup \{h_i(x) = 0, v_i \in C_l, \forall i\} \cup \{s_l(x) \geq 0\} \subset X. \quad (3.23)$$

Comparing Equation (3.23) with Equations (3.20)-(3.22), it is evident that the invariants become invalid at the same instant that any single guard becomes active. Therefore, the autonomous switches occur at the instant that the location invariant becomes invalid (i.e., any guard becomes active) where the new location can be derived from the behavioral description of Section 3.6.2. Tumbles and free-falls utilize the jumps of Definition 3.11 to achieve the instantaneous resolution of any would-be dynamic behavior.

Figure 3.11 depicts graphically the guards and corresponding location invariants for each location of the P2AT with respect to the arm angles (i.e., $(\phi_{23}, \phi_{24})^T \in T^2$) under the assumption that the terrain is simply the ground formed by the x -axis and is free of obstacles.²

$$\mathcal{O} = \{p \in \mathcal{W} \mid p_y \leq 0\}. \quad (3.24)$$

Each subfigure of Figure 3.11 represents a location with $|C_l| = 2$ where the gray regions represent $Inv(l)$, the solid blue lines are the guards of stable point additions/removals (these also correspond to locations where $|C| > 2$), and dashed red lines are the guards resulting from the stability measure. Associated with each guard is a label that depicts the new location l' that results from activating the guard.

In summary, we present our final formulation of the P2AT hybrid automaton as follows:

Formulation 3.1 (P2AT Kinematic Hybrid Automaton)

- L is the set of all combinations with cardinality greater than or equal to two made from elements of V .
- Since our model is kinematic, the state space $X = \mathcal{Q} = SE(2) \times T^2$.
- $W = \mathbb{R}^2$ is the set of system inputs with $u = (\dot{\phi}_{23}, \dot{\phi}_{24})^T \in W$.
- The set of edges E defined by the guards of Equations (3.20)-(3.22) with l' derived from the behavioral description of Section 3.6.2.

²Such terrain assumptions are not necessary in general and were only made here to produce Figure 3.11 (i.e., without this assumption the guards and location invariants become general functions of the robots state and the terrain and cannot be depicted graphically).

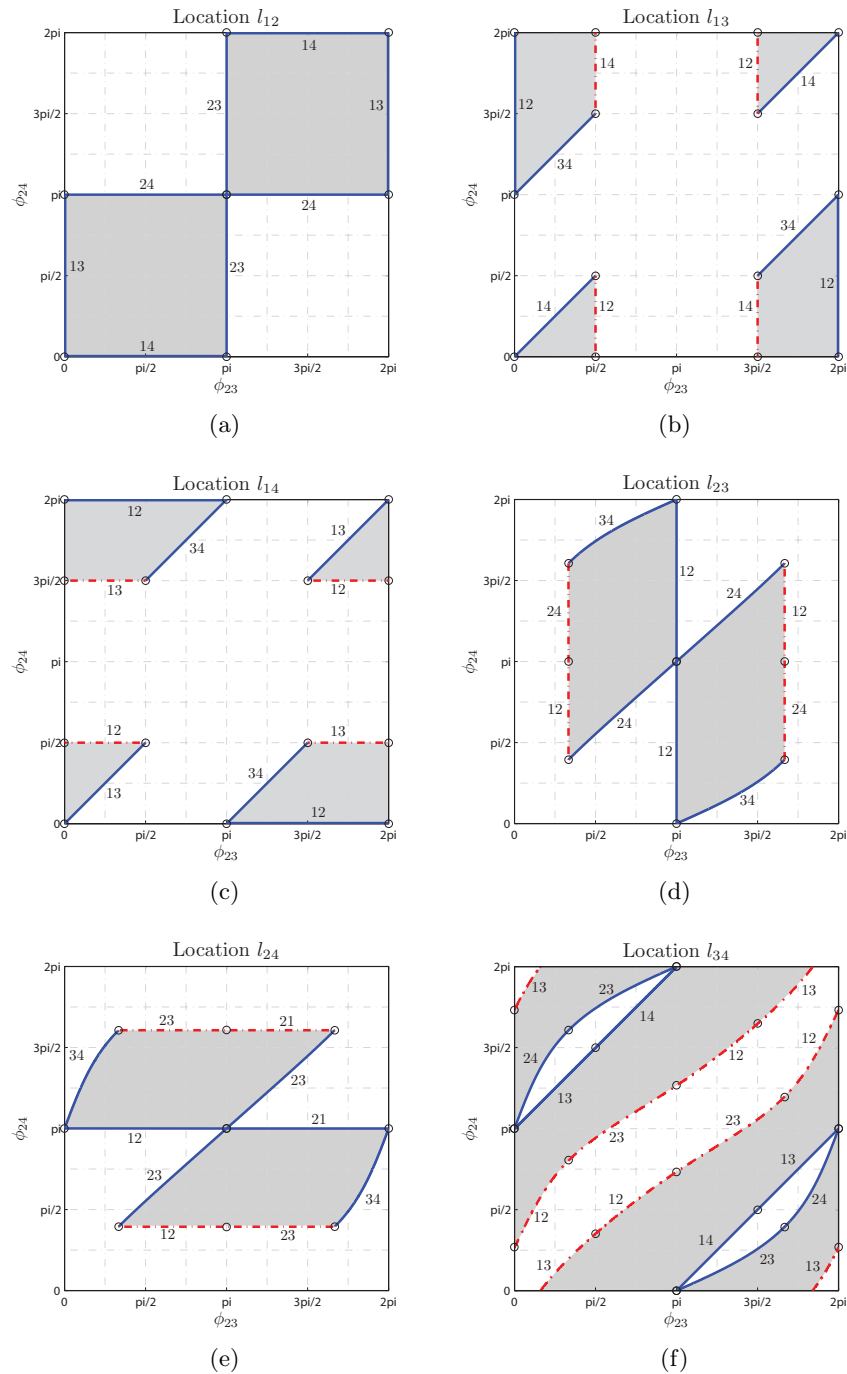


Figure 3.11: Guards and transitions for hybrid system representation of kinematic P2AT model.

-
- *Inv* defined as in Equation 3.23.
 - *Act* : $L \rightarrow F_l$ with f_{ij} defined as in Equations (3.14)-(3.16).
 $l_C \mapsto f_{ij}$

Chapter 4

The Adelopod Tumbling Robot

In this chapter we describe the Adelopod, a small two-armed tumbling robot we have developed specifically for use in our research (see Figure 4.1). The main purpose of the Adelopod is to provide a cost-effective hardware platform suitable for the study of robotic tumbling locomotion. In the following sections we overview the mechanical and electrical design of the Adelopod as well as some extensions that add extra functionality.

The Adelopod's main purpose is to provide an experimental platform for studying the merit of tumbling locomotion for miniature mobile robots. In addition to this primary goal, the Adelopod is also required to be cost-efficient, enabling multiple robots to be produced on (limited) research budgets. The resulting Adelopod design that we discuss in this chapter exhibits the following:

- **Functional Tumbling:** It is desirable, if not necessary, for any research platform designed for studying tumbling locomotion to be able to tumble. In terms of the Adelopod this requires generation of adequate torque at the arm joints to produce the characteristic end-over-end body motion required by tumbling. The Adelopod does this quite well; its capabilities regarding tumbling performance and mobility are discussed in the following Chapters 5 and 6.
- **Reconfigurability:** The Adelopod has been designed to be easily configurable, allowing for the study of various aspects of tumbling. The robot can be easily configured a variety of ways simply by switching out the shell, arms, arm angles, etc. Additionally, the robot contains several spaces left open for the addition

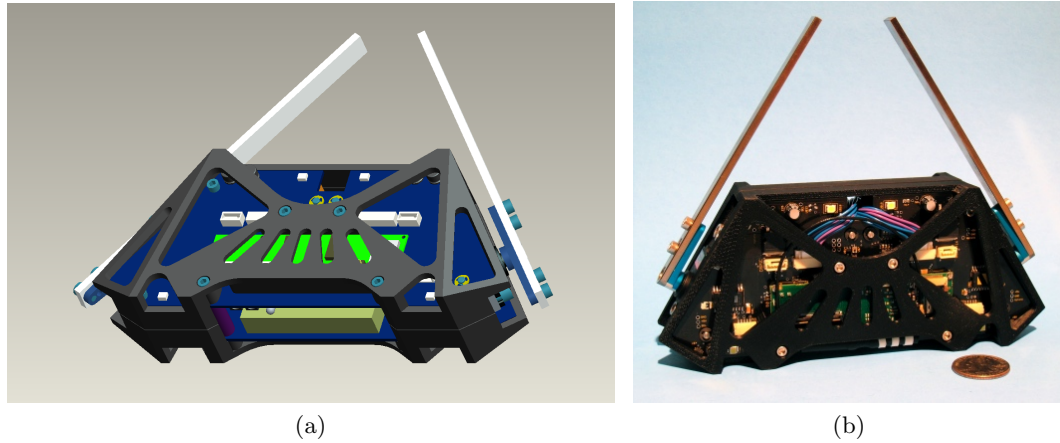


Figure 4.1: The Adelopod tumbling robot. (a) CAD model of the Adelopod design. (b) Hardware realization of the Adelopod tumbling robot shown next to a US quarter for size reference.

of sensors (e.g., cameras or GPS) as required. Lastly, extra degrees of freedom can be configured with relative ease; configurations we have developed include extra shoulder actuation (default configuration discussed in Section 4.1) as well as the addition of crawler treads that provide differential drive capabilities to the Adelopod (see Section 4.3 on the Adelopod-T).

- **Low Cost:** Low cost was achieved by designing the Adelopod with as few custom machined parts as necessary. To this end, the Adelopod makes use of its two PCBs as the main structural components and requires only four custom machined parts which themselves are relatively cheap and easy to manufacture. Additional savings were achieved through the use of a custom gearmotor solution that provides ample torque in a small and affordable package with accurate positional feedback (discussed in Section 4.1.2).

4.1 Morphology, Hardware, and Actuation

The Adelopod's morphology is based loosely on previous existing tumbling robots (e.g., see [8]). The general morphology consists of trapezoidal prism primary body with two long arms. The arms connect to the body through continuous revolute joints;

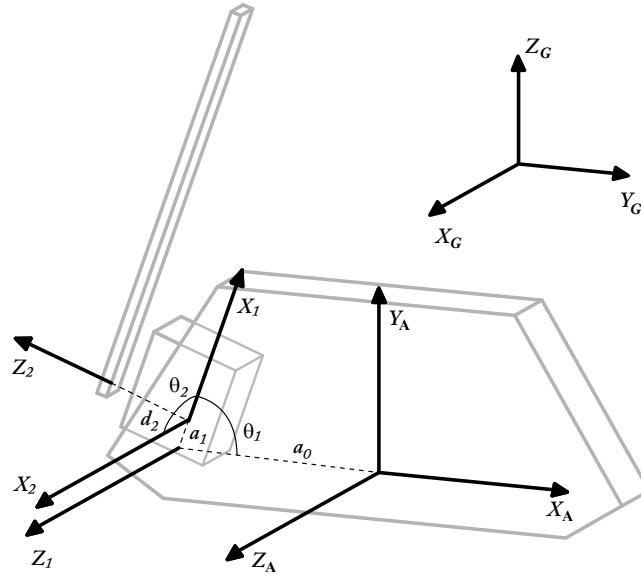


Figure 4.2: Frame assignments for the Adelopod with shoulder actuation equipped where a_0 , a_1 , and d_2 are fixed and θ_1 and θ_2 are the joint variables.

tumbling is achieved by rotating the arms about the body. The Adelopod’s tumbling classification, via Sections 3.3 and 3.4, is serial multiply-actuated self-propelled. The few existing tumbling robots that share this classification all have angular offsets between the planes in which the arms rotate, however, to our knowledge the reasons for such are not discussed. To enable the investigation of the impact of arm angles on performance, the Adelopod includes an extra degree of freedom (relative to existing designs) in each arm that allows the arm plane angle to be adjusted to values between 0 and 37 degrees off the sagittal plane (i.e. arms range from parallel to offset by 74 degrees with respect to each other). The resulting morphology is depicted in Figure 4.2 where we have labeled the various links and joints for a single arm of the Adelopod. The angles θ_1 and θ_2 are the joint variables and are controllable by the robot during operation. θ_1 and θ_2 of each arm are controlled by modified Hitec HS-5245MG (described in detail later in this section) hobby servo motors and Firgelli PQ12 linear actuators respectively.

The choice of linear actuation to control a revolute joint was made due to the space constraint imposed by the Adelopod’s primary body shape; the resulting mechanism is shown via CAD model in Figure 4.6. Here the arm servos are shown in dark gray

(located at extreme left and right of figures) and the linear actuators in orange (located at top center of figures). Figure 4.6(a) shows the left shoulder actuator fully contracted resulting in $\theta_1 \simeq 53^\circ$ while Figure 4.6(b) show the left shoulder actuator fully extended resulting in $\theta_1 \simeq 90^\circ$.

4.1.1 Arm Kinematics

With the aforementioned added shoulder actuation, each arm of the Adelopod is equivalent to a two degree of freedom kinematic chain (specifically an RR mechanism). The link-frame assignments corresponding to Figure 4.2 are shown in Table 4.1 using the Denavit-Hartenberg notation [108] and the frame notation of [109]. Here a_0 , a_1 , and d_2 are fixed while θ_1 and θ_2 are the joint variables. Following is the kinematic derivation of the left arm; the calculations for the right arm are identical with the exception that $-a_0$ and -90° of Table 4.1 are replaced with a_0 and 90° respectively.

Table 4.1: Left arm link parameters of the Adelopod robot.

i	α_{i-1}	a_{i-1}	d_i	θ_i
1	0	$-a_0$	0	θ_1
2	-90°	a_1	d_2	θ_2

The resulting link transformations are as follows:

$${}^A_1T = \begin{bmatrix} c_1 & -s_1 & 0 & -a_0 \\ s_1 & c_1 & 0 & 0 \\ 0 & 0 & 1 & 0 \\ 0 & 0 & 0 & 1 \end{bmatrix}, \quad {}^1_2T = \begin{bmatrix} c_2 & -s_2 & 0 & a_1 \\ 0 & 0 & 1 & d_2 \\ -s_2 & -c_2 & 0 & 0 \\ 0 & 0 & 0 & 1 \end{bmatrix}. \quad (4.1)$$

The complete transformation is then

$${}^A_2T = {}^A_1T {}^1_2T = \begin{bmatrix} c_1c_2 & -c_1s_2 & -s_1 & -s_1d_2 + c_1a_1 - a_0 \\ s_1c_2 & -s_1s_2 & c_1 & c_1d_2 + s_1a_1 \\ -s_2 & -c_2 & 0 & 0 \\ 0 & 0 & 0 & 1 \end{bmatrix}. \quad (4.2)$$

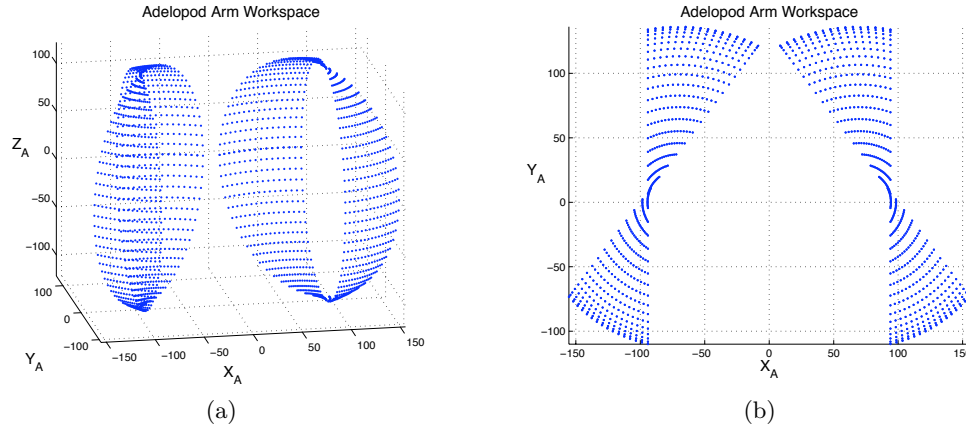


Figure 4.3: Workspace of the arm tips with $a_0 = 70$, $a_1 = 12$, $d_2 = 24$, and arm length of 122; all dimensions in [mm].

Figure 4.3 provides a graphical depiction of the space of trajectories that points on the end of each arm can take given the Adelopod’s actuation. The figure was generated by plotting the position of the arm tips in the robot’s frame (frame A) as θ_1 and θ_2 move through their entire ranges.

4.1.2 Low-cost High-torque Gearmotors with Positional Feedback

Locomotion of the Adelopod is achieved primarily through the rotation of the arms about its central primary body. Depending on the terrain, this can require significant amounts of torque to accomplish. Additionally, accurate positional feedback of the arms is required by the robot for position/velocity control of the arms as well as pose estimation of the system. Finding off-the-shelf motors that provide all of the above turns out to be quite a difficult task.

Precision micro gearmotors with encoders are often available on a per-order basis from manufacturers such as Portescap and Micromo. These motors often find their way into research robots due to their customization, efficiency, and accurate feedback. Such solutions, however, are usually quite expensive. Additionally, these types of motors tend to focus on gearhead efficiency over torque. With respect to the Adelopod design, this results in unwieldy long enclosures and limited torque for a given motor size/mass.

Orthogonal to the research field of robotics is the hobby market for recreational

robotics. This area of robotics is concerned primarily with low-cost solutions that enable individuals to build their own robotic creations. Common to many hobby creations, as well as commercially available hobby robot kits, is the use of hobby servomotors as gearmotors. By removing the internal mechanical stops and servo control circuitry, these servomotors can easily be converted to DC gearmotors. This results in very small high-torque motors available at a fraction of the price of the aforementioned precision solutions. The major drawbacks of this method are increased efficiency losses and more importantly, no internal feedback (the feedback mechanisms used in the servo design do not allow continuous rotation and must be removed for continuous DC gearmotor applications).

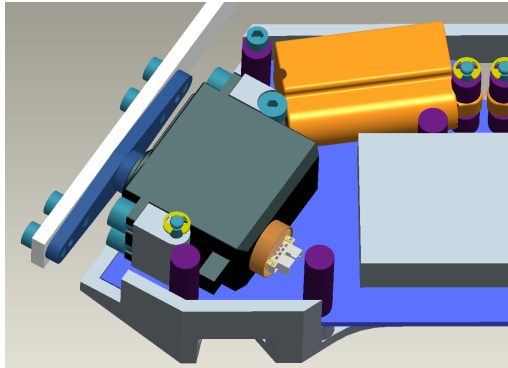
For the Adelopod, we came up with a simple design that adds accurate feedback to existing hobby servomotors resulting in a readily available low-cost solution with high torque and small form factor. This was achieved by selecting one of the highest torque hobby mini servo motors commercially available and adding a miniature continuous rotation rotary encoder that spins with the output shaft. For our application we chose the Hitec HS-5245MG digital mini servo capable of producing 5.5 kg·cm of torque at 6 volts and the US Digital MA3 rotary encoder that provides 10-bit accuracy and continuous rotation. Our modification requires removing the mechanical stop on the servo output gear as well as the servo circuitry and mounting the US Digital encoder in place of the existing limited rotation potentiometer. Mounting the encoder requires only a single adapter ring and eliminates the need for any additional moving parts. The adapter ring, shown as a drawing in Figure B.4, changes the outer diameter of the MA3 encoder to fit exactly within the HS-5245MG servo case. Flats are milled off of the MA3 encoder shaft to interface with the corresponding slot on the servo output shaft. The resulting assembly results in continuous rotation gearmotor with the attractive specifications outlined in Table 4.2 obtainable at a cost of approximately \$85-\$90 U.S. The placement and detail of the final motor as well as an exploded view is shown in Figure 4.4.

4.1.3 Structural Assembly

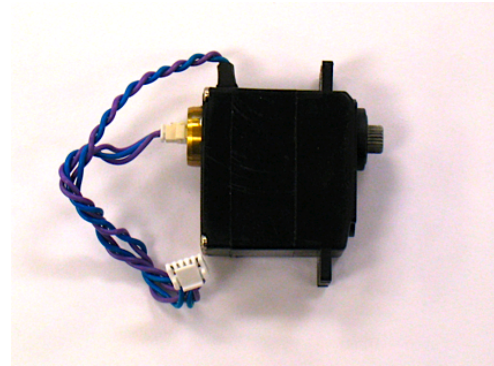
The inherent minimalism of (serial multiply-actuated) tumbling enables surprisingly simple designs. With respect to the Adelopod, only four custom machined parts are

Table 4.2: Adelopod Gearmotor Specifications

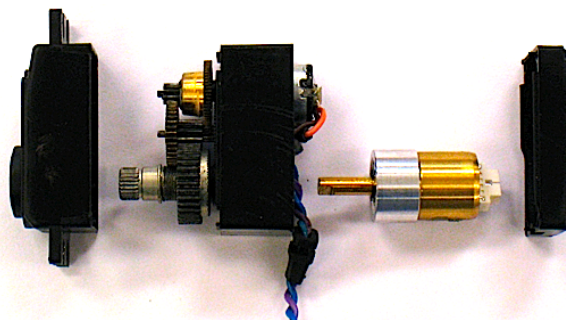
Nominal Voltage	6.0 V
Speed (6.0V)	500°/s no load
Stall Torque (6.0V)	5.5 kg·cm
Rotation	Continuous
Dimensions	32 x 17 x 31 mm
Mass	0.032 kg
Positional Resolution	10-bit
Positional Accuracy	$< \pm 0.5^\circ$
Sampling Rate	2.6 kHz



(a)



(b)



(c)

Figure 4.4: (a) CAD drawing of modified servo placement within the Adelopod. (b) Assembled servo with modifications. (c) Photo of servo internals with the encoder adapter ring installed.

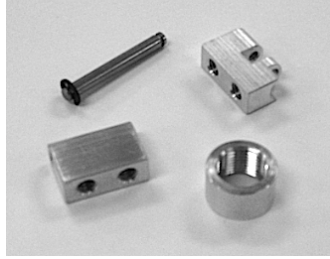


Figure 4.5: Photo of the four required machined parts for Adelopod construction. Shown are the arm mounting pins and hinges for the servo and linear actuation linkages along with the encoder adapter ring mentioned above in Section 4.1.2.

required, even with the extra actuated degree of freedom in the arms. Additionally, the custom machined parts (shown in Figure 4.5 and detailed in the drawings of Appendix B) exhibit few features and are thus relatively inexpensive and easy to manufacture.

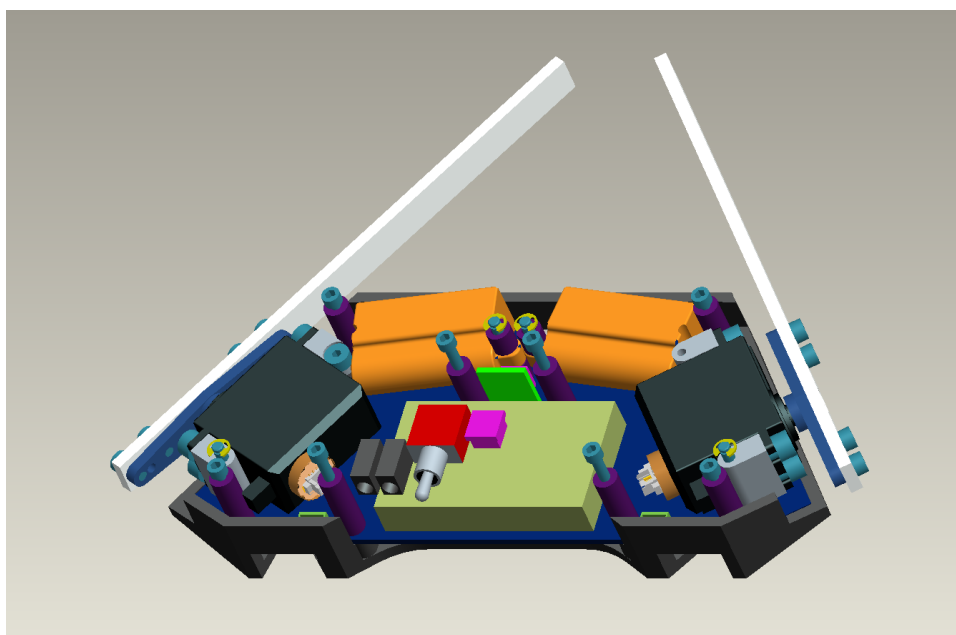
Another major contributing factor to the Adelopod's minimalism is the usage of the two PCBs as the main structural components of the robot. These two boards are separated by eight steel standoffs and together form the chassis of the robot. The PCBs are protected by two plastic shells that cover each PCB and mount using the inner four standoffs. These shells can take a variety of configurations; sample designs are discussed below in Section 4.1.4. All additional components (excluding arm linkages) mount directly to the PCBs using combinations of electrical connectors and small screws. Figure 4.6 shows the structural layout of the Adelopod with the top PCB and shell removed; here the eight standoffs are shown in purple with blue hex screws protruding.

The arm linkages float on steel pins (see Figure B.3) constrained by designated holes in the PCB and are secured by e-clips on either side of the robot. The pins constrain all motion of the linkage in the XY -plane of the robot (see Figure 4.2); the vertical motion in the Z -direction is constrained by Teflon pads adhered to a thin layer of silicone. The Teflon provides a low-friction surface for the linkage to slide against while the silicone provides some mechanical tolerance as well as shock-absorption. A photo of the Teflon pad assembly is shown in Figure 4.7.

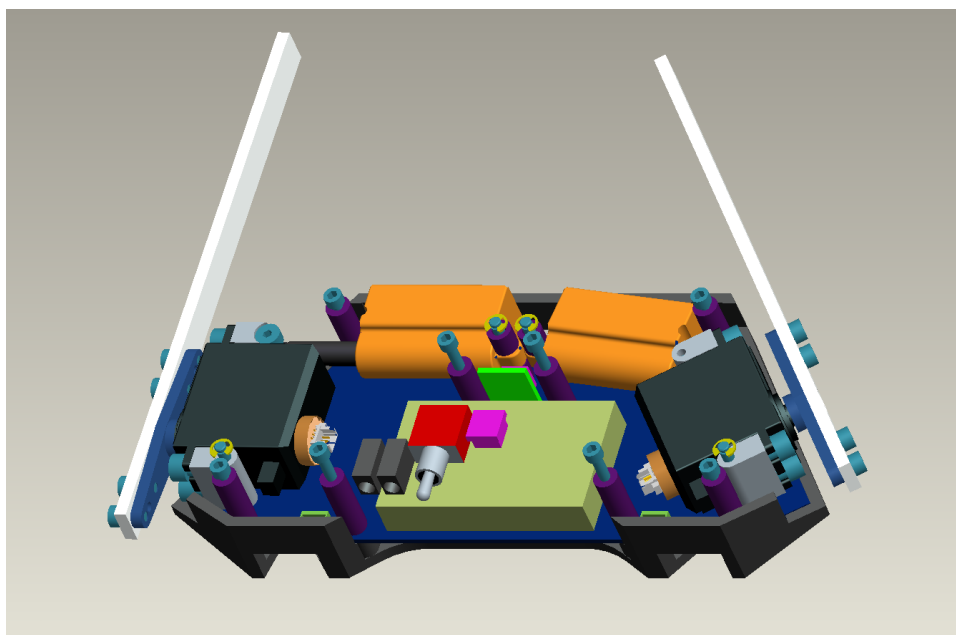
4.1.4 Shell Design

The shell of the robot protects the PCB and components from any damage that might result from tumbling while simultaneously serving as the robots primary interface with the terrain. Due to its interesting geometry and numerous features, machining such shells proved to be cost-prohibitive for our application. It is possible to injection mold such parts, however, the setup cost of creating the mold is very expensive and only makes sense for large production runs. In terms of the Adelopod, we are interested in testing multiple shell designs in small quantities; this was achieved at an affordable price using rapid prototyping fabricating.

Two sample shell designs are shown in Figure 4.8. The lower left shell is designed for indoor experimental use and allows for easy access to programming ports as well as good heat dissipation. The second shell in the figure is for outdoor environments that require increased mobility and protection. This ruggedized shell design is a solid version of the indoor shell with attached rubber tread, creating a high traction surface. Additional modifications include strategic shortening of the tread in specific areas to increase its step climbing ability (discussed further in Section 5.3.6).



(a)



(b)

Figure 4.6: CAD model of the Adelopod interior showing structural layout with (a) left shoulder contracted and (b) left shoulder extended.

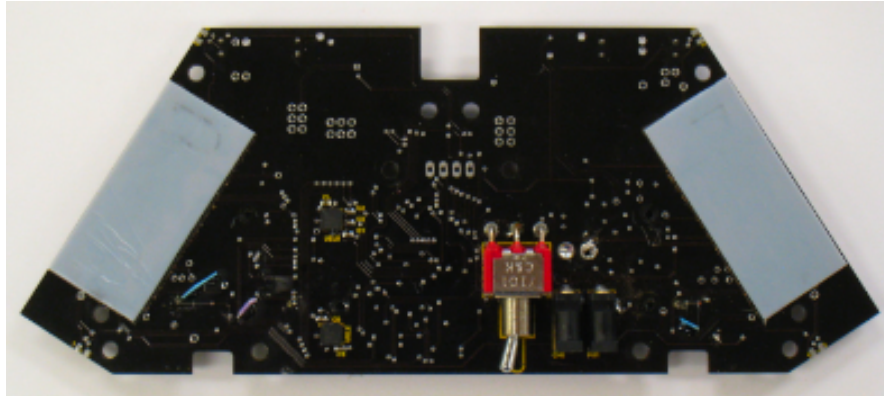


Figure 4.7: Photo of low-friction servo centering pads.

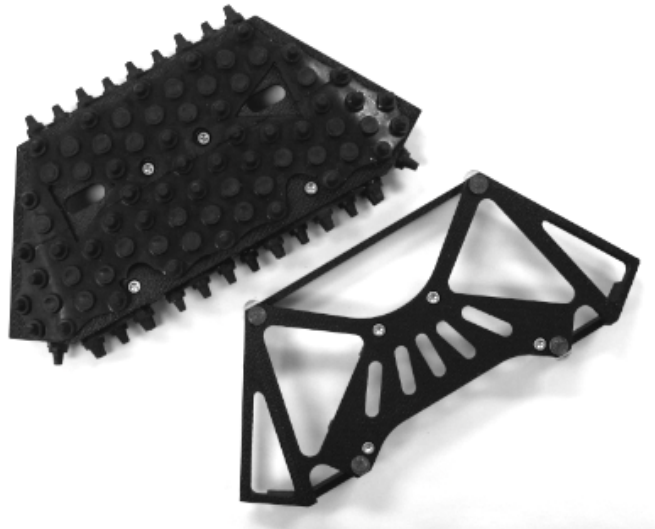


Figure 4.8: Two different Adelopod shells including indoor (lower-right) and ruggedized (upper-left) designs.

4.2 Electrical

When compared to existing tumbling robot designs, the Adelopod excels in terms of both sensing and processing power. Processing is accomplished onboard with a 600MHz Gumstix Verdex XL6P embedded computer that runs a version of the Linux operating system. For communication and off-board processing (when necessary) the Adelopod is Bluetooth enabled by default and supports the option of IEEE 802.11 wireless. For sensing the Adelopod has standard an array of light sensors, inertial measurement, and positional feedback within the motors. The light sensors are the only permanent exteroceptive sensors on the robot. For proprioceptive sensing, we have included full three-axis gyroscopic sensing along with six axes of linear acceleration sensing. This redundancy is included to help deal with gyro saturation during the later stages of a tumble where the angular velocity of the robot is quite high (after the gyros saturate, differences in observed acceleration between parallel sensors might be beneficial in reducing error). The robot additionally has a small sensor bay in the body that can house small sensors for a specific task or experiment; example sensor extensions include (omnidirectional) cameras for vision tasks and localization as well as GPS units for outdoor localization.

The full system is shown schematically in Figure 4.9 with detailed electrical schematics in Appendix C. As mentioned previously, the electronics exist on two PCBs that double as structural support for the robot. Items in blue are located on the top (main) PCB while the light red components are on the bottom (secondary) PCB.

Due to its prototype nature, the Adelopod design was not optimized for battery life. The current design is powered by a 730 mAh Li-polymer battery and draws between 350 mA and 1.5 A of current depending on the task being executed. With all motors stalled the robot can draw as much as 2 A, however, this is very rare and usually indicates a larger problem such as a immobile configuration for which battery life is not the greatest concern. With these characteristics the practical battery life of the robot ranges between 0.5 to 1.5 hours of runtime. Hardened designs for real-world applications would most likely require extended battery life.

Communication between the high-level software on the Gumstix and the low-level firmware (hardware control) is accomplished though a custom serial-peripheral-interface

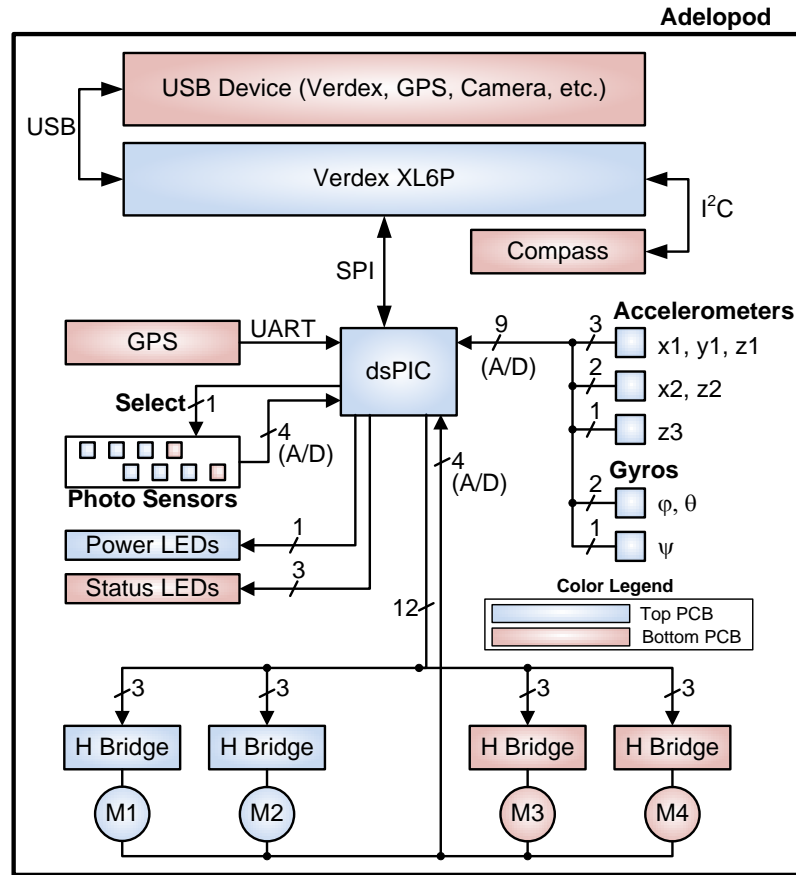


Figure 4.9: System schematic for the Adelopod tumbling robot. Hash marks designate multiple signals.

(SPI) protocol outlined in Appendix A. This method results in fast full-duplex communication. Included commands are used to set motor outputs (position or velocity control) and request sensor values as necessary. Sensor values can be requested individually, in small predefined groups, or all at once.

4.3 The Adelopod-T: A Hybrid Treaded-Tumbling Robot

The Adelopod-T (treaded Adelopod) is a configuration of the Adelopod where the shoulder actuation has been replaced with crawler treads; the result is a hybrid treaded-tumbling robot. Such a setup maintains the potential to tumble while adding differential

Table 4.3: Summary of Adelopod Specifications

	Indoor Shell	Ruggedized Shell
Body Length L_{body} [m]	0.072	0.089
Body Height H_{body} [m]	0.041	0.057
Body Width W_{body} [m]	0.172	0.172
Mass [kg]	0.444	0.568
Max Forward Velocity V_{max} [m/s]	0.120	0.141
Battery Life	0.5–1.0 hours	
Processing Speed	600MHz	
Memory	128MB RAM	
Onboard Data Storage	32MB Flash	
External Data Storage	2GB Flash	
Inertial Measurement	6-axis IMU	

drive capabilities over relatively smooth terrain. Additionally the treads can be utilized during tumbles to aid in establishing good terrain-body contacts required for tumbling as well as helping to align the robot with severe obstacles for optimal tumbles. The CAD model and a photo of the final design of the Adelopod-T are shown in Figure 4.10.

As mentioned previously, one of the primary design goals of the Adelopod was reconfigurability. As a result we were able to produce the Adelopod-T with little modification to the original design. The changes consisted of replacing the arm linkages with fixed brackets that double as supports for the track pulleys and printing a slightly larger shell that includes rollers for the tracks. Figure 4.11 shows the interior of the Adelopod-T, revealing the structural brackets (purple). Keeping with the low-cost design goal, the tracks are off-the-shelf large pitch double-sided timing belts that ride on two large timing pulleys. The top set of pulleys in the figure attach to two Hitec HS-5245MG servos modified only for continuous gearmotor operation (no encoders for positional feedback). Due to space constraints, the MA3 encoders are used to mount the second set of timing pulleys (lower two pulleys in the figure). These encoders mount in slots that allow for proper track tensioning; the left encoder of Figure 4.11 is shown in the most slack position while the right encoder is shown fully tightened.

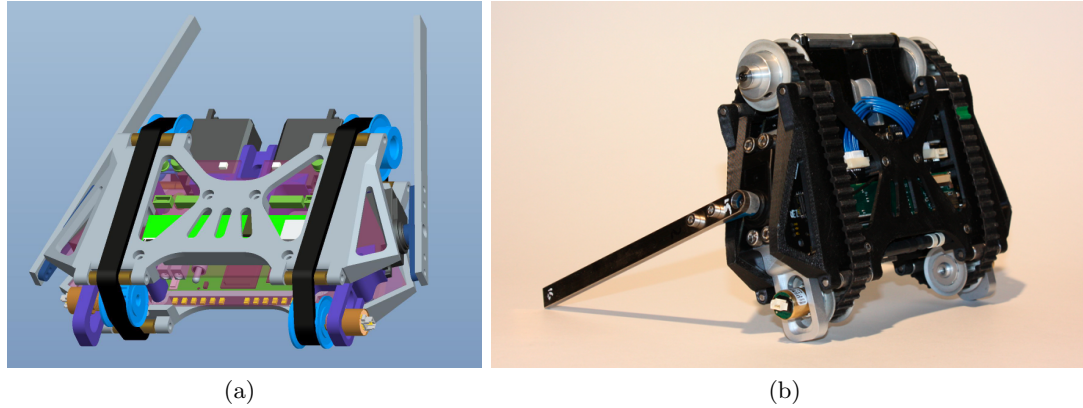


Figure 4.10: The Adelopod-T (treaded Adelopod). (a) CAD model of design. (b) Hardware implementation.

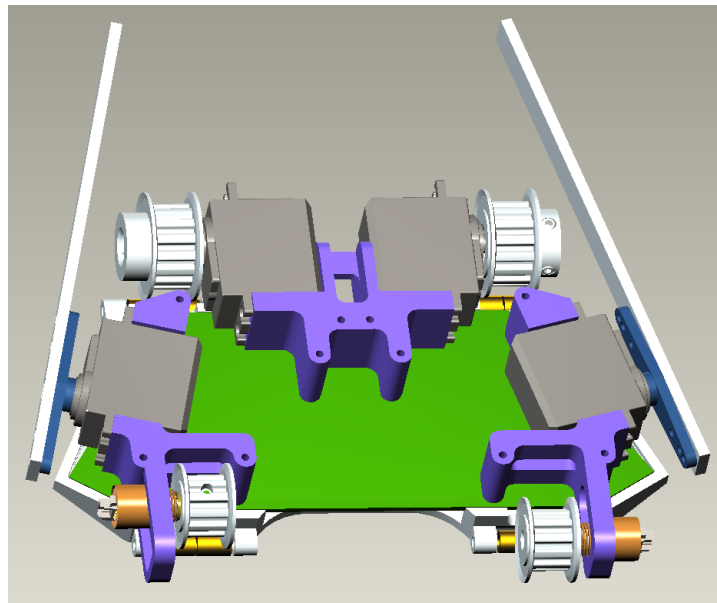


Figure 4.11: CAD model of the Adelopod-T interior showing crawler tread supports, drive motors, and idler pulleys.

Table 4.4: Summary of Adelopod-T Specifications

Body Length L_{body} [m]	0.126
Body Height H_{body} [m]	0.047
Body Width W_{body} [m]	0.172
Mass [kg]	0.664
Max Forward Tumbling Velocity $V_{t\text{-max}}$ [m/s]	0.150
Max Forward Differential Drive Velocity $V_{dd\text{-max}}$ [m/s]	0.050

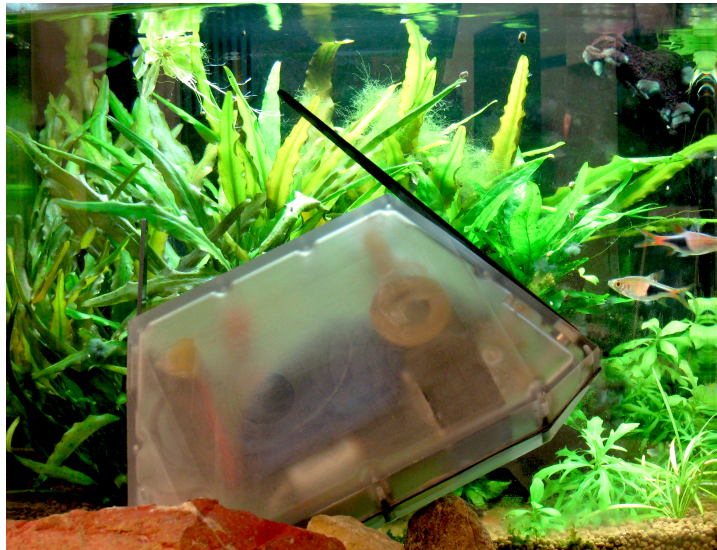


Figure 4.12: An early version of the Aquapod, an amphibious Adelopod with an active ballast to control buoyancy.

4.4 Other Variants

We wish to also note that other tumbling configurations are possible. One example we have begun investigating is the Aquapod (see Figure 4.12). This particular tumbling robot is completely waterproof and contains an active ballast system to control buoyancy. Such amphibious designs show promise as mobile sensors for monitoring environmental quality in harsh environments with abundant water (i.e., rivers, lakes, and wetlands).

Chapter 5

Terrainability of Serial Tumbling Locomotion

In this chapter, we examine the terrainability of tumbling, focusing on the class of serial tumbling robots. We present geometric and quasi-static (frictional) parametric configuration equations for a variety of idealized obstacles. These equations help identify the abilities inherent to tumbling by expressing the relationships between the robot’s configuration parameters, the environmental/task parameters, and performance. Results are illustrated through a series of mobility experiments conducted with the Adelopod tumbling platform over a variety of terrains and obstacles. Emphasis is placed on experimental rigor and repeatability in order to establish benchmarks for future performance comparisons regarding mobility of tumbling locomotion.

5.1 Robot Designs for Mobility

Central to mobile robots is the notion of mobility. From the highest level, *mobility* is concerned with the “ability to move or to be moved; capacity for movement or change of place; movableness, portability” (OED, n., 1.a [110]). In terms of mobile robots, this usually amounts to the robot’s ability to effectively generate motion from its current location in the environment to another of interest. There are many formalisms regarding mobile robot mobility; a particularly good example is the definition of [30] in which Apostolopoulos identifies three distinct indices of mobility for mobile robots as follows:

- **trafficability** – a robots ability to traverse soft soils or hard ground without loss of traction.
- **maneuverability** – a robots ability to navigate through an environment.
- **terrainability** – a robots ability to negotiate terrain irregularities.

The trafficability index is analogous to the classical studies of terramechanics by Bekker [12, 13, 14] and Wong [15] that examine the off-road performance of large vehicles with applications to transport, construction, and military use. Maneuverability is concerned with the robot’s ability to change its heading, achieve desired positions in the environment, and avoid obstacles. In this respect, maneuverability is concerned with the ability to effectively steer the robot. The final index, terrainability, is concerned with the ability of the robot to directly overcome any obstacles and is the focus of this chapter.

The above mobility indices are sufficient for describing the ability of particular robots over various terrain scenarios. In the presence of design constraints, such metrics are quite useful in quantifying and optimizing performance of various designs. For this work, however, we are interested in the relative performance of different forms of locomotion and make the observation that the same terrain for two different mobile robots can pose quite different challenges depending on their size, mass, method of locomotion, etc. Therefore, when comparing relative performance of two separate robot designs, issues such as size, complexity, efficiency, etc. must be taken into account. This turns out to be quite difficult to do in general. In terms of mobile robots, hardware is expensive and hard to obtain, researchers in general do not have access to other existing research robots, and design plans of such robots are rarely made public. In [32, 111], Thueer identified and addressed such issues for the case of wheeled all-terrain robots by creating a modular chassis for studying the relative merits of various suspension configurations under equivalent mass and size configurations. For less common robot designs, however, the issue of normalization is not so straightforward. Works such as [2, 26, 27] acknowledge that the issue exists and instead focus their efforts on measuring performance over repeatable terrains that enable comparisons with other similar (i.e., comparable size, shape, mass, etc.) robots.

We approach the issue by examining mobility-to-cost relationships in addition to a thorough performance analysis as in [2, 26, 27]. By this approach it is possible to

establish theoretical performance bounds based on various sets of assumptions regarding terrain-robot interfaces and terrain structure as well as producing actual measured performance of particular hardware instantiations. In particular, we wish to maximize terrainability while minimizing cost in terms of size and/or hardware complexity. This particular characteristic enables the realization of relatively small and inexpensive robots with applications in exploration, surveillance, and mobile sensing. This combination of attributes additionally lends itself well to deployable robots that are beneficial as members of larger heterogeneous teams of robots. In these scenarios, small size and high terrainability enables the robots to be deployed by larger, more efficient robots and retain sufficient mobility for their respective tasks. Additionally, low hardware complexity generally enables inexpensive designs and thus expendable platforms that can be left in the field if necessary/convenient for a particular mission.

In Chapter 3, we make the claim that certain types of tumbling robots provide the potential to produce high mobility with respect to their size and/or complexity. The two main classes of tumbling, serial and composite-bodied, are somewhat orthogonal in their abilities where serial tumbling exhibits emphasis on minimalistic design and composite-bodied tumbling on parallel configurations that sacrifice minimalism for the benefits of more complex morphing designs. While both are interesting, we are concerned with designs that are both small and inexpensive; therefore we limit our investigation to the terrainability of serial tumbling robots.

5.2 Terrainability Analysis of Serial Tumbling Robots

In this section we identify some of the advantages and thus motivating factors of serial tumbling in terms of terrainability, the ability of a robot to negotiate terrain irregularities. To achieve this, we use methods similar to [30] in which we formulate configuration equations that express the relationships between the robot's configuration parameters (morphology, geometry, mass, etc.), the environmental/task parameters (obstacle geometry, available coefficients of friction, etc.), and the performance parameters (obstacle difficulty, robot size/complexity, etc.). However, in contrast to focusing on optimizing parameters of a particular morphology (as in [30] for wheeled rovers), we wish to identify

fundamental properties common to tumbling locomotion and corresponding morphologies. In this respect, this section is concerned with establishing theoretical performance bounds of serial tumbling morphologies as well as the cost associated with realizing such devices.

5.2.1 Planar Framework

In real-world environments, interactions between the robot and terrain are often quite complex. In the case of serial tumbling, the robot-terrain interaction complexity is further compounded by the robot's inherent underactuation and resulting required use of sliding contacts. In order to form meaningful relations, it is necessary to perform some simplifying assumptions regarding the robot and/or terrain. For the purposes of this work we adopt a planar representation of the robot and terrain similar to those used in the works [15, 67, 32, 112]. Such a representation simplifies the analysis through a dimensionality reduction achieved by projecting the robot morphology and terrain features into two dimensions. The result is an easily parameterizable space capable of capturing many of the interactions of interest that simultaneously removes many issues regarding steering and control.

As an additional simplification, we perform all calculations under the quasi-static assumption that the robots move sufficiently slow such that any inertial effects are negligible.

Robot Models

Here we consider two-bodied planar tumbling morphologies with a single actuator. These morphologies contain a primary body as well as a second body used for producing necessary tumbling forces. Although relatively simple, this parameterization encapsulates representations of planar analogs to the singly-actuated spherical robots of Section 3.4.1, single-axle wheel(leg)-tail robots such as the UMN and Recon Scout robots [113, 114], and dedicated tumbling robots such as the Turbots and the Adelopod of Section 3.4.2. Schematic depictions of each are shown in Figure 5.1. The wheel-leg morphology, in the limits of the spoke count, actually captures a couple of different real-world robot designs, demonstrating their similarities. With a sufficient number of spokes the wheel-leg can be seen as an approximation to a wheel with a non-convex tread and

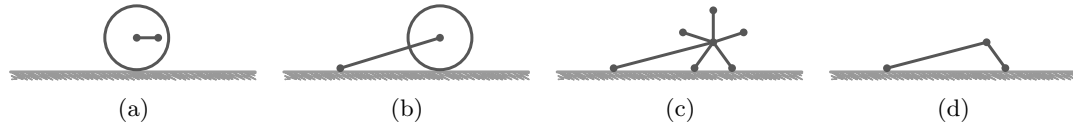


Figure 5.1: Considered morphologies for terrainability analysis. (a) Serial singly-actuated morphology. (b) Serial multiply-actuated wheel-tail morphology. (c) Serial multiply-actuated wheel-leg and tail morphology. (d) Serial multiply-actuated tumbling morphology.

in the limit as the number of spokes goes to infinity a perfectly smooth wheel that relies on frictional contacts only. Taking the limit in the other direction, we see that wheel-legs with one or two spokes form an approximation of the basic planar representations of the Turbot and Adelopod tumbling robots where the wheel-leg represents the body and the tail the arm; a two spoke design with legs opposing and of different lengths allows the representations of various actuator positions while a single-leg configuration puts the actuator at the far end of the body.

Idealized Obstacles

As obstacles in our planar framework we look at several idealized obstacles that represent worst-case geometric features of terrain while being easily parameterizable. Specifically we have chosen to consider steps, ditches, and overhangs shown with their respective parametrizations in Figures 5.2(a)–(c). Such obstacles are common choices in quantifying robot mobility and often appear in works pertaining to robot mobility analysis. These choices are popular due to their intuitive nature, encapsulation of terrain impulses, and convenient single parameter representations. Additionally, these idealized terrain features can be made more complicated by adding slope (grade) or through the combination of multiple idealized obstacles to make arbitrarily complex obstacles as motivated in [17]. An example 2-parameter obstacle made by combining an idealized step and ditch is shown in Figure 5.2(d).

Performance Evaluation

The final issue to discuss before continuing is how we wish to evaluate the cost of particular morphology configurations. As mentioned previously, we are primarily concerned

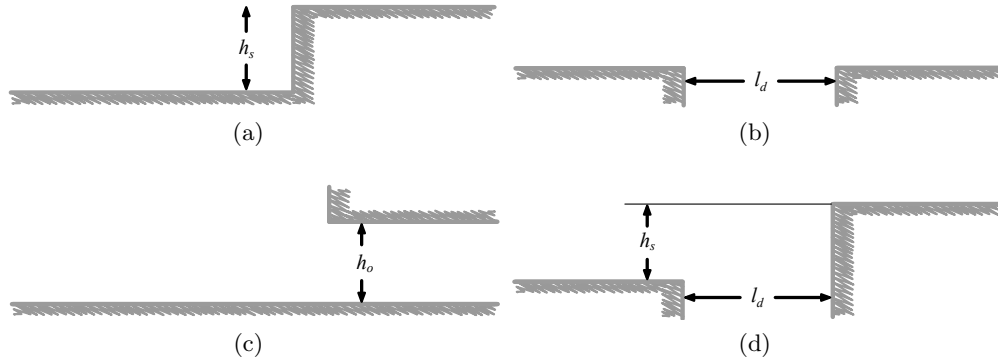


Figure 5.2: Idealized obstacles with their parametrizations. (a) Step obstacle parametrized by its height h_s . (b) Ditch obstacle parametrized by its height l_d . (c) Overhang obstacle parametrized by its height h_o . (d) Two-parameter step-ditch obstacle parametrized by both ditch length l_d and step height h_s .

with designs that maximize terrainability while minimizing the costs of mechanical complexity and size. For the purpose of this work we quantify hardware complexity by the number of bodies and actuators. We have chosen the morphologies of Figure 5.1 that we wish to examine such that they are all equivalent by this metric (i.e., two bodies and a single actuator). Size can be measured in a number of ways. Within our planar framework, measures of length and area both make sense. For calculating both length and area we take the minimal value over all of the configurations a particular morphology can take; this is equivalent to measuring the size of the robot in its most compact configuration that would most likely be used for transporting or storing the robots. For area, we use the minimum area convex hull of each morphology which is representative of the morphology’s footprint, a common measure of robots’ size.

Although we focus primarily on size and complexity, many other possible cost metrics exist. Some common choices are as follows:

- **Size** – Mentioned above, this common metric penalizes the size of a particular instantiation. This cost metric is commonly used in conjunction with mass for robots that must be transported and deployed either by another robot or humans where larger robots are less convenient. Possible formulations include length, volume, and footprint area where each can be calculated exactly or approximated from bounding areas such as the convex hull; additionally, each formulation can

be measured with the robot in its stowed or mobile configurations.

- **Mass** – Another popular metric in combination with size; this metric is again important for deployable systems where payloads are generally limited.
- **Hardware Complexity** – A primary metric of interest for this work; this metric places penalties on the complexity of a systems hardware instantiation. This can be measured in a number of ways including number of moving parts, total parts count, number of actuators, etc. This metric is strongly considered in industry, however, it is often overlooked in the area of research robots where emphasis is instead placed on novelty as well as proof-of-concept.
- **Efficiency** – A metric pertaining to the energetics of a robot in operation. This metric is of particular importance to mobile robots that rely on internal (limited) energy sources to remain functional. Measures usually involve some normalization with respect to forward velocity or distance along with the robot’s mass; examples include specific resistance [25] and cost of transport respectively.
- **Frictional Requirement** – A metric pertaining to the required friction at the terrain-robot interfaces to negotiate terrains of interest. This metric is popular in the study of wheeled space rovers and is based on the observation that friction is generally limited; a good discussion exists within [111].
- **Stability** – A metric commonly studied in legged locomotion pertaining to the “closeness” of a system to becoming unstable. As a cost, it is common to use the minimum stability observed over some motion or (periodic) gait or gait transition where higher minimum stability is desirable. Measures can be static or dynamic; see Section 2.4 for an overview of common metrics. This particular metric as a cost has little use with regard to tumbling due to the common utilization of unstable states during locomotion.

5.2.2 Step Climbing

One of the most common measures of a robot’s mobility is the largest step that it can climb. This idealized terrain feature approximates impulses in the terrain and captures the ability of the robot to overcome such irregularities. Therefore we begin our investigation of tumbling mobility with the analysis of step climbing of serial tumbling

robots. For our investigation we use the morphologies of Figure 5.1 and the idealized step parametrization of Figure 5.2(a).

Previous works examining the step climbing ability of robots include [115] and [116] where the step climbing ability of leading wheels and wheel-legs were examined respectively. In [115] Takahashi calculated the theoretical step heights at which the leading wheel of a robot will begin to climb as a function of the available coefficient of friction μ as

$$\theta < \operatorname{arccot} \left(\frac{1 - \mu\varepsilon}{\mu + \varepsilon} \right), \theta \in [0, \pi/2], \quad (5.1)$$

where θ is measured from the terrain interface to the step interface; the variable ε represents the ratio of forces F_1/N_1 , the forward force and weight respectively that the robot exerts on the wheel in question. This can be expressed in terms of step height h_s and wheel radius r as

$$h_s < r \left(1 - \cos \left(\operatorname{arccot} \left(\frac{1 - \mu\varepsilon}{\mu + \varepsilon} \right) \right) \right). \quad (5.2)$$

For $\mu\varepsilon$ greater than 1, $h_s = r$ and the leading wheel will begin to climb steps of height greater than its radius. Tantichattanont et al. in [116] extend the analysis to include wheel-leg hybrid robots and made the observation that a wheel-leg's maximum climbable step height is in general automatically greater than its radius.

Serial tumbling robots, however, in general lack the benefit of any external pushing forces and must generate the majority of climbing forces at the step interface. In terms of the above relations, this results in F_1 and therefore ε of Equations (5.1) and (5.2) equal to zero. By this observation, assuming the absence of any adhesive forces at the step interface (e.g., glue or magnets), the tumbling robot must at the very least be able to reach the top of the step to generate some non-zero vertical force in order to climb.

Body Profiles and Reach

In Figure 5.3, we show schematically the geometric maximum step reach of wheel-legs with one, three, and five spokes along with a wheel. Wheel-legs approximate body profiles of regular polygons with sides equal to the number of spokes; additionally a wheel can be approximated in the limit as the number of wheel-leg spokes approaches

infinity. From the figure, it is clear that the maximum step reach is achieved by the one-spoked wheel-leg model. With respect to tumbling robots where the body is used for overcoming obstacles, this suggests that bodies exhibiting high aspect ratios (i.e., long and narrow) are desirable for increased step climbing abilities. The actual values for the step reach, h' , are as follows (see [116] for a similar derivation):

$$h'_{\text{wheel}} = r, \quad (5.3)$$

$$h'_{\text{wheel-leg}} = r \left(\sin \left(\frac{\pi}{n} \right) + \cos \delta \right), \quad (5.4)$$

$$h'_{\text{tumbling}} = 2r, \quad (5.5)$$

where n is the number of spokes and δ the angle between the supporting leg and the ground normal which can be calculated as

$$\delta_1 = - \left\lfloor \frac{n+2}{4} \right\rfloor \frac{2\pi}{n} + \frac{\pi}{2} + \frac{\pi}{n}, \quad (5.6)$$

$$\delta_2 = - \left\lfloor \frac{n+2}{4} + 1 \right\rfloor \frac{2\pi}{n} + \frac{\pi}{2} + \frac{\pi}{n}, \quad (5.7)$$

$$\delta = \begin{cases} \delta_1, & \text{if } \delta_1 < |\delta_2| \\ \delta_2, & \text{otherwise} \end{cases}. \quad (5.8)$$

Figure 5.4 shows a plot of h'/r , maximum geometric step reach over the leg length, versus n from 2 to 50. Through observation we found δ to take one of three values; $\pi/2n$ for n odd (plotted in green), 0 for $n \in \{2, 6, 10, \dots\}$ (upper dashed red curve) and π/n for $n \in \{4, 8, 12, \dots\}$ (lower dashed red curve). From the plot we see that performance is maximum at $n = 2$ and as n goes to infinity, h'/r approaches 1 suggesting that a wheel will have the worst performance, with a maximum surmountable step height equal to its radius.

Geometric Maximum Step Height

Considering only tumbling robots capable of self-propulsion, the class of serial tumbling robots can be divided into singly and multiply-actuated tumbling robots. These two subclasses (defined in Section 3.3) depend on the number (and nature) of contacts made with the terrain. In our current analysis, singly-actuated tumbling is represented by the

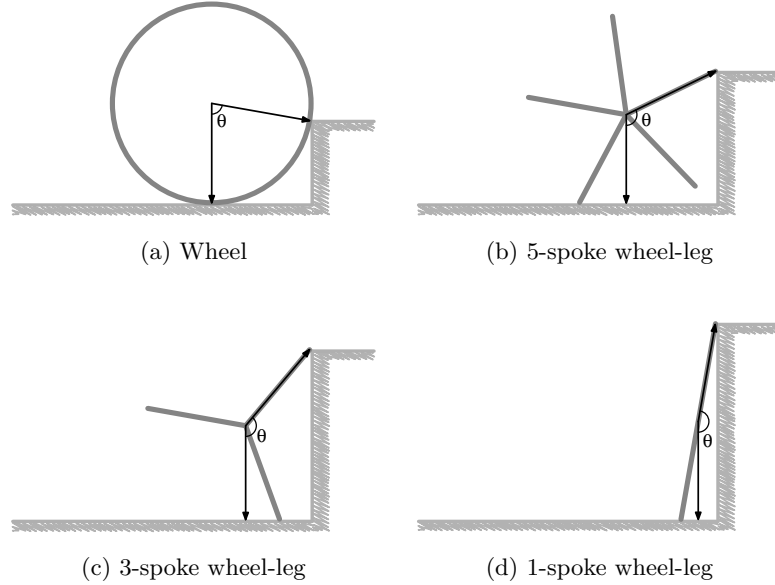


Figure 5.3: Schematic depiction of the geometric step reach of several spoked wheel-leg and wheel configurations; each is shown at θ equal to 10 degrees from optimal.

the singly-actuated robot morphology of Figure 5.1(a) and multiply-actuated tumbling by the morphologies of Figures 5.1(b)–(d).

Considering first the singly-actuated morphology of Figure 5.1(a), we can see that the above step reach analysis (which shows that circular body profiles have step climbing performance limited to heights less than or equal to their radius) is further limited by the singly-actuated internal force generation. For this particular morphology, locomotive forces are generated by manipulating the internal center of mass position. Here a successful step climb requires the center of mass to cross the vertical face of the step as depicted in Figure 5.9(a). This results in geometric surmountable step heights of

$$h_s < r - \sqrt{r^2 - l_m^2}, \quad (5.9)$$

where l_m is the effective length of the internal center of mass.

In contrast, multiply-actuated tumbling robots have the advantage of multiple bodies in contact with the terrain that can be utilized to generate forces external to their

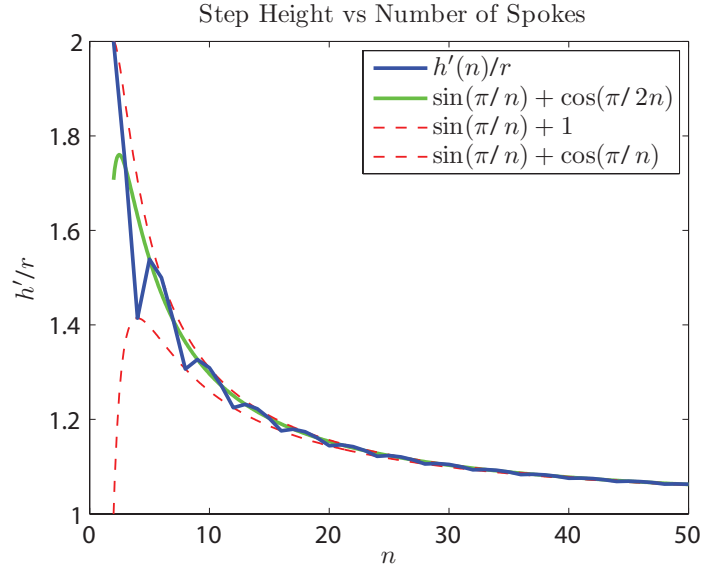


Figure 5.4: Plot of the geometric maximum step reach for n -spoked wheel-legs of radius r .

primary body. This is achieved via the tail/arms of the morphologies of Figures 5.1(b)–(d). With the external force generation, such robots are able to achieve geometric step climbing performance equivalent to their reach assuming that the tail/arm is long enough to apply the required forces throughout the entire climbing trajectory (see Figure 3.2(c) for a representative step climbing trajectory). The resulting geometric step performance is expressed as

$$h_s < \min\{r, \ell_{\text{tail}} - r\}, \quad (5.10)$$

$$h_s < \min\{\ell_{\text{body}}, \ell_{\text{arm}} - \ell_{\text{body}}\}, \quad (5.11)$$

for the wheel-tail and tumbling morphologies respectively.

It is important to realize that these calculated heights are purely geometric and ignore both the frictional effects and any forces exerted on the wheel from the robot. Despite this, however, the values are respective of actual performance in some scenarios. One such example is the interlocking of the wheel/body's tread and the step (see Figure 5.5(a) as well as Figure 5.6). In this case the robot is able to produce a downward force upon the top of the step, producing a significant reaction force and corresponding

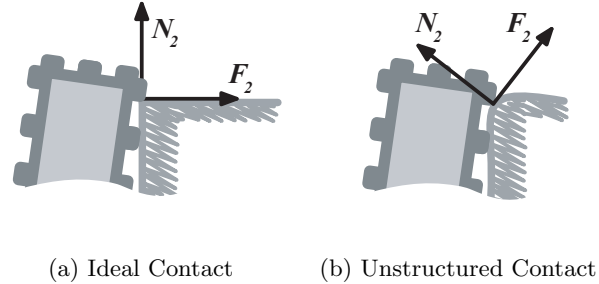


Figure 5.5: Schematic drawing of ideal and unstructured contacts.

frictional force to pull the robot over the step. When such contacts are not achievable (e.g., rounded corners or unstructured terrain as depicted in Figure 5.5(b)), it is necessary to perform a more detailed analysis that includes friction and external forces.

Frictional Step Interactions

In real-world scenarios often times a robot is not able to perfectly grip (interlock with) an obstacle while trying to overcome it. In these cases the robot's ability to sufficiently negotiate the obstacle is limited by the frictional contacts between itself and the obstacle in question. In this section we address the particular scenario of a robot climbing a vertical step with such non-ideal contacts. Here we must consider the type of contact along with the corresponding ground reaction and frictional forces. The result is a set of parametric configuration equations (see [30]) that express the relationships between the robot's configuration parameters (morphology, geometry, mass, etc.), the environmental/task parameters (step geometry, available coefficients of friction, etc.), and the performance parameters (step height).

To arrive at the configuration equations, we utilize quasi-static force balance equations with assumptions of static friction at the body-step interface and kinetic friction at the arm (tail)-ground interface where applicable. For the singly-actuated morphology, these assumptions approximate the robot slowly climbing the step by rotating about the step's edge. The single-axle morphologies of Figures 5.1(b)–(d) are more interesting due to their sliding contacts at the arm/tail of the robot. Under the aforementioned quasi-static assumptions, we approximate a robot slowly climbing the step by rotating

the body (wheel) about the step edge with the arm (tail) sliding along the ground. Such systems are analogous to slider-crank mechanisms and are depicted in Figure 5.7.

Idealized Serial Multiply-Actuated Tumbling Robot

For clarity we derive the configuration equations for an infinitely thin serial multiply-actuated tumbling robot with the center of mass at the arm joint shown in Figure 5.7(a). We wish to note, however, that it is relatively straightforward to extend the presented results to other tumbling robots with realistic body/arm geometries and mass properties.

There are three modes that our tumbling robot model can be in when climbing a vertical step. The mode of the robot is determined by the direction of the frictional force F_3 along with the type of contact between the body and step. F_3 can take two directions depending on whether the arms are pushing or dragging along the ground. When the angle between the body and arm (measured counterclockwise from the body) is less than π , the arm joint is below the line formed between the arm-ground contact and the body-step contact (ℓ_h in Figure 5.7(a)). In this configuration, the arm contact must push away from the step for the system to climb as a slider-crank mechanism. After the arm joint passes above the line ℓ_h , the arm begins to drag towards the step as the robot climbs, switching the direction in which F_3 acts. With regard to the type of contact at the body-step interface, we have two possible scenarios, one in which the corner of the step contacts the edge of the robot's body (type 1) and one where the corner of the robot's body contacts the top edge of the step (type 2); the difference in direction of forces in each of the modes is depicted by the rightmost insert of Figure 5.7(a)). Since it is impossible for the arm to be pushing away from the step during a type 2 contact (assuming convex body geometry), we have three total modes. From the geometry of the robot we can calculate the endpoints of the three modes as functions of the variable α as follows:

$$\text{mode 1} \iff \alpha \in \left[\arccos\left(\frac{h_s}{\ell_2}\right), \arccos\left(\frac{h_s}{\ell_2 + \ell_3}\right) \right), \quad (5.12)$$

$$\text{mode 2} \iff \alpha \in \left[\arccos\left(\frac{h_s}{\ell_2 + \ell_3}\right), \frac{\pi}{2} \right), \quad (5.13)$$

$$\text{mode 3} \iff \alpha \in \left[\frac{\pi}{2}, \pi \right]. \quad (5.14)$$

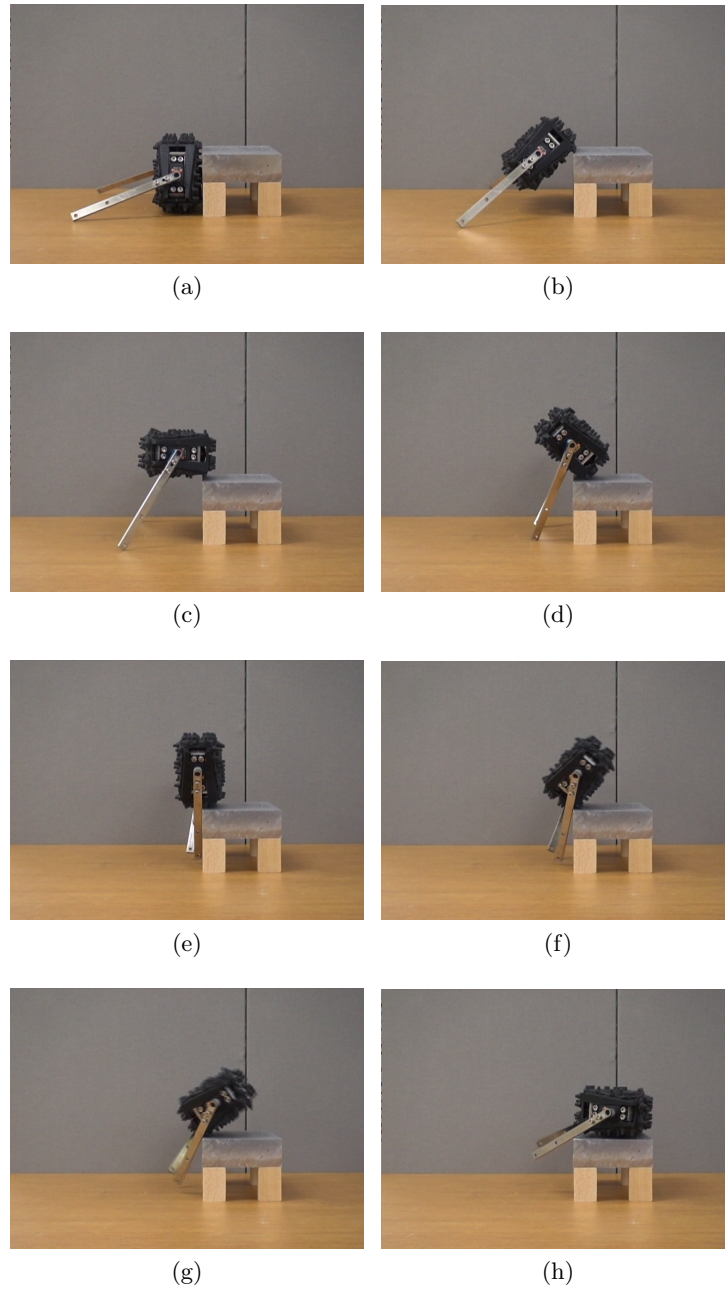


Figure 5.6: Consecutive frames from a video of the ruggedized Adelopod climbing an idealized step with height 0.8 times its body length. Here the robot is able to form an interlocking ideal contact with the step edge.

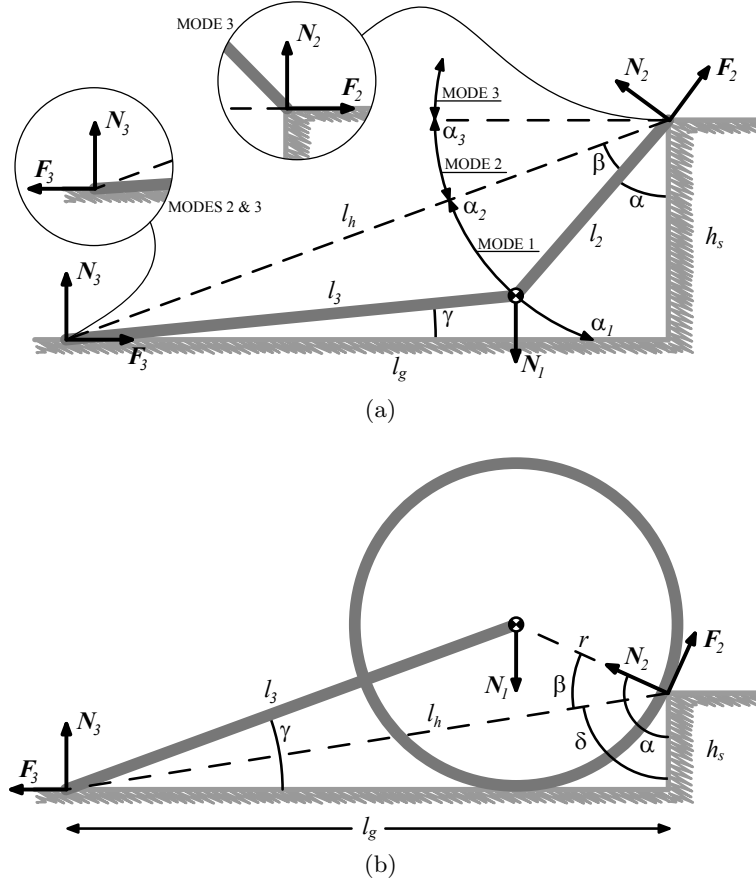


Figure 5.7: (a) Quasi-static forces acting on an idealized serial multiply-actuated tumbling robot while climbing a vertical step of height h_s . Here α parametrizes the climbing trajectory, N_1 is the weight of the robot, l_2 is the body length, l_3 is the arm length and N_2 , N_3 , F_2 , and F_3 are the ground reaction and frictional forces of the body-step and arm-ground interfaces respectively. The frictional force of modes 2 and 3 acting at the arm-ground interface are depicted by the left insert. The direction of the normal and frictional forces of mode 3 at the body-step interface with respect to the mode of climbing are depicted by the right insert. (b) Quasi-static forces acting on an idealized wheel-tail robot while climbing a vertical step of height h_s . Again α parametrizes the climbing trajectory, N_1 is the weight of the robot, N_2 , N_3 , F_2 , and F_3 are the ground reaction and frictional forces of the wheel-step and tail-ground interfaces respectively. The wheel diameter and tail length are represented by r and l_3 respectively.

Solving the system for equilibrium in mode 1 we get the following equations:

$$N_3 = N_1 - N_2 \sin \alpha - F_2 \cos \alpha, \quad (5.15)$$

$$F_3 = -F_2 \sin \alpha + N_2 \cos \alpha, \quad (5.16)$$

$$N_1 \ell_3 \cos \gamma = N_2 \ell_h \cos \beta + F_2 \ell_h \sin \beta. \quad (5.17)$$

The equations for modes 2 and 3 are similar with changes in sign and direction depending on the direction of F_3 and the angle of forces at the body-step interface. Because the arm is assumed to be dragging we can represent F_3 by the product $\mu_3 N_3$, where μ_3 is the kinetic coefficient of friction between the arm and ground and N_3 the normal force at the contact.

The set of equations from each mode represent the parametric configuration equations of an idealized tumbling robot climbing a step. From here it is possible to obtain relationships between parameters of interest by solving the equations for the parameter in question. As an example, one useful quantity is F_2/N_2 , the required friction at the body-step interface to prevent the body from sliding. With the aid of symbolic manipulation software we have found the above relationship for all three cases as follows:

$$\mu_{2\min} = \begin{cases} \frac{1 - \frac{\ell_3 \cos \alpha \cos \gamma}{\ell_h \mu_3 \cos \beta} - \frac{\ell_3 \sin \alpha \cos \gamma}{\ell_h \cos \beta}}{\frac{\ell_3 \cos \alpha \cos \gamma}{\ell_h \cos \beta} - \frac{\ell_3 \sin \alpha \cos \gamma}{\ell_h \mu_3 \cos \beta} - \tan \beta}, & \text{mode 1} \\ \frac{1 + \frac{\ell_3 \cos \alpha \cos \gamma}{\ell_h \mu_3 \cos \beta} - \frac{\ell_3 \sin \alpha \cos \gamma}{\ell_h \cos \beta}}{\frac{\ell_3 \cos \alpha \cos \gamma}{\ell_h \cos \beta} + \frac{\ell_3 \sin \alpha \cos \gamma}{\ell_h \mu_3 \cos \beta} + \tan \beta}, & \text{mode 2} \\ \frac{\ell_g - \ell_3 \cos \gamma}{h + \frac{\ell_3}{\mu_3} \cos \gamma}, & \text{mode 3} \end{cases} \quad (5.18)$$

Figures 5.14(b), (d), (f), (h), (i), and (j) show the value $\mu_{2\min}$ versus α and μ_3 plotted for step heights h_s equal $\ell_2/16, \ell_2/8, \ell_2/4, \ell_2/2, 3\ell_2/4$, and ℓ_2 with all units in meters-kilograms-seconds. For generating the plots, we set $N_1=1$, $\ell_2 = 1$, and $\ell_3 = 2$. The plots show the trend of the body-step frictional requirements over the trajectory of the climb (parametrized by α) for different values of μ_3 . For a robot to climb a step of height h_s , it must satisfy the maximum required μ_2 over the entire climbing trajectory.

That is, the robot must satisfy

$$\mu_{2robot} \geq \max_{\alpha} \mu_{2min}(\alpha, \mu_3) \quad (5.19)$$

for a particular μ_3 at its arm. Shown are only the values for μ_{2min} between 0 and 1, resulting in clipped regions which represent unrealistic or unachievable frictional requirements. Note that our choice of upper bound was made with plot clarity and the generally available coefficients of friction in nature in mind; specific applications and/or systems will present meaningful restrictions on allowed values such as μ_2 .

Figure 5.8(a) shows a contour plot of the surface in Figure 5.14(i). Here the three modes of climbing are separated by the two vertical black lines at α equals $\arccos(1/4)$ and $\pi/2$. The black dashed line shows the solutions to $\mu_2 = 0$ which represent configurations in which the friction at the arm-ground interface alone is sufficient to maintain climbing. Crossing this line results in a change in direction of F_2 ; combinations of α and μ_3 to the left of this line have the direction of F_2 as depicted in Figure 5.7(a) while combinations of α and μ_3 to the right of this line have the direction of F_2 opposite of that depicted in the figure. Physical configurations with F_2 opposite of Figure 5.7(a) represent those where the frictional contact at the step is actually resisting the tendency of the robot's body to slide *up* the step. Depending on the application, sliding up the step can be beneficial to the robot's climbing and thus the requirements on μ_2 can be relaxed by ignoring such regions of the plot when calculating μ_{2robot} of Equation (5.19).

Figure 5.8(b) plots μ_{2robot} of Equation (5.19), the minimum required body frictional coefficient, for the surface depicted in Figure 5.14(i). This plot represents the minimum required friction at the body-step interface to successfully climb the step. Surprisingly, the required body friction is not monotonic in the friction at the arms. The region with negative slope is limited by the requirements at the beginning of mode 1 ($\alpha = \arccos(h_s/\ell_2)$) while the region with positive slope is limited by the requirements at the beginning of mode 2 ($\alpha = \arccos(h_s/(\ell_2 + \ell_3))$). This behavior is explained by the fact that the arms push away from the step in mode 1 and drag towards the step in modes 2 and 3. While pushing, higher values of μ_3 can aid the robot climb by providing the force necessary to overcome its weight. In modes 2 and 3, however, the arms are always *pulling* the robot away from the step and thus hindering its ability to climb. Such

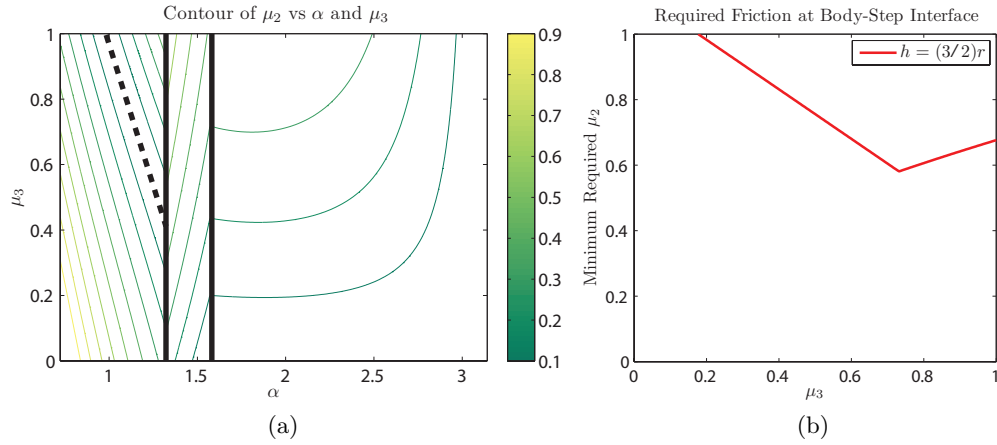


Figure 5.8: (a) Contour plot of the surface of Figure 5.14(i). Vertical solid black lines designate mode changes. Dashed black line represents solutions to $\mu_2 = 0$. (b) Plot of μ_{2robot} for the the tumbling robot with $h = 3\ell_2/4$.

behavior in general suggests that serial multiply-actuated tumbling robots exhibit non-zero optimal values for the coefficient of friction at the arms. Furthermore, looking at all of the tumbling surfaces of Figure 5.14, it can be seen that mode 3 never contributes to the minimum body friction requirement for the cases plotted. Such an observation might suggest that body designs that maximize the portion of the climbing trajectory spent in mode 3 can greatly increase the climbing ability of such tumbling robots.

Idealized Wheel-tail Robot

For a comparison we use the idealized wheel-tail model of Figure 5.7(b). This model is a planar representation of two-wheeled robots that make use of physical tails or castors to convert wheel torque into forward momentum. Examples of such robots include the UMN/Recon Scout [113, 114] and the Pioneer 3 DX [117]. These types of robots make a natural comparison because they are equivalent in complexity (i.e., they have the same type and number of actuators as the tumbling robots represented by the model addressed in the previous section).

We can repeat the above analysis for the idealized wheel-tail model where again we assume the center of mass to be at the wheel-tail joint; as with the tumbling case, this model can be generalized with relative ease. In contrast to serial multiply-actuated

tumbling robots, wheel-tail type robots exhibit only one mode of climbing due to the fact that the tail is always in opposition. Solving the system for equilibrium we get the following relations:

$$N_3 = N_1 + N_2 \cos \alpha - F_2 \sin \alpha, \quad (5.20)$$

$$F_3 = -N_2 \sin \alpha - F_2 \cos \alpha, \quad (5.21)$$

$$N_1 \ell_3 \cos \gamma = N_2 \ell_h \sin \beta + F_2 \ell_h \cos \beta. \quad (5.22)$$

From these it is again possible to solve for parameters of interest such as F_2/N_2 :

$$\mu_{2\min} = \frac{1 + \frac{\ell_3 \sin \alpha \cos \gamma}{\ell_h \mu_3 \sin \beta} + \frac{\ell_3 \cos \alpha \cos \gamma}{\ell_h \sin \beta}}{\frac{\ell_3 \sin \alpha \cos \gamma}{\ell_h \sin \beta} - \frac{\ell_3 \cos \alpha \cos \gamma}{\ell_h \mu_3 \sin \beta} - \cot \beta}. \quad (5.23)$$

It is worth noting that the wheel-tail case is equivalent to the tumbling robot case while in mode 2 with α and β shifted by $\pi/2$.

Equation (5.23) is plotted in Figures 5.14(a), (c), (g), and (e) for step heights of $r/8$, $r/4$, $r/2$, and r . Values of $h_s > r$ for wheel-tail systems do not have any real physical meaning, as they require N_2 to point into the step (opposite of that depicted in Figure 5.7(b)); physically, N_2 pointing into the step represents some form of attraction (e.g., adhesive, vacuum, or magnetism) between the wheel and step. Such cases are not within the scope of this work and are therefore excluded.

Idealized Singly-Actuated Robot

For the singly-actuated morphology we have the quasi-static forces as depicted in Figure 5.9. This required friction can be found using the above analysis of the wheel-tail morphology where N_3 and F_3 are now zero. Using Equation (5.21) we find the required body-step friction simply as

$$\mu_{2\min} = -\tan \alpha. \quad (5.24)$$

Frictional Analysis Comparison

Figure 5.14 plots the output of Equations (5.18) and (5.23) arranged in two columns with wheel-tail results on the left and tumbling results on the right. Additionally, the

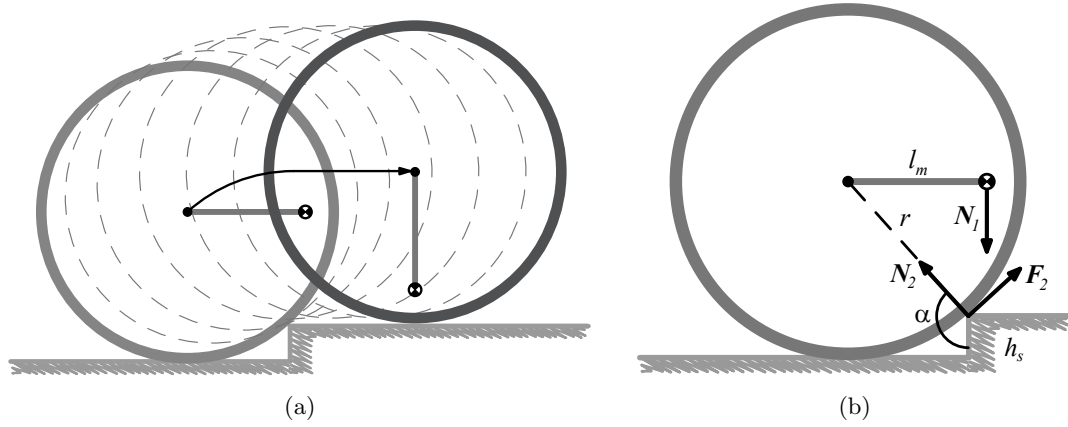


Figure 5.9: (a) Trajectory and (b) quasi-static force diagram for the singly-actuated circular morphology climbing an idealized step.

plots are arranged such that results for equivalent step sizes and body/wheel diameters (i.e., $l_2 = 2r$) are adjacent. Comparing the left and right columns, it can be seen that the frictional requirements of the tumbling robot are generally less than the wheel-tail robot for the selected values of h_s , N_1 , r , l_2 , and l_3 .

For direct comparison, we plot Equation (5.19) for the tumbling and wheel-tail systems for different values of h_s in Figure 5.10. Here the red lines represent tumbling scenarios while the blue represent wheel-tail scenarios. Three plots are shown for each type of robot for different step heights where equivalent heights between systems share line styles. In contrast to tumbling, we see that the required wheel friction is monotonically increasing with the tail friction due to the fact that the tail of wheel-tail robots is always in opposition to the forward motion of the robot. From this, it is possible to conclude that low-friction tails always outperform those with higher friction. Comparing the systems, it is clear that the tumbling robot has much more reasonable frictional requirements than the wheel-tail robot for equivalent step heights. Additionally, the figure suggests that tumbling is less sensitive in its body frictional requirements relative to the step height demonstrated by the tighter grouping of the plot lines for the same range of h values.

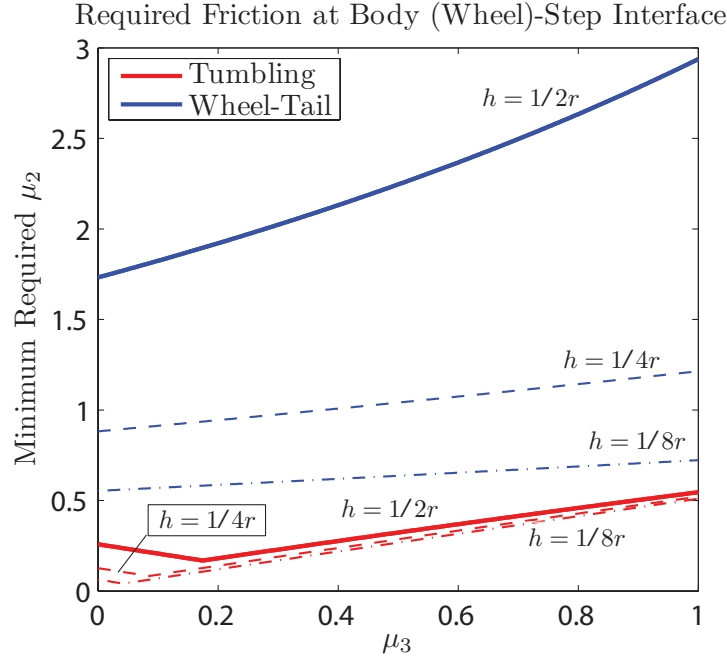


Figure 5.10: Plot of the minimum required coefficient of friction, μ_2 , at the body (wheel)-step interface for varying values of μ_3 , the coefficient of friction between the arm (tail) and the terrain.

Non-idealized Considerations

So far we have considered the frictional requirements of two idealized models of similar complexity while climbing steps. For each we have suggested that the idealized assumptions can be relaxed with relative ease. For serial multiply-actuated tumbling robots such relaxations include non-zero body/arm thicknesses and a center of mass position other than the body-arm joint. Wheel-tail systems are similar with the main difference between the idealized model and real-world implementations being that the center of mass is usually located some distance behind the wheel-tail joint to increase stability while descending slopes and decelerating. It turns out that, in general, such relaxations of both systems do little to alter the overall trends in the above results. Figure 5.11 shows a comparison between the ideal tumbling model of the above analysis and a non-ideal model with a translated center of mass (located at the body's centroid) and non-zero body width w . The cases shown in the figure include our theoretical results of

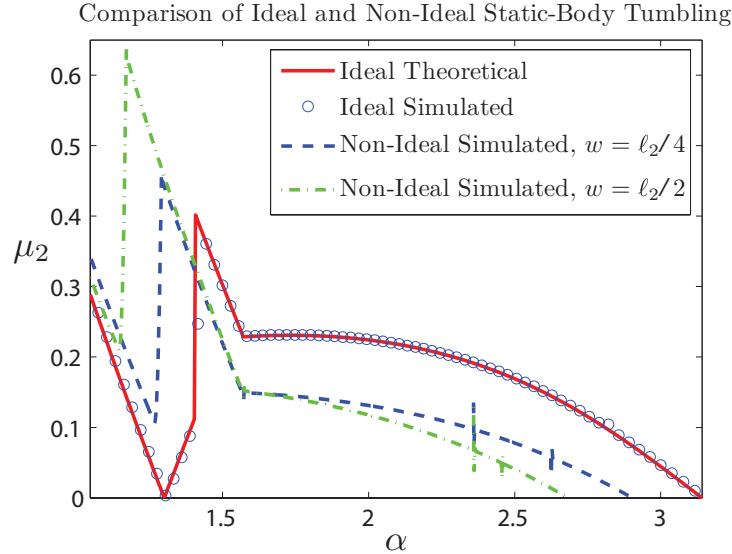


Figure 5.11: Figure comparing required coefficients of friction at the body-step interface with $h_s = 0.5$, $\ell_2 = 1$, $\ell_3 = 2$, and $\mu_3 = 0.5$ for idealized ($w = 0$, center of mass at the arm joint) and non-idealized ($w \neq 0$, center of mass at body's centroid) tumbling models with body widths w equal to $\ell_2/4$ and $\ell_2/2$. Results were generated using the open source physics engine Box2D. Also plotted are the theoretical results of the idealized model from Equation (5.18).

the ideal case, simulated results of the ideal case, and two non-ideal cases with w equal to $\ell_2/4$ and $\ell_2/2$. The simulated data was generated using Box2D [103], an open source physics engine which accurately simulates planar rigid-body dynamics with friction.

One noticeable difference between the idealized and non-idealized cases of Figure 5.11 is the vertical shift in required friction for modes 2 and 3. The cause for this is that the center of mass is located closer to the step in the non-idealized model which produces a larger ground reaction force at the step (relative to that at the arm). Because modes 2 and 3 have the arm frictional force in opposition, lower normal forces at the arm-ground interface reduce the required value of μ_2 . The other main differences between the two models arise from the geometric influence of the non-zero body width. This change affects the rate at which μ_2 goes to zero while in mode 3 as well as the value of α at which the robot transitions between modes 1 and 2. The greater body widths are beneficial in mode 3 but hinder performance in mode 2 (which is the limiting case in this scenario). This data supports our empirical observations of various hardware prototypes

where high ratios of body length to width are generally advantageous. The data also seems to suggest that locating the center of mass close to the body-step interface is beneficial, however, doing so removes some symmetry of the robot and leads to different performance values depending on the orientation of the robot when beginning the climb.

We have discovered some issues in non-idealized real-world systems of both types immediately after the step has been mounted and the robots begin to depart from the step. For both the wheel-tail and tumbling robots it is possible in some cases for the robot to successfully climb the step but fail to successfully continue forward immediately afterward. An example of such a scenario is depicted in Figure 5.12(a) where a tumbling robot of non-zero width has managed to tumble up onto a step and can no longer reach the lower terrain with its arm. In this configuration the arm must generate the next tumble by pushing against the step, however, in such a situation the ground reaction force at the arm-step interface is at such a radical angle that the robot will pull itself backward off the step. One way we have found to alleviate this issue is to pick an arm length such that the tumble to depart from the top of the step can be achieved by pushing off of the lower terrain. While effective, this strategy can lead to significant arm length requirements which increase the total size of the robot. An alternate strategy we have devised is to subtly alter the profile of the robot body such that it is less stable in the problem configurations and will either start the departing tumble earlier or never even reach a stable configuration where the robot is forced to push itself off of the step. Figure 5.12(b) shows a parallelogram profile body which will lead to two consecutive tumbles onto and away from the step (shown as dashed black curves) as soon as the robot completes its climbing trajectory of mode 3. Here the angles of the body have been chosen so that the tumble onto the step leaves the robot in an unstable configuration that immediately results in a tumble away from the step, thus preventing the aforementioned issue. Wheel-tail robots experience an equivalent situation that is exaggerated as the center of mass is moved farther backward from the wheel-tail joint, however we are unaware of a geometric solution similar to that for tumbling, thus appropriately long tails are necessary.

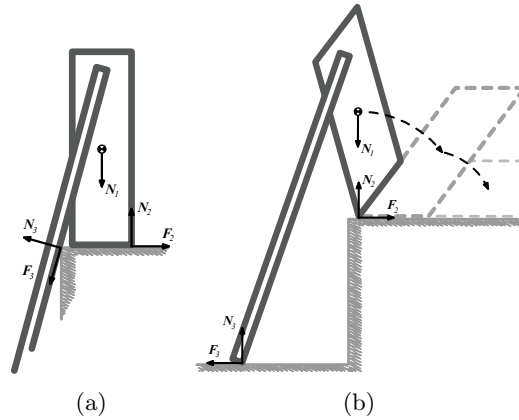


Figure 5.12: (a) Sample scenario depicting a tumbling robot after climbing a step where the next tumble must be generated by pushing off of the front of the step. (b) Depiction of altered body geometry that prevents the undesirable situation of (a).

Simulated Determination of Optimal Step Performance Versus Cost

Here we present some simulation results illustrating the drastic difference in size between wheel-tail and tumbling designs capable of climbing equally sized steps. The results were obtained by a direct search of the parameter spaces for simplified models of each system using the open-source physics engine Box2D [103]. For the wheel-tail model, the searched parameters were simply the wheel radius (r) and the tail length (ℓ_3). The tumbling model was slightly more complicated and involved searching over five parameters, body length (ℓ_2), body width (w), arm length (ℓ_3), tail friction (μ_3), and a fifth representing one of three possible arm joint positions. The arm joint positions were at the body's centroid, midway between the centroid and the body's half-length, and at the body's edge. The three models are referred to as tumbling-1, tumbling-2, and tumbling-3 respectively. For both models we set the step interface friction to $\mu_2 = 0.7$ and for all runs the step height was fixed at $h_s = 1$.

Each successful set of parameters was evaluated based on the min-max length of the robots along with the minimum area of their convex hull where the minimizations are over all possible joint angles. The best results for the wheel-tail model and the tumbling models with different arm joint locations are presented in Table 5.1. Additionally, visual representations of the optimal wheel-tail and tumbling-1 models are

Table 5.1: Experimental Results of Optimal Model Parameter Search

Model	Parameters			Length	Area
	r	ℓ_3			
Wheel-Tail	5.00	6.00		11.00	99.27
	ℓ_2	w	ℓ_3		
Tumbling-1	1.40	0.14	1.68	2.38	0.33
Tumbling-2	1.40	0.14	2.24	2.59	0.36
Tumbling-3	1.40	0.14	2.24	2.24	0.31

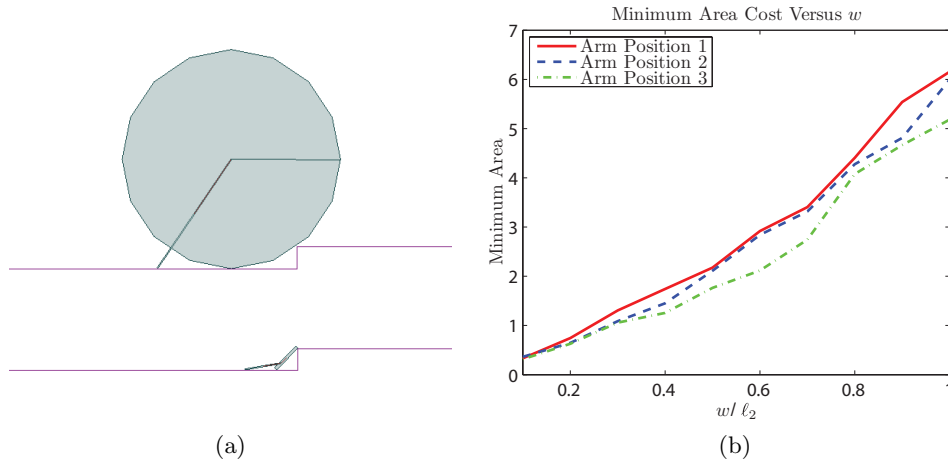


Figure 5.13: (a) Visual representation of optimal wheel-tail and tumbling robots mounting a step of height $h_s = 1$. (b) Plot of relationship between minimum area metric of optimal configurations versus w , the body width.

shown in Figure 5.13(a) where the difference in size is clearly evident. It is interesting to note that all three of the optimal tumbling models exhibit the minimum searched body width. In real-world implementations, however, design constraints will limit the minimum thickness of the robot body. To show how the minimum area cost varies with the width of the robot, we plot the cost of optimal tumbling configurations as the ratio of body width to length varies and approaches one (i.e., a square profile) in Figure 5.13(b). Even with a width to length ratio of 1 (worst case scenario) the minimum area is still orders of magnitude smaller than the best performing wheel-tail system. A related experiment with real hardware can be found below in Section 5.3.6.

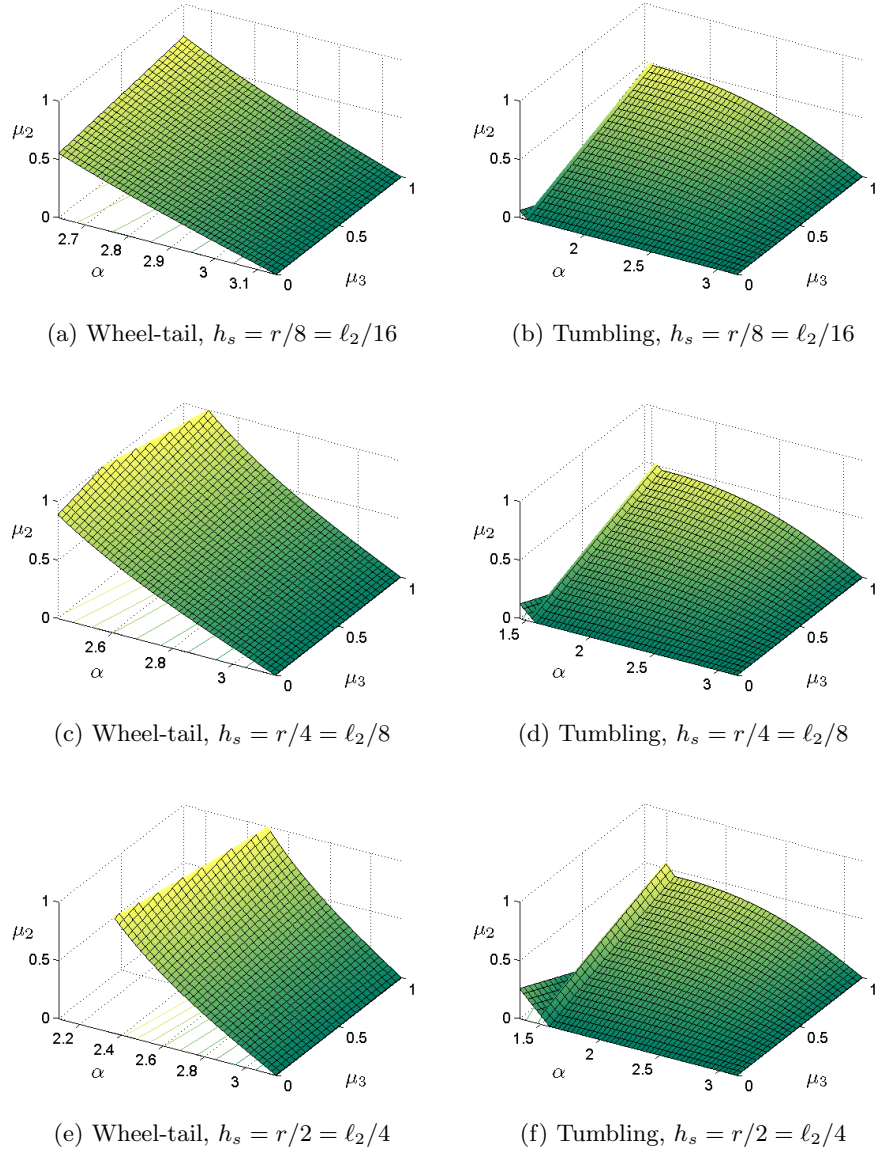


Figure 5.14: Minimum required coefficient of friction at body (wheel)-step interface, $\mu_{2\min}$, plotted for both a serial multiply-actuated tumbling robot and wheel-tail robot with varying step heights and $N_1=1$, $r = 0.5$, $\ell_2 = 1$, $\ell_3 = 2$. Wheel-tail cases with $h_s > r$ do not make physical sense and are thus excluded.

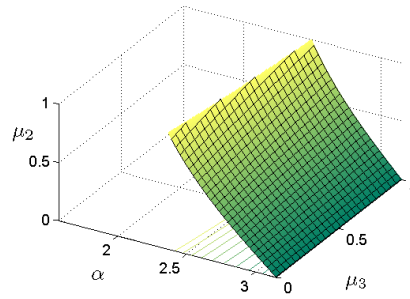
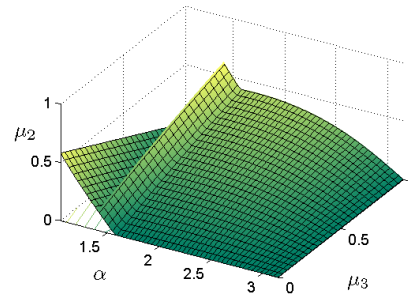
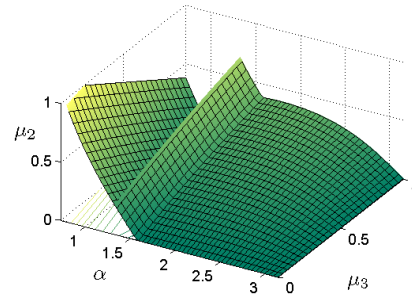
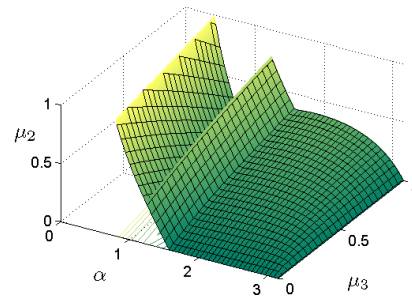
(g) Wheel-tail, $h_s = r = \ell_2/2$ (h) Tumbling, $h_s = r = \ell_2/2$ (i) Tumbling, $h_s = 3r/2 = 3\ell_2/4$ (j) Tumbling, $h_s = 2r = \ell_2$

Figure 5.14: Minimum required coefficient of friction at body (wheel)-step interface, $\mu_{2\min}$, plotted for both a serial multiply-actuated tumbling robot and wheel-tail robot with varying step heights and $N_1=1$, $r = 0.5$, $\ell_2 = 1$, $\ell_3 = 2$. Wheel-tail cases with $h_s > r$ do not make physical sense and are thus excluded. (cont.)

5.2.3 Ditch Crossing

Ditches are another popular idealized mobility metric that captures the ability of a robot to safely cross over sections of terrain that are hazardous and/or undesirable to come into contact with. Ditches as mobility measures appear in [19], [17], [67], etc. Using the parametrization of Figure 5.2(b), the robot must cross over a void of width ℓ_d .

Terrain irregularities that can be modeled as idealized ditches turn out to be relatively difficult to overcome for many wheeled or wheel-like robots due to the sinkage of the wheel into the terrain feature. As the wheel encounters the ditch, it begins to rotate downward about the leading edge until the wheel completely drops off the edge or the opposite edge is reached. From this configuration the obstacle is analogous to the previously examined idealized step. A sample trajectory representative of the singly-actuated circular and wheel-tail morphologies is shown in Figure 5.15(a). The resulting geometric crossable ditches for the two morphologies are

$$\ell_d < 2\ell_m \quad (5.25)$$

and

$$\ell_d < \min \left\{ 2r, \sqrt{\ell_{\text{tail}}^2 - r^2} \right\} \quad (5.26)$$

respectively. For the serial multiply-actuated morphology, a crossable ditch is limited primarily by the length of the body as well as the arm length. Assuming the arm has enough reach to establish tumbling moments throughout the entire trajectory, a tumbling robot of this type can cross ditches of length up to its body length. That is,

$$\ell_d < \min \left\{ \ell_{\text{body}}, \sqrt{\ell_{\text{arm}}^2 - \ell_{\text{body}}^2} \right\}. \quad (5.27)$$

Despite the seemingly equivalent ditch crossing performance of the wheel-tail and tumbling morphologies, it is important to consider the relative configurations of each morphology after spanning the ditch. The wheel-tail morphology, after entering the ditch, experiences the less than ideal situation analogous to the aforementioned step climbing (requiring significant friction at the wheel-ditch interface) while the tumbling morphology exhibits forces identical to those as if the ditch did not exist. While tumbling

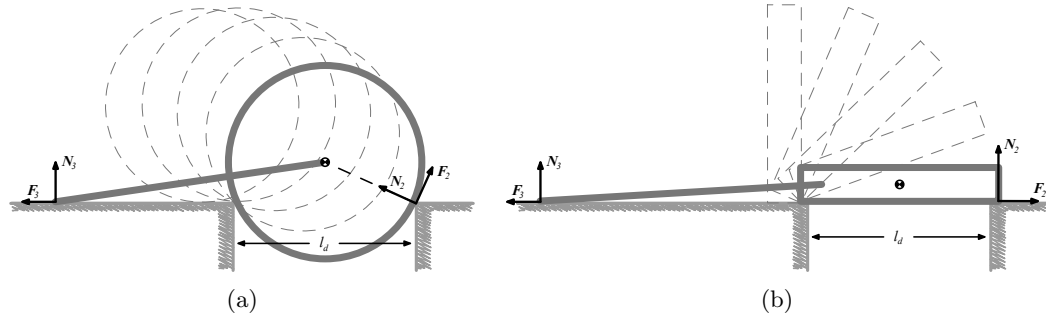


Figure 5.15: Graphical depictions of (a) wheel-tail and (b) serial multiply-actuated tumbling morphologies crossing an idealized ditch.

excels in this respect, it is extremely sensitive to the relative position/approach of the body to the ditch where improper approaches can lead to the catastrophic failure of the robot completely falling into the ditch. Take for instance the scenario depicted in Figure 5.15(b) where the robot is crossing a ditch with length near the maximum crossable by the robot; in this scenario, small shifts in the robot's trajectory to the left or right result in the aforementioned failure. We wish to stress this importance of obstacle alignment for optimal performance as well as the fact that such optimal configurations are not always achievable due to nonholonomic constraints possessed by many tumbling designs. Such is the focus of the Section 6.5.

5.2.4 Overhangs

Overhangs represent vertical confinements in the environment such as tunnels or low-hanging obstacles. Using the parametrization of Figure 5.2(c), it is possible to quantify the minimum required vertical height required for a particular robot to operate. For the morphologies we consider this is simply their wheel diameters and body lengths respectively for the case of forward locomotion. If the robot is required to change direction however, the tail/arm must switch sides, requiring additional height clearance (it is possible to generate backward motion by generating arm/tail forces on the ceiling of the overhang, however, the backward motion combined with the severe angles of the arm/tail require a relatively smooth surface to avoid any hang-ups). Interestingly for the 3D analog of the wheel-tail morphology the robot is in general able to turn in

place, removing the extra height requirement of flipping the tail; this is not so for the 3D tumbling analog. Therefore, the geometric overhang requirements for the wheel-tail and tumbling morphologies are

$$h_o > 2r \quad (5.28)$$

and

$$h_o > \ell_{\text{arm}} \quad (5.29)$$

respectively.

5.2.5 Composite Obstacles

As motivated in [17], it is possible to combine a number of idealized obstacles into single composite obstacles. Such obstacles contain multiple parameters and can be combined in various ways to create obstacles of arbitrary complexity. One example from the literature is the 2-parameter step-ditch obstacles shown in Figure 5.2(d). This obstacle combines the idealized step and idealized ditch by placing the ditch immediately in front of the step. Repeating our step reach calculations of Section 5.2.2 we arrive at the plots of Figure 5.16. These plots represent go/no-go configurations of the morphologies based on r ($\ell_{\text{body}} = 2r$), ℓ_d , and h_s where all combinations of ℓ_d and h_s under the curves are clearable by the morphology represented by the curve; all combinations on and over the curve result in failures. For $\ell_d = 0$ we have the case of the idealized step while $h_s = 0$ reduces to the idealized ditch. All curves assume that the tail or arms are sufficiently long to clear the ditch as with the above analysis.

5.3 Experimental Adelopod Performance Analysis

In this section we evaluate the performance of the Adelopod tumbling robot over a variety of terrains that were selected with repeatability in mind. To our knowledge, this is the first mobility data published regarding robotic tumbling locomotion (excluding any pertaining to spherical rolling robots). In this respect the results of this section motivate tumbling while simultaneously establishing benchmarks for any future terrainability comparisons regarding tumbling locomotion. In the following subsections we describe our experimental setup including the robot configurations, terrain selection,

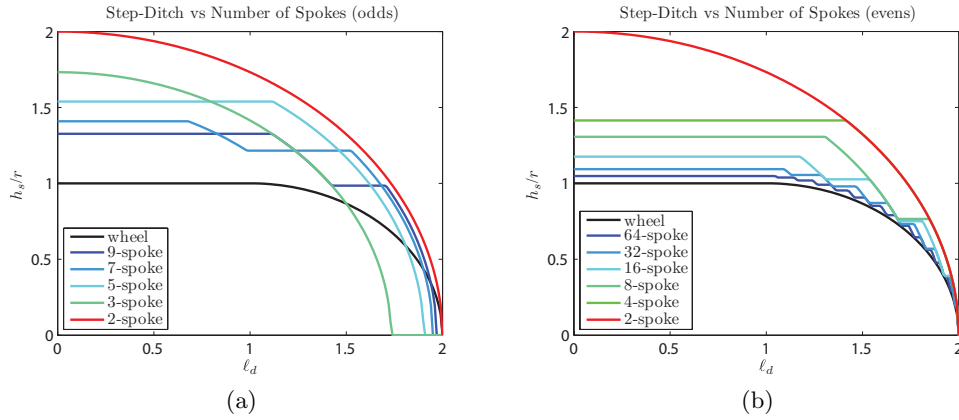


Figure 5.16: Plot of the geometric maximum step-ditch reach for n -spoked wheel-legs of radius r .

and test procedures before presenting our results.

5.3.1 Robot Test Platforms

As our test platform we use the Adelopod robot of Chapter 4 that we have designed specifically for this work. Due to the Adelopod’s flexibility in terms of configuration we were able to test a variety of different setups in our study of terrainability of tumbling locomotion. Specifically we have made use of the easily exchangeable outer shells and controllable second degree of freedom in the arms as well as its modular nature to realize the Adelopod-T. The specific test setups that we will refer to throughout the remainder of this thesis are shown in Figure 5.17. Included are the Adelopod in its basic configuration with both the indoor and ruggedized shells as well as the Adelopod-T. As a fourth test configuration, we have also fabricated a simple wheel-tail setup using the Adelopod in combination with late generation UMN COTS Scout wheels with diameters that are similar to the Adelopod’s stock body length. This configuration, shown in Figure 5.17(d), was easily achieved by mounting the wheels to the fully extended arm servos and adding an aluminum bar to serve as the tail. By our previous analysis, we expect this configuration to exhibit less mobility than the tumbling configurations, however, it is included to study the relative energetics of rolling versus tumbling with equivalent electromechanical setups. A summary of the various test platform characteristics is

Table 5.2: Test Platform Characteristic Summary

Robot	L_{body} [m]	M [kg]	V_{max} [m/s]	$V_{\text{max}}/L_{\text{body}}$
Adelopod	0.072	0.444	0.120	1.66
Adelopod (rugged)	0.089	0.568	0.141	1.85
Adelopod-T	0.126	0.664	0.150	1.19
Wheel-Tail	0.073	0.622	0.115	1.58

listed in Table 5.2.

5.3.2 Terrain Selection

As test terrains, we have selected a variety of different materials that both represent real-world terrain (generate meaningful results) and exhibit a suitable amount of repeatability (allow for comparisons). Additionally we have tried to select a variety of terrains that represent a multitude of environments ranging from indoor structured environments to relatively complex outdoor environments. Samples of the selected terrains are shown in Figure 5.18 and are detailed below.

- **Floor Tile** – Linoleum tiles common to indoor office environments. This terrain was selected as a control due to its smooth uniform surface and general ease of traversal.
- **CarpetA** – Low shag industrial carpet. Another terrain common to office environments, this terrain serves as transition between the easy to traverse office tile and more realistic outdoor terrains.

Specifications	
Manufacturer	Venture
Carpet	Passport
Weave	Levelloop
Material	Olefin
Pile Height	5 [mm]
Face Weight	45.5 [oz/s.y.]

- **CarpetB** – High shag residential carpet. This carpet is relatively thick and was chosen as a controlled/repeatable simulation of grass.

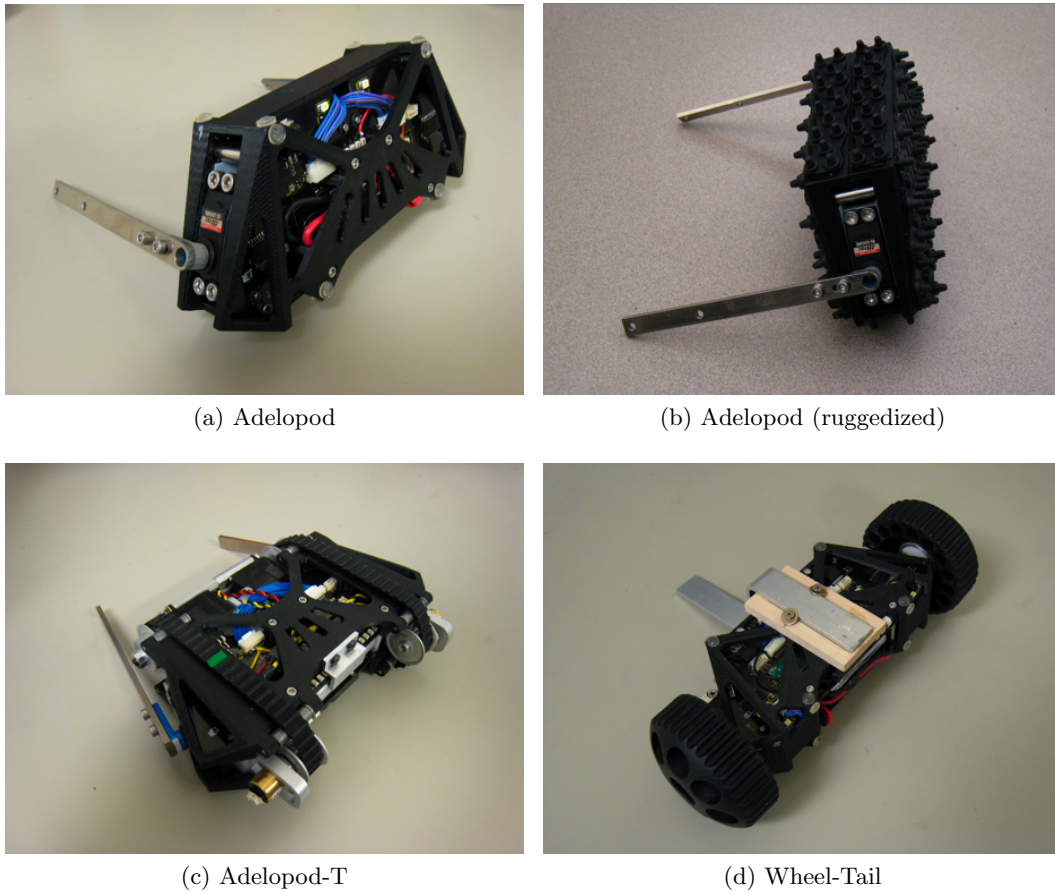


Figure 5.17: Experimental hardware platform configurations. (a) Adelopod configured for indoor use. (b) Adelopod configured for outdoor use with ruggedized shell. (c) The Adelopod-T. (d) Adelopod in wheel-tail configuration with UMN COTS Scout [113] wheels.



Figure 5.18: Experimental terrains with Adelopod posed for size reference.

Specifications	
Manufacturer	Mohawk
Carpet	Kingsport
Weave	Frieze
Material	Polyester
Pile Height	25 [mm]
Face Weight	50.0 [oz/s.y.]

- **Grass** – Cut lawn grass characteristic of residential areas. Kentucky Bluegrass of varying density and height. Thin Grass: Mean height of 24 mm. Thick Grass: Mean height of 62 mm.
- **Gravel** – Loose river gravel. A collection of semi-polished rocks that simulate terrain in and around rivers, streams, and lakes. Rocks average 28.7 mm in their smallest dimension and 54.0 mm in their largest dimension with standard deviations of 6.08 mm and 8.82 mm respectively. Manufacturer Specifications: TCC Materials, Nurserymens Preferred, River Cobble 2” rock.
- **Sand** – Dry sand. Screened and washed play sand. Manufacturer Specifications: TCC Materials, Nurserymens Preferred, Play Sand.
- **Complex** – For repeatable arbitrarily complex terrain, we use stepfields, a repeatable test terrain first used in [2] and later standardized in [27]. This particular terrain is comprised of a rectangular array of square posts with varying heights. Depending on the size and class of the robot the authors of [27] propose three sizes of stepfield (small, medium, and large). Robots of an appropriately sized stepfield should exhibit a footprint area of approximately one fourth to one third the area of a pallet. By this metric, our test platform is too small for the three standardized stepfield sizes. To remedy this we constructed a smaller stepfield by extrapolating the dimensions of existing standards to the next smaller size, resulting in pallets consisting of 10×10 grids of 1 in (≈ 2.5 mm) cubic steps. Each step is made of square posts cut into lengths of 0.5 in (≈ 1.25 cm), 1.0 in (≈ 2.5 cm), 2.0 in (≈ 5 cm), 3.0 in (≈ 7.5 cm), and 4.0 in (≈ 10 cm) represented by values of 0, 1, 2, 3, and 4 respectively in Figure 5.26. Standard stepfields use metric wood, however due to availability, we were forced to use posts with imperial units.

5.3.3 Forward Locomotion

As a first experimental look into the merit of tumbling as a method of mobile robot locomotion we investigate the forward locomotion capabilities and energetics of the Adelopod tumbling robot. Additionally we compare results with those of the wheel-tail Adelopod configuration; this comparison is interesting in that it parallels our previous terrainability analysis of Section 5.2.2 while also providing energetic comparisons between tumbling and wheel-tail locomotion for identical chassis, motors, and electrics.

This experiment involved running the ruggedized Adelopod and wheel-tail platforms of Figures 5.17(b) and 5.17(d) respectfully over a variety of terrains while measuring their forward progress, average velocity, and power consumption. This test procedure is similar to that advocated by the authors of [2] with the difference that we have removed any human interaction by running the tests open-loop. This is desirable in that it removes any human influence from the results and also decouples our study of tumbling locomotion from any particular controller. In this respect we test the raw ability of tumbling locomotion to overcome terrain irregularities in the absence of any positional feedback or planning. The terrains tested included approximately 1×0.5 meter sections of all those listed in Section 5.3.2 with the exception of any complex stepfields which were not tested in this experiment due to the low-probability of our open-loop control scheme producing successful runs (we address complex stepfield terrains separately in Section 5.3.4). Each run consisted of placing the robot in its starting position before giving the robot the command to drive forward (i.e., rotate arms in phase at full velocity). Successes were recorded as runs that reached the end of the terrain section without getting stuck (i.e., hang-up or pinching failure) or deviating from the course; course deviations resulted in an immediate stoppage of the run and a record of the forward progress up to that point.

In total, we conducted 210 total runs: 70 for the Adelopod with arms fully contracted (angled), 70 for the Adelopod with the arms fully extended (straight), and 70 for the wheel-tail Adelopod. The results are presented in Tables 5.3 and 5.4 as well as Figures 5.24 and 5.25.

Table 5.3: Forward Locomotion Experimental Statistics

	Tile	CarpetA	CarpetB	Thin Grass	Thick Grass	Gravel	Sand
Adelopod – Angled/Straight							
Total Runs	10/10	10/10	10/10	10/10	10/10	10/10	10/10
Successful Runs	10/10	10/10	10/10	-/10	-/10	2/6	-/10
Deviations	-/-	-/-	-/-	-/-	-/-	8/4	10/-
Hang-Up Failures	-/-	-/-	-/-	-/-	-/-	-/-	-/-
Arms Pinching	-/-	-/-	-/-	10/-	10/-	-/-	-/-
Wheel-Tail							
Total Runs	10	10	10	10	10	10	10
Successful Runs	10	10	10	10	-	-	10
Deviations	-	-	-	-	-	-	-
Hang-Up Failures	-	-	-	-	10	10	-

Tumbling Failures

With the arms in the straight configuration, the Adelopod was easily able to produce forward motion over all seven of the terrains while the angled arm setting failed to produce reliable forward motion only for the grass terrains (both thin and thick). It is interesting that the only observed tumbling failures were not due to body-obstacle interactions or lack of friction but instead were a result of the relative arm trajectories. The failed runs were all results of the arms pinching the terrain as they rotated in phase back to their starting positions where the ends are closest together (i.e., pointing along robot’s y -axis in the positive direction). This pinching issue is a direct result of the offset of the arms’ rotation planes in conjunction with driving the arms in phase and, therefore, this issue was only observed for the angled arm configuration. This phenomena is depicted in Figure 5.19 where we show the Adelopod tumbling in thick grass similar to that of the conducted experiment. As the robot progresses from 5.19(a) to 5.19(c) the ends of the arms in contact with the grass move closer together, eventually trapping grass between the arms and stalling the motors (resulting in a failed run). In general, such situations can be avoided by straightening out the shoulders or by driving the arms out of phase for any problematic terrains. Driving the arms out of phase in combination with angled arms generally results in some angular displacement that is not correctable with our open-loop driving scheme and thus was not investigated in this particular experiment.

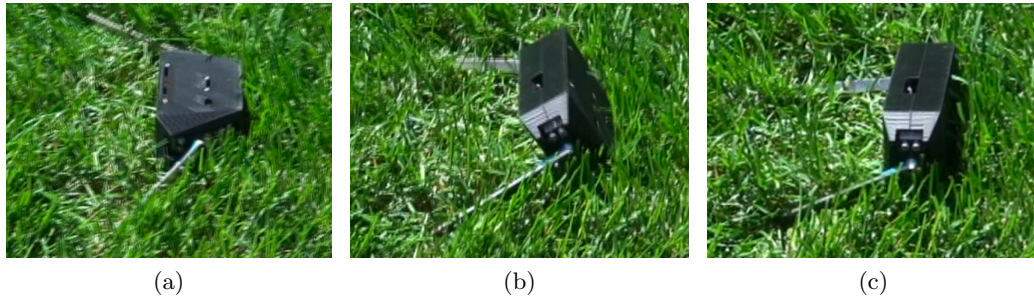


Figure 5.19: Example of pinching failure exhibited by the Adelopod on thick grass with angled arms.

Tumbling Course Deviations

During the experiments, we recorded 22 course deviations for the Adelopod; 18 of the deviations were for the angled arm configuration while the other 4 were observed during the straight arm configuration. All of the observed deviations for the straight arm configuration were on the gravel terrain and were a result of body-terrain interaction between the larger gravel pieces and the body which occasionally resulted in some angular displacement and eventual deviation. The increase in deviations for the angled arm setting can be explained by the same phenomena that resulted in the aforementioned pinching failures. As the arms rotate about the body, the angled planes of rotation result in a sweeping motion of the arm contacts that exhibit significant off-axis forces with respect to the forward motion. On smooth regular terrain such as the floor tile and carpets, the off-axis forces of each arm are equal and opposite when the arms are in phase. In more complex and less regular terrain, however, these forces are dependent on the relative area and strength of each set of arm contacts, resulting in generally unequal forces at the arms that result in turning moments.

The sand terrain was particularly interesting in terms of the off-axis force generation present in the angled arm configuration. Over this terrain, the arms penetrate the surface of the sand during forward locomotion and produce large off-axis forces during their sweeping motions where they act as paddles in the sand. These larger forces were much more sensitive to any differences in magnitude and resulted in course deviations for all ten runs over the sand terrain for the angled arm configuration. To help visualize this behavior, we have included photos of tracks left in the sand for comparison in

Figure 5.20 for all three Adelopod configurations. Figure 5.20(a) shows the tracks of the angled arm configuration under human operation where course corrections were made by continuously adjusting the phase of the arms as the robot traversed the sand. In this figure the aforementioned sweeping motion is clearly evident. Although this phenomena caused issues in this particular experiment due to the open-loop control scheme, it can be quite beneficial in terms of maneuverability, allowing for gradual heading changes if utilized correctly. Figures 5.20(b) and (c) show the relatively straight tracks left by the other two configurations.

Wheel-tail Failures

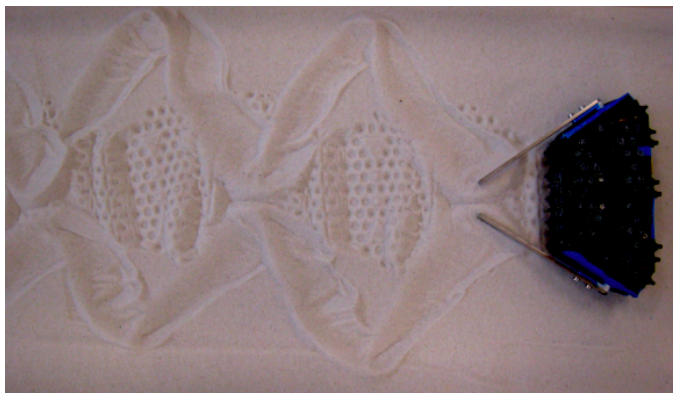
The wheel-tail setup had no issues with course deviations, however, it exhibited significant issues generating forward motion over the thick grass and gravel terrains due to hang-up failures where the terrain came into contact with the robots body. This failure is generally not an issue for tumbling due to the purposeful use of ground-body interactions but for the case of the wheel-tail configuration the hang-ups resulted in failures for the thick grass and gravel terrains for all 20 of its runs over these terrains.

Forward Velocity and Energetics

In Table 5.4 and Figures 5.24 and 5.25 we present experimental results pertaining to forward velocity and energetics. Table 5.4 shows the average forward velocity V_{avg} , the average power consumption P_{avg} , the average specific resistance ε_{avg} (calculated from the total power usage), and a modified average specific resistance that takes into account only the power used to generate forward locomotion $\varepsilon_{\text{drive}}$ (i.e., motor power) of all the runs for each combination of test platform and terrain. Also included are the standard deviations $\sigma_{V_{\text{avg}}}$ and $\sigma_{P_{\text{avg}}}$ for the average forward velocity and power consumption respectively. Figures 5.24 and 5.25 depict the distributions of collected data graphically as box plots.

Looking first at the velocities we see, as one might expect, that the type of terrain significantly influences the average forward velocities of the robots. The floor tile was the least difficult of all the terrains and resulted in each robot exhibiting its maximum forward velocity with negligible deviation between runs.¹ As the terrains become more

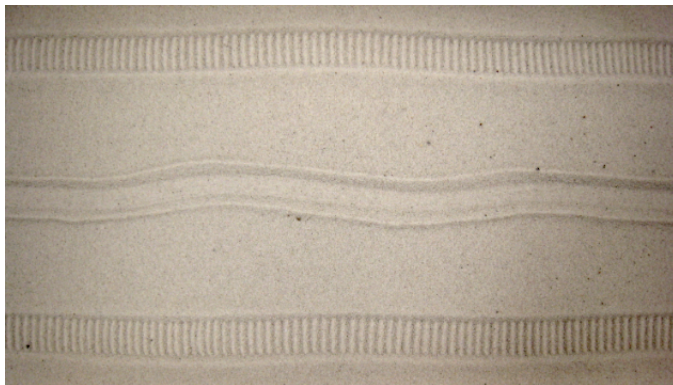
¹The wheel-tail configuration's slightly lower maximum velocity is a result of its wheels having a



(a)



(b)



(c)

Figure 5.20: Tracks left in sand by (a) Adelopod with angled arms, (b) the Adelopod with straight arms, and (c) the wheel-tail Adelopod.

Table 5.4: Forward Locomotion Average Velocity Statistics

	Tile	CarpetA	CarpetB	Thin Grass	Thick Grass	Gravel	Sand
Adelopod – Angled							
V_{avg} [m/s]	0.138	0.121	0.108	–	–	0.068	0.075
$\sigma_{V_{\text{avg}}}$ [m/s]	0.002	0.001	0.001	–	–	0.016	0.003
P_{avg} [W]	3.63	3.70	3.94	–	–	4.72	4.75
$\sigma_{P_{\text{avg}}}$ [W]	0.03	0.06	0.06	–	–	0.63	0.04
ε_{avg} [W·s ³ /kg·m ²]	4.72	5.48	6.55	–	–	13.76	11.42
$\varepsilon_{\text{drive}}$ [W·s ³ /kg·m ²]	1.96	2.33	3.02	–	–	7.71	6.31
Adelopod – Straight							
V_{avg} [m/s]	0.141	0.121	0.109	0.118	0.108	0.085	0.094
$\sigma_{V_{\text{avg}}}$ [m/s]	0.000	0.001	0.004	0.001	0.003	0.013	0.001
P_{avg} [W]	3.55	3.60	3.66	4.07	4.37	3.88	3.88
$\sigma_{P_{\text{avg}}}$ [W]	0.03	0.04	0.05	0.07	0.13	0.10	0.03
ε_{avg} [W·s ³ /kg·m ²]	4.52	5.36	6.02	6.18	7.28	8.43	7.39
$\varepsilon_{\text{drive}}$ [W·s ³ /kg·m ²]	1.82	2.20	2.53	2.95	3.74	3.83	3.35
Wheel-Tail							
V_{avg} [m/s]	0.114	0.107	0.107	0.110	–	–	0.100
$\sigma_{V_{\text{avg}}}$ [m/s]	0.000	0.001	0.001	0.001	–	–	0.002
P_{avg} [W]	3.25	3.36	3.71	3.68	–	–	3.60
$\sigma_{P_{\text{avg}}}$ [W]	0.03	0.03	0.19	0.10	–	–	0.10
ε_{avg} [W·s ³ /kg·m ²]	5.10	5.63	6.24	6.01	–	–	6.45
$\varepsilon_{\text{drive}}$ [W·s ³ /kg·m ²]	1.76	2.07	2.67	2.54	–	–	2.65

difficult, we see decreases in the average forward velocities and increased deviation between runs. Interestingly, this effect is less for the wheel-tail configuration over its traversable terrains than those of either tumbling configuration with a difference of only 0.014 seconds between the best and worst observed average velocities and standard deviations less than 0.002 m/s. Except for the wheel-tail on carpet A, all three robot configurations produced the same relative ordering of terrains based on their average forward velocities with the gravel being most “difficult” followed by the sand.

Comparing the angled and straight arm tumbling configurations, we see that overall the straight arm configuration outperformed the angled configuration with no failures, fewer deviations, faster forward velocities, and less power consumption; these differences are especially evident over the more difficult sand and gravel terrains. From observation, we have concluded that all of the performance issues are a result of the lateral (off-axis) forces generated by the arm angles and the aforementioned resulting sweeping trajectory at the arm ends. In addition to causing all of the failures (due to pinching) the presence of significant lateral forces increase the likelihood of deviations as well as increase the average motor current and thus the average power consumption. These observations along with the data suggest that angled arms are not beneficial for forward locomotion by tumbling.

In terms of energy usage and specific resistance, we generally expect tumbling to lose to wheeled configurations. This is the case for most of the experiment results. One interesting exception was observed with the straight armed tumbling configuration over the indoor terrains. Despite the higher current consumption, the straight armed tumbling configuration exhibited lower specific resistance over the floor tile, carpet A, and carpet B when compared to the wheel-tail configuration over the same terrain. We attribute such results to the smaller maximum velocity of the wheel-tail configuration along with drivetrain losses due to the gearmotor selection. As discussed in Section 4.1.2, the selected gearmotors were chosen for their high torque and low cost. As a result they exhibit relatively low driving efficiency and significant losses in their gear reduction. Over easy terrain, these losses are significantly large with respect to the driving forces and, in combination with the lower forward velocity due to the smaller wheel diameter

smaller circumference than that of the ruggedized Adelopod’s outer shell (measured as the sum of side lengths).

result in higher specific resistance. Better results for the wheel-tail configuration may be possible with different combinations of wheel diameter and/or motor selection.

In Table 5.4 we report two measures of specific resistance, ε_{avg} and $\varepsilon_{\text{drive}}$ where the first is calculated from the total power used by the robot during the run and the latter calculated only from the power consumed by the motors for producing locomotion. Historically, methods used to measure and report power usage of robot platforms vary greatly and include combinations of calculated/measured average/peak electrical/mechanical power of the actuators or system as a whole. The authors of [2] suggest that the most meaningful measure for mobile robots based on electrical power sources and actuation is the total power consumption (i.e., total actuation, sensing, and computing power). The reasoning being that mobile robots are isolated systems in which total power usage in combination with battery capacity determine runtime (operational time between required recharging). Despite this, however, we are primarily interested in tumbling locomotion and less with the actual system; therefore we believe that energetics as a function only of the power utilized by the actuators for locomotion are of interest as well as those of the entire system. In this respect we include results of both calculated as follows:

$$\varepsilon_{\text{avg}} = \frac{P_{\text{avg}}}{mgV_{\text{avg}}}, \quad (5.30)$$

$$\varepsilon_{\text{drive}} = \frac{P_{\text{avg}} - P_{\text{idle}}}{mgV_{\text{avg}}}, \quad (5.31)$$

where m is the robot mass, g gravity, and P_{idle} the power consumed by the robot while idle (i.e., LEDs, system processing, wireless communication, etc.). In Figure 5.21 we plot each of the above specific resistances for the Adelopod over all seven test terrains. For comparison, we have included in black data from [118] for a collection of legged robots as well as (plotted as red squares) data from [2] on the Rhex robot, a high mobility hexapod.

5.3.4 Complex Terrain

As a second experiment, we explore tumbling performance over more difficult terrain. Our choice of terrain consisted of stepfield pallets that are becoming popular in many

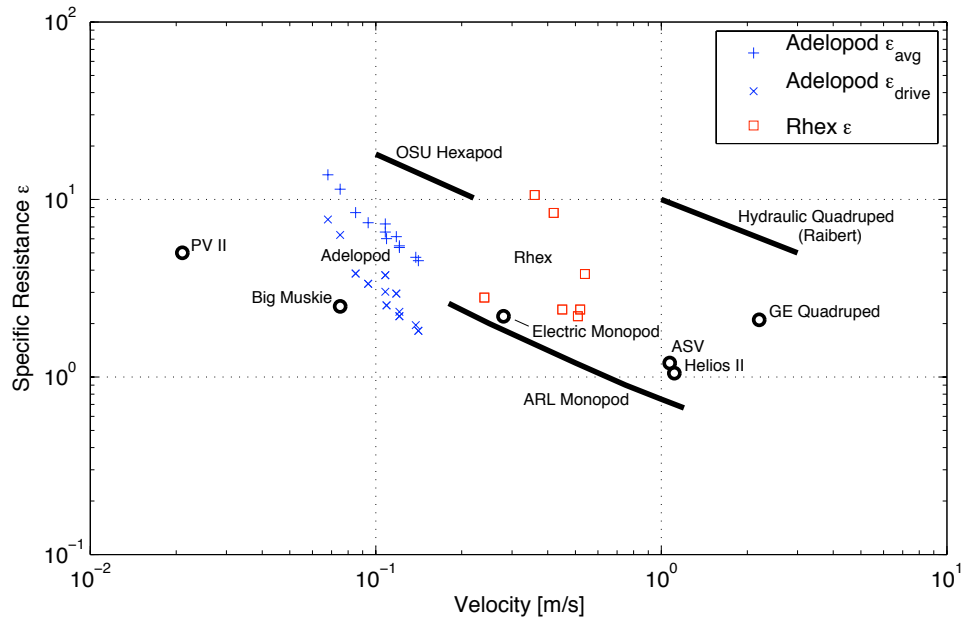


Figure 5.21: Adelopod specific resistances with comparisons to data from [118] (shown in black) and [2] (shown as red squares).

mobile robotics competitions and under investigation by the National Institute of Standards and Technology as a standard for mobility evaluation. This particular terrain is especially attractive due to both its ability to approximate arbitrarily complex terrains as well as its general low cost and repeatability. In particular for this experiment we used various 2×2 arrays of pallets consisting of different height configurations generated using both the pseudo-randomized and symmetric guidelines outlined in [27]. A sample course setup is shown in Figure 5.22 where we have added two retaining walls on either side of the pallet array to help prevent any course deviations.

Due to the increased difficulty of this terrain, it was necessary in this experiment to utilize human control to guide the robot over the terrain. Because of this added human element, as well as the generally increased difficulty of the terrain, we observed much larger deviations in the results when compared to those of the previous experiment. In this respect, the results are somewhat less meaningful in terms of forward velocities, however, they are still very beneficial in highlighting the ability of tumbling to negotiate complicated terrains.

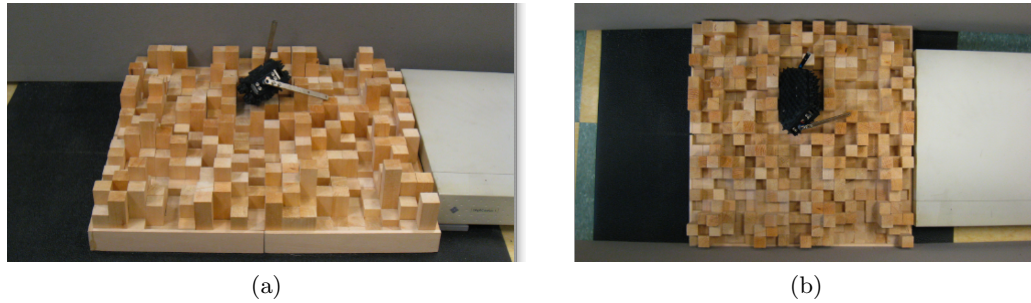


Figure 5.22: Example stepfield setup for Adelopod performance evaluation over the complex terrain. (a) Side view of setup with left wall removed for viewing. (b) Top view.

The actual layouts used are depicted in Figure 5.26 along with their reference names we use throughout the remainder of this section. The first of the layouts, the double randomized perpendicular hills, requires the robot to traverse two hills of height four that are perpendicular to the robot's path. Each of the four pallets of this particular stepfield are common to robot rescue competitions and used the randomized generation procedure outlined in [27] where the tallest steps of the hills are placed deterministically and all others selected randomly with rules pertaining to maximum height differences between neighboring steps. In an attempt to test the difficulties of off-angle slopes we selected as the second configuration the symmetric diagonal hill configuration. This stepfield consists of a large hill of height 4 that extends diagonally down the center of the terrain. In contrast to the perpendicular hills, this stepfield is completely deterministic as well as symmetric. The third stepfield, the symmetric peaks, is another completely deterministic configuration comprised of four peaks of height 4 with one peak centered on each pallet. As a final test we created a modification of the flat square layout of [27] common to robotics competitions. The flat square pallets consist of 4 steps of height 3 arranged in a square pattern with all other steps generated randomly following the constraint that no orthogonally neighboring steps can have a height difference of greater than 2. Our modification, randomized tall squares, increases the difficulty of the layout by increasing the deterministic tall steps from height 3 to height 4. For both the symmetric peaks and the randomized tall squares layouts, we tested two separate starting locations depicted in Figures 5.26(c), (d), (e), and (f). For each, the first

Table 5.5: Adelopod Complex Terrain Statistics

	Runs		Fwd Vel [m/s]		Pwr [W]	
	Total	Successful	V_{avg}	$\sigma_{V_{\text{avg}}}$	P_{avg}	$\sigma_{P_{\text{avg}}}$
Adelopod – Angled						
Double Rand Perp Hills	15	10	0.035	0.030	5.52	0.90
Quad Sym Ctr Peaks (1)	10	10	0.024	0.012	4.98	0.54
Quad Sym Ctr Peaks (2)	10	10	0.025	0.028	4.77	0.90
Sym Diagonal Hill	21	10	0.015	0.009	5.30	0.47
Tall Rand Squares (1)	21	10	0.012	0.005	6.10	0.45
Adelopod – Straight						
Double Rand Perp Hills	10	10	0.121	0.236	4.10	0.56
Quad Sym Ctr Peaks (1)	10	10	0.087	0.009	3.51	0.22
Quad Sym Ctr Peaks (2)	10	10	0.048	0.026	4.61	0.87
Sym Diagonal Hill	10	10	0.025	0.015	4.41	0.75
Tall Rand Squares (1)	10	10	0.069	0.030	4.54	1.25
Tall Rand Squares (2)	10	10	0.052	0.020	4.28	0.70

starting location consisted of the robot aligned with the terrain's centerline while the second positioned the robot off center and aligned with the tallest (height 4) posts of each terrain.

Runs were conducted until 10 successes were recorded where failures were defined as any run where the robot became immobile or failed to traverse the terrain in under two minutes; Table 5.5 shows the statistical results of the runs in terms of total runs and successes as well as average forward velocity and power consumption. Graphical depiction of the data distributions are available as box plots in Figures 5.27, 5.28, and 5.29.

In terms of tumbling, we have found stepfields to be very difficult for tumbling configurations with angled arms. Due to the stepfields' limited compliance (step posts can only rock slightly within their dedicated position within the field) and numerous pinching hazards (due to the discrete height changes), a tumbling robot is constantly at risk of getting into difficult configurations. Additionally, any pinching situations required out of phase arm inputs that resulting in significant heading changes that then had to be corrected while avoiding any successive pinches. An example failure documented during the conducted experiments is shown below in Figure 5.23 where the arm entered a deep hole and was unable to proceed. In all, the Adelopod with angled arms failed 27 of the total 77 runs due to immobile configurations and timeout failures.

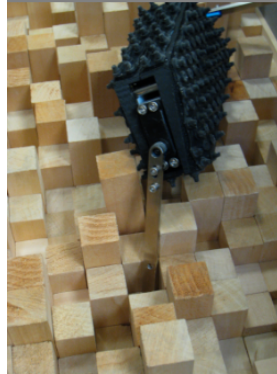


Figure 5.23: Example of Adelopod failure over a randomized stepfield where the arm became stuck within a hole formed by a small step surround by all larger steps.

Additionally, power usage of the robot was quite high due to both the increased terrain complexity and numerous motor stalls.

In the straight arm configuration, the Adelopod had very little issues traversing all of the stepfields tested. Surprisingly, the robot exhibited no failures for any of its 60 runs. Compared with the results of the angled arm configuration, the straight arm runs exhibited average velocities over twice those of the angled arm configuration for almost every stepfield. Additionally, the straight arm configuration required significantly less power over all of the stepfields tested. These results suggest that straight armed configurations are beneficial for complex and/or non-compliant discrete-like terrain.

5.3.5 Hybrid Tumble-tread Locomotion

The original idea for the Adelopod-T (i.e., adding treads to the Adelopod; see Figure 5.17(c)) was a result of trying to address the maneuverability constraints of the Adelopod (addressed in the next chapter), however, the addition of treads is also interesting in terms of terrainability. Similar to the Adelopod-T is the iRobot 110 FirstLook [119]; as described in Chapter 4, the Adelopod-T is primarily a tumbling robot with the addition of crawler treads while the Firstlook can be considered primarily a treaded

Table 5.6: Complex Terrain Statistics: Adelopod-T

	Runs		V_{\min}	V_{\max}	V_{avg}	$\sigma_{V_{\text{avg}}}$
	Total	Successful				
Double Rand Perp Hills						
-Tumbles only	12	10	0.098	0.007	0.018	0.021
-Treads only	10	-	-	-	-	-
-Tumbles+Treads	10	10	0.089	0.009	0.023	0.031

robot with the addition of some tumbling capabilities.² In [120] an idealized step climbing sequence of the Firstlook’s prototype is shown that utilizes both the treads and flippers, however, we are also interested in the benefits of utilizing treads in conjunction with tumbling over non-idealized terrain. To test the benefits of using both modes of locomotion in conjunction we conducted a small experiment consisting of running the Adelopod-T over the randomized perpendicular hills stepfield using three different driving modes: tumbling alone, treads alone, and tumbling and treads together. The results are presented in Table 5.6.

With the treads alone, the Adelopod-T was not able to complete any successful runs due to hang-up failures between the steps and the body. It is possible that better ground clearance for the treads might improve this result, however, the tested terrain is quite difficult for treaded vehicles and proves generally difficult even for larger robots. For the tumbling driving mode, we observed 2 failures out of the 12 total in which the robot became immobile while the tumbling with treads did not exhibit any failures. Tumbling with the treads resulted in better a success ratio, however, the observed increase in average forward velocity is relatively small compared to the standard deviations of the data. Overall, we find the results promising in terms of success rates in that they seem to suggest that treads are advantageous, however, we believe that further investigation should be conducted into the terrainability benefit of treads to a tumbling robot.

²Although the Firstlook is capable of executing discrete tumbles, the short arms are not conducive to repeated tumbles in the same direction (i.e., no net body rotations) and therefore the Firstlook is not a tumbling robot by Definition 3.5.

5.3.6 Idealized Step Climbing

As a final terrainability experiment, we set out to determine the maximum step height climbable by the Adelopod with varying coefficients of friction at the body and arms; for this experiment, we use the indoor configuration of the Adelopod (see Figure 5.17a). The test-rig used for the experiment involved an aluminum step mounted on a tripod next to a table. The robot was placed with the leading edge on the corner of the step and the arms in contact with the table. The robot was then given the command to quasi-statically climb the step, and the current height was given a pass/fail score depending on whether the robot successfully climbed the step or slipped off it. Consecutive trials were run to determine the maximum height (to the nearest millimeter) that the robot could climb. Coefficients of friction were varied through the application of various materials to the robot's body, step, arms, and/or the ground. Materials used in varying the coefficients included teflon, ABS plastic, vinyl, silicon, and foam rubber. A subset of this experiment involved determining the approximate coefficients of friction between the various combinations of materials. Each combination of materials was tested by applying one material to an object and the other to a flat surface; the inclination of the surface was then increased until the object began to slide.³

The results of our experiment can be seen in Table 5.7 where we see that generally higher frictional values at the body paired with lower frictional values at the arms result in greater performance. As expected, the maximum step height varies greatly depending on the relative frictional coefficients, with the results falling within the geometric bounds established in Section 5.2.2. Particularly exciting results are the maximum climbable step heights observed for any body-step interface involving silicone; examining these results we see that they are close to the geometric maximum step performance achievable by the wheel-tail morphology ($h < r$). Additionally all runs of silicone-silicone at the body-step interface actually produced maximum climbable step heights greater than geometric maximum for the wheel-tail morphology.

In addition to the pure frictional contacts, we also conducted several runs in which an ideal interlocking contact between the robot's body and step was approximated by adding small silicone bumpers to the edges of the robot's body. With these in place we

³We wish to note that certain coefficients could not be effectively evaluated with this method, primarily the silicon interactions. Such interactions are designated in Table 5.7 by $\mu \geq 1$.

Table 5.7: Experimental results for maximum step height versus measured values of μ_2 and μ_3

Body-Step Cfg.	Arm-Ground Cfg.	$\bar{\mu}_2$	$\bar{\mu}_3$	\bar{h}	\bar{h}/ℓ_2
ABS-Teflon	Steel-Teflon	0.09	0.21	6	0.08
ABS-Alu.	Steel-Vinyl	0.35	0.22	16	0.22
ABS-Alu.	Steel-Foam	0.35	0.45	0	0.00
ABS-Silicone	Steel-Vinyl	0.68	0.22	32	0.44
ABS-Silicone	Steel-Foam	0.68	0.45	24	0.33
Silicone-Alu.	Steel-Teflon	≥ 1	0.21	31	0.42
Silicone-Alu.	Steel-Vinyl	≥ 1	0.22	29	0.40
Silicone-Alu.	Steel-Foam	≥ 1	0.45	22	0.30
Silicone-Silicone	Steel-Teflon	≥ 1	0.21	55	0.75
Silicone-Silicone	Steel-Vinyl	≥ 1	0.22	54	0.74
Silicone-Silicone	Steel-Foam	≥ 1	0.45	42	0.58
Ideal	Steel-Vinyl	-	0.22	69	0.95
Ideal	Steel-Silicone	-	≥ 1	69	0.95

observed performance close to the geometric max of $h < \ell_2$, suggesting that the shape and texture of a tumbling robot’s body is critical to achieving good performance. This is also supported by the empirically observed performance benefit of the ruggedized shell in comparison to the indoor shell over complex terrain.

5.4 Final Thoughts

In Chapter 3 we made the claim that tumbling robots exhibit the potential to produce better terrainability-to-cost ratios than many conventional methods of robotic locomotion. In this chapter we provide support for this claim for costs related to both size and mechanical complexity using example mobility tasks involving the negotiation of various idealized terrain features.

We showed geometrically that the serial multiply-actuated tumbling robots have very good reach properties and therefore exhibit improved bounds on their range of negotiable terrain features. Conducting further analysis with respect to frictional requirements, we showed that even in the presence of non-ideal contacts tumbling requires significantly less friction than other systems of similar mechanical complexity. For step climbing we identified for serial multiply-actuated tumbling morphologies three possible modes while climbing. For each of the modes we showed that it is possible to derive

parametric configuration equations that describe the relationships between the robot configuration, environmental/task, and performance parameters. Using these configuration equations we focused on the relation $F2/N2$, the frictional coefficient required at the body-step interface to enable climbing. When compared to a wheel-tail system of similar complexity it was shown that tumbling is much less demanding in its frictional requirements. Experimentally this was verified by comparing relative sizes of optimal tumbling and wheel-tail designs where we found that tumbling systems can exhibit equal step climbing performance with cost (measured in size) orders of magnitude less than their wheel-tail counterparts.

To verify the performance suggestions of our analysis we conducted physical experiments with the Adelopod tumbling robot over a variety of terrains of varying complexity. Terrains were chosen to be representative of those experienced in real-world scenarios while also exhibiting a high degree of repeatability for future comparisons. For each terrain we presented results regarding velocity and energetics. Multiple configurations of the Adelopod were considered including both straight and angled arm configurations. To our knowledge, these results comprise the first formal evaluation of a tumbling robot's terrainability and thus serve as benchmarks for future comparisons.

Perhaps the most interesting of these results are those concerning the terrainability of the Adelopod over the complex stepfield terrains. These terrains were the most difficult of those tested and are commonly used in many robotics competitions. The Adelopod with straight arms exhibited remarkable performance over this terrain and did not fail a single run. These results indicate that tumbling is capable of producing forward locomotion over competitive terrain with only two actuated degrees of freedom. Additionally, we would like to note that we have selected dimensions for the stepfields based on the suggested standards with respect to the Adelopod's dimensions. In practice, however, we have observed that many competitions allow larger robots for similarly scaled stepfields, further supporting the improved terrainability of tumbling.

In general we have observed very promising performance of the Adelopod over a wide variety of terrains. Many of these results were observed with simple open-loop control schemes or by human control. Overall tumbling performance, due to numerous motion constraints and utilization of terrain-body interaction, is inherently related to the overall quality of motion planning available to the robot. In this respect we believe

that the full potential of tumbling has yet to be observed. We turn our focus to this issue in the next chapter where we begin to address the motion planning problem for tumbling locomotion.

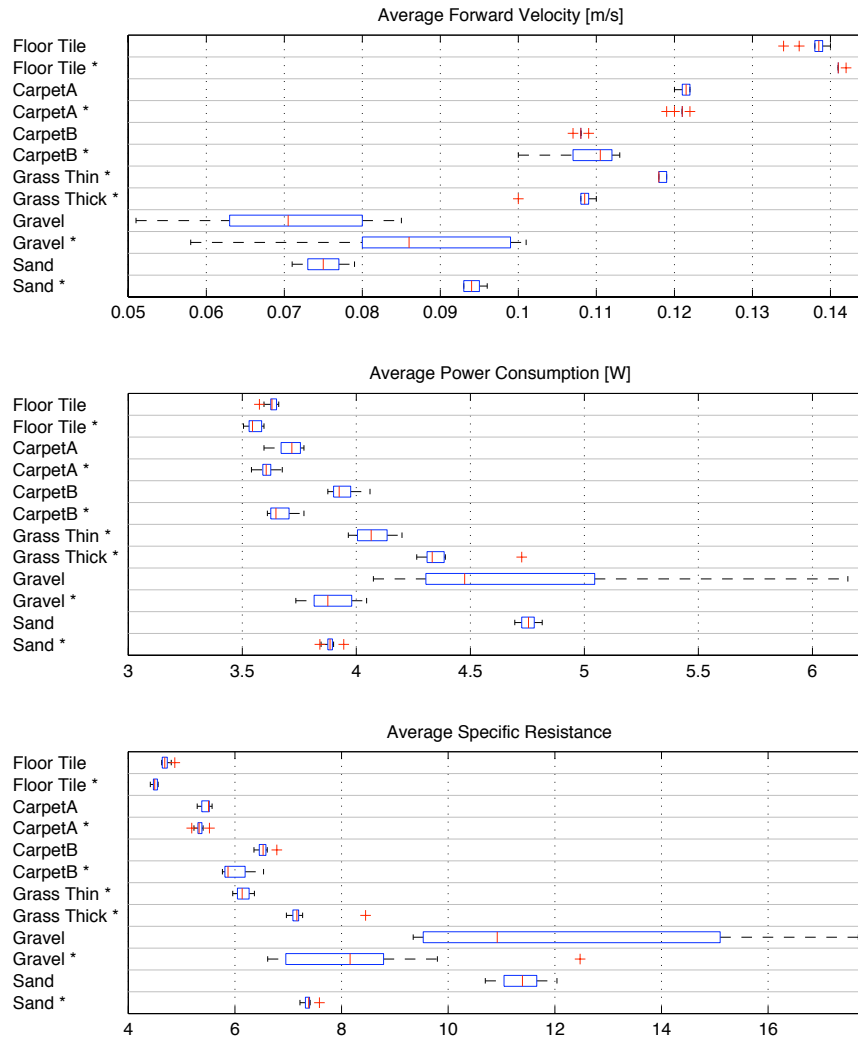


Figure 5.24: Comparison of average forward velocity, power consumption, and specific resistance for the ruggedized Adelopod over various test terrains.

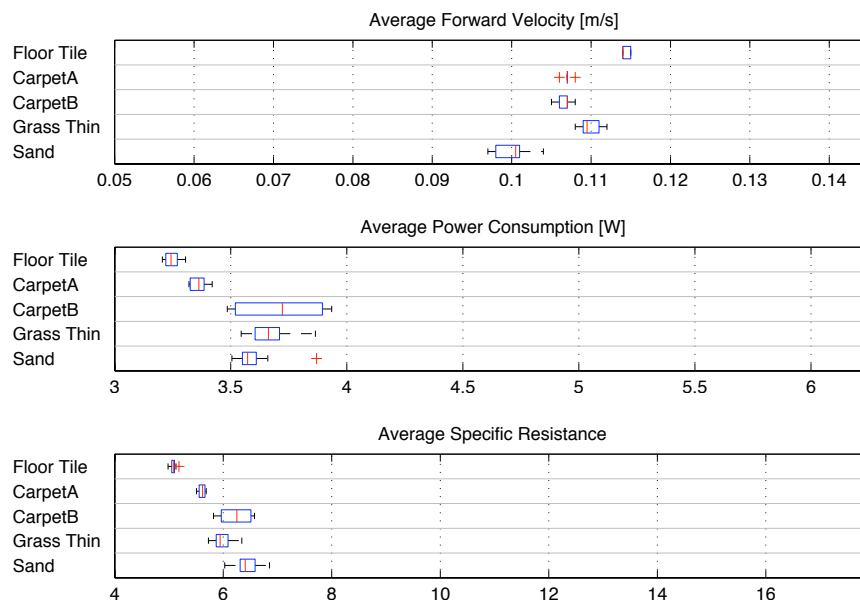
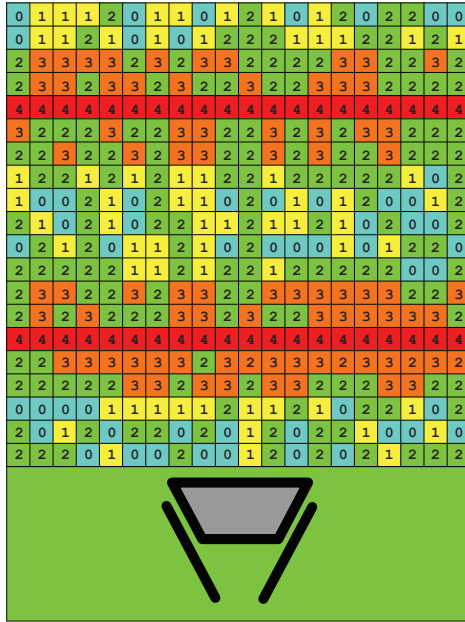
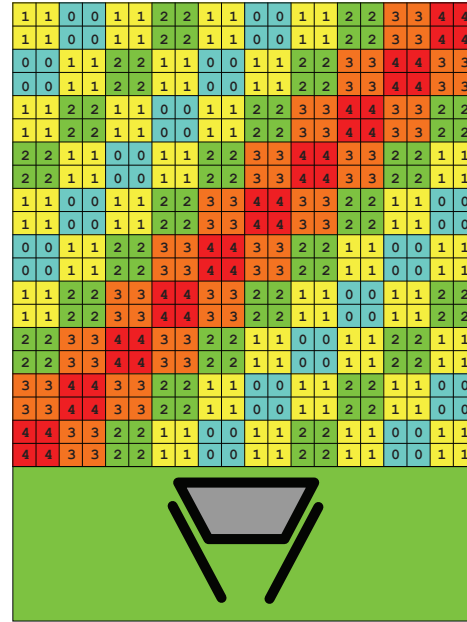


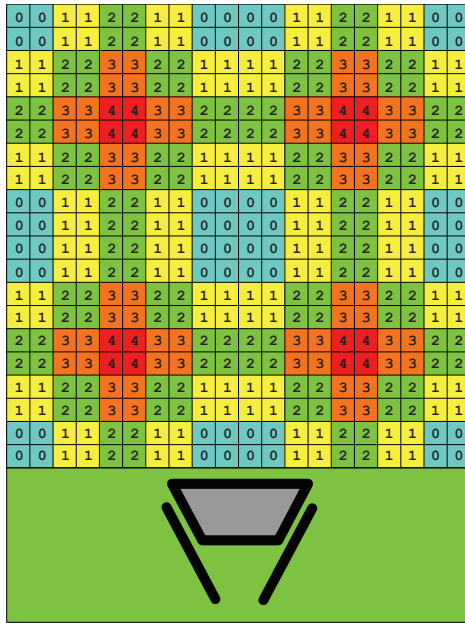
Figure 5.25: Comparison of average forward velocity, power consumption, and specific resistance for the wheel-tail Adelopod over various test terrains.



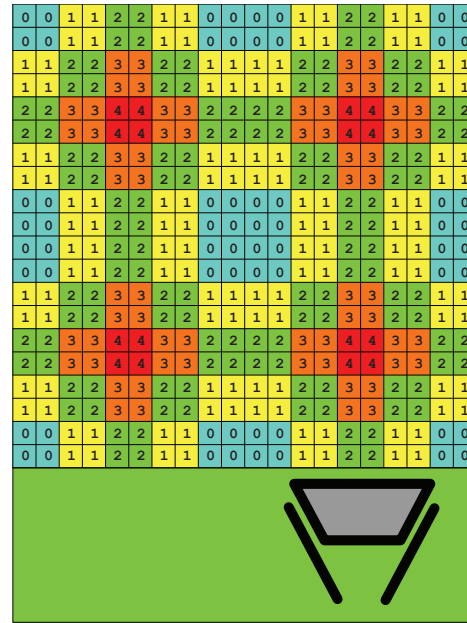
(a) Double Randomized Perpendicular Hills



(b) Symmetric Diagonal Hill

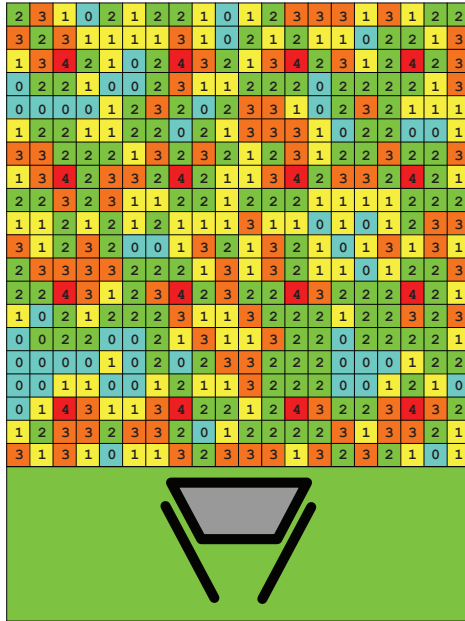


(c) Quad Symmetric Central Peaks - 1

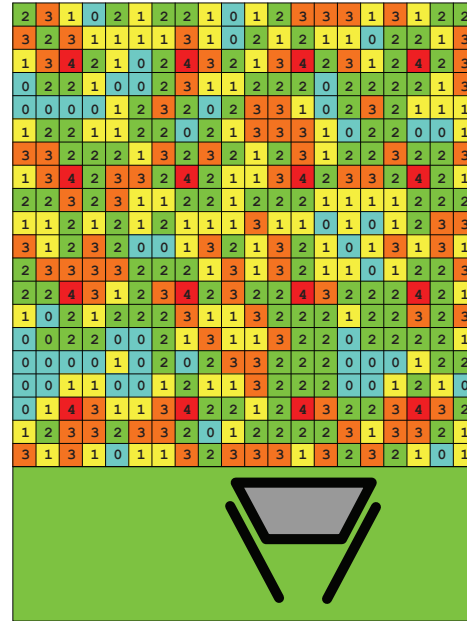


(d) Quad Symmetric Central Peaks - 2

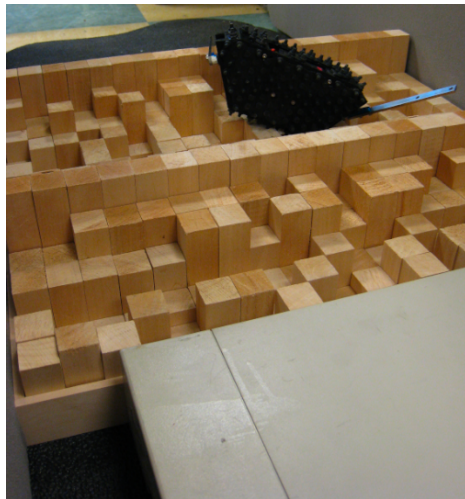
Figure 5.26: Stepfields used for testing complex terrain negotiation for the Adelopod and Adelopod-T.



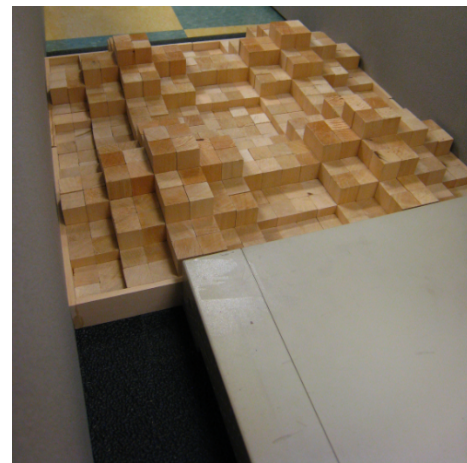
(e) Randomized Tall Squares – 1



(f) Randomized Tall Squares – 2



(g) Photo: Double Randomized Perpendicular Hills



(h) Photo: Quad Symmetric Central Peaks

Figure 5.26: Stepfields used for testing complex terrain negotiation for the Adelopod and Adelopod-T. (cont.)

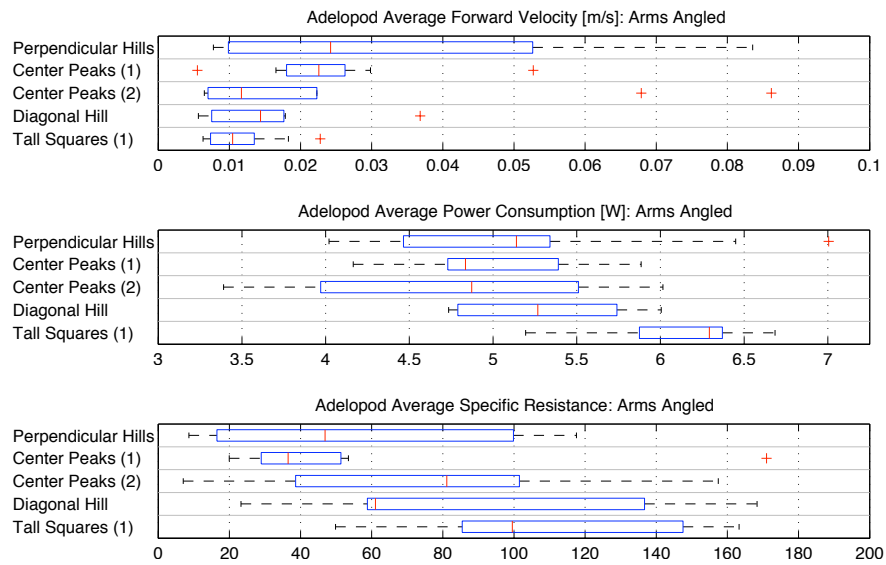


Figure 5.27: Comparison of average forward velocity, power consumption, and specific resistance for the ruggedized Adelopod with arms angled over complex stepfields.

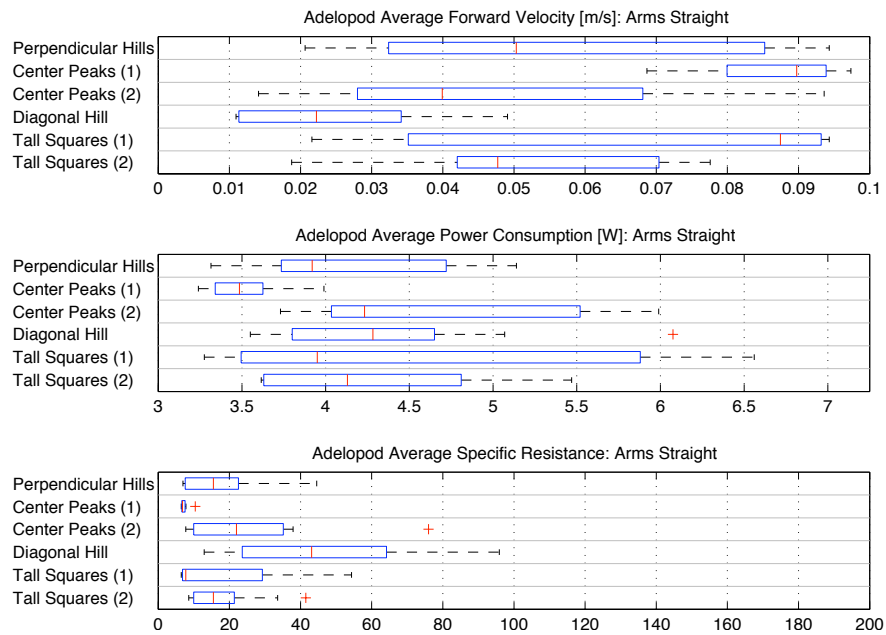


Figure 5.28: Comparison of average forward velocity, power consumption, and specific resistance for the ruggedized Adelopod with arms straight over complex stepfields.

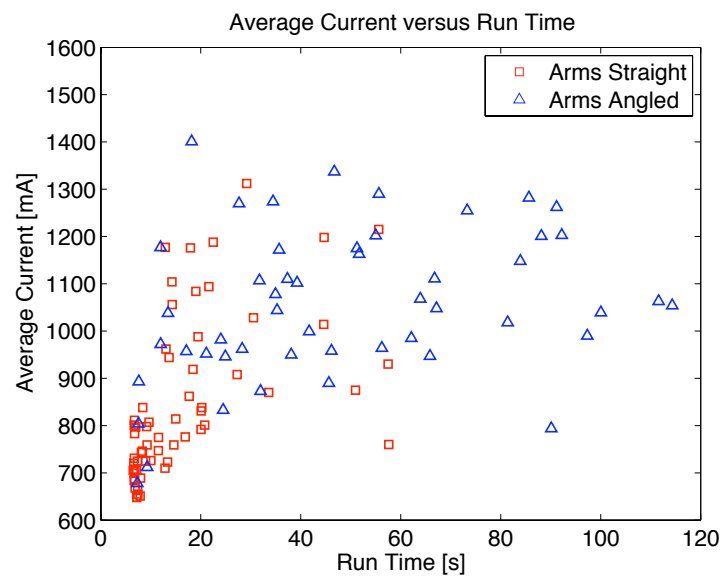


Figure 5.29: Comparison of average current and runtime for the ruggedized Adelopod over complex stepfields for arms both angled and straight.

Chapter 6

Maneuverability and Motion Planning of Serial Multiply-actuated Tumbling

In this chapter we are primarily concerned with establishing effective methods for driving serial multiply-actuated tumbling robots such as the Adelopod. As discussed in Chapter 3, serial multiply-actuated tumbling robots form a class of tumbling that utilize unrestricted ground-body interactions to enable minimalistic (often underactuated) designs with sufficient mobility. While this class of robots is attractive in terms of its generally low required hardware complexity, its underactuation greatly limits maneuverability resulting in difficult planning and control. In the following sections we present the motion planning problem, examine motion constraints common to the class of serial multiply-actuated tumbling robots, and present several motion planning techniques capable of dealing with such constraints.

6.1 Motion Planning Formulation

The area of robot motion planning is concerned with finding paths that bring the robot from its initial starting state to some final goal state. As one can imagine, this particular issue is central to the study of mobile robots as it is generally required to achieve any

useful motion for a given task. In general, the problem varies greatly with the types of systems (robots) considered and their respective motion constraints as well as issues pertaining to any real-time or optimality constraints. For the purpose of this work we are interested only in answering the feasibility question; that is, does a path exist from some initial state to a final goal state that satisfies the motion constraints of the system (robot and terrain)? For a given terrain, this question is directly related to the maneuverability of the robot in question where sufficient mobility results in the existence of feasible paths. To state precisely our problem, we use the well-established framework of robot motion planning (see [107, 121]).

Let A represent the robot and \mathcal{W} the physical workspace in which the robot exists (for our purposes \mathcal{W} equals \mathbb{R}^2 or \mathbb{R}^3). We assume A to be a system of rigid bodies connected by joints with body i referred to as A_i . A fixed frame $\mathcal{F}_{\mathcal{W}}$ is assigned to \mathcal{W} and moving frames \mathcal{F}_{A_i} are assigned to each of the rigid bodies that make up A . With this we can formally define the configuration space [107].

Definition 6.1 *A configuration q of A is a specification of the position and orientation of all \mathcal{F}_{A_i} with respect to $\mathcal{F}_{\mathcal{W}}$. The **configuration space** of A is the space \mathcal{Q} of all possible configurations of A . A unique configuration of \mathcal{Q} is arbitrarily selected and is called the **reference configuration** of A . It is denoted by 0 .*

Obstacles are assumed to be rigid bodies in \mathcal{W} and can be represented in the configuration space as well. Let B_i represent obstacle i , its representation in \mathcal{Q} (referred to as a \mathcal{Q} -obstacle) is then

$$\mathcal{Q}B_i = \{q \in \mathcal{Q} \mid A(q) \cap B_i \neq \emptyset\}, \quad (6.1)$$

where $A(q)$ denotes the subset of \mathcal{W} occupied by A in configuration q . The free space is defined as the set of all configurations where the robot does not intersect obstacles;

$$\mathcal{Q}_{free} = \mathcal{Q} \setminus \bigcup_i \mathcal{Q}B_i. \quad (6.2)$$

In addition to the free space there is also the contact space $\mathcal{Q}_{contact}$ that captures all

configurations where the robot is touching an obstacle; formally, this is defined as

$$\mathcal{Q}_{contact} = \{q \in \mathcal{Q} \mid A(q) \cap \bigcup_i B_i \neq \emptyset, \text{int}(A(q)) \cap \bigcup_i \text{int}(B_i) = \emptyset\}. \quad (6.3)$$

Traditionally, in robotics collisions are avoided and only subsets of \mathcal{Q}_{free} are considered. In contrast to this, tumbling generally makes use of contacts with the terrain for achieving locomotion and thus utilizes configurations within both the free and contact spaces; this relaxed space, called the valid space, is defined as

$$\mathcal{Q}_{valid} = \mathcal{Q}_{free} \cup \mathcal{Q}_{contact}. \quad (6.4)$$

With the above notations, our problem can be formally stated as follows: find a valid path

$$\tau : [0, 1] \rightarrow \mathcal{Q}_{valid} \quad (6.5)$$

such that

$$\tau(0) = q_{init} \quad (6.6)$$

$$\tau(1) = q_{goal} \quad (6.7)$$

where q_{init} and q_{goal} are the initial and goal configurations respectively. In many cases it is not necessary for the robot to obtain a particular configuration but rather reach some area in \mathcal{W} . Therefore we define a goal set \mathcal{G} of configurations that result in success and require instead that $q_{goal} \in \mathcal{G}$.

Although desirable, a complete path τ is not as useful as it might seem. Depending on the motion model used in calculating τ there will be some error that grows as the path is executed caused by any inaccuracies in the model. Using our above definitions of τ we can define the configuration error as follows:

$$\tilde{q} = q - \hat{q} = q - \tau(x), x \in [0, 1]. \quad (6.8)$$

Due to the nature of tumbling locomotion \tilde{q} can grow quite rapidly and periodic replanning is often necessary. In practice final executed tumbling paths are piecewise,

$$\tau(x) = \begin{cases} \tau_0(x), x = 0 \\ \tau_1(x), x \in [0, t_1) \\ \vdots \\ \tau_{N-1}(x), x \in [t_{N-2}, t_{N-1}) \\ \tau_N(x), x \in [t_{N-1}, 1] \end{cases}, \quad (6.9)$$

where replanning occurs at $x = \{t_1, \dots, t_{N-1}\}$.

If the system is dynamic, the idea of the configuration space can be extended to a more general state space, \mathcal{X} . In this space the state of the system (configuration and velocities as opposed to the configuration alone) is expressed as a single point. The benefit to this representation is that the second order acceleration constraints inherent to dynamic systems can be represented by a set of first-order derivatives. For the majority of this work, however, we make the quasi-static assumption resulting in $\mathcal{X} = \mathcal{Q}$.

In the next few sections, we discuss several different planning approaches with respect to tumbling locomotion for the class of serial multiply-actuated tumbling robots.

6.2 Motion Primitives for Tumbling

As mentioned in Chapter 3 and discussed further later in this chapter (Section 6.5), the class of serial multiply-actuated tumbling robots exhibits minimalistic trends that result in motion constraints that limit the maneuverability of the robot as well as making motion planning more difficult. As a first method of generating motion plans for tumbling, we present in this section a method that makes use of motion primitives. By discretizing the the system into a set of relatively simple motions it is possible to find feasible paths using discrete search and thus avoid the complex dynamics and motion constraints of the system.

Motion primitives are a valuable tool and prove useful in solving complex problems such as motion planning [121]. Due to the non-intuitive motion of a tumbling robot, deriving useful motion primitives is not straightforward. In this section we present an approach that produces useful motion primitives along with convenient notation

for representing the resulting primitives. We begin by discretizing both the inputs and possible configurations of the tumbling robot. By executing the complete set of discretized inputs starting from each of the discrete configurations, it is possible to construct a directed configuration graph that represents the relationship between various configurations of the robot. In the last step we associate global displacements with each of the configuration graph edges, the result of which is a compact representation of the motion primitives for the discretized inputs. In the following subsections we discuss in detail the aforementioned process and apply them to the Adelopod robot.

6.2.1 Discretization

The first step in deriving motion primitives is to discretize the possible configurations of the particular robot. For the example of the Adelopod, we have two inputs and have chosen to discretize by starting with arm angles equal to multiples of $\pi/2$, producing 4 possible configurations of each arm. The motion of this particular robot is a function of the arm configurations as well as the body's orientation, therefore we also discretize the body's configuration as angles equal to multiples of $\pi/2$. This discretization produces a maximum of 4^3 possible states for our robot. However, as we will see in the following sections, the symmetry of the robot along with the elimination of unreachable states greatly reduces the number of unique states.

To simplify the transitions between configurations, it is useful to have the arms touching the ground whenever possible. Under the assumption that the robot is on a smooth level surface, the arms require a constant $\Delta\theta$ for each configuration in order to ensure contact with the ground. By this definition we can now represent the arm angles by the following equation:

$$\theta_n = n(\pi/2) + \Delta\theta_n, \quad n \in \{0, 1, 2, 3\}. \quad (6.10)$$

The values of n and $\Delta\theta$ for the left arm-body configurations of our robot are shown in Table 6.1. The right arm-body values of n and $\Delta\theta$ can be calculated with the following relations:

$$n_{right} = (n_{left} + 2) \bmod 4 \quad (6.11)$$

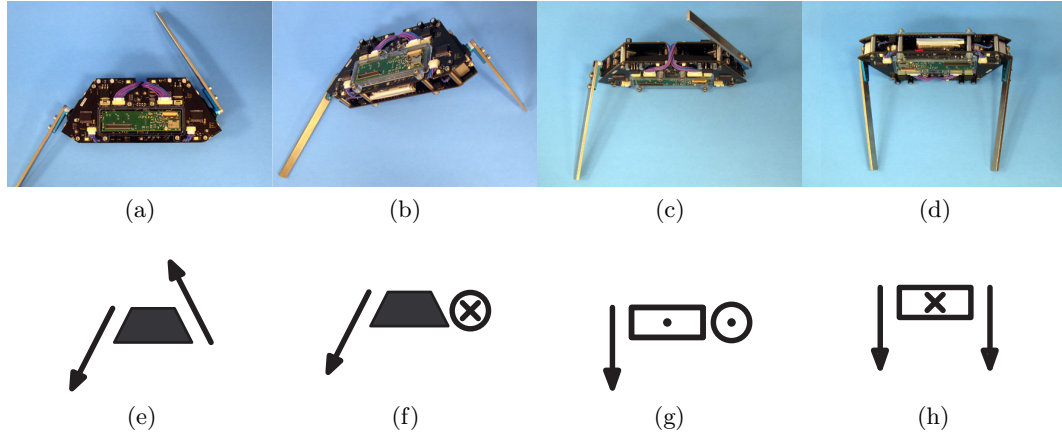


Figure 6.1: Sample configurations with corresponding chart icons.






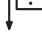



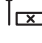

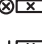



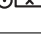
and

$$\Delta\theta_{right} = -\Delta\theta_{left}. \quad (6.12)$$

Let us briefly pause here to introduce the notation in the first column of Table 6.1; this notation is used throughout the rest of the paper to compactly represent our discretized configurations. Each of the 4^3 configurations is expressed as a 3-tuple with components representing the orientation of each arm along with the body. The order of the 3-tuple is as follows: left arm, body, right arm. Each element is defined as the orientation of the particular component looking in the negative direction onto the robot along the Z_G -axis (see Figure 4.2) where the orientations are described verbally as *up*, *down*, *dot*, or *cross* (additionally, don't-cares are represented with a '-'). Figure 6.1 shows four pictorial representations of possible configurations along with a picture of the actual robot in the respective configuration (for example, Figure 6.1(b) shows the robot as described by the $(down, up, cross)$ 3-tuple and is pictorially represented by Figure 6.1(f)).

We now have a unique representation for each of the 4^3 configurations along with the actual arm angles (from Equation 6.10) for each configuration, thus completing the discretization.

Table 6.1: Arm-body configuration parameters for the Adelopod robot.

Arm-body Configuration	n	$\Delta\theta$	Arm-body Configuration	n	$\Delta\theta$
	3	$+7^\circ$		0	$+17^\circ$
	0	0°		1	0°
	1	-7°		2	-17°
	2	0°		3	0°
	1	$+7^\circ$		2	$+15^\circ$
	2	0°		3	0°
	3	-7°		0	-15°
	4	0°		1	0°

6.2.2 Configuration Graph

In general, a tumbling robot is restricted in its motions by its current configuration. Therefore, the motion primitives must be arranged in such a way that their dependence is accounted for; we achieve this with a directed graph where each node corresponds to a configuration and each edge to a control input.

A graph is built as follows. We start by placing our robot in an arbitrary configuration as described in the previous section and execute a discretized control input (for our graph, a control input corresponds to moving one of the motors in a single direction, providing 4 possible inputs). We stop the robot when it has reached a new discretized configuration and then update the $\Delta\theta$ of the arm not influenced by the executed control input so that it matches perfectly the new configuration (these updates are small and have little influence on the position of the robot). At this point we add a directed edge corresponding to the executed input to the configuration graph. By iterating over all possible inputs for every discrete configuration, it is possible to construct a directed graph that relates the various discrete configurations according to the control inputs.

Figure 6.2 shows the configuration graph derived for the Adelopod robot by applying the above method (the graph was derived for the robot on a smooth, level surface with the robot operating at quasi-static speed). We have separated the graph into 4 sub-graphs for clarity, where each graph focuses on a different body configuration.

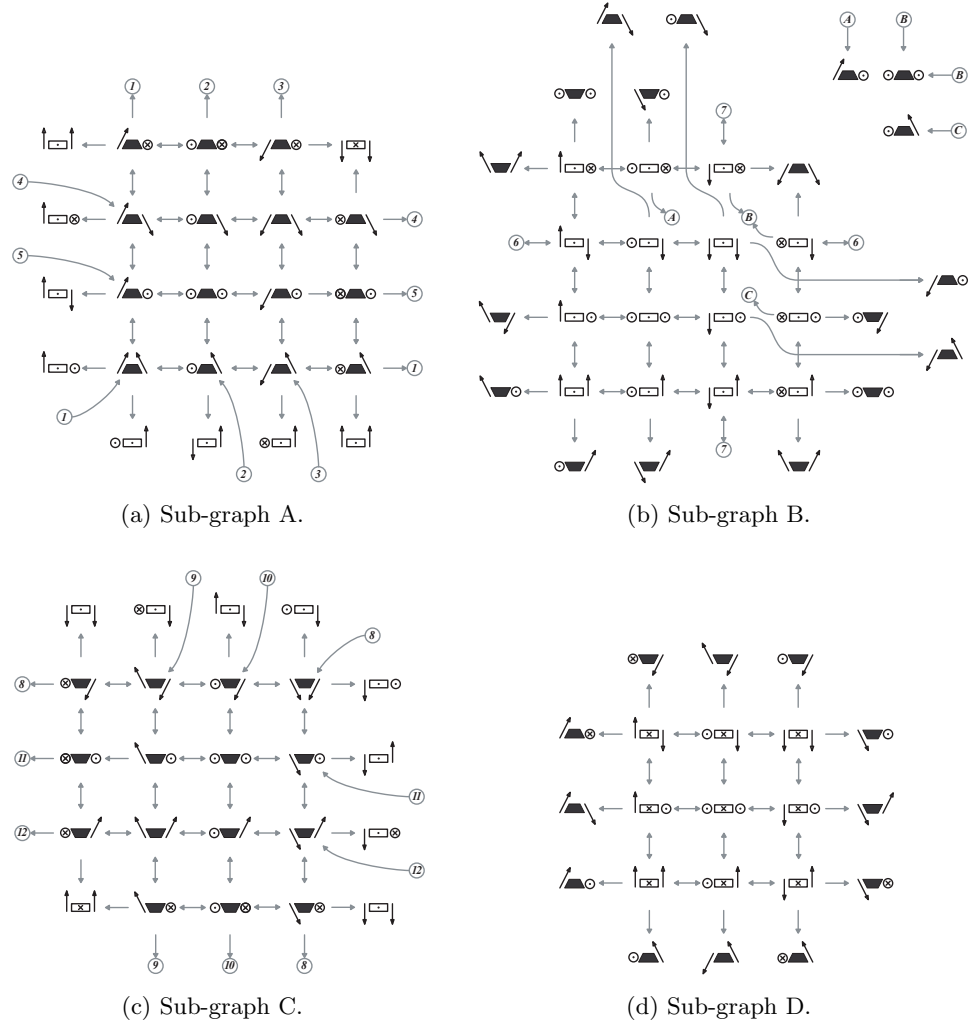


Figure 6.2: Configuration graph derived from discretizations of Section 6.2.1. As shown, an upward transition corresponds to a positive θ_{right} , a downward transition corresponds to a negative θ_{right} , a leftward transition corresponds to a positive θ_{left} , and a rightward transition corresponds to a negative θ_{left} .

As presented, the graph exhibits abundant symmetries. For example, Figure 6.2(c) can be produced by rotating Figure 6.2(a) by 180° and subsequently reflecting each configuration about the vertical axis. Other symmetry in the graph is apparent about diagonals from the lower left to the upper right of each sub-graph. Additionally some sub-graphs exhibit symmetry about diagonals from the lower right to the upper left; this can be seen in Figure 6.2(d) and also, though less apparent, partially in Figure 6.2(b). These symmetries are a desirable characteristic and greatly reduce the memory requirements necessary to represent the graph on an actual robot.

Other useful properties of the graph include the identification of transitions that do not affect the body and transitions that induce a tumble. In each sub-graph, there exists a 3-by-3 region of configurations centered about $(dot, -, dot)$ in which transitions have no effect on the body. We refer to these as free moves and are useful for changing the relative orientation of the arms in respect to the body. Any unidirectional edge of the graph corresponds to a transition that induces a tumble and is thus irreversible.

We also wish to point out that there are some configurations that do not exist on the configuration graph. In general, these are any configurations that are of the form $(cross, -, cross)$, $(-, cross, cross)$, or $(cross, cross, -)$. These are configurations of unstable equilibria and are not reachable from any configuration through the execution of the discretized control inputs. They serve no useful purpose and, therefore, have been excluded from the graph.

6.2.3 Displacement

Up until this point we have concerned ourselves only with the configuration of the robot. For the final step in our method, we associate global displacement with each edge in the configuration graph to produce the actual motion primitives. For the purpose of deriving the primitives, we are only interested in the robot's position and orientation on the XY_G -plane. Therefore we define the configuration of the robot, q , as a vector containing its 2-D position and orientation. Each transition is then characterized by the difference, Δq between the configurations.

$$\Delta q = (\Delta x, \Delta y, \Delta \phi)^T. \quad (6.13)$$

All of these values are expressed in the robot's frame. From Equation 6.13 we get the update equation,

$$q_{k+1} = \begin{pmatrix} x_k + C_{Z_G}(\phi_k) \Delta x_k \\ y_k + C_{Z_G}(\phi_k) \Delta y_k \\ \phi_k + \Delta \phi_k \end{pmatrix}, \quad (6.14)$$

for the configuration of the robot, where $C_{Z_G}(\phi_k)$ is the rotation about Z_G of ϕ_k .

Because the robot's body is unrestricted in its rotation about x_0 (necessary for tumbling), the calculation of Δq is not as straightforward as one might assume. The issues revolve around the representation of the robot's orientation. If represented as a single vector, there exist orientations in \mathbb{R}^3 that result in an undefined orientation in \mathbb{R}^2 . Additionally, as the robot tumbles, the orientation vector loses meaning. To overcome this issue we instead represent the orientation of the robot as the YZ_0 -plane of the robot's frame. With this representation, we define orientation in \mathbb{R}^2 as the direction of the line created by the intersection of the YZ_0 -plane with the XY_G -plane. This representation gives us two possible values of ϕ , however, if we arbitrarily assign ϕ one of the two directions and limit $\Delta \phi$ to the interval $[-\pi/2, \pi/2]$, ϕ remains well defined over all discretized configuration transitions¹.

The elements of Δq are calculated with the following expressions:

$$Y_{proj}^{(k)} = Z_G \times {}^G C X_0, \quad (6.15)$$






$$\Delta y_k = \frac{\Delta P_k \cdot Y_{proj}^{(k)}}{\|Y_{proj}^{(k)}\|}, \quad (6.16)$$

$$\Delta x_k = \frac{\Delta P_k \cdot (C_{\hat{Z}_G}(-90^\circ) Y_{proj}^{(k)})}{\|Y_{proj}^{(k)}\|}, \quad (6.17)$$

and

¹By this method, ϕ is undefined only when the YZ_0 -plane is parallel to the XY_G -plane, which does not exist in our configuration chart.

Table 6.2: Experimental results for displacements of 5 configuration transitions.

Transition		Results [mm, mm, deg]			
1		Δx	-24.9	$var(x)$	2.9
		Δy	12.6	$var(y)$	1.0
		$\Delta\phi$	5.0	$var(\phi)$	0.1
2		Δx	19.7	$var(x)$	0.8
		Δy	49.8	$var(y)$	0.7
		$\Delta\phi$	12.4	$var(\phi)$	0.8
3		Δx	2.4	$var(x)$	1.2
		Δy	58.3	$var(y)$	6.4
		$\Delta\phi$	3.8	$var(\phi)$	3.6
4		Δx	4.0	$var(x)$	0.2
		Δy	64.9	$var(y)$	0.2
		$\Delta\phi$	4.6	$var(\phi)$	0.8
5		Δx	5.3	$var(x)$	4.6
		Δy	57.9	$var(y)$	9.0
		$\Delta\phi$	15.4	$var(\phi)$	11.0

$$\Delta\phi_k = \text{acos} \left(\frac{Y_{proj}^{(k)} \cdot Y_{proj}^{(k+1)}}{\|Y_{proj}^{(k)}\| \|Y_{proj}^{(k+1)}\|} \right), \quad (6.18)$$

where $\Delta P_k = {}^G P_{k+1} - {}^G P_k$ is the difference of the robot's position between time steps k and $k + 1$ in the global frame.

In Table 6.2, we list the elements of Δq of our robot for five of the configuration transitions of Figure 6.2. We derived each of these values experimentally using a Vicon motion capture system over 25 runs of each primitive. Additionally Figure 6.3 depicts the positional results graphically. With this characterization of displacement, our configuration chart becomes a map of the robot's motion primitives.

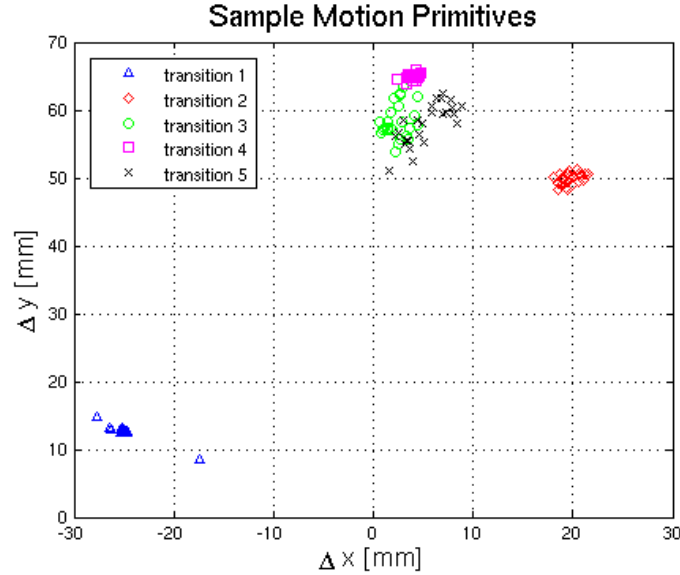


Figure 6.3: Graphical depiction of $G_{P_{k+1}}$ with $G_{P_k} = (0, 0)^T$ and $\phi_k = \pi/2$ for the 5 transitions given in Table 6.2.

6.2.4 Gaits

In addition to providing a compact representation of the previously derived motion primitives, the configuration chart can also be used to develop periodic gaits for the robot. By exploiting the properties of the configuration chart, we are able to derive useful sequences of motion that exhibit desirable characteristics. For instance forward motion can be generated by traversing the configuration chart while choosing primitives with large forward displacement, minimal lateral motion, and small changes in orientation. Conversely, turning motion can be generated by choosing primitives with large successive changes in orientation. As examples, we have included three periodic gaits developed in this manner and show them in Figure 6.4.

Figure 6.4(a) shows a gait developed to produce forward motion. In this situation, we have chosen primitives for their large positive Δy . Additionally, we have chosen the sequence of primitives to stay close to the aforementioned lines of symmetry. By doing so, it is possible to alternate between identical sequences on either side of the symmetry, which effectively eliminates lateral and orientational offsets. This results in a gait of large forward displacement with small periodic oscillations along the forward axis (the

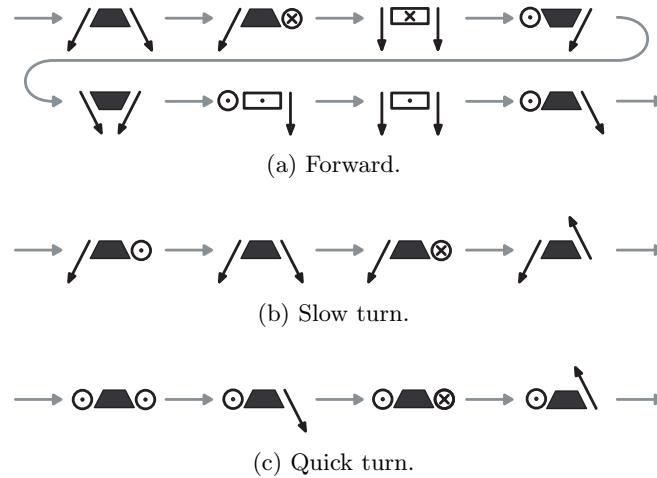


Figure 6.4: Gaits derived from motion primitives.

transitions of Table 6.2 were chosen to demonstrate these qualities).

The turning gaits were developed by selecting configurations from the chart and traversing in a single direction until small loops were found that produced large orientational displacements with minimal positional displacement. The turning gait of Figure 6.4(b) is easily identifiable by traversing loop 3 of Figure 6.2(a) while the gait of Figure 6.4(c) can be derived by following loop 2 of Figure 6.2(a).

These gaits comprise only a small sub-set of the possible sequences provided by the configuration graph, however, the ability to both turn and move forward enable the execution of directed motion.

6.2.5 Planning

After constructing the above described configuration graph and associated displacements, the calculation of feasible trajectories through the environment can be found with almost any discrete search algorithm. This portion of planning is well established and thus a wide variety of selections exist. An issue not yet addressed exists for any form of heuristic search where nodes chosen for expansion are selected based on some notion of estimated cost-to-go where more promising nodes are expanded first. In terms of efficient and timely search, a good heuristic is very important. As an example, naively searching the above Adelopod motion primitives without a heuristic (e.g.

breadth-first-search) results in the number of nodes expanded in the order of millions for displacements of only one third of a meter; even a simple heuristic based only on Euclidean distance can bring this number down to around only 50,000 and even less with heuristics that manage to capture the motion constraints of the particular tumbling robot. It turns out, however, that the formulation of a perfect heuristic is as difficult as solving the original motion planning problem itself. For a serial multiply-actuated tumbling robot, even finding a meaningful heuristic representative of its motion can be quite difficult due to their general underaction and nonintuitive motion. In Section 6.8 we address this issue and present a promising method we have developed for finding useful heuristics for tumbling robots that also applies to other systems with significant motion constraints.

6.2.6 Final Thoughts on Motion Primitives for Tumbling

The above method is attractive in that it manages to avoid many of the complexities inherent to tumbling by considering only discrete subsets of the possible inputs. Additionally, the above method has the benefits of being generally applicable to multiple classes of tumbling; although we performed all calculations with respect to the Adelpod, with minor modifications the ideas presented can be extended to other tumbling robots such as the composite-bodied TETwalker. Despite these benefits, however, this method has flaws when it comes to real-world applications requiring the benefits of tumbling discussed in Chapter 3. This particular method makes several assumptions regarding the smoothness and uniformity of the terrain, thus limiting its practicality. Additionally, this method relies on the manual selection of the input and configuration discretizations which, if improperly chosen can lead to poor performance. While a good first step and useful for studying tumbling locomotion within controlled environments, the full utilization of tumbling locomotion in unstructured and complex terrains requires investigation into other planning methods capable of handling complex non-uniform terrain.

6.3 Support Set Planning

Although it avoids the above awkward input discretizations, planning using support set transitions is significantly more complicated than the above due to its dependence on both the continuous and discrete dynamics of the system. We have made some progress utilizing such motions directly using the schema shown in Figure 6.5(a) where we focus on generating lists of discrete tumbles for use by a high-level discrete planner. This schema breaks the problem into separate modules contained within two groups, pre-processing and planning. The overall idea is to produce a set of feasible tumbles in the pre-processing section that are then passed to a planner which assembles sequence of control inputs from the feasible set. By solving for discrete tumbles, the nonholonomic phenomena inherent to tumbling locomotion are effectively removed from the planning problem. Additionally, this method enables the use of discrete planning methods such as A^* or dynamic programming [121]. A typical implementation of the schema outlined in Figure 6.5(a) would proceed as follows:

1. For a given configuration q_0 , calculate a set of feasible tumbles using information of the robot morphology.
2. Propagate all tumbles to the global frame using a dynamic model of the robot. This produces a set of tumble axes in the global frame as well as a set of new configurations resulting from the tumbles.
3. Iterate as desired for increased look-ahead.
4. Plan trajectory using set of tumble axes from pre-processing.

In this manner, we create several subproblems, or modules, that can be solved separately and then combined as a final solution. Specifically, the subproblems involve calculating possible tumbles, predicting future states based on robot/terrain dynamics, and high-level planning using sets of feasible tumbles. We believe that our approach provides an intuitive geometric solution to the tumbling control problem through a more natural discretization that considers the actual discrete changes in the vector fields.

For the purpose of this section, we assume the following:

- $V = \{v_1, \dots, v_n\}$ is a finite set of vertices that serve as an approximation to the hull of the robot; points in V are, in general, functions of the control inputs. The

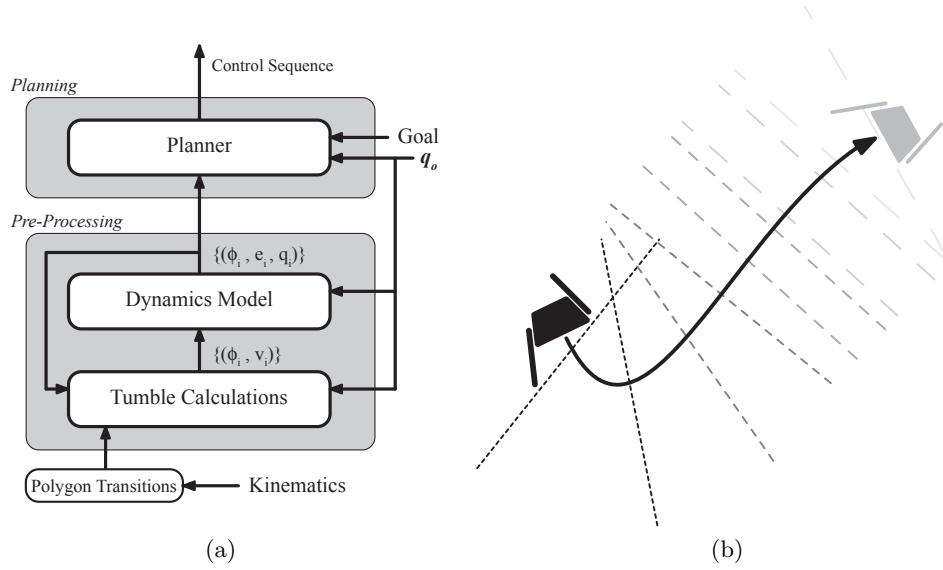


Figure 6.5: (a) Flow diagram of proposed modular schema for control of serial multiply-actuated tumbling robots. (b) A sample depiction of consecutive tumble axes used for turning.

construction of this set is at the discretion of the implementer, however it should generally include all points of the robot that commonly come in contact with the ground and/or obstacles. For level terrain these points are simply the vertices of the convex hulls of each component (arm, body, etc.) of the robot.

- C is the support set of vertices from V in contact with the terrain.
- $P = \{p_1, \dots, p_m\}$ is the set of vertices from V that make up the extreme vertices of the support polygon $\mathcal{P} = \mathcal{CH}(C)$.

From the above we have the following relation

$$P \subseteq C \subseteq V. \quad (6.19)$$

6.3.1 Tumble Calculations

Discrete tumbles occur when stability of the system vanishes; therefore, control inputs resulting in discrete tumbles can be found by finding where the stability of the system vanishes. Using the static stability margin, s_{static} defined previously in Definition 3.2, we

again refer to the Figure 3.1 of the Adelopod robot on level terrain. Here the support set is $C = \{v_d, v_e, v_n\}$ and the corresponding support polygon $\mathcal{P} = \mathcal{CH}(C_{\text{proj}})$. The points p_d , p_e , and p_n all in \mathcal{P} correspond to the projections of v_d , v_e , and v_n respectively. The dashed lines of the figure then represent the distances from the projected center of mass, p_{proj} , to each of the three edges of the support polygon ($\overline{p_e p_d}$, $\overline{p_d p_n}$, and $\overline{p_n p_e}$). Expressing s_{static} in terms of p_{proj} and \mathcal{P} we get the following relation:

$$s_{\text{static}} = \min_{p_i, p_j \in \mathcal{P}} \sqrt{\|p_{\text{proj}} - p_i\|^2 - \langle p_{\text{proj}} - p_i, p_j - p_i \rangle^2}, \quad (6.20)$$

where s_{static} is positive if $p_{\text{proj}} \in \mathcal{P}$ and negative otherwise.

Because tumbles occur over edges of the support pattern, we can examine each edge individually to test for feasible tumbles, thus removing the minimization from Equation (6.20). On a per edge basis, tumbles occur at the zeros of the following expression:

$$f(\phi) = \|p_{\text{proj}} - p_i\|^2 - \langle p_{\text{proj}} - p_i, p_j - p_i \rangle^2, \quad (6.21)$$

where $\phi = (\phi_1, \phi_2, \phi_3, \phi_4)$ is the input vector of arm angles. It is important to note that the above expression only holds for the given support set defined by C . If the support set changes, stability must be redefined in terms of the new resulting support polygon. Therefore when evaluating $f(u)$ for a particular \mathcal{P} , constraints must be enforced similar to the location invariant of Equation (3.23) that enforces the support set.

We plot $f(\phi)$ from Equation (6.21) for $C = \{v_d, v_e, v_n\}$ in Figure 6.6 where each subplot represents an edge of the support polygon. For clarity, we have plotted f versus only ϕ_2 and ϕ_4 ; the shoulder variables have been set to the fully contracted position. Only values for which ϕ satisfies the support set invariants are plotted. This figure provides insight on the behavior of the robot for the given support polygon. We can see from Figure 6.6(b) that the robot can tumble over edge $\overline{p_e p_d}$ for appropriate values of ϕ_2 and ϕ_4 . Conversely, Subfigures 6.6b and 6.6c indicate that it is not possible to tumble about edges $\overline{p_d p_n}$ or $\overline{p_n p_e}$ from the support set $C = \{v_d, v_e, v_n\}$. Additionally we can see that ϕ_4 (rotation of arm in contact) has a much greater impact than ϕ_2 on the stability. In fact, the only effect ϕ_4 has on the stability comes from its influence on the robot's composite center of gravity.

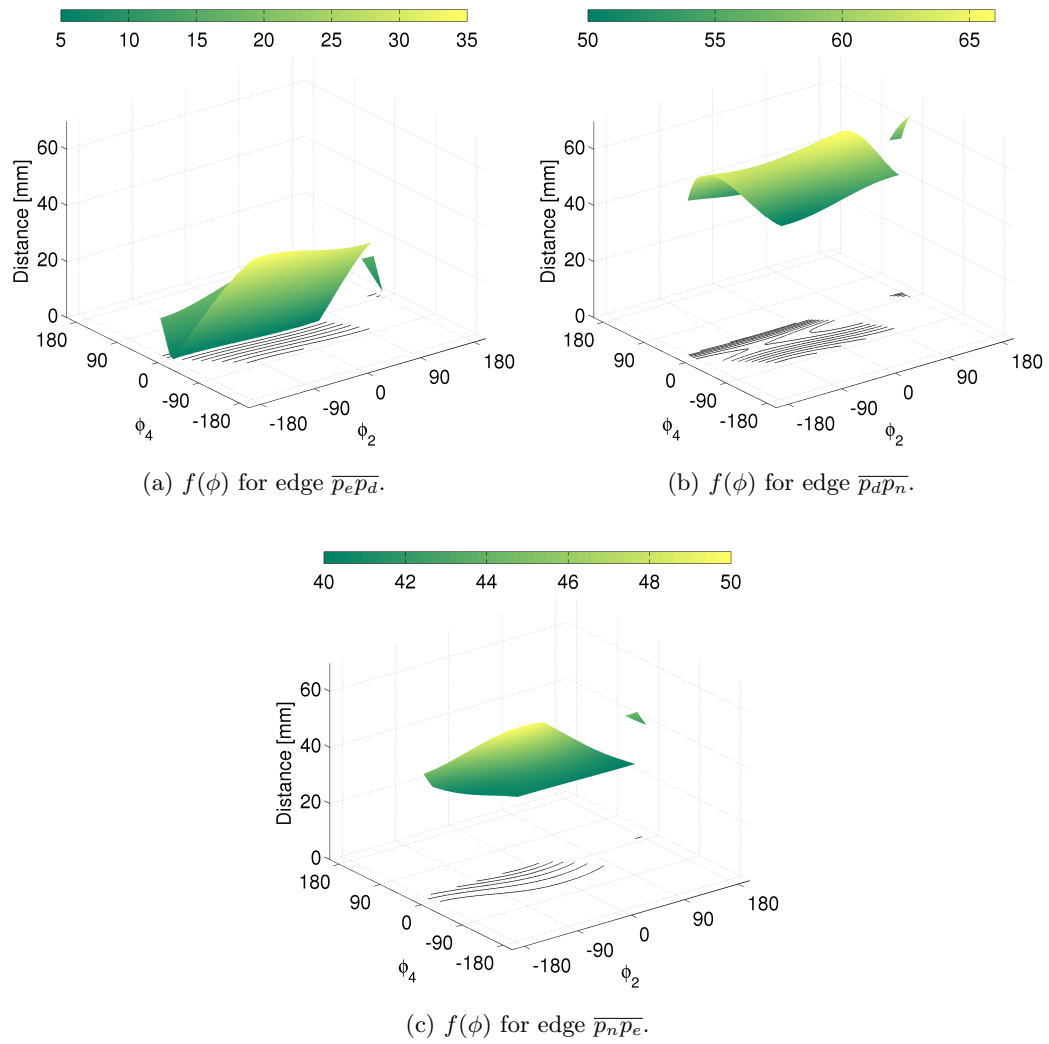


Figure 6.6: Distances of projected center of gravity, p_{proj} , to specified edges. Tumbles occur when $f(\phi) = 0$.

6.3.2 Dynamics Propagation and Planning

The solutions from the tumble calculation module are relative to the robot's frame and take into account only the robot's kinematics. In order to use these calculations for any useful planning, we must predict how the robot will react in the real world as the control vector u changes with time. The purpose of the dynamics propagation module is just that, it is responsible for transforming the feasible tumbles into the global frame, taking into account the robot's interaction with the environment (ground reaction forces and sliding friction). Such behavior is explained by the equations of motion for the robot.

The planner module takes the set of discrete global tumbles and chooses a sequence accordingly to produce motion toward the desired goal state. In Figure (6.5(b)) we show a sample scenario where the dashed lines represent the sequence of tumbles chosen by the planner. Because the tumbles are discrete at this point any form of discrete planning can be used. Due to the issues regarding accurate state propagation in tumbling robots we highly suggest using a receding horizon planning scheme where planning happens periodically during the task. If the horizon is chosen appropriately the inaccuracies of the state estimation can be managed.

Although feasible for the P2AT, application of this method to the Adelopod proved intractable. In practice we are able to calculate arm angles that result in tumbles but accurate modeling of the robot's frictional interactions still needs much attention. Additionally, we have found that any trajectories of practical length also need to deal with stable transitions of the support polyhedra in addition to the already considered unstable transitions. In this respect it might be more appropriate to discretize based on the support set transitions rather than just discrete tumbles. Additional motivation for this extension can be motivated by [122] in which the authors address the issue of motion planning for systems that exhibit both continuous and discrete dynamics similar to that exhibited by serial multiply-actuated tumbling robots. Their methods are shown to be able to produce near-optimal trajectories for such systems with the requirement that the sequence of discrete transitions is known a priori. Our method, if extended could possibly provide such information, however, the issue of accurate descriptions of the continuous dynamics still exists. In the next section we present a method we have had the most success with that effectively deals with many of the complex dynamics of tumbling.

6.4 Path Planning with RRTs

As expressed in the previous two sections, there are many issues regarding tumbling that make motion planning difficult. One overarching issue is that of effectively dealing with and incorporating the complex system dynamics of tumbling. While we managed to avoid the issue in the motion primitive approach of Section 6.2 we were forced to make inconvenient assumptions regarding the terrain that greatly limit the method's practicality. While the approach of Section 6.3 can be applied to more general terrain, its complexity currently limits its applications to unrealistically simple systems. In this section we present a motion planning technique based on randomized exploration of the configuration space well suited for tumbling that effectively handles many of the aforementioned issues; specifically, we utilize rapidly exploring random trees (RRT) to quickly explore the space of feasible paths within the configuration space. In our experience, the method of this section combined with the metrics derived later in Section 6.8 show the most promise for producing practical methods for real-world application of tumbling over complex terrain.

This section addresses the application of RRTs [123] to serial multiply-actuated tumbling robots. RRTs have exhibited much success in the literature and have been shown to effectively solve many difficult planning problems that were previously unsolvable [124, 125, 126, 127, 128, 129, 130, 131]. In general, RRTs scale well to high dimensional problems with complicated system dynamics, making them attractive for serial multiply-actuated tumbling. Additionally, this technique is well-suited for tumbling locomotion as tree construction is mostly independent of the system dynamics and requires only an approximation of the state equation

$$\dot{x} = f(x, u), \tag{6.22}$$

where x is the robot's state and u the input vector (arm velocities or torques). This benefit removes the need for an explicit motion model and thus allows the use of any black-box method capable of producing approximations for \dot{x} .

Figure 6.7 presents pseudo-code for our slightly modified version of the algorithm presented in [123]. The algorithm grows an RRT in the state space of the robot until a goal state is found, which is then returned. By using the RRT, the sequence of control

inputs that will bring the robot from the initial state to the goal state can be assembled by tracing the RRT back to the root from the final node. The function `RandState`

```

RRTSearch(initialStateTree)
1: repeat
2:   if Probability(goalBias) then
3:     xRand = RandState(goalLimits)
4:   else
5:     xRand = RandState(randLimits)
6:   end if
7:   xNear = NearNeighbor(stateTree, xRand)
8:   for  $i = 1$  to NUM_INPUTS do
9:      $x_k = x_{\text{Near}}$ 
10:    deltaTime = RandTime(timeLimits)
11:     $x_{k+1} = \text{RunSim}(x, u_i, \text{deltaTime})$ 
12:    xNew[i] =  $x_{k+1}$ 
13:  end for
14:  TreeInsert(bestState)
15: until IsInGoal(bestState)
16: return bestState

```

Figure 6.7: Rapidly exploring random tree search of the robots state space.

returns a random point in the state space bounded by some specified limits that reflect the area of interest; the value returned by this function is what drives the expansion of the RRT. Non-uniform sampling distributions can be used to influence the shape of the RRT; in this case the tree is biased towards a region in the neighborhood of the goal with a probability determined by `goalBias`. The function `NearNeighbor` returns the node of `stateTree` that is closest to `xRand`. This function requires some distance metric which we discuss later in detail. `RunSim` simply steps the motion model (using the supplied approximation to Equation (6.22) by time `deltaTime` using the control vector from `RandInput`. The final two functions `TreeInsert` and `IsInGoal` are responsible for maintaining the tree representation and testing for goal states respectively.

As we can see, the above algorithm is relatively straightforward. The biggest issue revolves around the selection of an appropriate distance metric used for selecting nodes for expansion. The authors in [124] present results using a simple weighted Euclidean

metric defined as follows:

$$\rho(x_1, x_2) = w_p \|p_1 - p_2\|^2 + w_q (1 - |h_1 \cdot h_2|)^2 + w_v \|v_1 - v_2\|^2 + w_\omega \|\omega_1 - \omega_2\|^2 \quad (6.23)$$

where w_p , w_q , w_v , and w_ω are weights for position, orientation, linear velocity, and angular velocity respectively; vectors p, h, v and ω are the position, unit quaternions representing orientation, and linear/angular velocities respectively. The above metric assumes that *close* configurations in Euclidean space correspond to *close* configurations in the configuration space; in general, this is not true. For systems with nonholonomic motion constraints the quality of the generated tree (and thus solution quality and run time) are greatly influenced by the quality of the chosen metric. Unfortunately, calculation of a perfect metric is as hard as solving the original motion planning problem and is one of the biggest issues regarding the application of RRTs to motion planning.

Despite the sensitivity to metric choice, the randomness of the algorithm can often make up for poorly selected metrics. By naively applying the above generic weighted Euclidean metric with varying weights we have had significant success in finding feasible trajectories of the Adelopod over various terrains including both traversable and non-traversable (mazes) obstacles. These results attest to the power of RRTs as they were able to find feasible trajectories for the significantly underactuated Adelopod of significant length over interesting terrain using the generic Euclidean metric. Sample trees using this metric are shown in Figure 6.8.

Despite the ability to generate feasible trajectories in the presence of the Adelopod's motion constraints, the runtimes of the algorithm using the Euclidean metric are less than ideal and exhibited prohibitively high variance. In formulating the motion planning problem at the beginning of this chapter, we mentioned that tumbling trajectories are of limited use due to the rapid propagation of error. Additionally, with the restricted set of available motions due to nonholonomy, tracking and error reduction for a planned trajectory is not generally possible after error begins to accumulate. In this respect the planned trajectory is only feasible for small horizons. In order for the paths to be useful the runtimes for generation must be small enough to run in real-time with replanning occurring constantly. For the same reasons lower variance is also desirable in the runtimes. With these goals in mind we spend the remainder of this chapter looking into

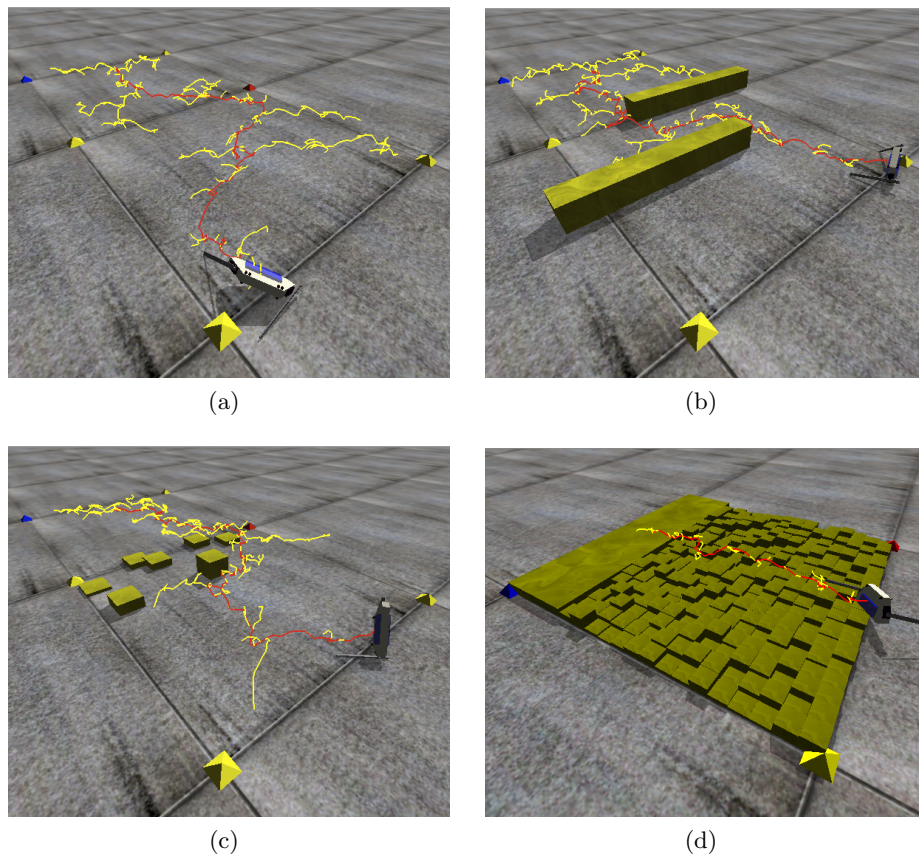


Figure 6.8: Example RRTs generated for the Adelopod over various terrain using a simple weighted Euclidean metric.

the development of useful metrics for planning for tumbling. We begin our discussion by introducing the concept of maneuverability and its application to serial multiply-actuated tumbling locomotion in the next section before presenting analysis of a metric for the Adelopod derived from its maneuverability characteristics in Section 6.8.

6.5 Maneuverability of Serial Multiply-Actuated Tumbling Robots

Maneuverability in general is the ability of a mobile robot to effectively change its heading to avoid obstacles and steer the robot to any places of interest in its environment. In terms of traditional wheeled, tracked, and legged mobile robots, maneuverability is easily measured in terms of turning radius, steering resolution, steering accuracy, etc. For tumbling robots, many of these common measures are not directly applicable. Take the common turning radius as an example; for a wheeled robot this is calculated simply as the radius of the tightest turn the robot can make. With respect to tumbling, application of such a measure is not immediately obvious. For the Adelopod, turning motions are generally not smooth and depend upon the executed sequence of support set transitions. Due to the general insufficiency of existing metrics regarding maneuverability to tumbling, we must examine other aspects of tumbling locomotion to gain insight into their ability to effectively steer.

One possible measure of maneuverability applicable to tumbling is the degree and nature of a robot's motion constraints where we make the observation that motion constraints generally lead to decreased maneuverability. The underactuation common to serial multiply-actuated tumbling leads to nonholonomic constraints on the possible motions obtainable from a given configuration. By looking at the range of motions with respect to the range of all possible configurations, it is possible to comment on the degree of actuation available and respective maneuverability of the robot. We have had success using this approach for simple systems such as the P2AT and present results below in Section 6.5.1. For more sophisticated and many real-world tumbling systems, application of this method becomes more difficult due to issues of asymmetry, drift, friction and non-smooth dynamics. With some assumptions regarding behavior, analysis is possible but not representative of the real-world behavior of the modeled

robot.

Another approach to accessing the maneuverability of tumbling focuses on an indirect approach that uses the minimum path cost through the configuration space. In this method, maneuverability is reflected through the relative cost of achieving various configurations within the environment. Ideally, we would use the actual path cost, however, direct calculation of such is as hard as solving the motion planning problem and is not currently possible for the systems we consider. As an approximation, we use a randomized sampling-based approach that uses rapidly exploring random trees. Our methods are discussed in Section 6.6 as well as results applying the technique to examine the performance impact of shoulder angles on the Adelopod tumbling robot with respect to maneuverability.

6.5.1 P2AT

Defined in Chapter 3, the toy tumbling robot P2AT is a planar example serial multiply-actuated tumbling robot with a primary body and two arms connected by actuated revolute joints. In this section we examine various issues related to the maneuverability of this particular robot by examining directly the motion constraints of the system.

The configuration space for the P2AT was shown in Chapter 3 to be

$$Q_{\text{P2AT}} = \mathbb{R}^2 \times S^1 \times T^2 = SE(2) \times T^2,$$

where the body's position and orientation are specified by the special Euclidean group $SE(2)$ (3 degrees of freedom) and the arm angles (relative to the body) by the 2-dimensional torus T^2 (2 degrees of freedom). This representation makes up a set of generalized coordinates where unique configurations of the robot can be expressed as points on the 5-dimensional manifold Q_{P2AT} . The inputs of the system correspond to the velocities of the two arms ($u = (\dot{\phi}_{23}, \dot{\phi}_{24})^T \in \mathbb{R}^2$) resulting in two control vector fields $g_{\phi_{23}}^C, g_{\phi_{24}}^C \in \mathcal{G}$ that express the evolution of the system for a support set C and unit inputs for the controls $\dot{\phi}_{23}$ and $\dot{\phi}_{24}$ respectively. The set of all linear combinations of these control vector fields form the set of all feasible velocities of the systems; specifically, they form a distribution $\mathcal{D}(q, C) = \text{span}(\{g_{\phi_{23}}^C, g_{\phi_{24}}^C\}) = \dot{\phi}_{23}g_{\phi_{23}}^C + \dot{\phi}_{24}g_{\phi_{24}}^C, \dot{\phi}_{23}, \dot{\phi}_{24} \in \mathbb{R}^2, C \in \mathcal{C}$. As discussed in Chapter 3, tumbling robots of the class we are interested in

are generally hybrid in that they exhibit both continuous and discrete dynamics. The continuous dynamics are captured by the vector fields in \mathcal{G} while the discrete changes are accounted for by the dependence of each $g \in \mathcal{G}$ on the particular support set C . Because of this dependency, the vector fields of \mathcal{G} are generally non-smooth at the support set transitions (depicted graphically for the P2AT by the labeled edges of Figure 3.11).

In terms of maneuverability, we are interested in the set of reachable configurations by following vector fields in \mathcal{D} . At this point it should be clear that the P2AT is significantly underactuated, as it has only 2 control vector fields available for producing motion along its 5-dimensional manifold of configurations. In addition to considering reachable configurations on all of $\mathcal{Q}_{\text{P2AT}}$, it is also interesting to consider a relaxed problem where we consider only the reachability of the submanifold $\mathcal{Q}_{\text{body}} = SE(2)$. This relaxation takes into account only the body's configuration and is meaningful for many real-world scenarios where we are primarily concerned with the body's positioning and orientation (e.g., for positioning/pointing sensors). For this relaxed problem, we are interested in the configurations reachable by following vector fields in $\mathcal{D}_{\text{body}}$, created simply by dropping the last two elements (corresponding to the arm angles; T^2) from the vector fields of \mathcal{D} . By this formulation we again have two control vector fields, however, the configuration manifold of interest is only of dimension three. Interestingly, despite the more attractive appearance of the latter relaxed formulation, the distribution $\mathcal{D}_{\text{body}}$ lacks regularity (i.e., the dimension of $\mathcal{D}_{\text{body}}$ is not the same for all configurations q).

It is possible in some scenarios to generate locally motions not contained within \mathcal{D} , thus increasing the set of configurations reachable from a given starting configuration. By examining the Lie brackets of vector fields in \mathcal{D} , it is possible to identify such motions that can be approximated by infinitesimal motions from the vector fields in \mathcal{D} .

As examples we consider the support sets $C = \{v_2, v_3\}$ and $C = \{v_3, v_4\}$. For each of

these support sets we get the following control vector fields derived from Equation (3.16):

$$\begin{aligned}
 h_1 = g_{\phi_{23}}^{C_{23}} &= \begin{pmatrix} \frac{d\psi}{d\phi_{23}} \ell_2 \sin \theta \\ -\frac{d\psi}{d\phi_{23}} \ell_2 \cos \theta \\ \frac{d\psi}{d\phi_{23}} \\ 1 \\ 0 \end{pmatrix} & h_2 = g_{\phi_{24}}^{C_{23}} &= \begin{pmatrix} 0 \\ 0 \\ 0 \\ 0 \\ 1 \end{pmatrix} \\
 h_3 = g_{\phi_{23}}^{C_{34}} &= \begin{pmatrix} -\frac{d\psi}{d\phi_{34}} \ell_3 \sin(\theta + \phi_{23}) \\ \frac{d\psi}{d\phi_{34}} \ell_3 \cos(\theta + \phi_{23}) \\ -\frac{d\psi}{d\phi_{34}} - 1 \\ 1 \\ 0 \end{pmatrix} & h_4 = g_{\phi_{24}}^{C_{34}} &= \begin{pmatrix} \frac{d\psi}{d\phi_{34}} \ell_3 \sin(\theta + \phi_{23}) \\ -\frac{d\psi}{d\phi_{34}} \ell_3 \cos(\theta + \phi_{23}) \\ \frac{d\psi}{d\phi_{34}} \\ 0 \\ 1 \end{pmatrix}.
 \end{aligned} \tag{6.24}$$

$$\tag{6.25}$$

Here we can see an example of the aforementioned lack of regularity in $\mathcal{D}_{\text{body}}$. Let h'_i represent the portion of the control vector field h_i corresponding to the body configuration (first three elements). The lack of regularity can be shown by observing that $\dim(\text{span}(h'_1, h'_2))$ is one (motions available from $C = \{v_2, v_3\}$ are constrained to one dimension) while $\dim(\text{span}(h'_3, h'_4))$ is two (motions available from $C = \{v_3, v_4\}$ are 2-dimensional). In fact, $C = \{v_3, v_4\}$ is the only support set configuration at which the dimension of $\mathcal{D}_{\text{body}}$ is two (it may seem at first that support sets with three vertices in contact might also exhibit this dimensionality, however, the geometric constraints that preserve the support set effectively limit the range of motions to a 1-dimensional space); the support set $C = \{v_1, v_2\}$ (i.e., body lying flat on the ground with both arms in the air) results in a zero dimensional $\mathcal{D}_{\text{body}}$. In terms of the Lie brackets, it can be shown that

$$[h_1, h_2] = 0 \tag{6.26}$$

$$[h_3, h_4] = 0. \tag{6.27}$$

In fact, for the P2AT $[g_{\phi_{23}}, g_{\phi_{24}}] = 0$ for all C , indicating that for a fixed support set no new motions are generated by using infinitesimal motions along the control vectors. By this result, the P2AT is not small-time locally accessible when confined to a single

support set. Interestingly, however, we have found an analog to Lie brackets for the case where the P2AT is in the neighborhood of $C = \{v_2, v_3, v_4\}$ and support set transitions are allowed. In this configuration, small cycles of the inputs result in motion not in \mathcal{D} . This result is similar to that of vector fields generated from Lie brackets with the exception that we rely on discrete changes in the support set and resulting non-smooth vector fields. Specifically, the motion we are interested in is generated by moving along h_4 for a small time (causing v_2 to leave C), then along h_3 for a small time (v_2 returns to C), then along $-h_2$ for a small time (v_4 leaves C), then finally along $-h_1$ for a small time (v_4 returns to C). This motion is described by

$$q(2\epsilon_1 + 2\epsilon_2) = \varphi_{\epsilon_2}^{-h_1} \left(\varphi_{\epsilon_1}^{-h_2} \left(\varphi_{\epsilon_2}^{h_3} \left(\varphi_{\epsilon_1}^{h_4} (q_0) \right) \right) \right), \quad (6.28)$$

where $\varphi_t^g(q)$ represents the state of the system after starting from q and following the vector field g for time t ; Figure 6.9 depicts the input cycle graphically along with a depiction of the resulting system motion. It can be shown that the resulting motion is some horizontal displacement of the body not contained in \mathcal{D} . Considering the relaxed problem regarding $\mathcal{D}_{\text{body}}$, the span of this new motion along with those already in $\mathcal{D}_{\text{body}}$ has rank equal to the submanifold of body configurations thus implying small-time local accessibility. Furthermore, the system in this particular configuration is symmetric and drift-free, implying small-time local controllability as well.

In conclusion, we can see that, even for a greatly simplified planar model, the reachability and resulting maneuverability of the system can be quite interesting. For the P2AT, we have shown that the system is generally constrained in its motion with the exception of the body in the special case in the neighborhood of $C = \{v_2, v_3, v_4\}$. It is possible to utilize this information in any planning algorithms; for example, a basic algorithm could proceed as follows:

1. Use discrete tumbles to quickly generate large displacements until sufficiently close to the goal.
2. Transition to a locally controllable configuration with $C = \{v_2, v_3, v_4\}$.
3. Make use of local controllability to maneuver arbitrarily close to the target body position.

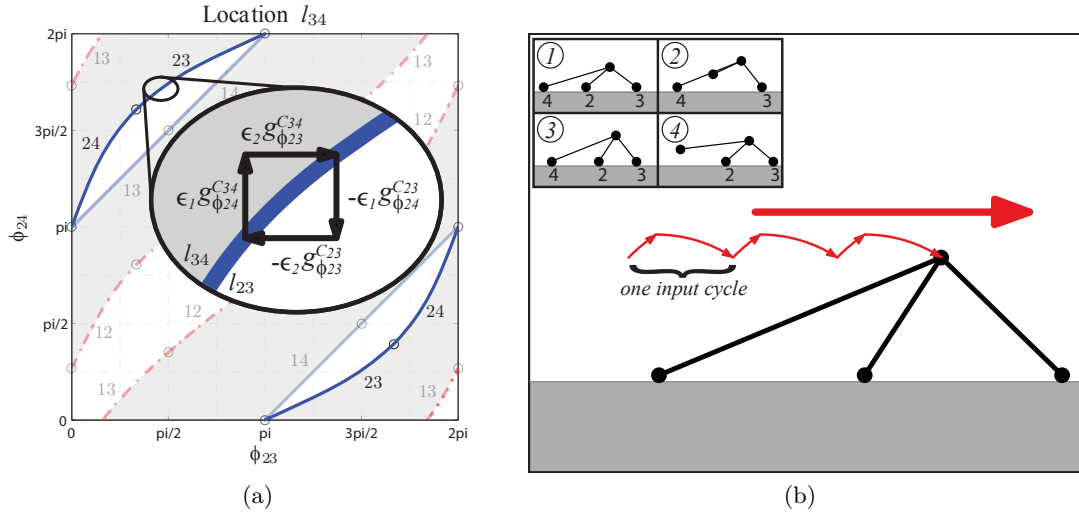


Figure 6.9: Depiction of the P2AT configuration with local controllability.

6.5.2 Adelopod

The Adelopod follows the same principles as the above P2AT with the configuration space

$$\mathcal{Q}_{\text{adelopod}} = \mathbb{R}^3 \times SO(3) \times T^2 = SE(3) \times T^2, \quad (6.29)$$

and vector fields determined by the physical laws of the physical workspace. Immediately obvious is the drastic increase in the dimensionality of the configuration space (unique configurations of the Adelopod exist on an 8-dimensional manifold) with again only two actuated degrees of freedom. In this respect, the Adelopod is more underactuated than the P2AT. Furthermore, the system's behavior is governed by complex dynamics involving chains of physical bodies with multiple frictional contacts between the robot and terrain that are often required to slide to generate locomotion. With these issues, the controllability analysis is not nearly as straightforward as with the P2AT and turns out to be quite difficult.

Due to the aforementioned difficulty of finding analytical solutions concerning the accessibility/controllability of tumbling robots such as the Adelopod, we focus our efforts on evaluating the maneuverability performance of the robot through the approximation of its cost of displacement through the configuration space. We address this specifically in Section 6.6. In addition to this method, we have identified two main methods of

globally steering tumbling robots with morphologies similar to the Adelopod. The first method relies primarily on the sweeping motions of the arms along with their relative interactions with the terrain; this method was empirically derived and has proven useful for direct human control of the Adelopod. The second method, referred to as support set turning, utilizes ground-body interactions fully to produce sequential changes in the support set that result in desired motion; the utilized transitions are both stable and unstable (discrete tumbles) in nature. This method is much more general than the above arm-sweeping method and is the method utilized by the planning methods described above in Sections 6.2-6.4. Each of the two methods are described briefly below.

Arm Turning

In the previous chapter we observed evidence that the relative angles of the arms' rotational planes have a significant effect on the turning motion of the robot. This was observed as significant increases in course deviations for configurations with angled arms. While inconvenient in terms of the previous chapter's experiments, the use of arms for turning can be useful for steering purposes if utilized correctly.

Gradual turning motions are made possible by the angles in the arm shoulders and the resulting sweeping motion of points on the arms in the plane tangent to the terrain; such motions can be seen in the arms' workspace of Figure 4.3 where the trajectory of points on an arm are functions of both θ_1 and θ_2 . Using the distance from an arm tip to the sagittal plane (YZ -plane of \mathcal{F}_A) we can express the sweeping motions mathematically as follows:

$$d_x(\theta_1, \theta_2) = \ell_{\text{arm}} \cos \theta_1 \cos \theta_2 - \sin \theta_1 d_2 + \cos \theta_1 a_1 - a_0. \quad (6.30)$$

Trajectories for several fixed values of θ_1 (shoulder angles) are shown in Figure 6.10(a) where it can be seen that the magnitude of the sweeping motion increases as the rotational plane of the arms leaves parallel ($\theta_2 = \pi/2$).

During forward tumbling locomotion, the driving arms (i.e., those in contact with the terrain) of serial multiply-actuated tumbling robots remain relatively parallel with the terrain itself while the body undergoes large net rotations (see Figure 6.10(b) for a

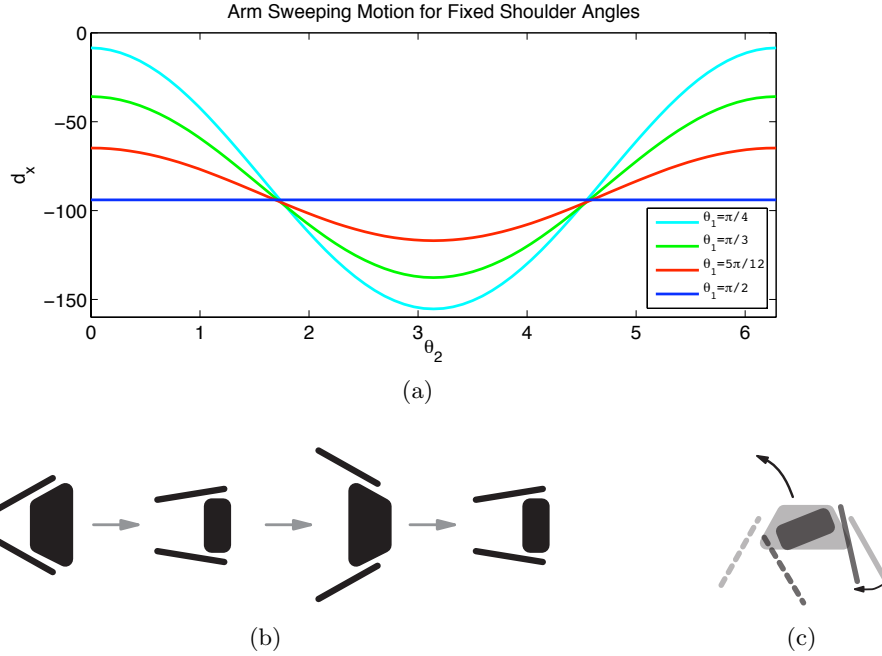


Figure 6.10: (a) Plot of distance between the arm tip and robot's sagittal plane as a function of θ_2 for various fixed values of θ_1 . (b) Sequence of configurations during forward locomotion depicting sweeping arm motion with arms in phase. (c) Generation of turning moments from arm sweeps; the solid arm is in contact with the terrain (driving) while the dashed arm is suspended in the air.

schematic description of a top-down view of forward tumbling locomotion with two driving arms). Loosely speaking, a majority of the forces resulting from the arms' sweeping motion is transferred as a moment acting on the robot's body that contributes to any body rotation about a vector normal to the terrain passing through the body's center of mass; the direction of the moment is related to the sign of $\partial d_x / \partial \theta_2$. Figure 6.10(c) depicts a moment produced by the right arm while sweeping towards the body with $\text{sign}(\partial d_x / \partial \theta_2) < 0$ and the resulting counter-clockwise rotation of the body.

Depending on the terrain-arm interactions, moments from the sweeping arm trajectories can be strategically employed to steer the robot. By altering the phase of the arms while driving forward, the robot can strategically select driving arms depending on the desired heading and signs of $\partial d_x / \partial \theta_2$ for each arm. As an example we show in Figure 6.11 captured frames of the Adelopod employing such a turning method in

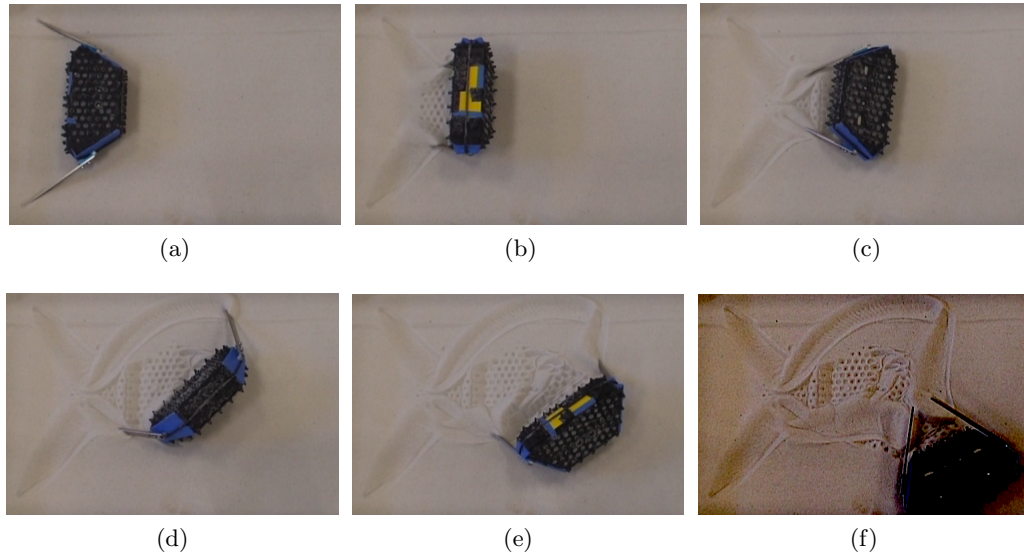


Figure 6.11: Frames taken from video of ruggedized Adelopod turning in sand through the use of sweeping arm motions due to shoulder angles. (f) Final position after turn with color levels adjusted for better viewing of arm trajectories.

loose sand. In this case the arms remain in phase until a time occurring between Figures 6.11(b) and 6.11(c) at which the left (top-most) arm is set to lag slightly behind the right creating a moment imbalance and resulting clockwise turn. After the turn (Figures 6.11(d)-(f)) the arms are again set to be in phase allowing the robot to continue straight with its new heading.

As one can imagine, this technique is very sensitive to the terrain due to the dependence on the terrain-arm interactions. Additionally, permanently angled arms require canceling moments from all of the driving arms to achieve straight motion. As discovered in the experiments of the previous chapter, this can be quite difficult or even impossible to achieve on some terrains. Specifically, any terrain that can generate large forces at the arm tips such as those with high coefficients of friction or significant compliancy where the arms are able to penetrate the surface layer as well as any terrains that have many surfaces orthogonal to the arm sweeping motions result in the ability to steer the robot. Maintaining a constant heading over such terrains turns out to be directly related to their smoothness and uniformity. Terrains such as sand and carpet allow effective steering while also allowing straight locomotion with angled arms. More

complex terrains such as larger gravel and the complex stepfields of the previous chapter allow ample turning but make maintaining a particular fixed heading with angled arms near impossible.

This method of steering tumbling robots was effectively utilized in our work [132] resulting from a collaboration with the Army Research Laboratory (ARL). In this work we mapped the relative phase of the arms along with a turn-in-place command to a single joystick allowing for one-handed human operation of the Adelopod.

Support Set Turning

Although intuitive and useful, the above method of steering uses only a small portion of the motions available to tumbling robots. By allowing the arms to rotate independently (in contrast to rotating together with some phase difference), tumbling robots can transition through various support sets to change their heading and negotiate terrain. This type of motion is much more general and exhibits many of the characteristics of tumbling discussed in Chapter 3. In general the result of such motion is a series of major tumbles achieved by combinations of stable and unstable (discrete tumbles) support set transitions. An example turn using support set transitions is shown for the Adelopod in Figure 6.12(b); Figure 6.12(a) shows the motion of the same input with the left arm in a different starting position that results in no heading change.

The motion planning algorithms of Sections 6.2-6.4 utilize support set turning.

6.5.3 Adelopod-T

The Adelopod-T, as described in Section 4.3, is an Adelopod tumbling robot with additional crawler treads that wrap around the body. This robot has all of the maneuverability of tumbling available to the Adelopod as well as differential drive capabilities where the terrain allows. On relatively smooth terrain, the treads add the ability to skid-steer and thus turn in place if desired. On more complex terrain, the treads are limited by the contacts they make with the terrain surface, however they are still very useful for small heading corrections and complement the tumbling capabilities quite well.

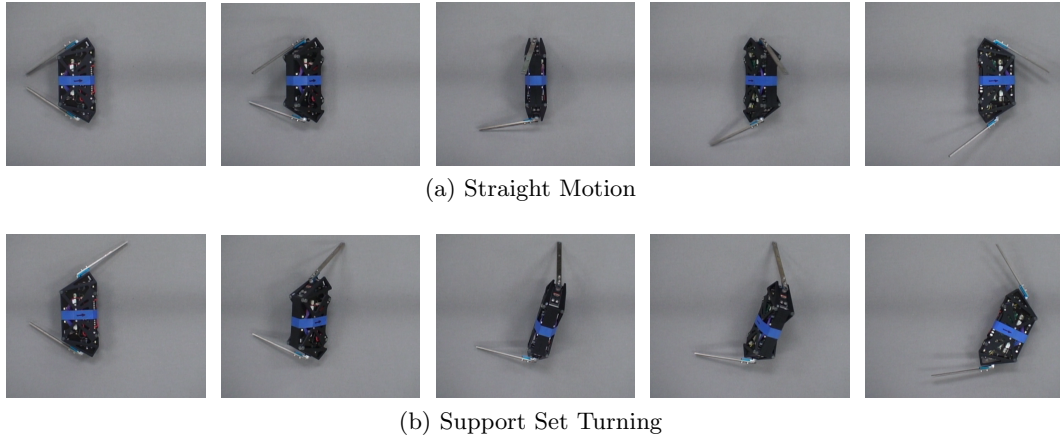


Figure 6.12: Two example support set manipulation sequences of the Adelopod tumbling robot on smooth terrain resulting in (a) straight motion and (b) turning motion. Each sequence was generated by driving the right (bottom-most) arm 180 degrees; the resulting motion (straight or turning) is determined by the respective support sets due to the position of the left (top-most) arm.

6.6 Maneuverability Analysis with Isochronal Surfaces

Previously we expressed the difficulty in quantifying the maneuverability of tumbling robots due to the difficulty in applying existing metrics and proposed using the degree and nature of motion constraints as indicators of maneuverability. While direct analysis of such properties is useful, it is not always possible due to complexity issues. In this section we motivate an alternate approach that indirectly captures motion constraints through the examination of costs associated with achieving displacement in the configuration space. Here we make the claim that maneuverability is reflected in such costs where cost is inversely related to maneuverability; unreachable configurations are assumed to exhibit infinite cost. In addition to providing measures of maneuverability, this method is attractive in that it can provide visual representations a robot's maneuverability and thus provide intuition regarding a particular robot's capabilities (useful for shedding light on the non-intuitive nature of tumbling). An additional benefit of this method is that it can be applied to the examination of maneuverability over arbitrarily complex general terrains.

Similar ideas exist in the works [133, 134] where the authors propose evaluating the mobility of a mobile robot based on its statistical performance (in terms of time and energy) over terrain. Of particular interest to our work is their formulation of isochronal contours.

Definition 6.2 *The locus points equidistant in time of traverse from some common origin is called an **isochronal contour***[133].

These contours depict the cost of displacement in the workspace radiating outward from the robots starting location. For simple holonomic systems, calculating the isochronal contour is equivalent to solving the shortest path problem in the workspace. A holonomic point robot in the planar workspace $\mathcal{W} = \mathbb{R}^2$ exhibits an isochronal contour comprised of concentric circles with their origins centered at the robots starting position. If obstacles are added, the contours wrap around the obstacles in a wavelike fashion propagating outward from the starting position. Such contours can be calculated in the presence of polygonal obstacles using continuous versions of Dijkstra’s algorithm in two dimensions [135, 136]; the three dimensional case with polyhedral obstacles has been shown to be NP-hard and thus only approximate solutions exist [137, 138].

Applying the above ideas directly to the configuration space (as opposed to just the workspace) we can capture directly the maneuverability of the robot. While it is not clear how to calculate these contours directly in the higher dimensions of the configuration space, we have had significant success approximating the contours using sampling-based techniques. Our goal is to approximate the cost of displacement within the configuration space given some starting configuration; that is, we wish to find a reasonable approximation to the mapping

$$d_{\text{iso}} : \mathcal{Q}_{\text{valid}} \times \mathcal{Q}_{\text{valid}} \rightarrow \mathbb{R} \quad (6.31)$$

$$(q, q_0) \mapsto d_{\text{iso}}(q, q_0), \quad (6.32)$$

which assigns a real number representative of the cost of reaching each final configuration q starting from q_0 . The samples we use for constructing our approximation consist of paths through the configuration space as defined in Equation (6.5) where for sample i we have $q = \tau_i(1)$ and the observed cost of reaching q represented by $\hat{c}_{q, q_0}^i = t_q - t_{q_0}$ (the time taken to execute the path τ_i). A valid sample requires that $\tau_i(x) \in \mathcal{Q}_{\text{valid}}$ for

$x \in [0, 1]$. Because we are interested in minimum costs, we construct our approximation of d_{iso} using the minimum observed cost for a particular configuration expressed formally as

$$\hat{d}_{\text{iso}}(q, q_0) = \min_i \hat{c}_{q, q_0}^i, \quad (6.33)$$

where in practice we compute the above over discrete bins assigned to the configuration space; the size of the bins is chosen with respect to the number of samples available in conjunction with the desired resolution of the final approximation.

With the above established, the issue becomes that of how to effectively generate sample paths through the configuration space. Samples can be taken deterministically by executing all paths for some time horizon created by executing permutations of discretized system inputs. Additionally, we can use randomized techniques that do not require predetermined discretizations and thus have the potential of effectively searching finer resolutions of the configuration space. Both of these approaches are analogous to the ideas behind the above described planning algorithm of Sections 6.2 and 6.4 respectively. In the following section (Section 6.7) we present an example application of the above outlined method using randomized sampling by RRTs to explore the effect of shoulder angles and arm friction on the maneuverability of the Adelopod tumbling robot.

6.7 Experimental Analysis Regarding the Impact of Arm Angles and Friction on the Adelopod Maneuverability

In the previous Chapter, we looked at the terrainability of the Adelopod and observed a general trend of decreased terrainability performance (e.g., lower speed, increased power consumption, and increased failure rate) in the experiments for configurations with the arms angled. Interestingly, all existing serial multiply-actuated tumbling robots (i.e., turbots) exhibit some form of asymmetry in the form of non-parallel rotational planes for the arms. Unfortunately, to our knowledge, there is no recorded justification for such morphological choices.

In this section we examine the possible advantages of angled arms for this class of tumbling in terms of their maneuverability through the application of the above

presented method of maneuverability analysis using isochronal surfaces of the configuration space. Specifically, we examine the relative maneuverability of the Adelopod robot in various configurations regarding combinations of shoulder angles and frictional coefficients of the arms. The results serve to demonstrate our above method while simultaneously providing insight into the overall maneuverability of the Adelopod as well as the impact of arm angles and friction on serial multiply-actuated tumbling.

Our experimental setup involved using the above outlined method on an Adelopod tumbling robot simulated over smooth terrain using the ODE physics engine [104]. We investigated four configurations of the Adelopod in total; two with the arms fully contracted (angled arms) and two with the arms fully extended (parallel arms). For each of the shoulder configurations we assigned different frictional values at the arms, one with the arm friction equal to that at the body and the other with arm friction one tenth that at the body. For each of the four configurations, we generated 750,000 samples over a 0.448 m horizon (measured in the xy -plane; this particular horizon corresponds to two complete forward major tumbles of the Adelopod) using a randomized sampling scheme. The randomized sampling scheme we used utilizes rapidly exploring random trees (RRT) to explore the configuration space within our chosen horizon (described further in Section 6.4 and overviewed in [124]). RRTs are attractive due to their ability to effectively explore high dimensional spaces. As our distance metric between two configurations $q_1, q_2 \in \mathcal{Q}$, we used the weighted Euclidean metric

$$\begin{aligned}
 d(q_1, q_2) = & \\
 & w_p \|p_1 - p_2\|^2 + w_b (1 - |h_1 \cdot h_2|)^2 + \\
 & (w_a/4) (2 - \cos(\phi_{l1} - \phi_{l2}) - \cos(\phi_{r1} - \phi_{r2}))^2, \tag{6.34}
 \end{aligned}$$

where $p_1, p_2 \in \mathbb{R}^3$ are the body positions; h_1, h_2 are the unit quaternions of the body orientations; and $\phi_{li}, \phi_{ri} \in S^1$ the driving angles of the left and right arms of configuration q_i respectively. For the weights w_p, w_b , and w_a we have chosen the values 1.00/0.448, 0.33, and 0.33 respectively. This metric with the chosen weights promotes exploration of the configuration space where the position of the body is given weight equal to the body arm orientations combined.

The 750,000 nodes were generated with 50 trees of 15,000 nodes each. Additionally,

we placed emphasis on five different positional goals placed on the sampling horizon in quadrant one of the global XY -plane at increments of $\pi/5$ radians; 10 trees of the 50 were assigned to each of the 5 goals where the RRT was run with a 10% bias in expanding nodes chosen closest to the goal. This implementation choice was made to ensure that regions of interest were sufficiently explored.

The sampling results for the four tested configurations are shown in Figure 6.13 as isochronal surfaces in polar coordinates where we have projected the sampled costs in the configuration space into the XY -plane for visual purposes. In this respect, the figures represent the cost of the Adelopod to achieve displacement in the plane where the Y -axis ($\theta = \pi/2$) represents forward motion and the X -axis ($\theta = 0$) lateral motion. In general, projections can be made onto any subset of the configuration space. Due to the symmetry of the robot we are able to transform all of the sampled data into a single quadrant to increase the effective number of samples.

Surprisingly, we observe striking similarities across the observed costs for all four different test configurations. Common to all four surfaces we can see trends in the cost suggesting (as expected) that pure forward locomotion (along the Y -axis) is generally cheaper to achieve than pure lateral motion (along the X -axis). Comparing the surfaces, we see that the friction available at the arms has more of an effect on cost than the arm angles. This can be better observed by comparing parameters of a model fit for each of the surfaces. In choosing an appropriate model, we made the observation that the costs exhibit linear trends along each of the axes with some inverse exponential decay around the origin. Additionally, looking at the data for fixed radii we observe cubic looking curves. With this in mind we have chosen the following model for the results using polar coordinates where the model is comprised of two linear functions with inverse exponential decay and cubic mixing:

$$\begin{aligned} \hat{t}(\rho, \theta) = & \\ & (m_\alpha \rho + b_\alpha) \left(1 - e^{d_\alpha \rho}\right) (a_1 \theta^3 + a_2 \theta^2 + a_3 \theta + 1) + \\ & (m_\beta \rho + b_\beta) \left(1 - e^{d_\beta \rho}\right) (1 - (a_1 \theta^3 + a_2 \theta^2 + a_3 \theta + 1)). \end{aligned} \quad (6.35)$$

Here m_α and m_β are the slopes, b_α and b_β the z -intercepts, and d_α and d_β are the inverse decay rates of the two linear functions; mixing is determined by the cubic with

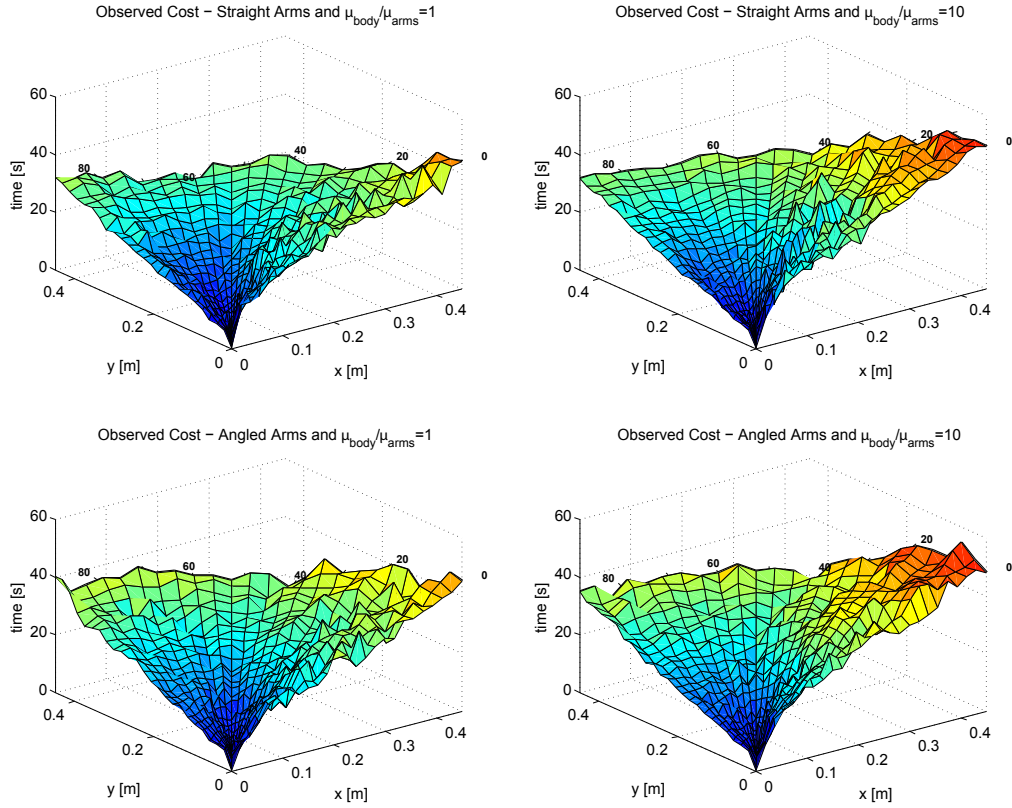


Figure 6.13: Observed minimum costs for XY -displacement with varying arm angles/friction.

parameters a_1 , a_2 , and a_3 . Performing a best fit for the above model on each of the four surfaces results in the parameter values listed in Table 6.3 and the resulting modeled surfaces are shown in Figure 6.15 along with comparisons to the observed data and their contours. Due to the cubic mixing the first (α) term of the chosen model represents pure lateral motion along the X -axis (i.e., $\theta = 0$). The second (β) term of the model represents pure motion along values of θ such that the cubic $(a_1\theta^3 + a_2\theta^2 + a_3\theta + 1) = 0$.

For direct comparison, we show in Figure 6.14 the modeled cost versus θ for several fixed values of ρ . In the figure, the arm friction is designated by the line style (dashed lines have $\mu_{rel} = \mu_{body}/\mu_{arms} = 10$ and solid lines have $\mu_{arms} = \mu_{body}$) while the shoulder angles by the line color (red for angled arms and blue for straight arms). Here

Table 6.3: Table of Best Fit Parameters for Equation (6.35)

	m_α	b_α	d_α	m_β	b_β	d_β	a_1	a_2	a_3
Str., $\mu_{\text{rel}} = 1$	36.98	23.07	-29.78	52.59	7.69	-267	1.36	-2.10	-0.56
Str., $\mu_{\text{rel}} = 10$	73.95	17.66	-53.15	61.28	6.21	-10834	0.83	-1.43	-0.45
Ang., $\mu_{\text{rel}} = 1$	58.24	17.01	-27.39	65.24	6.58	-190	1.31	-1.80	-0.86
Ang., $\mu_{\text{rel}} = 10$	66.11	21.69	-24.07	65.72	5.87	-1261	1.04	-1.91	-0.16

we see further evidence that the frictional coefficients at the arms have greater effect than the angle of the shoulders. This is represented by the similarities between the respective curves. For ρ very small (i.e., 0.05) we can see that the costs are all very similar; as ρ increases however the models begin to diverge with the equivalent arm angle configurations exhibiting similar shape differing mainly in magnitude. For angled arms we see less effect of arm friction on the cost than with the straight arms. Surprisingly, the best performing model was the straight arms with $\mu_{\text{arms}} = \mu_{\text{body}}$.

In conclusion, our results suggest that straight arms do not exhibit any significant maneuverability penalties compared with angled arms over smooth terrain. This surprising result suggests that, despite the lack of existence, straight arm configurations of serial multiply-actuated tumbling robots provide a feasible design choice. This conclusion is further strengthened when the results of the previous chapter regarding terrainability are taken into account. One issue to note, however, was that the simulation used in generating the above results assumed sufficient torque in the robot's actuators to generate motion. In practice we have observed several cases with the Adelopod in combination with the ruggedized shell (high body friction) where the motors could not generate sufficient torque for some input trajectories.

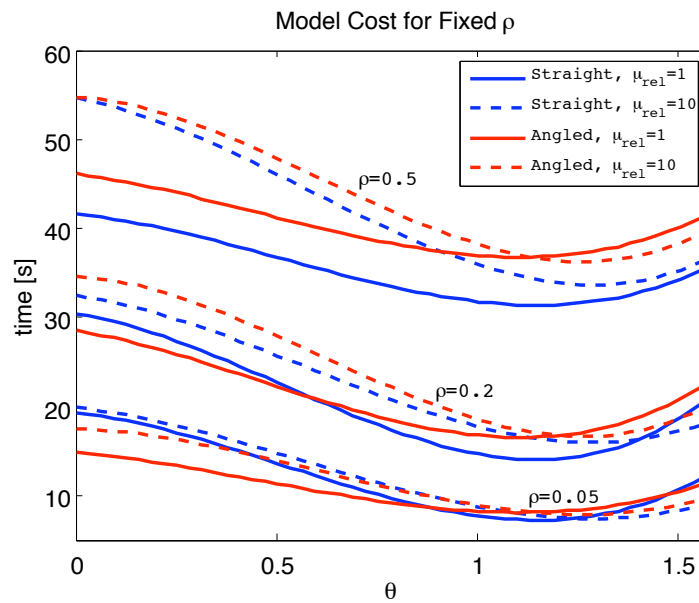


Figure 6.14: Modeled cost versus heading for the four tested Adelopod configurations for $\rho = 0.05, 0.2$, and 0.5 .

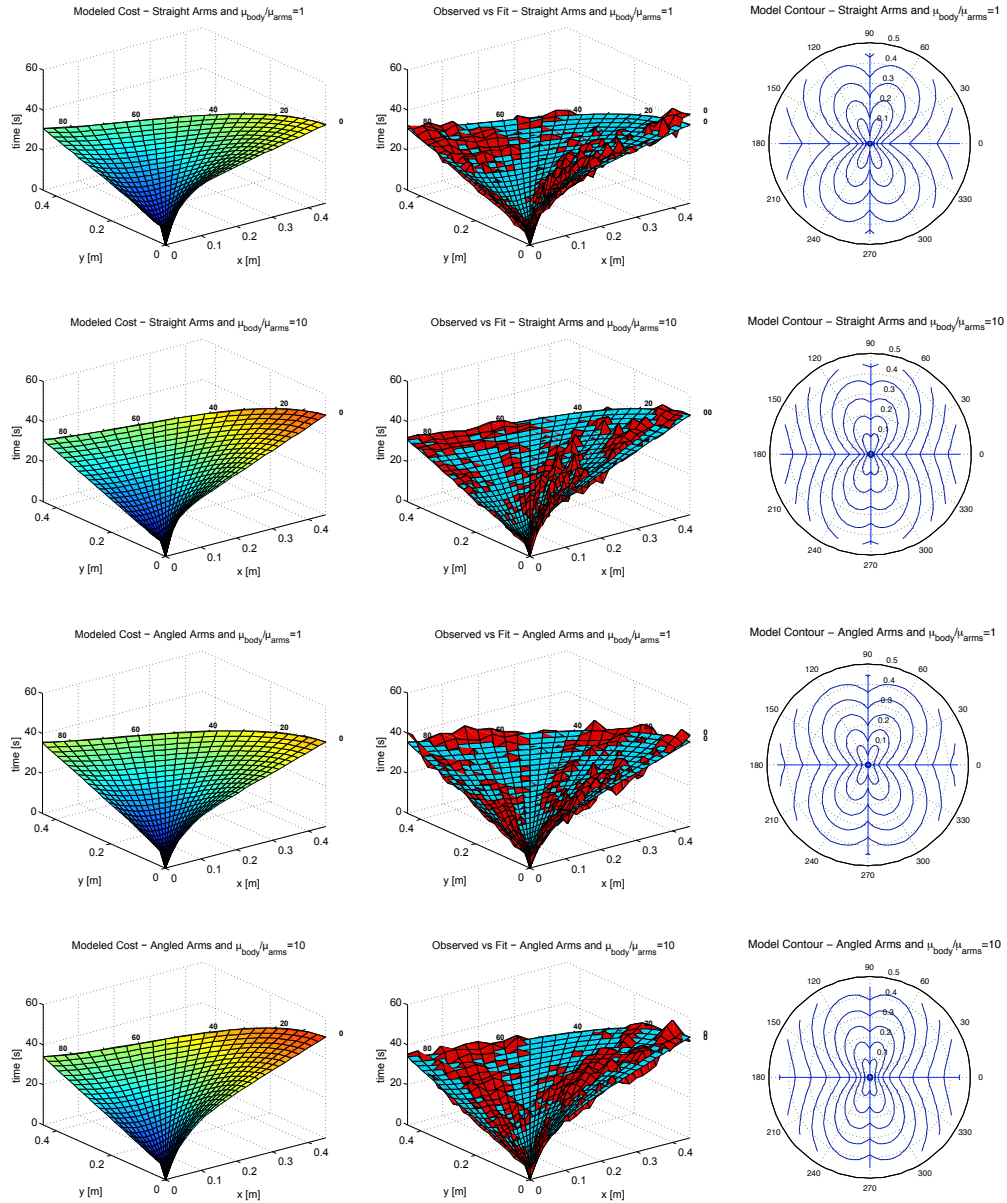


Figure 6.15: Resultant fits from least squares fit from model of Equation...

6.8 Distance Metrics for Serial Multiply-actuated Tumbling

Perhaps more interesting than the above evaluation of arm angles and friction are the actual surfaces produced by the isochronal analysis. These surfaces depict the approximate minimum (optimal) cost-to-go between configurations. In this respect, they naturally encapsulate the notion of distance between configurations and thus make an ideal bases for formulating meaningful distance metrics. Using this observation, we have had good success with using models of the isochronal surfaces as distance metrics for the above outlined motion planning algorithms (as a heuristic for A^* over motion primitives and as the distance metric used for nearest neighbor calculations for the RRT algorithm). Details and results of this method applied to the Adelopod are presented below.

6.8.1 Metric Results Applied to RRT's

In this experiment we test performance of several distance metrics for use with common motion planning problems. Specifically we evaluate performance using the Adelopod tumbling robot with the RRT algorithm described in Section 6.4. A total of four metrics are considered, three are derived from the isochronal surface generation and the fourth chosen as the weighted Euclidean metric to serve as the control. In an attempt to gain insight into the scaling of metrics produced with our isochronal technique, we evaluate the performance of three isochronal distance metrics based on data taken over three different horizons; the horizons (corresponding to approximately one, two, and six major tumbles of the Adelopod in its forward direction) have distances of 0.224, 0.448, and 1.5 meters. We refer to the metrics corresponding to each horizon as $d_{\text{iso}_{r224}}$, $d_{\text{iso}_{r448}}$, and $d_{\text{iso}_{r1.5}}$ respectively; the weighted Euclidean control is referred to by d_{we} .

Metric Formulation

The data used for producing the isochronal metrics was collected in a manner similar to that used in the previous section. For each metric we generated a total of 750,000 samples within the respective horizon using RRTs. A single RRT was expanded until it contained 15,000 nodes. Ten trees were created for each of five goal locations placed at the horizon at angles of $0, \pi/8, \pi/4, 3\pi/8,$ and $\pi/2$ measured from the global

X -axis. The robot's initial configuration for each run was centered at the origin with the body and both arms vertical and its sagittal plane oriented with the global Y -axis (described as (dot, dot, dot) with the notation of Section 6.2). With this setup, goal 1 ($\theta = 0$) corresponds to pure lateral motion while goal 5 ($\theta = \pi/2$) corresponds to pure forward motion.

For modeling the isochronal data we have again chosen the cubic mixed linear model of Equation (6.35) applied to the binned data projected into polar coordinates over the global XY -plane. The number of bins was chosen to be 25 along both θ and ρ . The resulting parameters from the fit are displayed in Table 6.4 and the resulting surfaces and contours for each of the three isochronal metrics are shown in Figure 6.16. The final metrics used for planning are

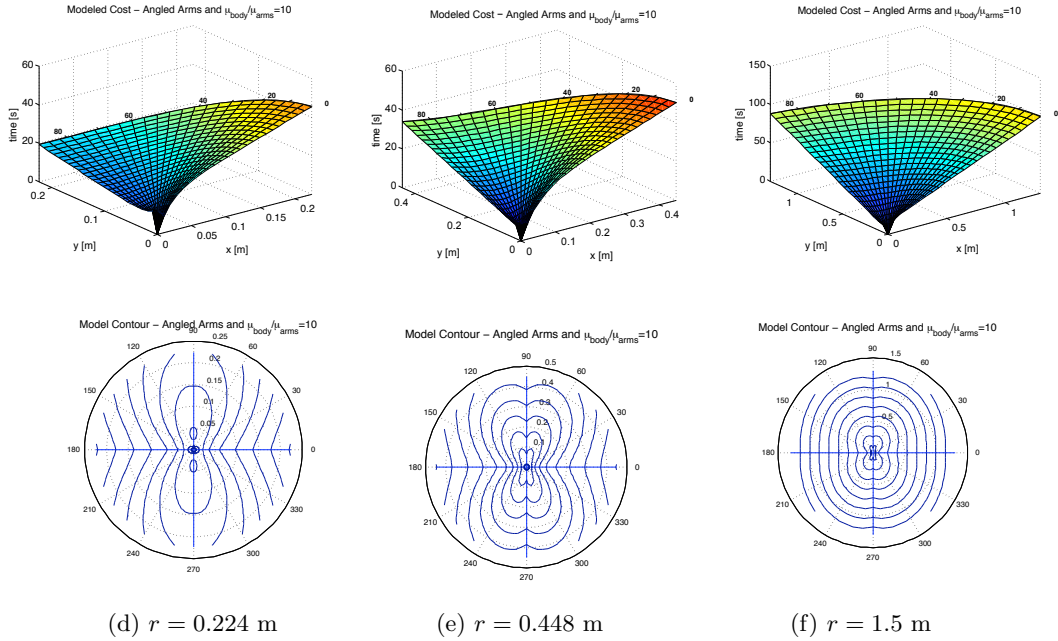
$$d_{iso}(q_1, q_2) = w_p \hat{t}(\rho, \theta) + (w_a/4) (2 - \cos(\phi_{l1} - \phi_{l2}) - \cos(\phi_{r1} - \phi_{r2}))^2, \quad (6.36)$$

$$d_{we}(q_1, q_2) = w_p \|p_1 - p_2\|^2 + w_b (1 - |h_1 \cdot h_2|)^2 + (w_a/4) (2 - \cos(\phi_{l1} - \phi_{l2}) - \cos(\phi_{r1} - \phi_{r2}))^2, \quad (6.37)$$

for the isomorphic and weighted Euclidean metrics respectively. The approximate costs returned by $\hat{t}(\rho, \theta)$ (Equation (6.35)) represent distances between relative body configurations and thus replace the $w_{q_{body}}$ term of the weighted Euclidean metric. For a fair comparison we reassign this weight to the positional term of the isochronal metrics to assign equal importance the body configuration for each type of metric. Because the isochronal surfaces only capture the distance between body configurations, it is necessary to maintain the arm position terms from the weighted Euclidean metric. Additionally, all w_p terms are normalized for a horizon of 0.448 meters; with the selected weights, each metric produces values within equivalent intervals.

Table 6.4: Parameters for RRT Metric Evaluation

	d_{we}	$d_{iso_{r,224}}$	$d_{iso_{r,488}}$	$d_{iso_{r,1.5}}$
w_p	$\frac{1.00}{0.448}$	$\frac{1.33}{0.448m_\alpha + b_\alpha}$	$\frac{1.33}{0.448m_\alpha + b_\alpha}$	$\frac{1.33}{0.448m_\alpha + b_\alpha}$
$w_{q_{body}}$	0.33	—	—	—
$w_{q_{arms}}$	0.66	0.66	0.66	0.66
m_α	—	125.3	66.11	68.07
b_α	—	18.5	21.69	14.81
d_α	—	-60	-24.07	-49
m_β	—	76.6	65.72	67.65
b_β	—	9.8	5.87	10.09
d_β	—	-10000	-1261	-10000
a_1	—	0.71	1.04	2.63
a_2	—	-1.45	-1.91	-4.70
a_3	—	-0.32	-0.16	-0.37

Figure 6.16: Modeled costs of displacement based on data collected over horizons of $r = 0.224, 0.448,$ and 1.5 meters.

Metric Evaluation

Each of the metrics was applied to 10 different motion planning tasks involving moving from the starting configuration to within 0.08 meters. Tasks were created systematically by placing the goal at either 0.33 or 1.125 meters from the origin at angles of $0, \pi/8, \pi/4, 3\pi/8$, and $\pi/2$, measured from the global X -axis. The distances of 0.33 and 1.125 correspond to the planning horizons of 0.448 and 1.5 meters and were arbitrarily chosen as 0.75 times the horizon to enable sufficient reach of the planner. For each task the RRT planner was run until a solution was found; each run resulted in the total number of nodes expanded by the planner as well as the cost in seconds of the final selected trajectory being recorded. For the experiment we used two different goal biases, 10% and 50%, for the RRT where the 10% bias was run over all 10 tasks and the 50% bias only for the tasks with the goal positioned at 1.125 meters from the horizon.

The results are shown graphically in Figure 6.17 where we plot the mean expanded nodes and cost for all 15 experiments along with their standard deviations in the form of error bars. The data corresponding to the isochronal metrics derived over 0.224, 0.448, and 1.5 meters are shown in green, red, and cyan with the data points marked with triangles, squares, and diamonds respectively; the weighted Euclidean metric results are shown in dark blue with circular markers. Immediately obvious is the general poor performance of d_{we} with respect to the other three metrics. Looking at the results pertaining to expanded nodes, we can see that the isochronal metrics on average result in about half the expanded nodes of the planner run using the weighted Euclidean metric. Of particular interest is the plot of Figure 6.17(a) showing the mean expanded nodes over a 0.448 meter horizon (goals at 0.33 meters from the origin) with a 10% RRT goal bias. Here we can see markedly different performances between the isochronal and Euclidean metrics for goals 1, 2, and 3 ($\theta = 0, \pi/4$, and $\pi/2$) while for goals four and five the performance with all four metrics was observed to be equivalent. This is interesting in that it captures for the smaller horizon the importance of considering sagittal plane orientation within the distance metric for Adelopod-like tumbling robots. At the horizon of 0.448 meters, goals straight ahead are relatively easy for both types of metrics while the laterally placed goals are much more difficult for the Euclidean approach.

As the horizon is increased to 1.5 meters, we observe a more consistent difference in the observed number of expanded nodes for all the metrics for all goals; we believe that

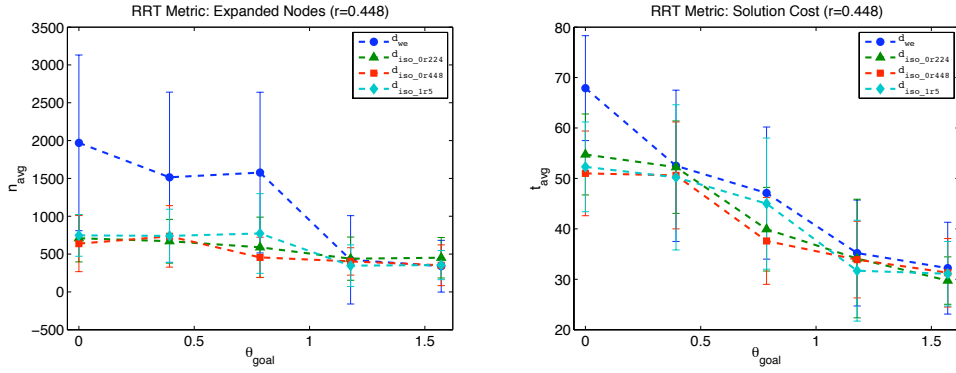
this difference is due to the increase in required trajectory length to reach the goal for the increased horizon; for these longer trajectories, the robot must execute at least twice as many major tumbles and is more likely to exhibit some heading deflection (due to the randomness inherent to the RRT algorithm). These deflections are more difficult to correct for the Euclidean metric and thus poorer performance is observed. Additional support for this claim can be found by visually examining the trees produced using each type of metric. In Appendix E we show a compilation of various selected trees resulting from running the RRT planner with both the d_{we} and $d_{iso0r448}$ metrics. In selecting trees to include, we have been careful to try and select a set representing both the best and worst case performance for each of the distance metrics. The above described difficulty in heading corrections is apparent in comparing the curvatures of trajectories resulting from each type of metric.

One issue of concern for the above conclusions are the large standard deviations that might lead one to question the significance of the results. Testing the hypothesis that the isochronal metrics produce better mean performance in the number of expanded nodes than that of the weighted Euclidean, we conducted significance tests using a two-tailed Students t-test assuming unequal variances. The results show that the observed means exhibit a significant difference with $p < 0.05$ for all horizons and goals except for the aforementioned cases with $r = 0.448$, goals 4 and 5; and for the mean difference between d_{we} and $d_{iso0r224}$ for $r = 1.5$ over goal 2 (for this one case we have $p < 0.058$).

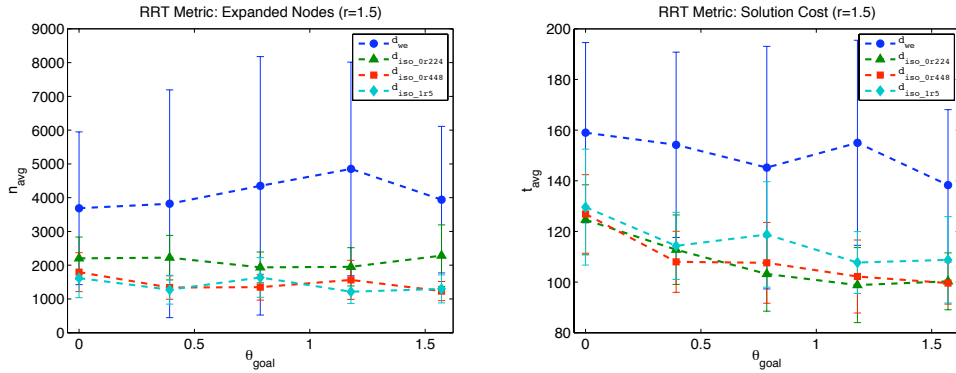
Comparing the relative differences between performance concerning the three isochronal metrics, we see significantly less difference. In general $d_{iso0r448}$ and d_{iso1r5} perform similarly while $d_{iso0r224}$ shows slightly worse performance for the increased horizon experiments of $r = 1.5$ meters. We believe that this is due mainly to scaling issues. Looking at the modeled slopes m_α and m_β we can see for the $d_{iso0r224}$ the slopes are different while for $d_{iso0r448}$ and d_{iso1r5} we see that $m_\alpha \simeq m_\beta$. In general, for $m_\alpha \neq m_\beta$, we see increased importance placed on orientation as the positional difference between to compared configurations increases and the slopes of Equation 6.35 dominate. In contrast, for $m_\alpha = m_\beta$, as the positional difference between to compared configurations increases, the slopes grow equally with the cost difference coming only from the difference in intercepts of each linear term. From a practical viewpoint, this suggests that the relative parameters from the model fits reflect the appropriateness of the chosen

sampling horizon when generating the isochronal surfaces. In the case of the Adelopod, a sufficient horizon is achieved when we see the best fit exhibit $m_\alpha \simeq m_\beta$.

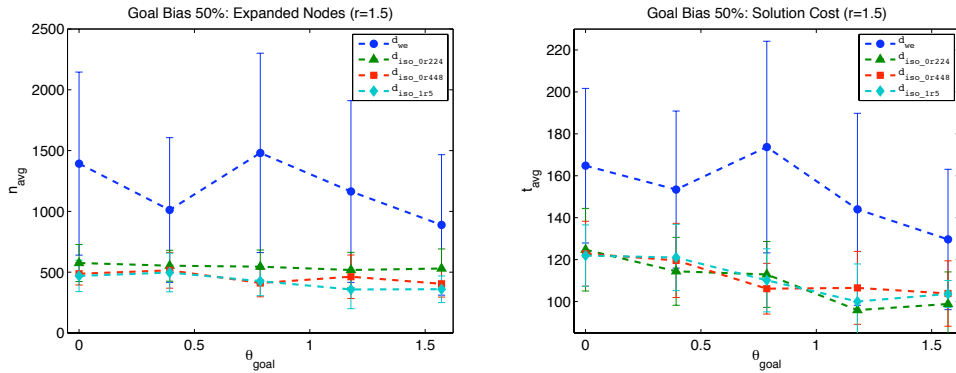
In addition to considering the number of expanded nodes, we also considered the cost of the returned solution paths measured in seconds. Again we see marked performance differences between the weighted Euclidean and isochronal metrics. Testing significance we found that the average cost differences for $r = 0.244$ meters were in general not significant, however, for all runs of $r = 1.5$ meters we found that the average cost differences between the Euclidean and isochronal metrics to be significant for all goal locations with $p < 0.05$. Cost performance between the isochronal metrics was similar with a majority of the results lacking significance with respect to their differences in mean trajectory cost.



(a) $r = 0.448$ m; 10% Goal Bias



(b) $r = 1.5$ m; 10% Goal Bias



(c) $r = 1.5$ m; 50% Goal Bias

Figure 6.17: RRT planner results comparing relative performance of weighted Euclidean and isochronal tumbling distance metrics.

6.9 Final Thoughts on Maneuverability and Planning

Planning for tumbling robots is in general a difficult problem. For the case of serial multiply-actuated tumbling, issues consist of motion constraints due to underactuation and the resulting nonholonomy of the systems. In this chapter we presented several motion planning approaches in respect to this particular class of tumbling. Most applicable to real-world tumbling robots such as the Adelopod was shown to be the randomized planner based on the utilization of rapidly exploring random trees to quickly explore the configuration space while satisfying any motion constraints. We showed experimental results for this planner stressing the importance of an intelligently selected distance metric. Generally, for systems with sufficient actuation (and thus minimal motion constraints) a simple Euclidean approximation of distance between configurations provides satisfactory planning results. For tumbling systems, however, such metrics provide generally poor performance with large variations between runs.

Design of perfect metrics is as difficult as the original motion planning problem. In this chapter we motivated the use of isochronal contours to examine maneuverability characteristics of mobile robots. Additionally we proposed the use of such surfaces to aid in developing good metrics for planning. Actual metrics were derived for the Adelopod robot over various horizons and their quality evaluated experimentally. When compared with the naive Euclidean metrics, performance increased were observed for both the average number of expanded nodes and cost of the final selected path. On average, our metrics derived from the isochronal contours expanded only half as many nodes when compared with the Euclidean metric.

Chapter 7

Summary

This research brings to light a new method of mobile robot locomotion called tumbling that leverages tumbling body motions and terrain-body interactions. Through the full utilization of these previously avoided methods, tumbling is able to provide the potential to produce highly mobile systems for little in terms of overall size and/or required hardware. Interestingly, we have found that many of the same properties responsible for the aforementioned attractive qualities of tumbling are also responsible for many of the issues that complicate practical implementations of such systems. This research, in establishing the foundations of tumbling, has identified and begun to address many of these issues with focus on terrainability, maneuverability, and planning for the class of serial multiply-actuated tumbling.

We have applied many of our analysis and methods to two prototype tumbling robots developed as part of this work, the Adelopod and Adelopod-T. A major portion of this work is dedicated to establishing performance benchmarks with respect to the terrainability of tumbling robots. This is achieved using our developed robots over a variety of repeatable terrains. These benchmarks provide the first published data regarding the capabilities of such systems and, in addition to demonstrating the capabilities of tumbling, provide a basis for future evaluation of tumbling designs.

In addition to establishing performance benchmarks, we have looked into issues regarding planning for tumbling robots. The methods presented in this work enable planning of feasible open-loop trajectories for a class of tumbling robots within the

accuracy of their respective motion models. Even with good motion models, the characteristics common to ideal tumbling terrain result in rapid accumulation of error in the executed planned trajectories. Because of this, as well as the general inability to effectively track arbitrary trajectories due to significant motion constraints, frequent replanning is necessary in achieving useful motion. To address these issues we have developed a novel method of creating useful distance metrics that result in significant speedup for any heuristic planning that brings tumbling closer to the realm of practical use.

Other advancements made regarding practical application of tumbling include the design of the Adelopod-T which provides differential drive capabilities in addition to tumbling, greatly relaxing the planning requirements.

7.1 Contributions

The following are the main contributions of this thesis:

- Develops definitions and identifies basic principles of tumbling locomotion. These definitions are the first of their kind and establish a framework for future work pertaining to robotic tumbling.
- Presents classification of tumbling robots based on identified fundamental properties of tumbling robots.
- Establishes the state of the art by assembling a catalog of existing tumbling robots.
- Demonstrates theoretical advantages of tumbling robots through quasi-static terrainability analysis of planar tumbling morphologies over idealized obstacles.
- Provides electrical and mechanical designs for a serial multiply-actuated tumbling robot, the Adelopod. All hardware designs and electrical schematics are available as open source.
- Extends state of the art tumbling designs through the incorporation of crawler treads to the Adelopod design. The result is a hybrid tumbling-treaded robot that is capable of multi-modal locomotion using both tumbling and differential drive.

- Demonstrates real-world performance of serial multiply-actuated tumbling through the terrainability analysis of the Adelopod and Adelopod-T using repeatable terrains. Presented results establish performance benchmarks for future comparisons of tumbling locomotion.
- Presents several planning algorithms applicable to tumbling locomotion.
- Formulates method of deriving meaningful distance metrics for tumbling applicable to other systems with nonholonomic motion constraints. Performance benefits of derived metrics are evaluated using the Adelopod tumbling robot.

While we have focused primarily on the class of serial multiply-actuated tumbling robots, many of the ideas explored within this work are applicable to other classes of tumbling locomotion.

7.2 Future Work Directions

While we have made significant strides in robotic tumbling locomotion, the area is still in its infancy and thus there remains a multitude of avenues still left open for exploration. Tumbling locomotion provides a new way of looking at mobile robots. As such it provides a new platform for application and study many of the existing ideas within the field of robot locomotion including design, sensing, localization, control, planning, etc.

Due to scope issues, this work has focused on the particular class of serial multiply-actuated tumbling. Other classes of tumbling, specifically composite-bodied tumbling, contain many interesting ideas still left to explore. Although there are a few existing works in this area, we believe that the full potential of such robots has yet to be identified. More importantly, however, this work would greatly benefit from the resolution of issues currently complicating the practical application of tumbling in scenarios of complex and dynamic terrain. In this respect we believe the following issues are of primary interest to the future of tumbling locomotion.

- Trafficability analysis of tumbling — In this work we have examined the terrainability and maneuverability of a class of tumbling. Performance regarding sinkage, drawbar pull, and gradeability over loose soil has yet to be identified.

- In-depth study of tumbling dynamics with emphasis on producing accurate models of tumbling over complex terrains — Locomotion for many classes of tumbling requires the use of sliding contacts with the ground resulting in chains of bodies with multiple frictional contacts with the terrain which significantly complicate the problem.
- Local terrain modeling using onboard sensors — Central to the performance of any applied motion model is accurate representation of the terrain. Tumbling relies on interactions between the robot's body and terrain, thus requiring accurate sensing and representation of such.
- Efficient planning for systems that exhibit both continuous and discrete dynamics — In general, we have found little work in this area and even less applicable to tumbling. Many of the existing works focus on hybrid systems with controlled switching; for tumbling, however, the discrete changes in system dynamics are autonomous switches and in general are functions of the configuration and terrain. Optimal planning methods for tumbling will have to take such issues into account.
- Implementation of closed-loop tumbling systems — Currently we are able to produce tumbling locomotion in a lab environment, however, we have yet to compile a system capable of exhibiting autonomous directed locomotion over more complicated outdoor terrains. While tumbling provides many interesting problems from a theoretical perspective, we believe that successful practical applications are crucial to its future acceptance as a feasible method of mobile robot locomotion.

References

- [1] M. Yim, D. G. Duff, and K. D. Roufas. Polybot: A modular reconfigurable robot. In *IEEE International Conference on Robotics and Automation*, volume 1, pages 514–520, 2000.
- [2] U. Saranli, M. Buehler, and D. E. Koditschek. Rhex: A simple and highly mobile hexapod robot. *International Journal of Robotics Research*, 20(7):616–631, 2001.
- [3] R. D. Quinn, G. M. Nelson, R. J. Bachmann, D. A. Kingsley, J. Offi, and R. E. Ritzmann. Insect designs for improved mobility. In Berns and Dillmann, editors, *Climbing and Walking Robots Conference*, pages 69–76, 2001.
- [4] U. Scarfogliero, C. Stefanini, and P. Dario. Design and development of the long-jumping ”grillo” mini robot. In *IEEE International Conference on Intelligent Robots and Systems*, pages 467–472, 2007.
- [5] M. Kovac, M. Fuchs, A. Guignard, J.-C. Zufferey, D. Floreano, and S. Hutchinson. A miniature 7g jumping robot. In *IEEE International Conference on Robotics and Automation*, pages 373–378, 2008.
- [6] S. Hirose. *Biologically Inspired Robots: Snake-like Locomotors and Manipulators*. Oxford University Press, 1993.
- [7] C. Paul, F. J. Valero-Cuevas, and H. Lipson. Design and control of tensegrity robots for locomotion. *IEEE Transactions on Robotics*, 22(5):944–957, 2006.
- [8] M. W. Tilden. Nervous networks and the architecture of ”living” machines. Goddard Scientific Colloquium. http://mediaman.gsfc.nasa.gov/Colloquia_asx/Public/SCI/2001/SCI20010323.asx, March 2001.

- [9] P. E. Clark, M. L. Rilee, S. A. Curtix, W. Truszkowski, G. Marr, C. Cheung, and M. Rudisill. Bees for ants: Space mission applications for the autonomous nanotechnology swarm. *AIAA 1st Intelligent Systems Technical Conference*, 2004.
- [10] B. Hasslacher and M. W. Tilden. Living machines. *Robotics and Autonomous Systems*, 15:143–169, 1995.
- [11] Solarbotics Ltd. The solarbotics turbot tumbling robot. http://www.solarbotics.com/assets/documentation/solarbotics_turbot_kit_feb122008.pdf, February 2008.
- [12] M. G. Bekker. *Theory of Land Locomotion: The Mechanics of Vehicle Mobility*. University of Michigan Press, Ann Arbor, MI, 1956.
- [13] M. G. Bekker. *Off-the-Road Locomotion: Research and Development in Terramechanics*. University of Michigan Press, Ann Arbor, MI, 1960.
- [14] M. G. Bekker. *Introduction to Terrain-vehicle Systems*. University of Michigan Press, Ann Arbor, MI, 1969.
- [15] J. Y. Wong. *Theory of Ground Vehicles*. John Wiley Sons, Inc., Hoboken, NJ, fourth edition, 2008.
- [16] K. Waldron. Mobility and controllability characteristics of mobile robotics platforms. In *Proceedings of the 1985 IEEE International Conference on Robotics and Automation*, pages 237–243, 1985.
- [17] K. J. Waldron. The mechanics of mobile robots. *Robotics*, 2(2):113–121, 1986.
- [18] K. J. Waldron, V. J. Vohnout, A. Pery, and R. B. McGhee. Configuration design of the adaptive suspension vehicle. *International Journal of Robotics Research*, 3(2):37–48, 1984.
- [19] S. M. Song, K. J. Waldron, and G. L. Kinzel. Computer-aided geometric design of legs for a walking vehicle. *Mechanism and Machine Theory*, 20(6):587–596, 1985.
- [20] S. Hirose, N. Ootsukasa, T. Shirasu, H. Kuwahara, and K. Yoneda. Fundamental considerations for the design of a planetary rover. In *Proceedings of the 1995*

-
- IEEE International Conference on Robotics and Automation*, volume 2, pages 1939–1944, September 1995.
- [21] K. R. Lietzau. Mars micro rover performance measurement and testing. Master’s thesis, Massachusetts Institute of Technology, Department of Aeronautics and Astronautics, December 1993.
- [22] D. B. Gennery. Traversability analysis and path planning for a planetary rover. *Autonomous Robots*, 6(2):131–146, 1999.
- [23] H. Seraji. Fuzzy traversability index: A new concept for terrain-based navigation. *Journal of Robotics Systems*, 17(2):75–91, 2000.
- [24] H. Seraji. New traversability indices and traversability grid for integrated sensor/map-based navigation. *Journal of Robotics Systems*, 20(3):121–134, 2003.
- [25] G. Gabrielli and I. von Karman. What price speed? *Mechanical Engineering*, 72(10):775–781, 1950.
- [26] B. McBride, R. Longoria, and E. Krotkov. Measurement and prediction of the off-road mobility of small robotic ground vehicles. In *The 3rd Intelligent Systems Workshop for Performance Metrics*, 2003.
- [27] A. S. Jacoff, A. J. Downs, A. M. Virts, and E. R. Messina. Stepfield pallets: Repeatable terrain for evaluating robot mobility. In *Performance Metrics for Intelligent Systems (PerMIS) Workshop*, pages 29–34, 2008.
- [28] V. Molino, R. Madhavan, E. Messina, A. Downs, S. Balakirsky, and A. Jacoff. Traversability metrics for rough terrain applied to repeatable test methods. In *IEEE International Conference on Intelligent Robots and Systems*, pages 1787–1794, 2007.
- [29] D. Apostolopoulos. Systematic configuration of robotic locomotion. Technical Report CMU-RI-TR-96-30, The Robotics Institute, Carnegie Mellon University, Pittsburgh, PA, July 1996.
- [30] D. S. Apostolopoulos. *Analytical Configuration of Wheeled Robotic Locomotion*. PhD thesis, Carnegie Mellon University, April 2001.

-
- [31] T. Thueer, A. Krebs, R. Siegwart, and P. Lamon. Performance comparison of rough-terrain robots – simulation and hardware. *Journal of Field Robotics*, 24(3):251–271, 2007.
- [32] T. Thueer and R. Siegwart. Mobility evaluation of wheeled all-terrain robots. *Robotics and Autonomous Systems*, (58):508–519, February 2010.
- [33] E. Garcia, J. Estremera, and P. Gonzalez de Santos. A comparative study of stability margins for walking machines. *Robotica*, 20:595–606, 2002.
- [34] P. Gonzalez de Santos, E. Garcia, and J. Estremera. *Quadrupedal Locomotion*. Springer-Verlag, London, 2006.
- [35] R. B. McGhee and A. A. Frank. On the stability properties of quadruped creeping gaits. *Mathematical Bioscience*, 3:331–351, 1968.
- [36] R. B. McGhee and G. I. Iswandhi. Adaptive locomotion for a multilegged robot over rough terrain. *IEEE Transactions on Systems, Man, and Cybernetics*, 9(4):176–182, 1979.
- [37] C. Zhang and S. Song. Stability analysis of wave-crab gaits of a quadruped. *Journal of Robotics Systems*, 7(2):243–276, 1990.
- [38] D. Messuri and C. Klein. Automatic body regulation for maintaining stability of a legged vehicle during rough-terrain locomotion. *IEEE Journal of Robotics and Automation*, 1(3):132–141, 1985.
- [39] S. Hirose, H. Tsukagoshi, and K. Yoneda. Normalized energy stability margin and its contour of walking vehicles on rough terrain. In *IEEE International Conference on Robotics and Automation*, pages 181–186, 2001.
- [40] B.-S. Lin and S.-M. Song. Dynamic modeling, stability and energy efficiency of a quadrupedal walking machine. In *IEEE International Conference on Robotics and Automation*, volume 3, pages 367–373, 1993.
- [41] E. G. Papadopoulos and D. A. Rey. A new measure of tipover stability margin for mobile manipulators. In *IEEE International Conference on Robotics and Automation*, pages 3111–3116, 1996.

-
- [42] D. Orin. *Interactive Control of a Six-legged Vehicle with Optimization of Both Stability and Energy*. PhD thesis, Ohio State University, 1976.
- [43] D.-O. Kang, Y.-J. Lee, S.-H. Lee, Y. S. Hong, and Z. Bien. A study on an adaptive gait for a quadruped walking robot under external forces. In *IEEE International Conference on Robotics and Automation*, volume 4, pages 2777–2782, 1997.
- [44] P. Gonzalez de Santos, J. Estremera, E. Garcia, and M. Armada. Including joint torques and power consumption in the stability margin of walking robots. *Autonomous Robots*, 18(1):43–57, 2005.
- [45] A. Ghasempoor and N. Sepehri. A measure of machine stability for moving base manipulators. In *IEEE International Conference on Robotics and Automation*, volume 3, pages 2249–2254, 1995.
- [46] J. P. Laumond. Singularities and topological aspects in nonholonomic motion planning. In Zexiang Li and J. F. Canny, editors, *Nonholonomic Motion Planning*, The Kluwer International Series in Engineering and Computer Science. Kluwer Academic Publishers, 1992.
- [47] H. J. Sussmann and V. Jurdjevic. Controllability of nonlinear systems. *Journal of Differential Equations*, 12:95–116, 1972.
- [48] Z. Li, J. Canny, and G. Heinzinger. Robot motion planning with nonholonomic constraints. In Hirofumi Miura and Suguru Arimoto, editors, *Robotics Research: The Fifth International Symposium*, pages 309–316, 1990.
- [49] J.-P. Laumond and J.-J. Risler. Nonholonomic systems: Controllability and complexity. *Theoretical Computer Science*, 157:101–114, 1996.
- [50] J. P. Laumond. Feasible trajectories for mobile robots with kinematic and environment constraints. In *International Conference on Intelligent Autonomous Systems*, pages 346–354, 1986.
- [51] J.-P. Laumond. Controllability of a multibody mobile robot. *IEEE Transactions on Robotics and Automation*, 9(6):755–763, 1993.

-
- [52] G. Lafferriere and H. J. Sussmann. Motion planning for controllable systems without drift. In *IEEE International Conference on Robotics and Automation*, pages 1148–1153, 1991.
- [53] J. Barraquand and J. C. Latombe. Nonholonomic multibody mobile robots: Controllability and motion planning in the presence of obstacles. *Algorithmica*, 10(2–4):121–155, October 1993.
- [54] R. M. Murray and S. S. Sastry. Nonholonomic motion planning: Steering using sinusoids. *IEEE Transactions on Automatic Control*, 38(5):700–716, 1993.
- [55] Y. Aiyama, M. Inaba, and H. Inoue. Pivoting: A new method of graspless manipulation of object by robot fingers. In *IEEE International Conference on Intelligent Robots and Systems*, pages 136–143, 1993.
- [56] M. Erdmann, M. T. Mason, and G. Vanecek. Mechanical parts orienting: The case of a polyhedron on a table. *Algorithmica*, 10:226–247, 1993.
- [57] A. Marigo, Y. Chitour, and A. Bicchi. Manipulation of polyhedral parts by rolling. In *IEEE International Conference on Robotics and Automation*, pages 2992–2997, 1997.
- [58] A. Marigo, M. Ceccarelli, S. Piccinocchi, and A. Bicchi. Planning motions of polyhedral parts by rolling. *Algorithmica*, 26:560–576, 2000.
- [59] A. Bicchi, A. Marigo, and B. Piccoli. On the reachability of quantized control systems. *IEEE Transactions on Automatic Control*, 47(4):546–563, 2002.
- [60] A. Bicchi, Y. Chitour, and A. Marigo. Reachability and steering of rolling polyhedra: A case study in discrete nonholonomy. *IEEE Transactions on Automatic Control*, 49(5):710–726, 2004.
- [61] A. Bicchi, A. Marigo, and B. Piccoli. Discrete and hybrid nonholonomy. In R. Alur and G. Pappas, editors, *Hybrid Systems: Computation and Control*, volume 2993 of *LNCS*, pages 157–172, Berlin Heidelberg, 2004. Springer-Verlag.

-
- [62] P. Gonzalez de Santos, M. A. Jimenez, and M. A. Armada. Dynamic effects in statically stable walking machines. *Journal of Intelligent and Robotics Systems*, 23(1):71–85, 1998.
- [63] *The Oxford English Dictionary*. “body, n., V.17.b”. Oxford University Press, third edition, 2010.
- [64] *The Oxford English Dictionary*. “body, n., II.5”. Oxford University Press, third edition, 2010.
- [65] R. Hodoshima, Y. Fukumura, H. Amano, and S. Hirose. Development of track-changeable quadruped walking robot TITAN X - design of leg driving mechanism and basic experiment -. In *Proceedings of the 2010 IEEE/RSJ International Conference on Intelligent Robots and Systems*, pages 3340–3345, Taipei, Taiwan, October 2010.
- [66] P. Bartlett, D. Wettergreen, and W. L. Whittaker. Design of the scarab rover for mobility and drilling in the lunar cold traps. In *International Symposium on Artificial Intelligence, Robotics, and Automation in Space (iSAIRAS)*, 2008.
- [67] M. Yim. *Locomotion with a Unit-modular Reconfigurable Robot*. PhD thesis, Stanford University, December 1994.
- [68] R. Armour and J. Vincent. Rolling in nature and robotics: A review. *Journal of Bionic Engineering*, 3(4):195–208, 2006.
- [69] J. Suomela and T. Ylikorpi. Ball-shaped robots: An historical overview and recent developments at tkk. In Peter Corke and Salah Sukkariah, editors, *Field and Service Robotics, STAR*, volume 25, pages 343–354. Springer, Berlin, 2006.
- [70] R. Mukherjee, M. A. Minor, and J. T. Pukrushpan. Simple motion planning strategies for Spherobot: A spherical mobile robot. In *Proceedings of the 38th IEEE Conference on Decision and Control*, pages 2132–2137, Phoenix, Arizona, December 1999.
- [71] A. Homayoun A. Javadi and P. Mojabi. Introducing August: A novel strategy for

- an omnidirectional spherical rolling robot. In *Proceedings of the 2002 IEEE International Conference on Robotics and Automation*, pages 3527–3533, Washington, DC, May 2002.
- [72] A. Homayoun A. Javadi and P. Mojabi. Introducing Glory: A novel strategy for an omnidirectional spherical rolling. *Journal of Dynamic Systems, Measurement, and Control*, 126(3):678–683, September 2004.
- [73] R. Mukherjee, M. A. Minor, and J. T. Pukrushpan. Motion planning for a spherical mobile robot: Revisiting the classical ball-plate problem. *Journal of Dynamic Systems, Measurement, and Control*, 124(4):502–511, December 2002.
- [74] T. Das and R. Mukherjee. Reconfiguration of a rolling sphere: A problem in evolute-involute geometry. *Journal of Applied Mechanics*, 73(4):590–597, July 2006.
- [75] T. Yohimitsu, I. Nakatani, and T. Kubota. New mobility system for small planetary body exploration. In *Proceedings of the 1999 IEEE International Conference on Robotics and Automation*, pages 1404–1409, 1999.
- [76] J. Antol, P. Calhoun, J. Flick, G. Hajos, R. Kolacinski, D. Menton, R. Owens, and J. Parker. Low cost mars surface exploration: The mars tumbleweed. Technical Report NASA/TM-2003, NASA, 2003.
- [77] A. Behar, J. Matthews, F. Carsey, and J. Jones. NASA/JPL tumbleweed polar rover. In *Proceedings of the 2004 IEEE Aerospace Conference*, pages 389–395, 2004.
- [78] L. Southard, T. M. Hoeg, D. W. Palmer, J. Antol, R. M. Kolacinski, and R. D. Quinn. Exploring Mars using a group of tumbleweed rovers. In *Proceedings of the 2007 IEEE International Conference on Robotics and Automation*, pages 775–780, Roma, Italy, April 2007.
- [79] J. R. Frigo and M. W. Tilden. Analog neural network control method proposed for use in a backup satellite control mode. In *SPIEs International Symposium on Intelligent Systems and Advanced Manufacturing*, 1998.

- [80] K. R. Moore, J. R. Frigo, and M. W. Tilden. A novel microsatellite control system. In *International Symposium on Engineering of Intelligent Systems*, 1998.
- [81] V. C. Beiu, J. R. Frigo, and K. R. Moore. On the reliability of the nervous (nv) nets. In *Computational Intelligence for Modelling Control and Automation*, February 1999.
- [82] B. Hemes, D. Fehr, and N. Papanikolopoulos. Motion primitives for a tumbling robot. In *IEEE International Conference on Intelligent Robots and Systems*, 2008.
- [83] B. Hemes, N. Papanikolopoulos, and B. O'Brien. The Adelopod tumbling robot. In *IEEE International Conference on Robotics and Automation*, 2009.
- [84] A. Carlson and N. Papanikolopoulos. Aquapod: Prototype design of an amphibious tumbling robot. In *Proceedings of the 2010 IEEE/RSJ International Conference on Robotics and Automation (to appear)*, 2010.
- [85] NASA ANTS Project. Tet walker motion. http://ants.gsfc.nasa.gov/features/4tet_1an.mov, April 2011.
- [86] NASA ANTS Project. 12 tet rover beyond the basics. http://ants.gsfc.nasa.gov/features/12tet_totalact_medium.mov, April 2011.
- [87] M. Abrahantes, A. Silvert, and L. Wendtt. Gait design and modeling of a 12-tetrahedron walker robot. In *2007 Thirty-Ninth Southeastern Symposium on System Theory*, pages 21–25, March 2007.
- [88] M. Abrahantes, D. Littio, A. Silver, and L. Wendt. Modeling and gait design of a 4-tetrahedron walker robot. In *40th Southeastern Symposium on System Theory*, pages 269–273, 2008.
- [89] M. Abrahantes, P. Doorn, J. Richard, and S. Barbachyn. Implementation and control of a reconfigurable 4-tetrahedral robot. In *41st Southeastern Symposium on System Theory*, pages 344–349, 2009.
- [90] M. Izadi, M. J. Mahjoob, M. Soheilypour, and H. Vahid-Alizadeh. A motion planning for toppling-motion of a tet walker. In *Proceedings of the 2nd International Conference on Computer and Automation Engineering*, pages 34–39, 2010.

-
- [91] A. Mozeika, E. Steltz, and H. M. Jaeger. The first steps of a robot based on jamming skin enabled locomotion. In *Proceedings of the 2009 IEEE/RSJ International Conference on Intelligent Robots and Systems*, pages 408–409, 2009.
- [92] E. Steltz, A. Mozeika, N. Rodenberg, E. Brown, and H. M. Jaeger. Jsel: Jamming skin enabled locomotion. In *IEEE/RSJ International Conference on Intelligent Robots and Systems*, pages 5672–5677, 2009.
- [93] Y. Sugiyama and S. Hirai. Crawling and jumping by a deformable soft robot. In *Proceedings of the 2004 IEEE/RSJ International Conference on Intelligent Robots and Systems*, pages 3276–3281, Sendai, Japan, October 2004.
- [94] Y. Sugiyama, A. Shiotsu, M. Yamanaka, and S. Hirai. Circular/spherical robots for crawling and jumping. In *IEEE International Conference on Robotics and Automation*, volume 3595–3600, Barcelona, Spain, April 2005.
- [95] Y. Sugiyama and S. Hirai. Crawling and jumping by a deformable robot. *International Journal of Robotics Research*, 25(5-6):603–620, May-June 2006.
- [96] A. Kangi. Wormsphere rover pattern for discovering underground water on mars’ surface. *Journal of the British Interplanetary Society*, 57(9/10):298–300, 2004.
- [97] B. Hemes, D. Canelon, J. Dancs, and N. Papanikolopoulos. Robotic tumbling locomotion. In *IEEE International Conference on Robotics and Automation (to appear)*, 2011.
- [98] B. Kratochvil, I. T. Burt, A. Drenner, D. Goerke, B. Jackson, C. McMillen, C. Olson, N. Papanikolopoulos, A. Pfeifer, S. A. Stoeter, K. Stubbs, and D. Waletzko. Heterogeneous implementation of an adaptive robotic sensing team. In *Proceedings of the 2003 International Conference on Robotics and Automation*, pages 4264–4269, May 2003.
- [99] D. E. Stewart. Rigid-body dynamics with friction and impact. *SIAM Review*, 42(1):3–39, January 2000.
- [100] J. C. Trinkle, J.-S. Pang, S. Sudarsky, and G. Lo. On dynamic multi-rigid-body

- contact problems with coulomb friction. *Z. Angew. Math. Mech.*, 77(4):267–279, 1997.
- [101] D. E. Stewart and J. C. Trinkle. An implicit time-stepping scheme for rigid body dynamics with inelastic collisions and coulomb friction. *International Journal for Numerical Methods in Engineering*, 39:2673–2691, 1996.
- [102] J.-S. Pang and J. C. Trinkle. Complementarity formulations and existence of solutions of dynamic multi-rigid-body contact problems with coulomb friction. *Mathematical Programming*, 73(2):199–226, 1996.
- [103] Box2D Physics Engine. <http://box2d.org/> [Last accessed: April 2011].
- [104] R. Smith. Open dynamics engine. <http://www.ode.org> [Last accessed: April 2011].
- [105] B. Nguyen and J. C. Trinkle. dVC3d: A three dimensional physical simulation tool for rigid bodies with contacts and Coulomb friction. In *Proceedings of the 1st Joint International Conference on Multibody System Dynamics (to appear)*, 2010.
- [106] A. J. van der Schaft and J. M. Schuacher. *An Introduction to Hybrid Dynamical Systems*. Springer-Verlag, London, 2000.
- [107] J. C. Latombe. *Robot Motion Planning*. Kluwer Publishing Co., 1991.
- [108] J. Denavit and R. S. Hartenberg. A kinematic notation for lower-pair mechanisms based on matrices. *Journal of Applied Mechanics*, pages 215–221, 1955.
- [109] J. J. Craig. *Introduction to Robotics: Mechanics and Control*. Pearson Education, Inc., third edition, 2005.
- [110] *The Oxford English Dictionary*. “mobility, n., 1.a”. Oxford University Press, third edition, 2010.
- [111] T. Thüer. *Mobility Evaluation of Wheeled All-terrain Robots*. PhD thesis, Eidgenössische Technische Hochschule Zürich, Zurich, January 2009.

- [112] A. Krebs, T. Thueer, S. Michaud, and R. Siegwart. Performance optimization of all-terrain robots: A 2d quasi-static tool. In *Proceedings of the 2006 IEEE/RSJ International Conference on Intelligent Robots and Systems*, pages 4266–4271, 2006.
- [113] S. A. Stoeter, P.E. Rybski, K. N. Stubbs, C. P. McMillen, M. Gini, D. F. Hougen, and N. Papanikolopoulos. A robot team for surveillance tasks: Design and architecture. *Robotics and Autonomous Systems*, 40:173–183, 2002.
- [114] Recon Robotics. Recon scout throwbot. <http://www.reconrobotics.com/index.cfm>.
- [115] M. Takahashi, K. Yoneda, and S. Hirose. Rough terrain locomotion of a leg-wheel hybrid quadruped robot. In *IEEE International Conference on Robotics and Automation*, pages 1090–1095, 2006.
- [116] P. Tantichattanon, S. Songschon, and S. Laksanacharoen. Quasi-static analysis of a leg-wheel hybrid vehicle for enhancing stair climbing ability. In *IEEE International Conference on Robotics and Biomimetics*, pages 1601 – 1605, 2007.
- [117] MobileRobots Inc. Pioneer P3-DX. <http://www.mobilerobots.com/researchrobots/researchrobots/pioneerp3dx.aspx> [Last accessed: April 2011].
- [118] P. Gregorio, M. Ahmadi, and M. Buehler. Design, control, and energetics of an electrically actuated legged robot. *IEEE Transactions on Systems, Man, and Cybernetics–Part B: Cybernetics*, 27(4):626–634, 1997.
- [119] iRobot Inc. irobot 110 firstlook. http://www.irobot.com/gi/more_information/irobot_110_firstlook.
- [120] P. E. Rudakevych. *Mobile Robotic Vehicle*. iRobot Corporation, US, June 2010. US 2010/0139995 A1.
- [121] S. M. LaValle. *Planning Algorithms*. Cambridge University Press, New York, NY, 2006.

-
- [122] M. Zefran, J. P. Desai, and V. Kumar. Continuous motion plans for robotic systems with changing dynamic behavior. In *2nd Int. Workshop on Algorithmic Foundations of Robotics*, Toulouse, France, 1996.
- [123] S. M. LaValle. Rapidly-exploring random trees: A new tool for path planning. Technical Report TR 98-11, Computer Science Dept., Iowa State University, October 1998.
- [124] S. M. LaValle and Jr. J. J. Kuffner. Randomized kinodynamic planning. *The International Journal of Robotics Research*, 20:378–400, 2001.
- [125] J. J. Kuffner and S. M. LaValle. Rapidly exploring random trees: Progress and prospects. In *Algorithmic and Computational Robotics New Directions International Workshop on the Algorithmic Foundations of Robotics*, pages 293–308, 2000.
- [126] A. Ettlín and H. Bleuler. Randomised rough-terrain robot motion planning. In *IEEE/RSJ International Conference on Intelligent Robots and Systems*, pages 5798–5803, 2006.
- [127] E. Frazzoli, M. A. Dahleh, and E. Feron. Robust hybrid control for autonomous vehicle motion planning. Technical Report LIDS-P-2468, Laboratory for Information and Decision Systems, Massachusetts Institute of Technology, 2000.
- [128] L. Jaillet, J. Cortes, and T. Simeon. Sampling-based path planning on configuration-space costmaps. *IEEE Transactions on Robotics*, 26(4):635–646, 2010.
- [129] A. M. Ladd and L. E. Kavraki. Motion planning in the presence of drift, underactuation and discrete system changes. In *Robotics: Science and Systems I*, pages 233–241, Boston, MA, June 2005. MIT Press.
- [130] S. R. Lindemann and S. M. LaValle. Current issues in sampling-based motion planning. *Robotics Research: Springer Tracts in Advanced Robotics*, 15:36–54, 2005.
- [131] K. I. Tsianos, I. A. Sucas, and L. E. Kavraki. Sampling-based robot motion

- planning: Towards realistic applications. *Computer Science Review*, 1(1):2–11, August 2007.
- [132] B. O’Brien and B. Hemes. A tumbling robot in an integrated environment. In *The Applied Vehicle Technology Panel (AVT) Symposium on Morphing Vehicles*, 2009.
- [133] G. S. Sukhatme and G. A. Bekey. An evaluation methodology for autonomous mobile robots for planetary exploration. In *Proceedings of The First ECPD International Conference on Advanced Robotics and Intelligent Automation*, pages 558–563, 1995.
- [134] G. S. Sukhatme. Measuring mobile robot performance: Approaches and pitfalls. In A. M. Meystel, editor, *Proceedings of the 2000 PerMIS Workshop*, volume E. R. Messina, pages 281–288, 2000.
- [135] J. Hershberger and S. Suri. Efficient computation of Euclidean shortest paths in the plane. In *Proceedings of the 1995 IEEE Symposium on Foundations of Computer Science*, pages 508–517, 1995.
- [136] J. S. B. Mitchell. Shortest paths among obstacles in the plane. *International Journal of Computational Geometry and Applications*, 6(3):309–332, 1996.
- [137] C. H. Papadimitriou. An algorithm for shortest-path motion in three dimensions. *Information Processing Letters*, 20(5):259–263, 1985.
- [138] J. Choi, J. Sellen, and C. K. Yap. Precision-sensitive euclidean shortest path in 3-space. In *Proceedings of the ACM Symposium on Computational Geometry*, pages 350–359, 1995.

Appendix A

Adelopod SPI Interface

The Adelopod robot has two main levels of processing, the high-level processing (Gumstix Verdex computer) and the low-level firmware (dsPic 33F series microcontroller). All user code runs at the high-level within the Linux operating system with communication to the firmware over a serial peripheral interface (SPI) bus.

The main processor of the Adelopod communicates to the firmware (motor and sensor control) through consecutive 4-byte SPI transmissions. Transmissions are full-duplex (data is sent and received simultaneously), therefore data is received on the transfer immediately following the request. Aside from regular commands, there are two special commands, NULL and RESET, that allow for control of data reception (i.e., NULL can be used for receiving data without sending a new command; RESET is used to cancel a multiple byte transmission or re-synchronize the firmware with the high-level control).

A.1 Notation

The notation in Table A.1 is used in the SPI command set specification (Section A.2).

Table A.1: SPI notational conventions

Notation	Description
D	Direction bit; 0 for positive rotation about the motor’s Z-axis and 1 for negative rotation about the motor’s Z-axis.
dataSpec12	12-bit specification of data request; see Table A.2 for descriptions of the values.
E	Enable bit; 1 to enable enable motors, 0 to disable motors. Disabled motors will not accept commands or hold position.
M	Motor specification; 2-bit value of motor (M = motorNumber - 1).
mode4	Mode specification; 4-bit value of firmware mode.
position10	Motor position; 10-bit value of a motor encoder.
speed9	Motor speed; 9-bit value of motor speed. Speeds are represented linearly from stop to full over the range (0x000-0x1FF).

A.2 Command Set

The implemented SPI commands are summarized in Figure A.1. Following their summary are individual descriptions of each command along with examples using the Adelopod

	15	14	13	12	11	10	9	8	7	6	5	4	3	2	1	0	
Mode Independent																	
NULL	0000				000000000000												
RESET	1111				111111111111												
REQUEST_DATA	0001				dataSpec12												
SET_MOTOR_ENABLE	0011				000000000000											E	
SET_MODE	0010				00000000								mode4				
Mode 0																	
SET_MOTOR_DIR/SPEED	0111				M	D	speed9										
Mode 1																	
SET_MOTOR_HOME_POS	0100				M		position10										
SET_MOTOR_SPEED	0101				000			speed9									
SET_MOTOR_POS	0110				M		position10										

Figure A.1: Formats of the Adelopod SPI instructions.

NULL

Encoding

15	14	13	12	11	10	9	8	7	6	5	4	3	2	1	0
0000				000000000000											

Operation

Dummy packet is transmitted; data packet is received.

Description

This command is used for receiving data without transmitting a new command. It normally follows a data request a number of times equal to the number of packets expected (or one less if a new command is to be issued).

Examples

```

SPI( REQUEST_DATA(Motor Values) )           // request 4 values of the motor encoders
val1 = SPI( NULL )                          // receive first motor value
val2 = SPI( NULL )                          // receive second motor value
val3 = SPI( NULL )                          // receive third motor value
val4 = SPI( NULL )                          // receive fourth motor value

SPI( REQUEST_DATA(Motor Values) )           // request 4 values of the motor encoders
val1 = SPI( NULL )                          // receive first motor value
val2 = SPI( NULL )                          // receive second motor value
val3 = SPI( NULL )                          // receive third motor value
val4 = SPI( REQUEST_DATA(Gyro X-Axis) )     // receive fourth motor value
                                           // ... and request value of gyro
val5 = SPI( NULL )                          // receive gyro value

```

RESET

Encoding

15	14	13	12	11	10	9	8	7	6	5	4	3	2	1	0
1111				111111111111											

Operation

SPI state within firmware is reset, thus canceling any current command. A new command can be sent immediately following a reset.

Description

This command allows the interruption of multiple packet commands however its main use is for re-synchronizing the high and low-level SPI controllers in case of malfunction or other data loss. In practice it serves as a debugging tool and is rarely used.

Examples

```

SPI( REQUEST_DATA(Motor Values) )           // request 4 values of the motor encoders
val1 = SPI( NULL )                          // receive first motor value
val2 = SPI( RESET )                          // receive second motor value
SPI( REQUEST_DATA(Gyro X-Axis) )           // cancel previous request
                                           // ... and request value of gyro
val3 = SPI( NULL )                          // receive gyro value

```


Table A.2: Values of dataSpec12

	dataSpec12	Value	
Sensor Values (0x000-0x2F)	0x000	Gyro X-Axis	
	0x001	Gyro Y-Axis	
	0x002	Gyro Z-Axis	
	0x003	Accelerometer X-Axis 1	
	0x004	Accelerometer Y-Axis 1	
	0x005	Accelerometer Z-Axis 1	
	0x006	Accelerometer X-Axis 2	
	0x007	Accelerometer Z-Axis 2	
	0x008	Accelerometer Z-Axis 3	
	0x009	Motor 1 Encoder (Left Arm)	
	0x00A	Motor 2 Encoder (Right Arm)	
	0x00B	Motor 3 Encoder (Left Peripheral)	
	0x00C	Motor 4 Encoder (Right Peripheral)	
	0x00D	Photocell 1/2	
	0x00E	Photocell 3/4	
	0x00F	Photocell 5/6	
	0x010	Photocell 7/8	
Bulk Requests (0x030-0x05F)	0x030	All Sensors	(18: 0x000-0x010)
	0x031	All Status Values	(5: 0x060-0x064)
	0x032	Motor Values	(4: 0x009-0x00C)
	0x033	Motor Home Positions	(4: 0x061-0x064)
Status Values (0x060-0xFFF)	0x060	MotorEnable	
	0x061	Motor 1 Home Position	
	0x062	Motor 2 Home Position	
	0x063	Motor 3 Home Position	
	0x064	Motor 4 Home Position	
	0x065	Battery Voltage	

SET MOTOR ENABLE

Encoding

15	14	13	12	11	10	9	8	7	6	5	4	3	2	1	0
0011				00000000000											E

Operation

PID control of motors is enabled or disabled depending on the value of E; 1 = enabled, 0 = disabled.

Description

This command is used for enabling and disabling the motors on the robot. When enabled, the motors are controlled by the internal PID controller and obey SET_MOTOR commands; when disabled, the motors are allowed to coast. On transitions from disabled to enabled, the motors will hold the position occupied at the time of the enable command (equivalent to a SET_MOTOR_POSITION for each motor with the current positions as arguments).

Examples

```
SPI( SET_MOTOR_ENABLE(Enable) )           // enable motors
SPI( SET_MOTOR_POS(1, 500) )              // set motor 1 to position 500
:
SPI( SET_MOTOR_ENABLE(Disable) )          // disable motors
```

SET MODE

Encoding

15	14	13	12	11	10	9	8	7	6	5	4	3	2	1	0
0010				00000000								mode4			

SET MOTOR DIR/SPEED

Encoding

15	14	13	12	11	10	9	8	7	6	5	4	3	2	1	0
0111				M		D	speed9								

Operation

Set motor M for continuous rotation as speed specified by speed9 and direction by D.

Description

This command is used for setting the motors to constant angular velocity. This is useful for implementing directional control of the robot where absolute position of the motors need not be controlled directly (i.e., joystick tele-operation of the robot).

Examples

```
DO
  // map joystick input to directions and speeds
  :
  // update motor directions and speeds
  SPI( SET_MOTOR_DIR/SPD(1, dir1, spd1) ) // update motor 1 direction / speed
  SPI( SET_MOTOR_DIR/SPD(2, dir2, spd2) ) // update motor 2 direction / speed
WHILE(in_joystik_control)
```

SET MOTOR HOME POS

Encoding

15	14	13	12	11	10	9	8	7	6	5	4	3	2	1	0
0100				M		position10									

Operation

Set position10 as home position for motor M.

Description

This command is used to tell the firmware to use the value position10 as the home position for a given motor (on power-up all home positions default to 0x000 until set). All motor positions are specified relative to the home position (i.e., a SET_MOTOR_POS(position10) will instruct the PID controller to bring the motor to HOME_POS + position10). This command is usually used once during initialization where home positions from a calibration file on the high-level data storage are sent to the Adelopod after start-up.

Examples

```
// robot start-up initialization
:
hPos1 = home_position_1_from_file
hPos2 = home_position_2_from_file
SPI( SET_MOTOR_HOME_POS(1, hPos1) )           // motor 1 home position = hPos1
SPI( SET_MOTOR_HOME_POS(2, hPos2) )           // motor 2 home position = hPos2
:
```

SET MOTOR SPEED

Encoding

15	14	13	12	11	10	9	8	7	6	5	4	3	2	1	0
0101				000			speed9								

SET MOTOR POS

Encoding

15	14	13	12	11	10	9	8	7	6	5	4	3	2	1	0
0110				M		position10									

Operation

Set position10 value as target for the PID positional controller of motor M.

Description

This command will bring a motor from its current position to the one specified by position10 at a speed specified by the command SET_MOTOR_SPEED (speed is quasi-static if not previously set). The value of position10 is specified relative to the respective motor's home position (i.e., a position10 of 0x000 is equivalent to the motor's home position as specified by the command SET_MOTOR_HOME_POSITION). The motor's direction is selected automatically based on the shortest path to the target position.

Examples

```
SPI( SET_MOTOR_ENABLE(Enable) )           // enable motors
SPI( SET_MOTOR_SPEED(0x1ff) )             // set speed to full
SPI( SET_MOTOR_POS(1, 0d500) )           // set motor 1 to position 500 (full speed)
```

Appendix B

Adelopod Mechanical Drawings

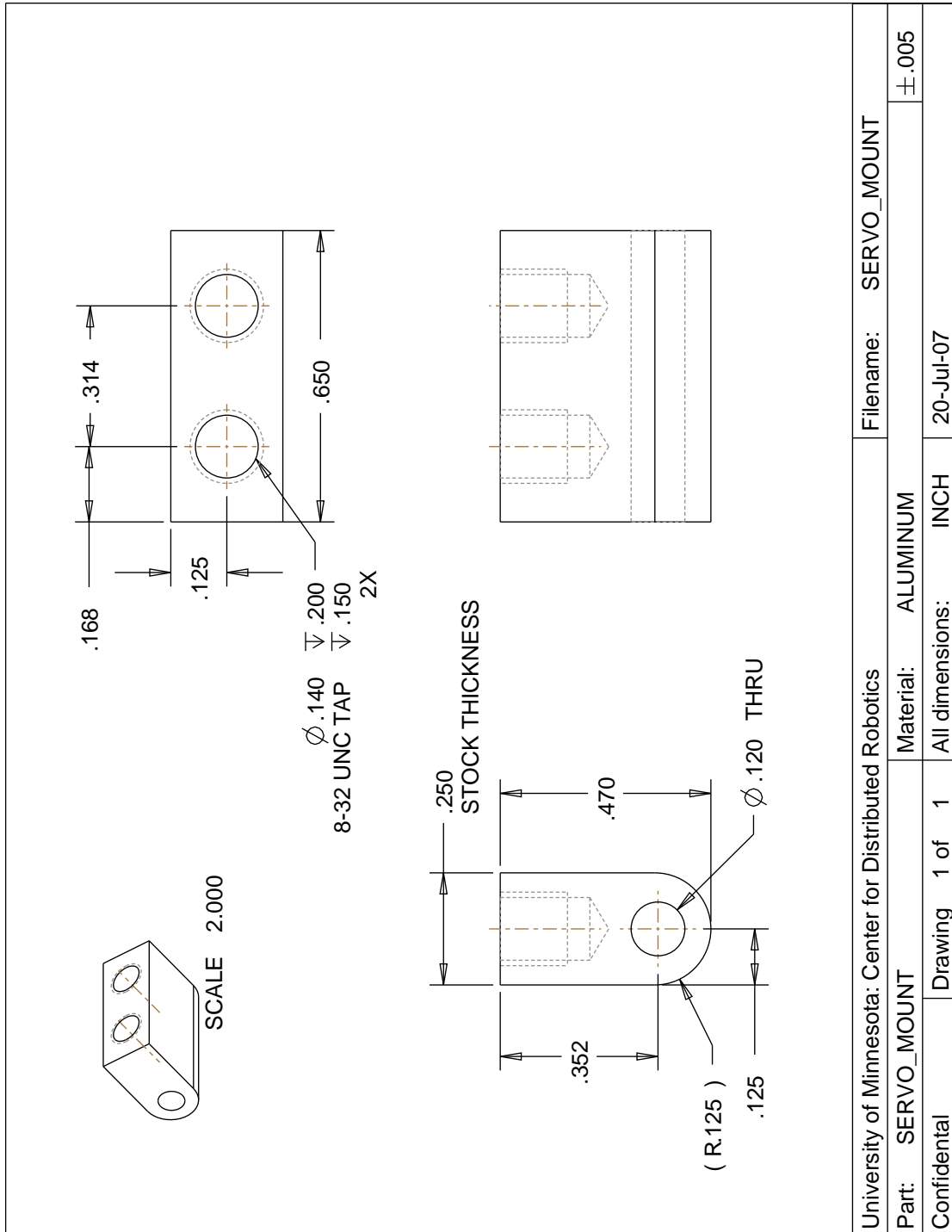


Figure B.1: Servo Mount

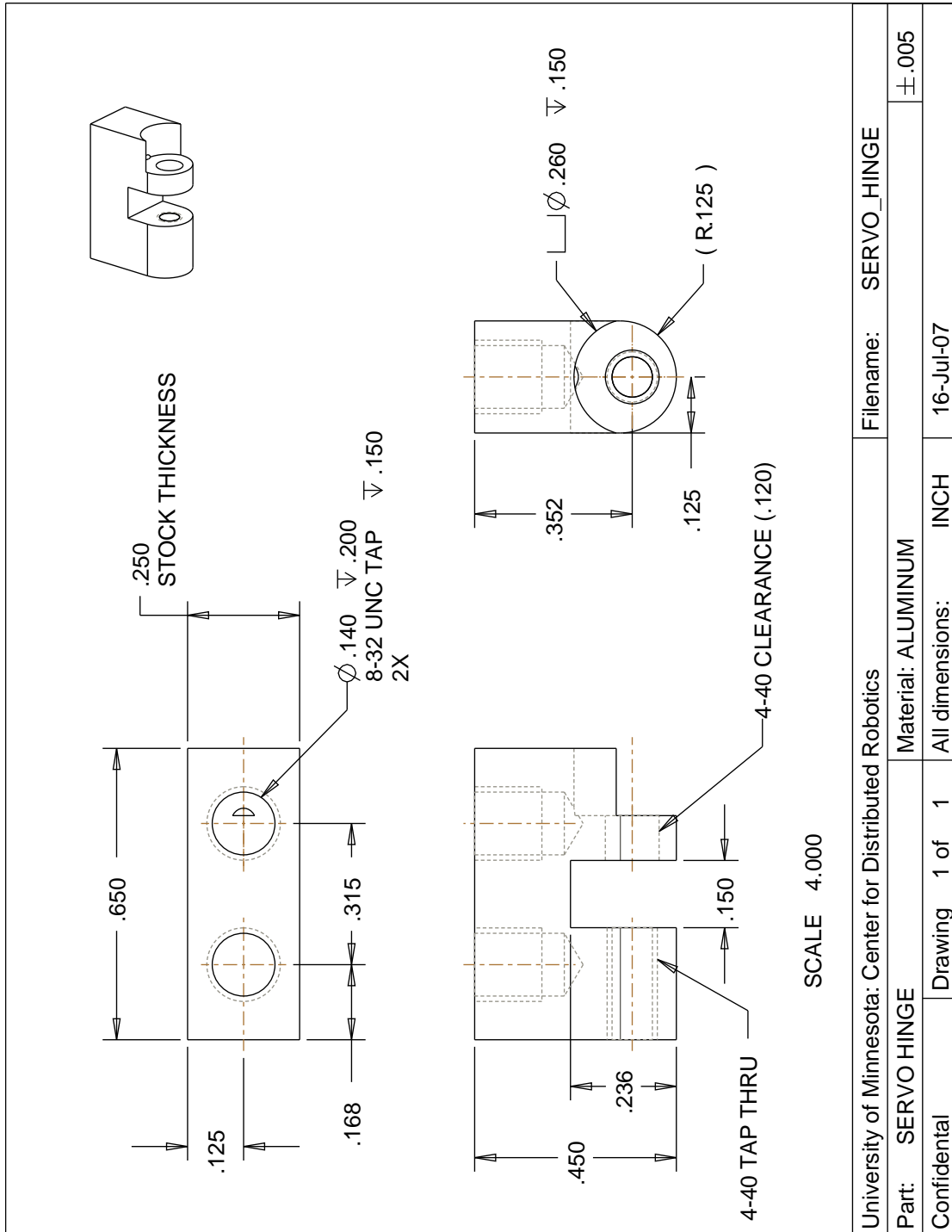


Figure B.2: Servo Hinge

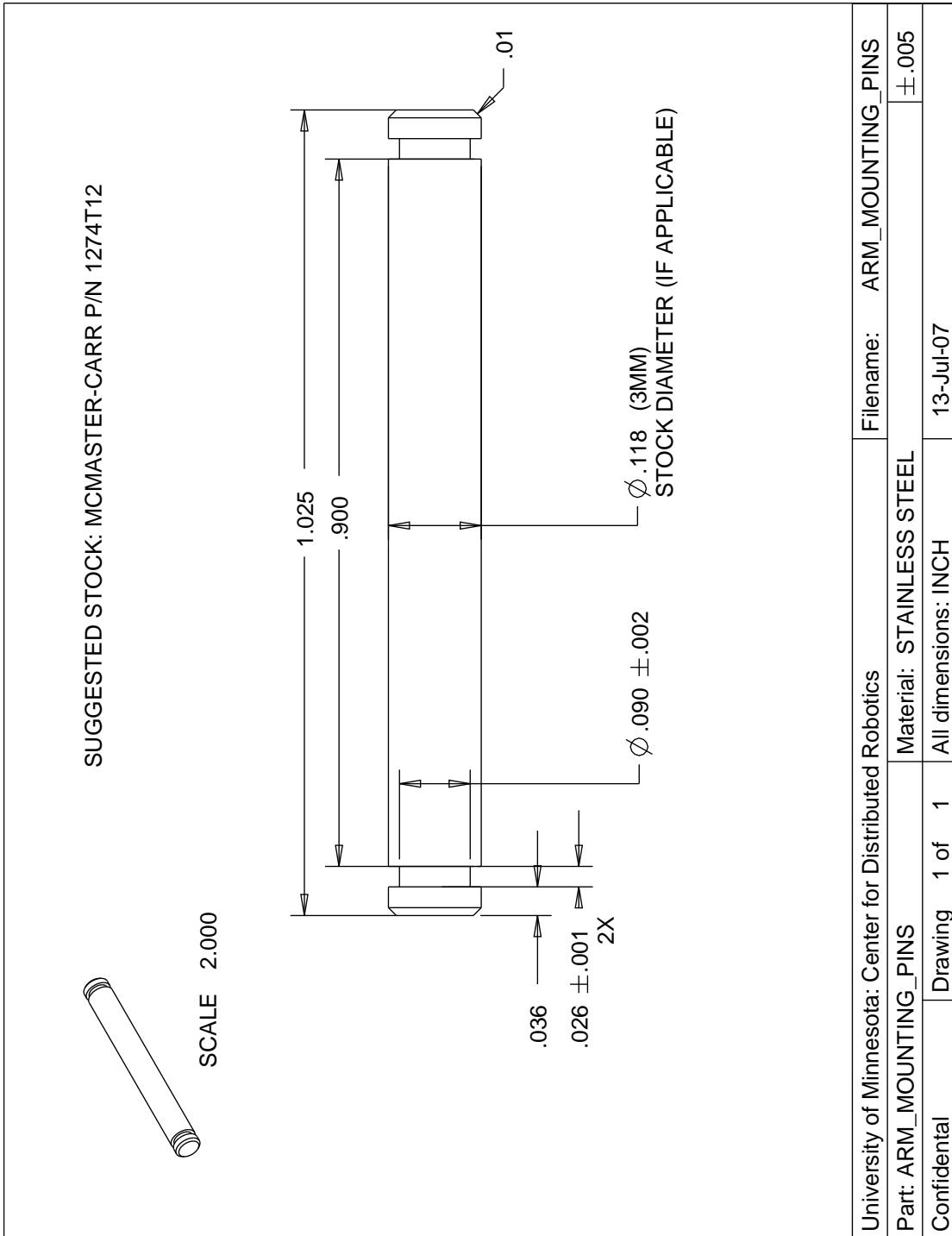


Figure B.3: Arm Mounting Pins

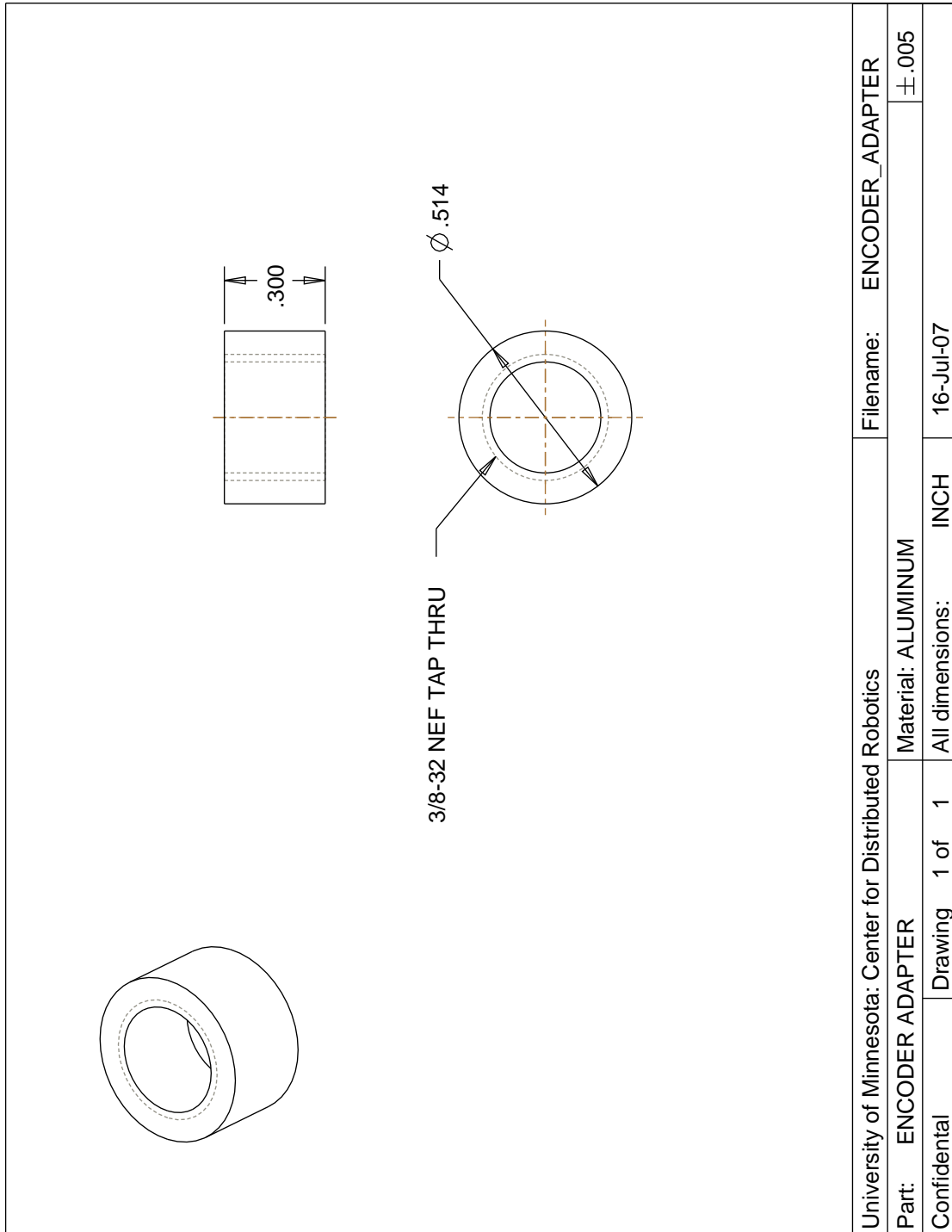


Figure B.4: Arm Mounting Pins

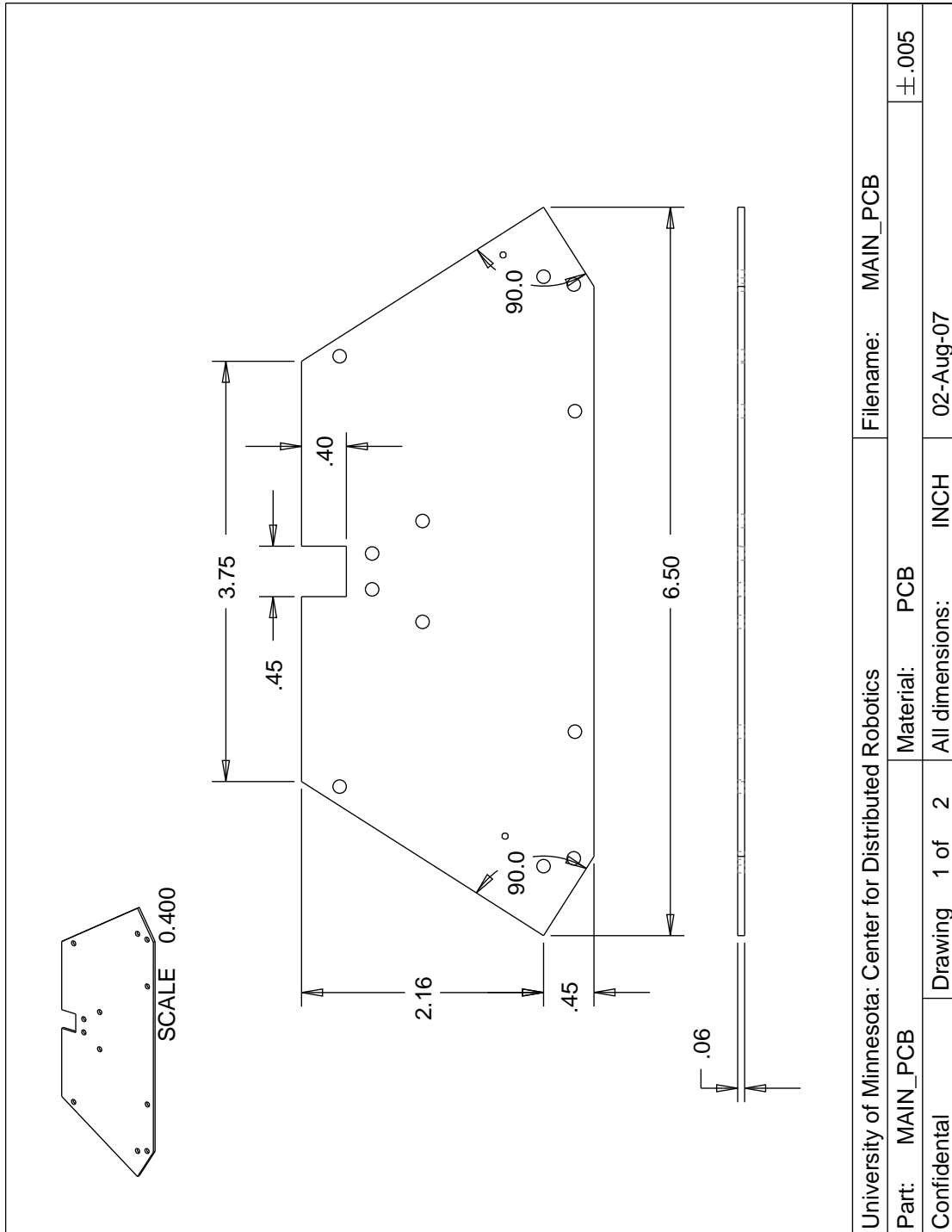


Figure B.5: PCB Dimensions 1 of 2

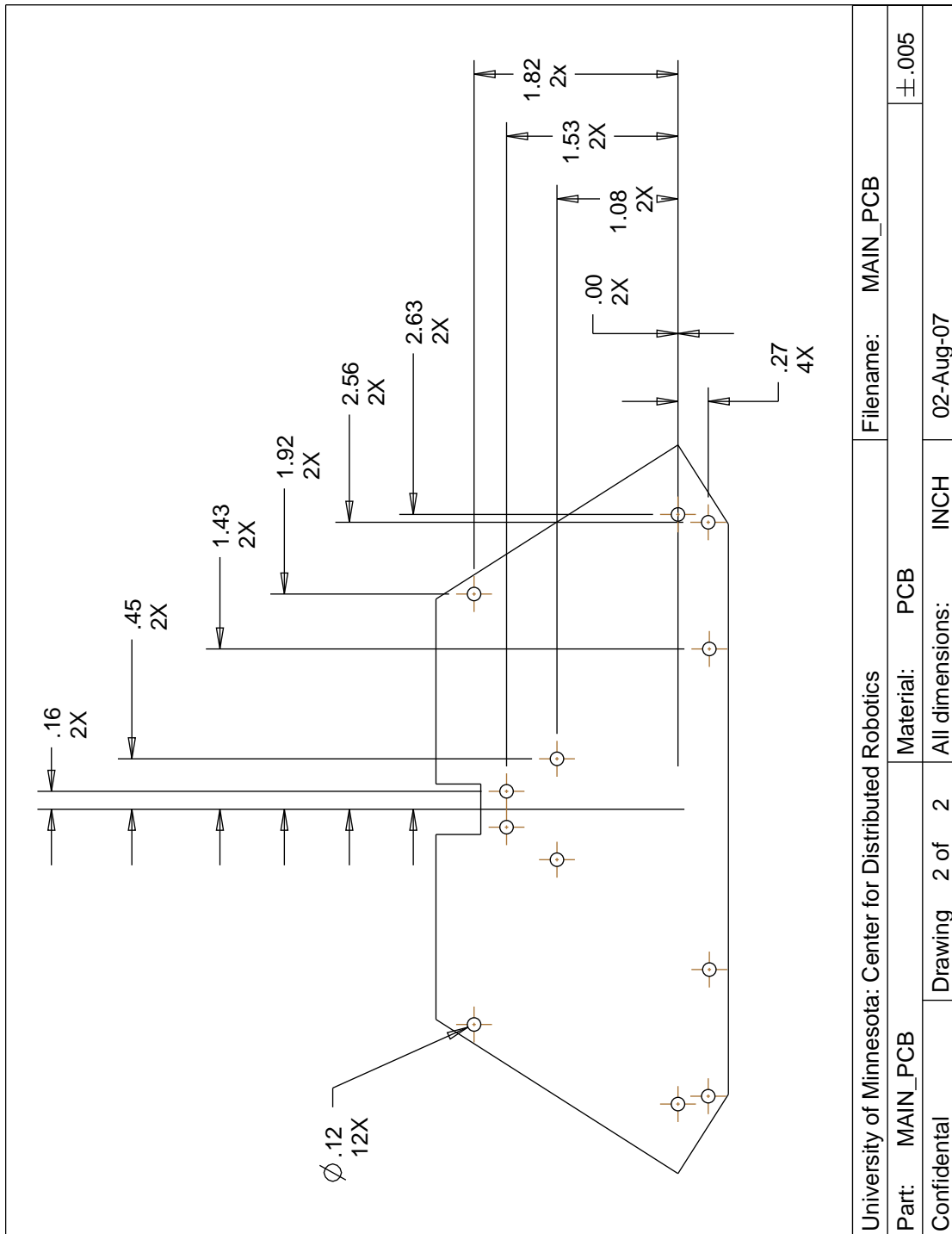
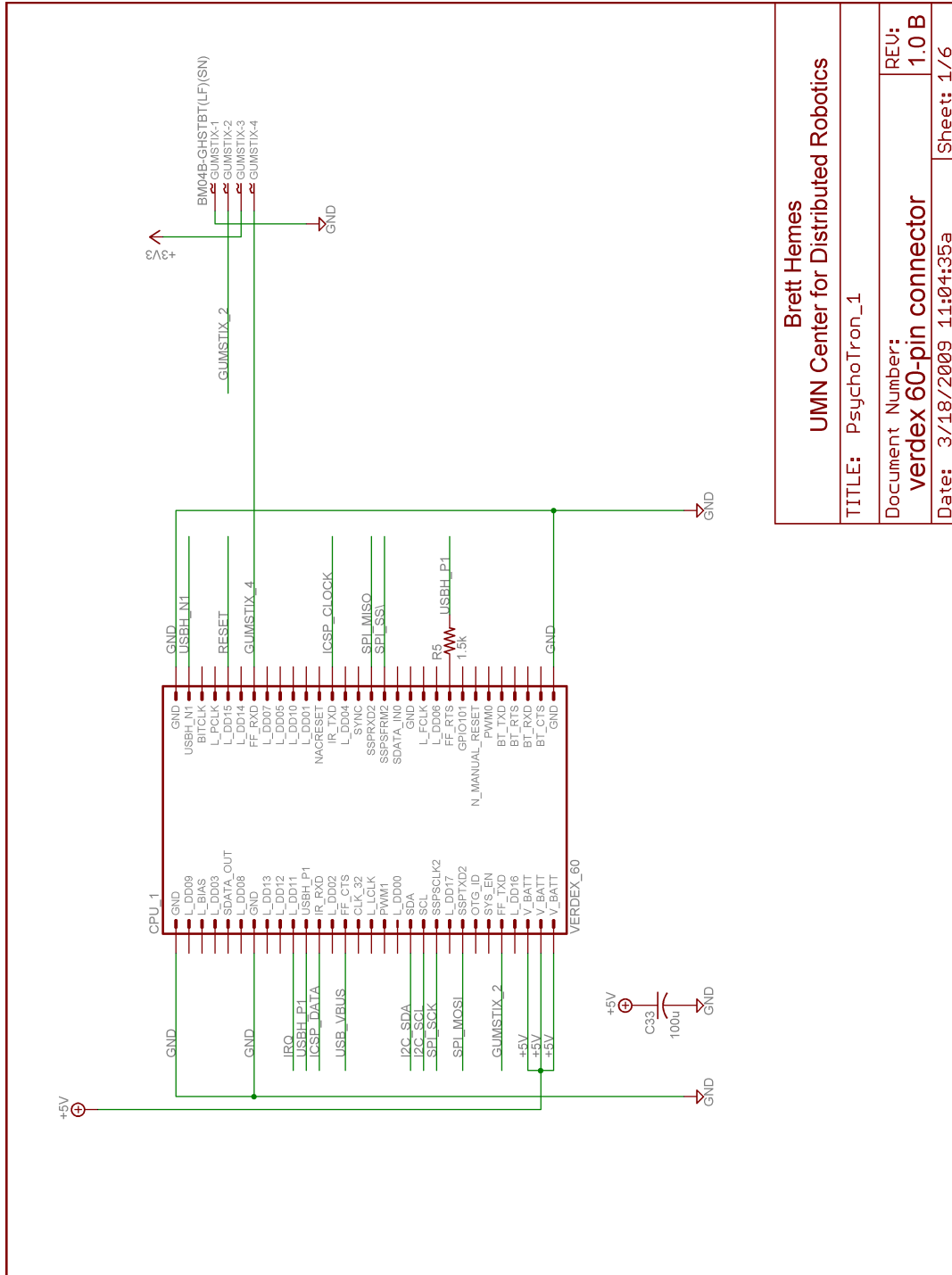


Figure B.6: PCB Dimensions 2 of 2

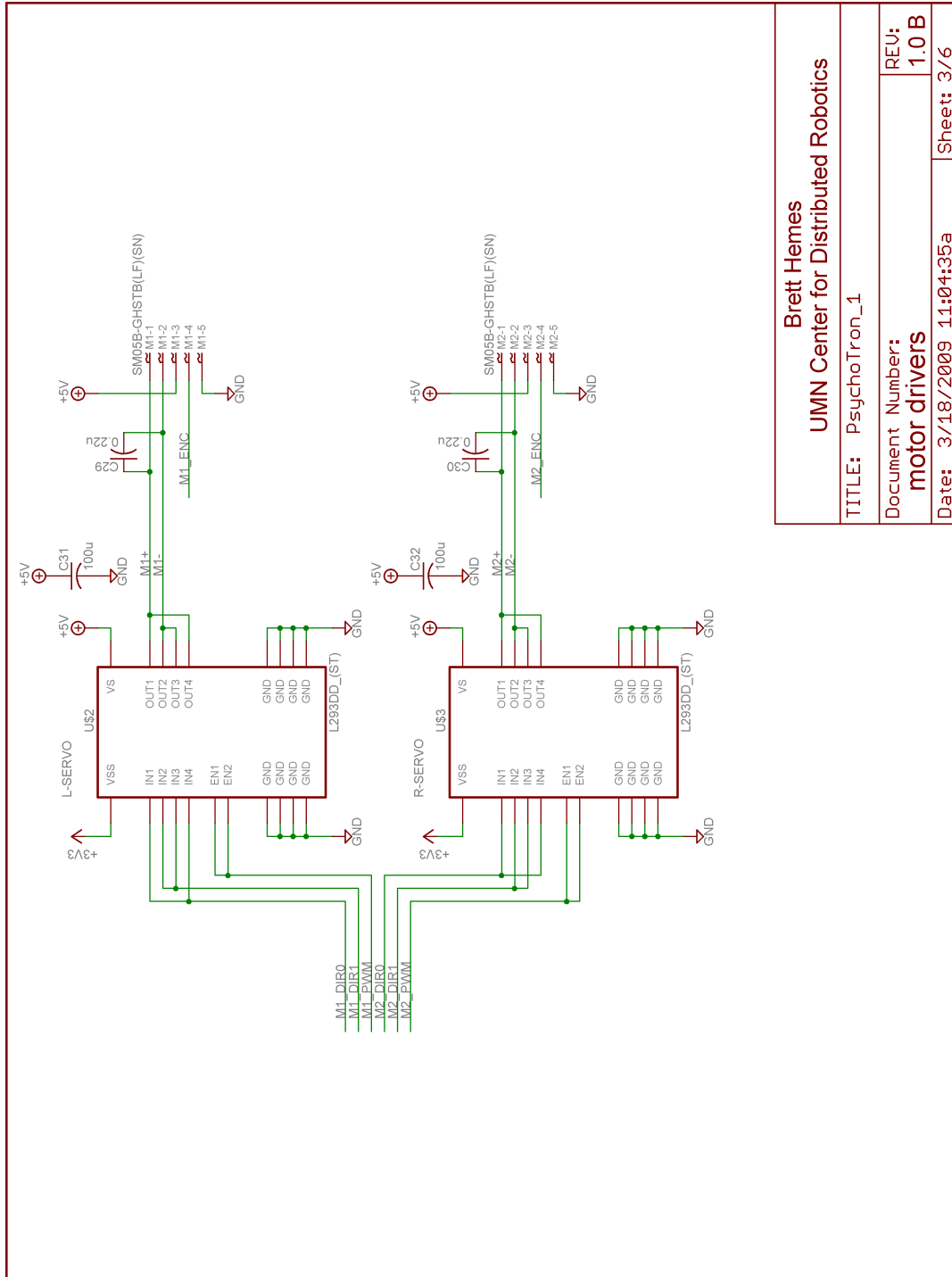
Appendix C

Adelopod Schematics



Brett Hemes	
UMN Center for Distributed Robotics	
TITLE: PsychoTron_1	REU:
Document Number:	1.0 B
Verdex 60-pin connector	Sheet: 1/6
Date: 3/18/2009 11:04:35a	

Figure C.1: Schematic: Top PCB (sheet 1 of 6).



Brett Hemes		
UMN Center for Distributed Robotics		
TITLE: PsychoTron_1	REV:	1.0 B
Document Number:	motor drivers	
Date: 3/18/2009 11:04:35a	Sheet:	3/6

Figure C.3: Schematic: Top PCB (sheet 3 of 6).

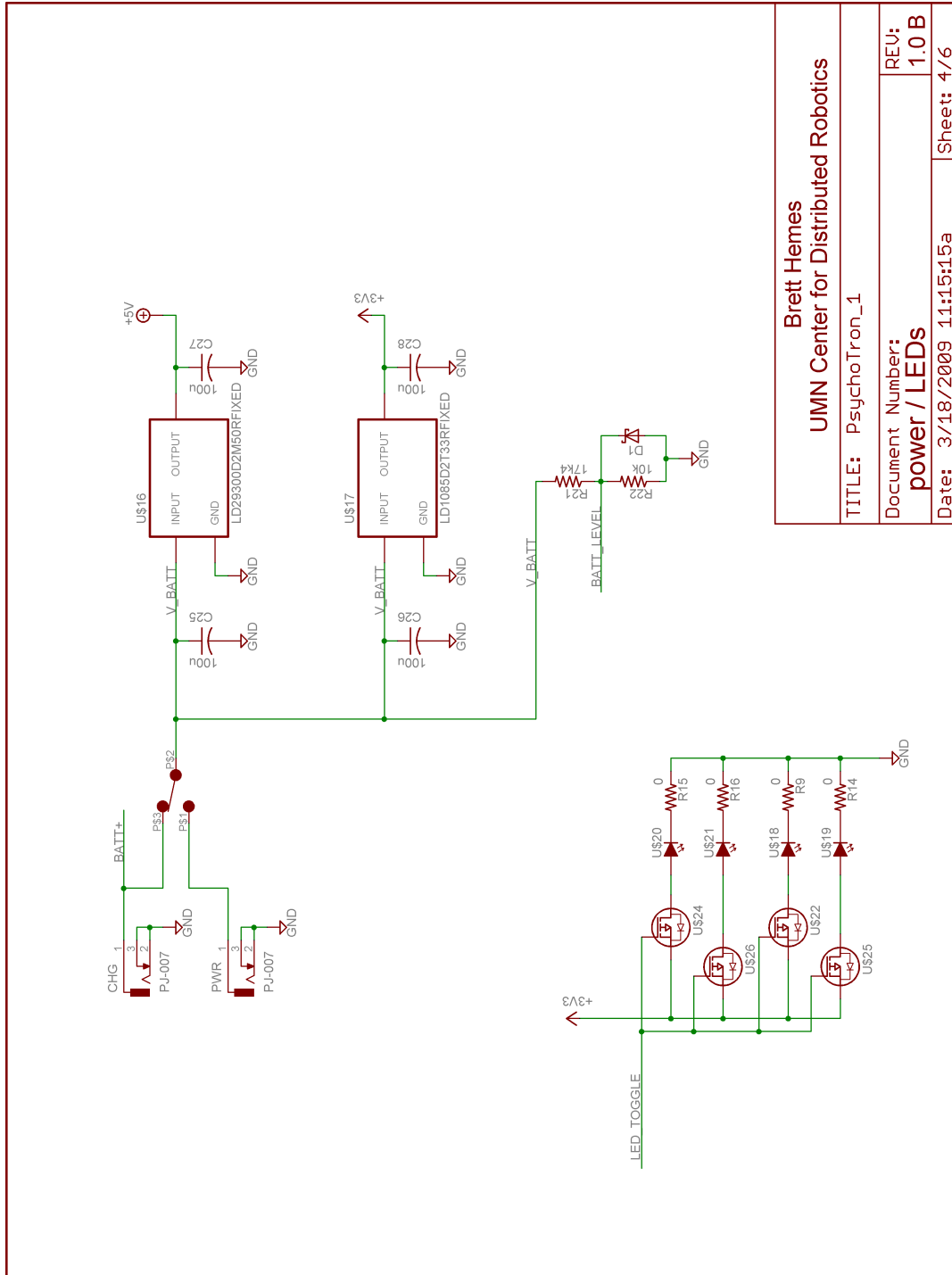


Figure C.4: Schematic: Top PCB (sheet 4 of 6).

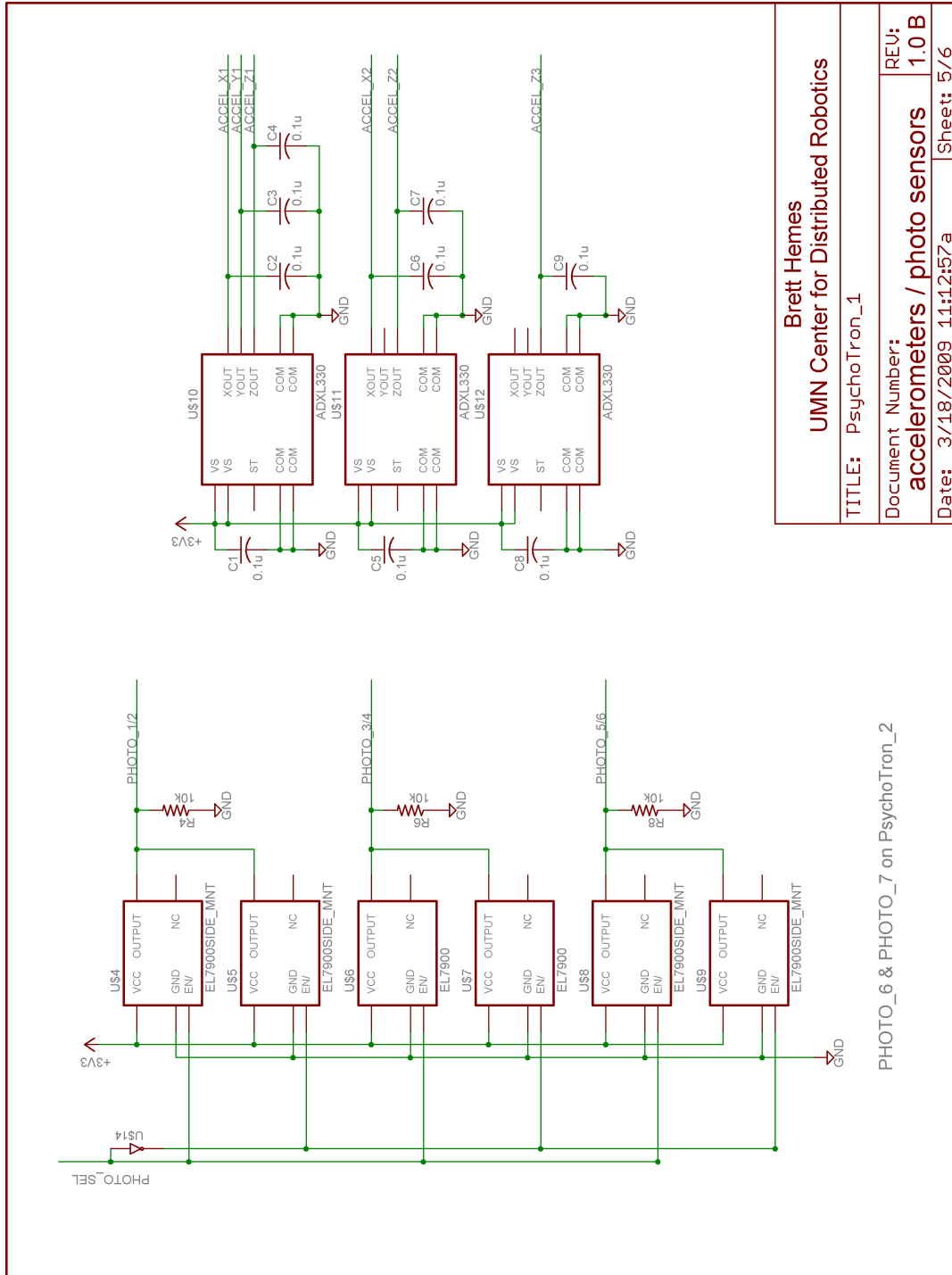
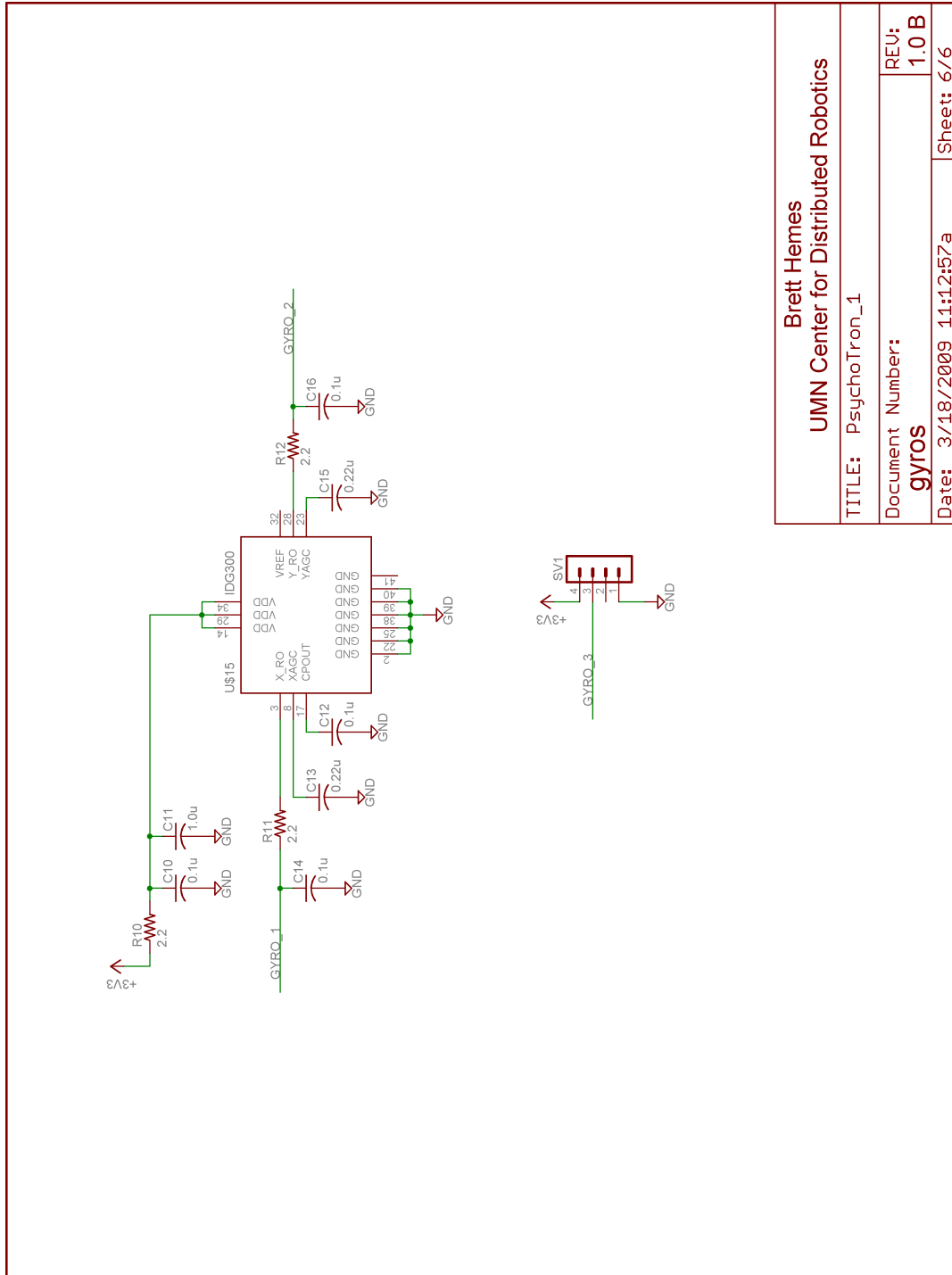
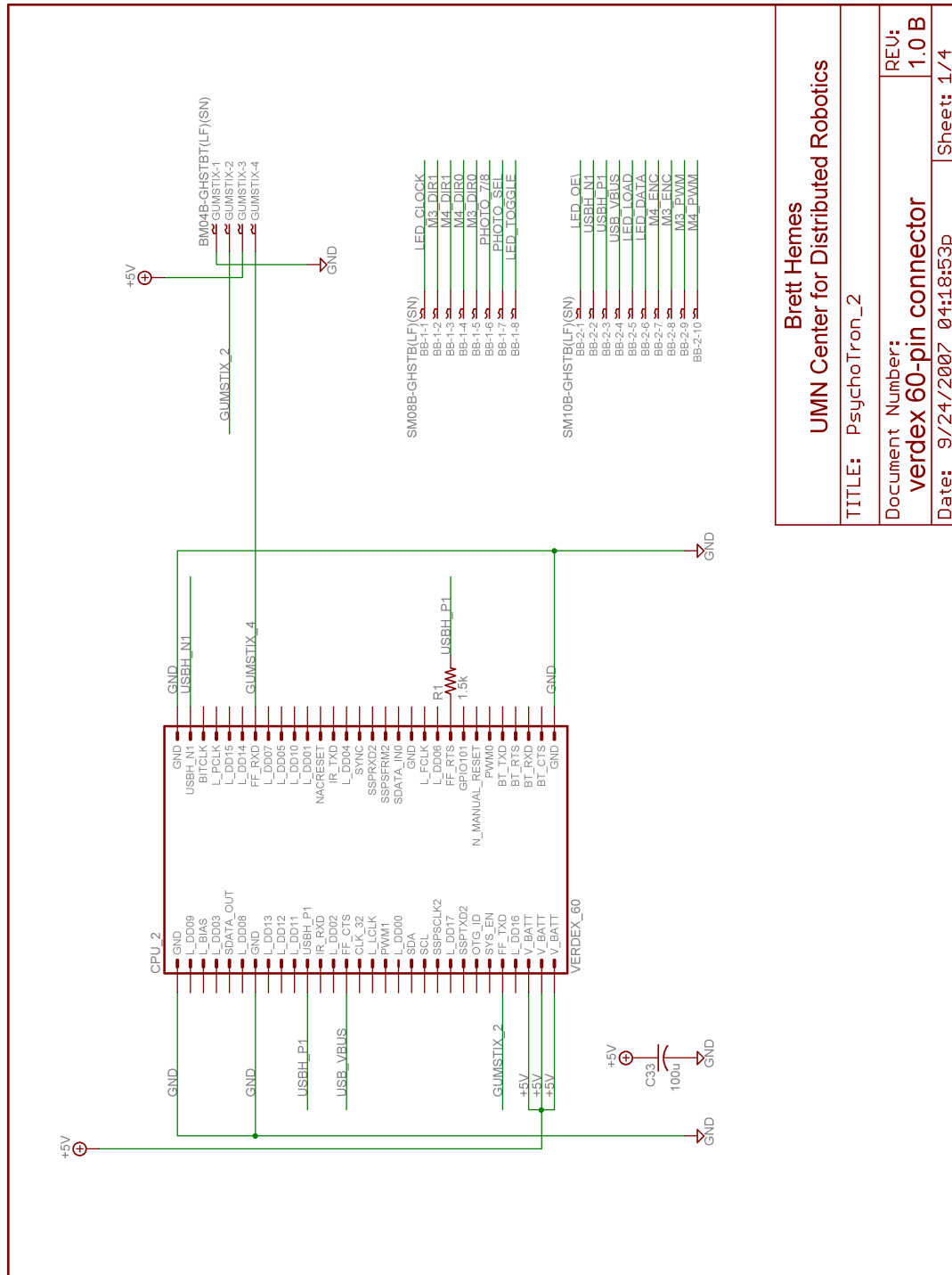


Figure C.5: Schematic: Top PCB (sheet 5 of 6).



Brett Hemes UMN Center for Distributed Robotics	
TITLE: PsychoTron_1	REV: 1.0 B
Document Number: gyros	Sheet: 6/6
Date: 3/18/2009 11:12:57a	

Figure C.6: Schematic: Top PCB (sheet 6 of 6).



Brett Hemes	
UMN Center for Distributed Robotics	
TITLE: PsychoTron_2	REV: 1.0 B
Document Number: verdex 60-pin connector	Sheet: 1 / 4
Date: 9/24/2007 04:18:53p	

Figure C.7: Schematic: Bottom PCB (sheet 1 of 4).

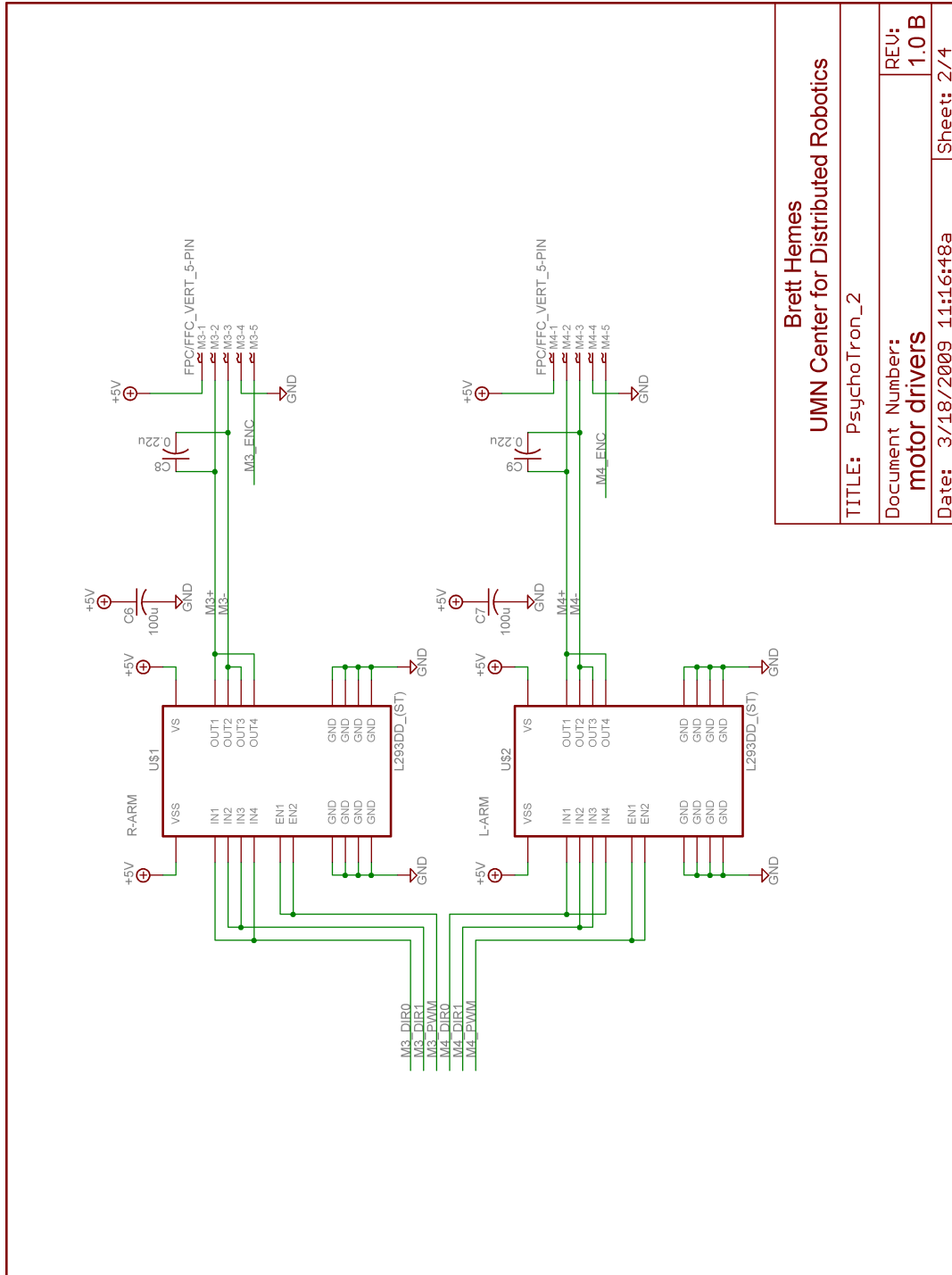
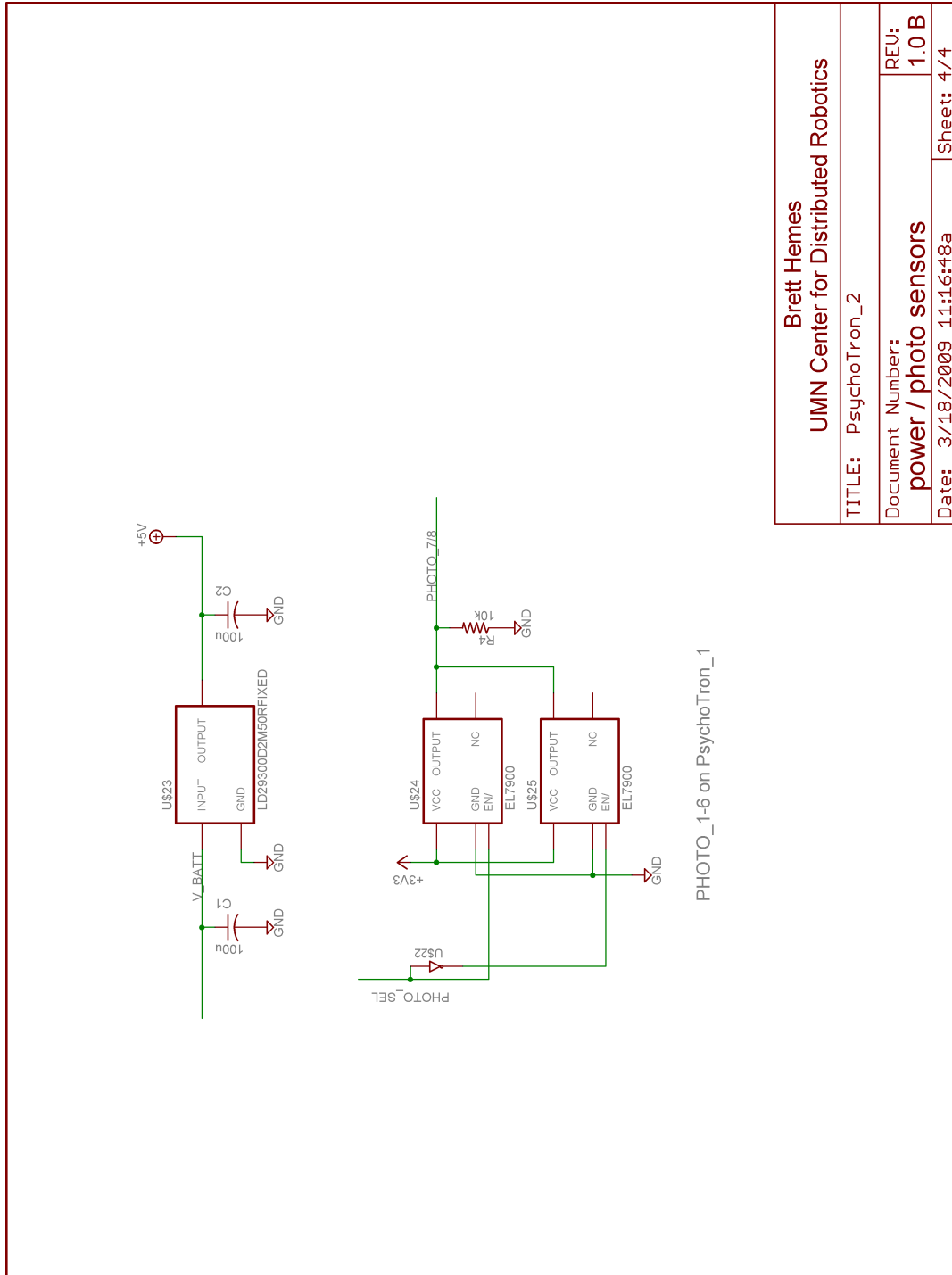


Figure C.8: Schematic: Bottom PCB (sheet 2 of 4).



Brett Hemes UMN Center for Distributed Robotics	
TITLE: PsychoTron_2	REV: 1.0 B
Document Number: power / photo sensors	Sheet: 4/4
Date: 3/18/2009 11:16:48a	

Figure C.10: Schematic: Bottom PCB (sheet 4 of 4).

Appendix D

Adelopod Printed Circuit Board Layout

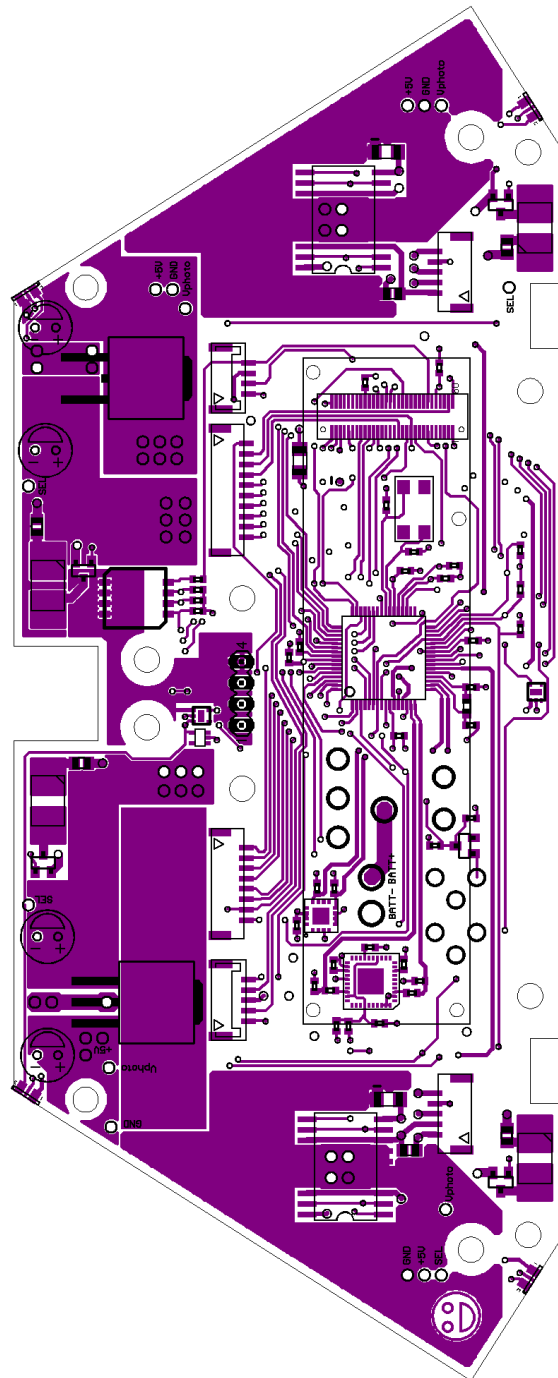


Figure D.2: Layout: Top PCB top traces

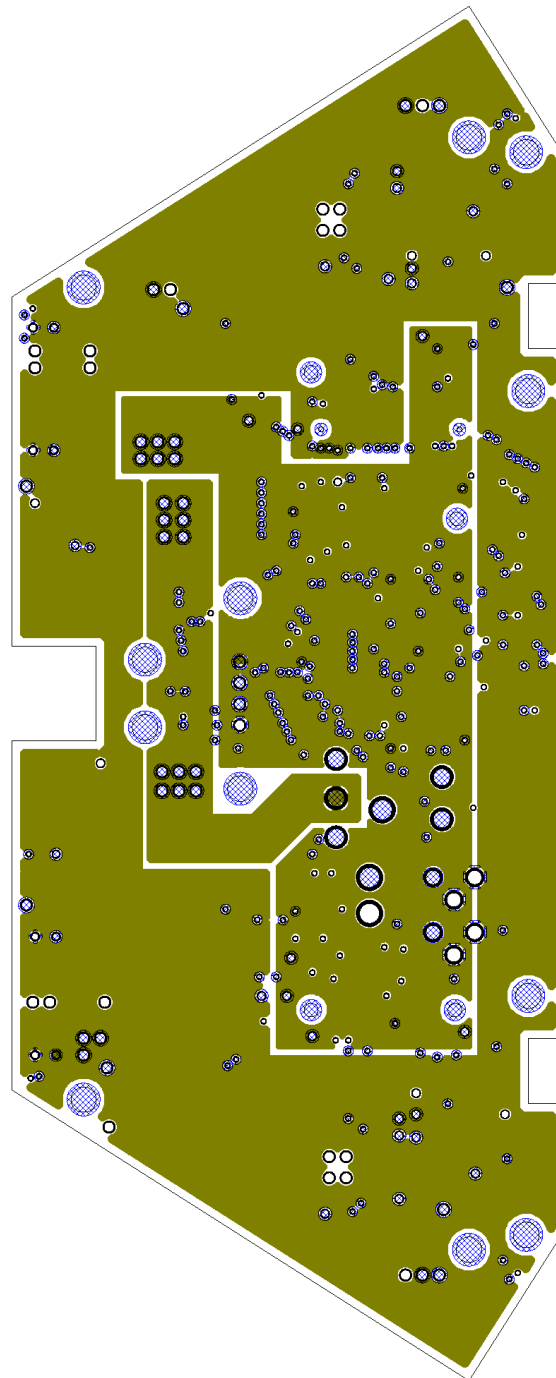


Figure D.3: Layout: Top PCB supply and ground layers

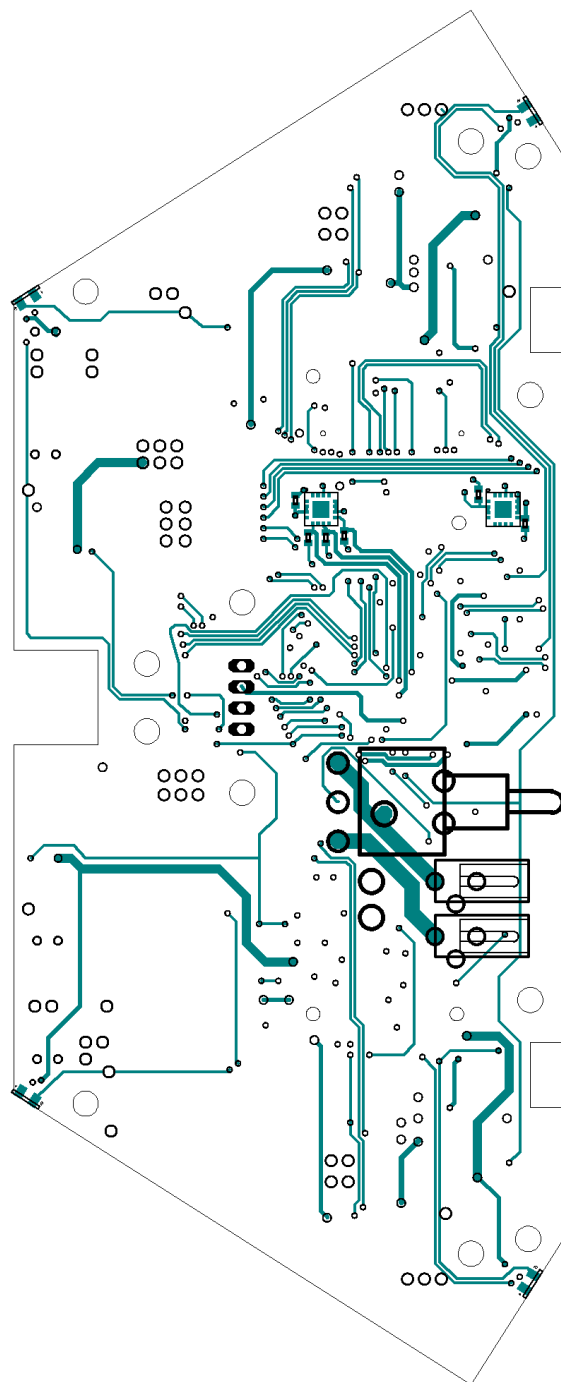


Figure D.4: Layout: Top PCB bottom traces

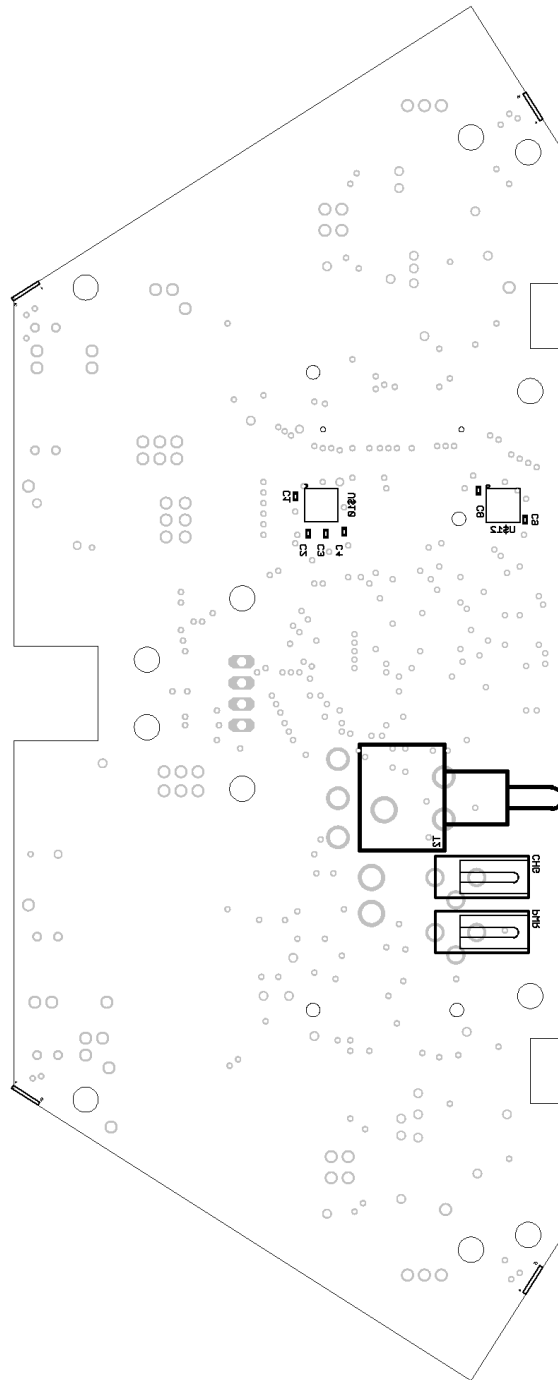


Figure D.5: Layout: Top PCB bottom documentation

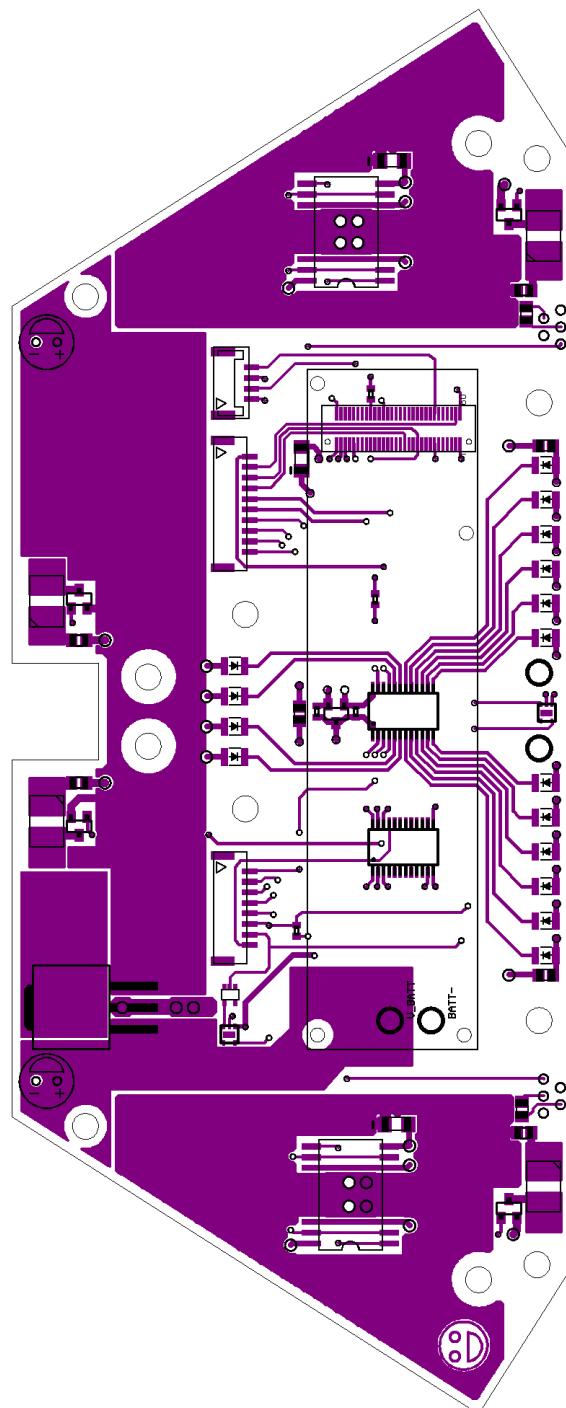


Figure D.7: Layout: Bottom PCB top traces

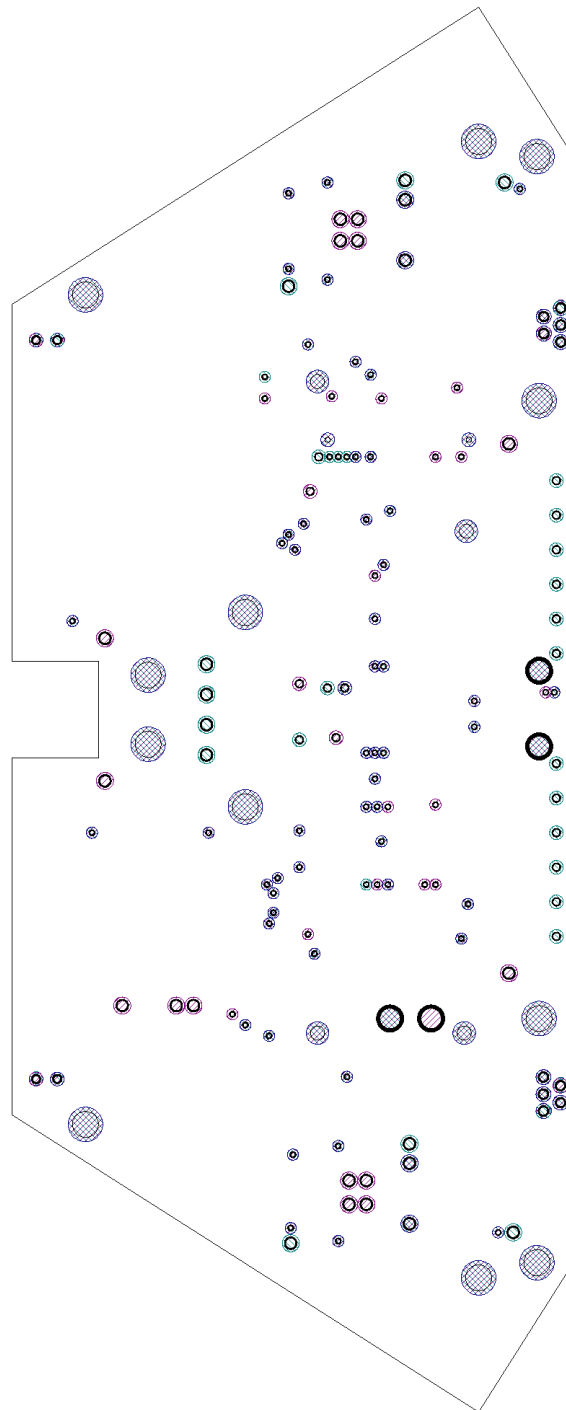


Figure D.8: Layout: Bottom PCB supply and ground layers

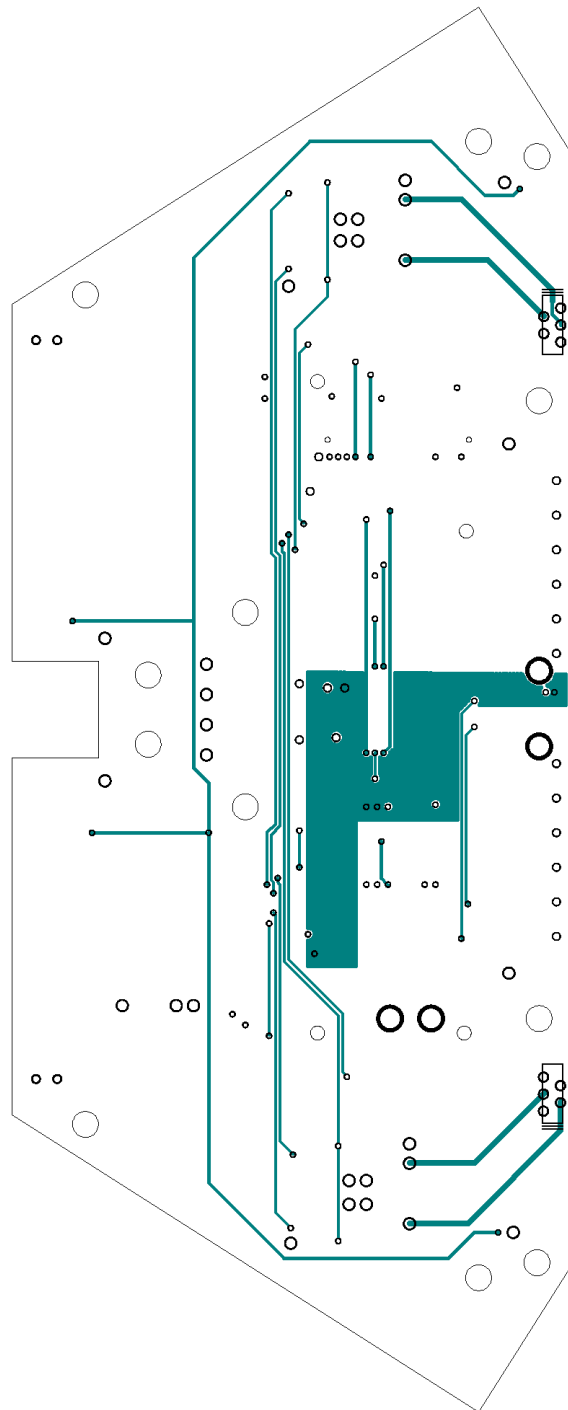


Figure D.9: Layout: Bottom PCB bottom traces

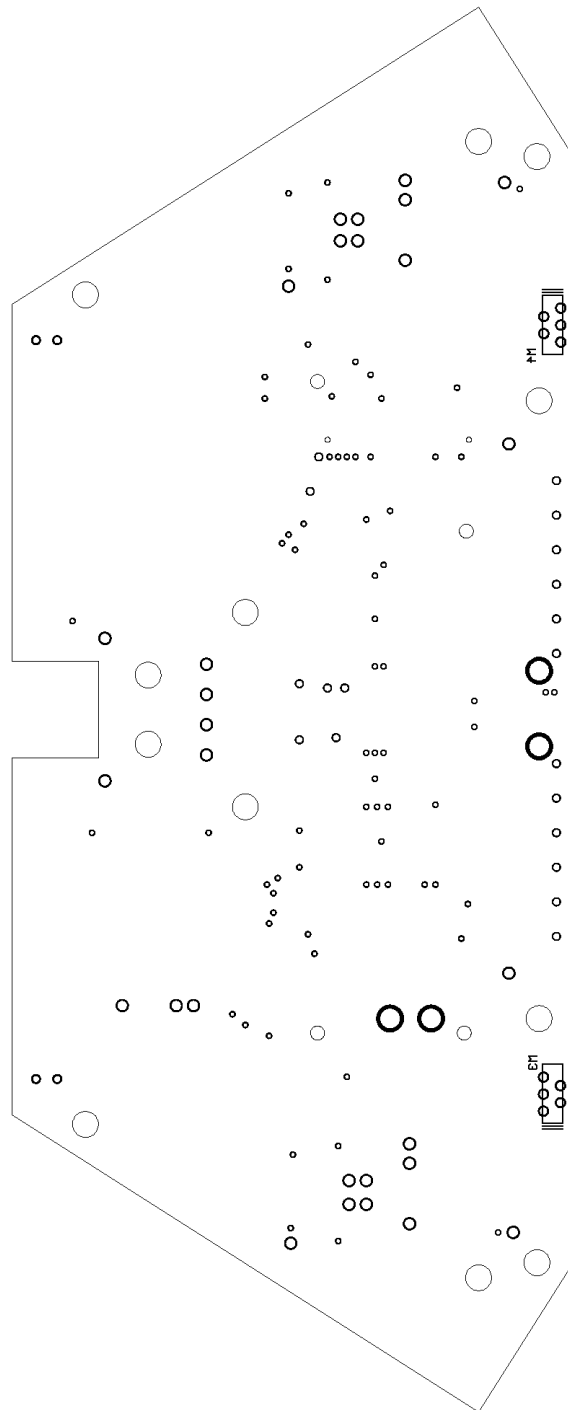


Figure D.10: Layout: Bottom PCB bottom documentation

Appendix E

Adelopod RRT Metric

Evaluation: Example Trees

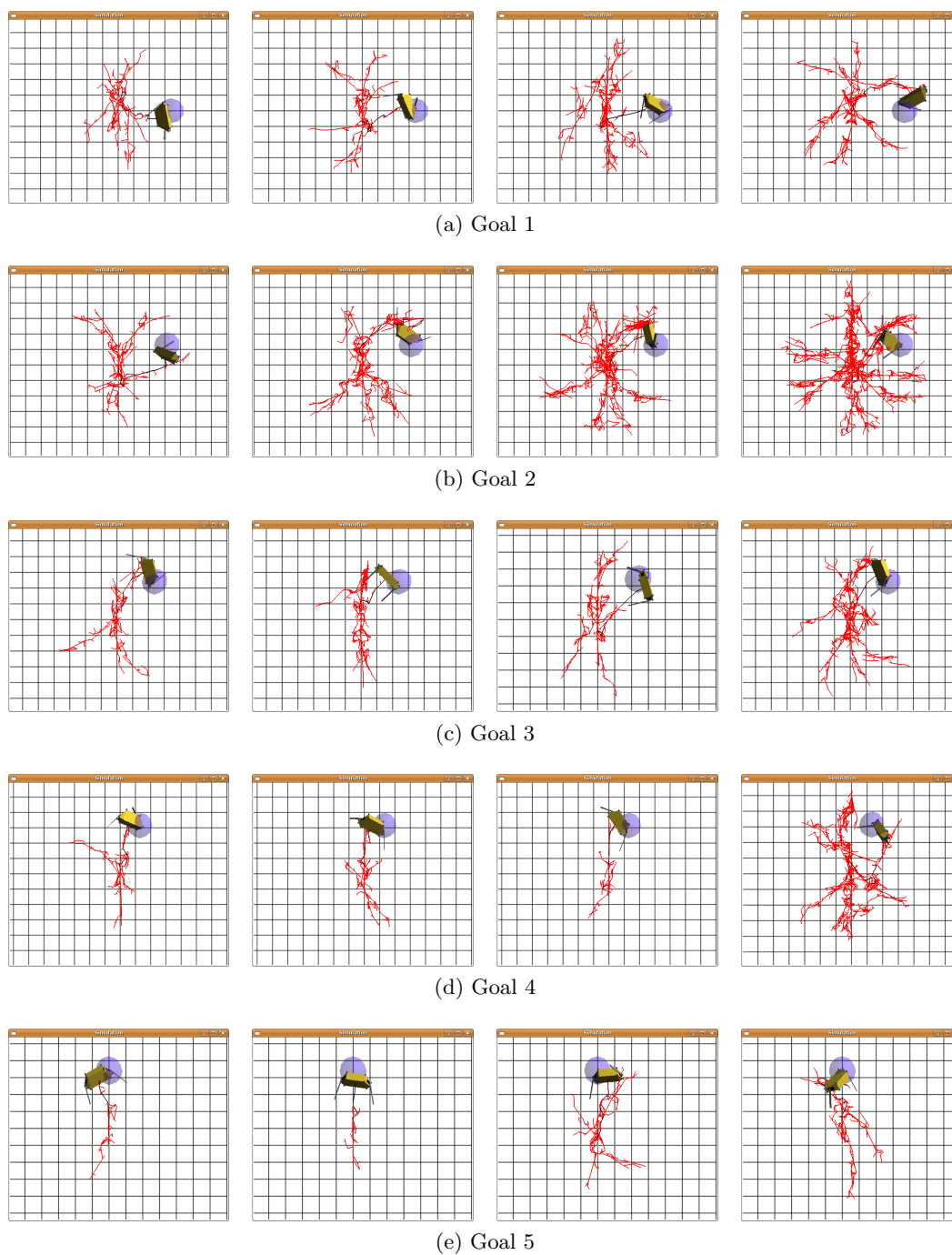


Figure E.1: Weighted Euclidian pseudo-metric d_{we} example RRTs for $r = 0.448$ m.

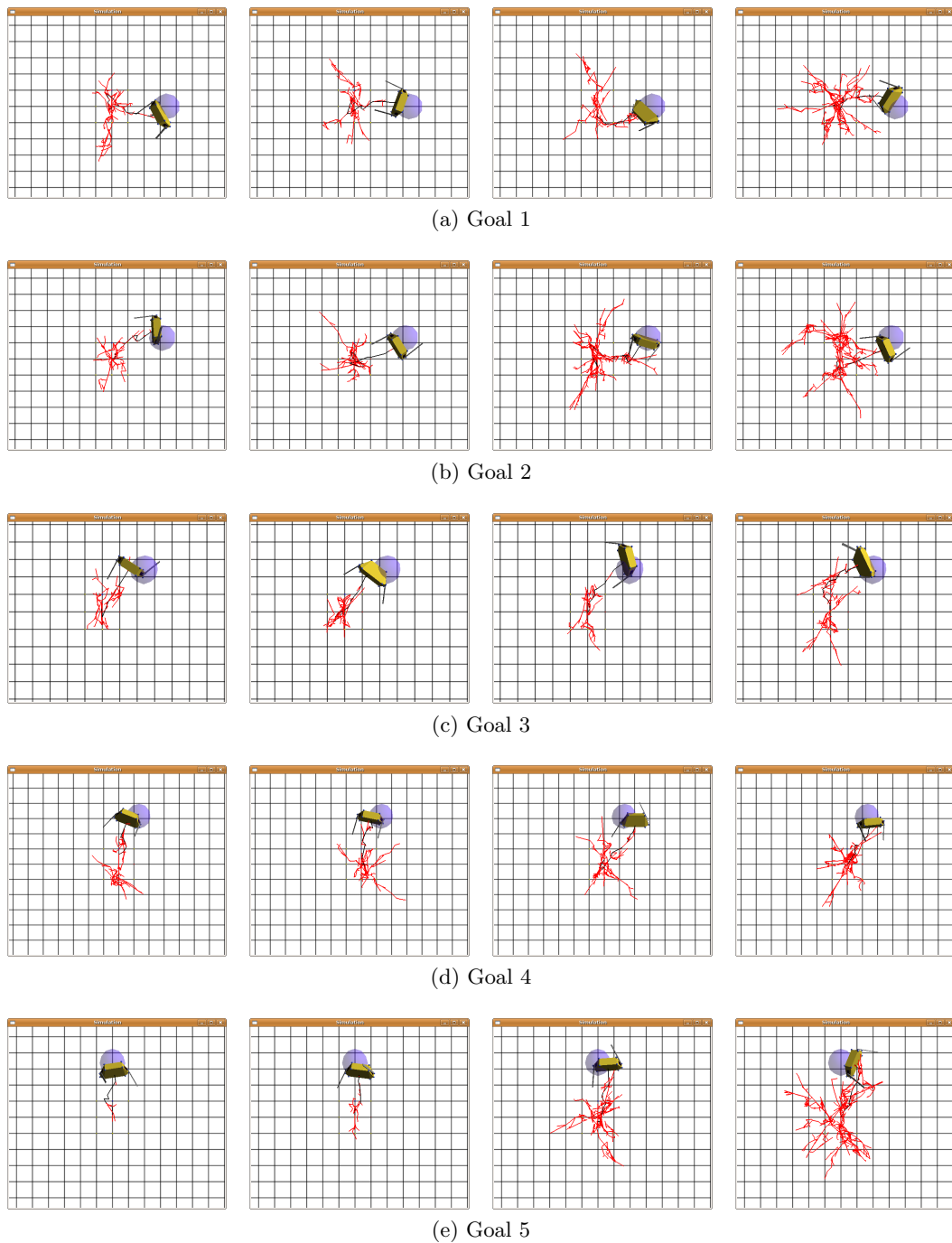


Figure E.2: Isochronal pseudo-metric $d_{iso0r448}$ example RRTs for $r = 0.448$ m.

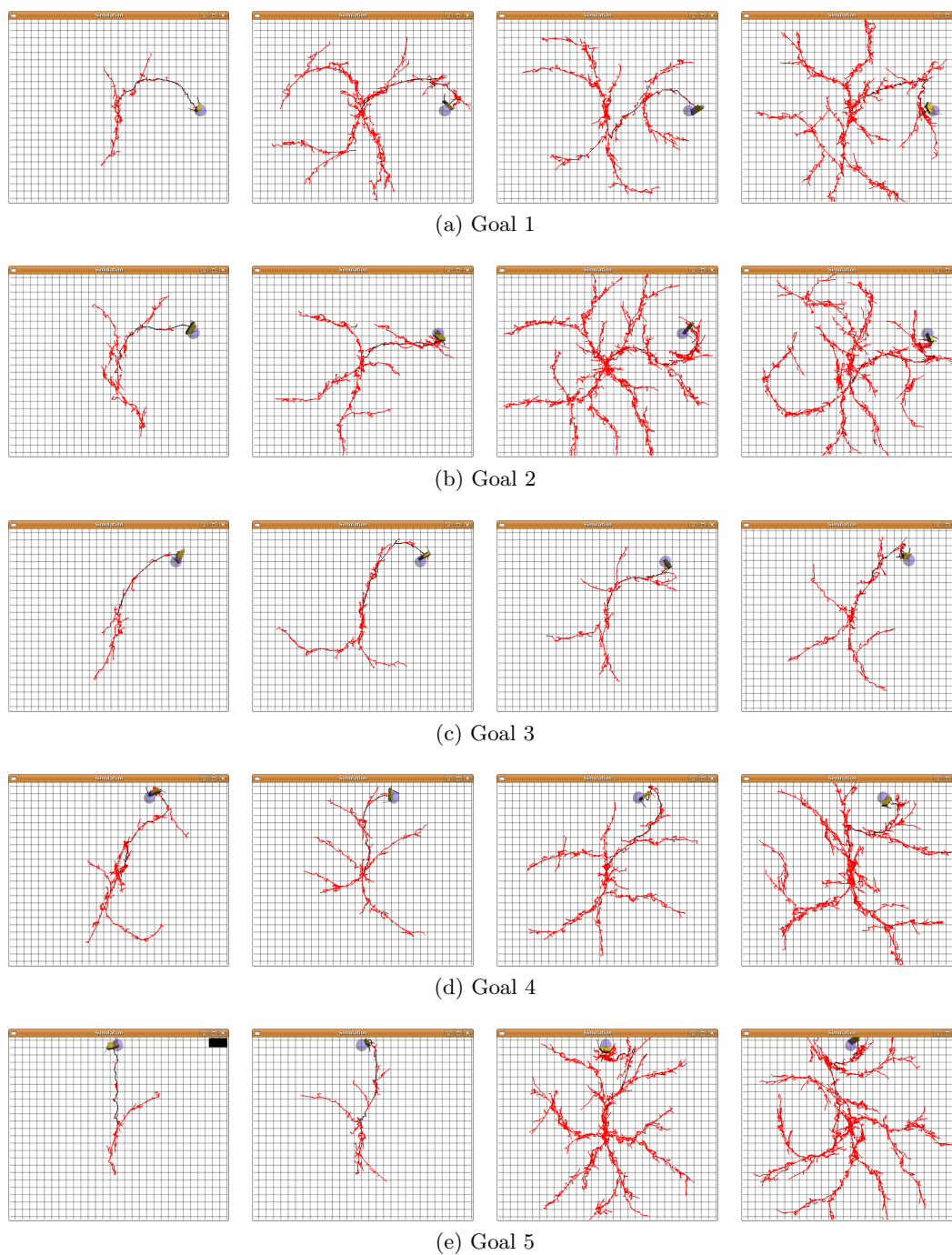


Figure E.3: Weighted Euclidian pseudo-metric d_{we} example RRTs for $r = 1.5$ m.

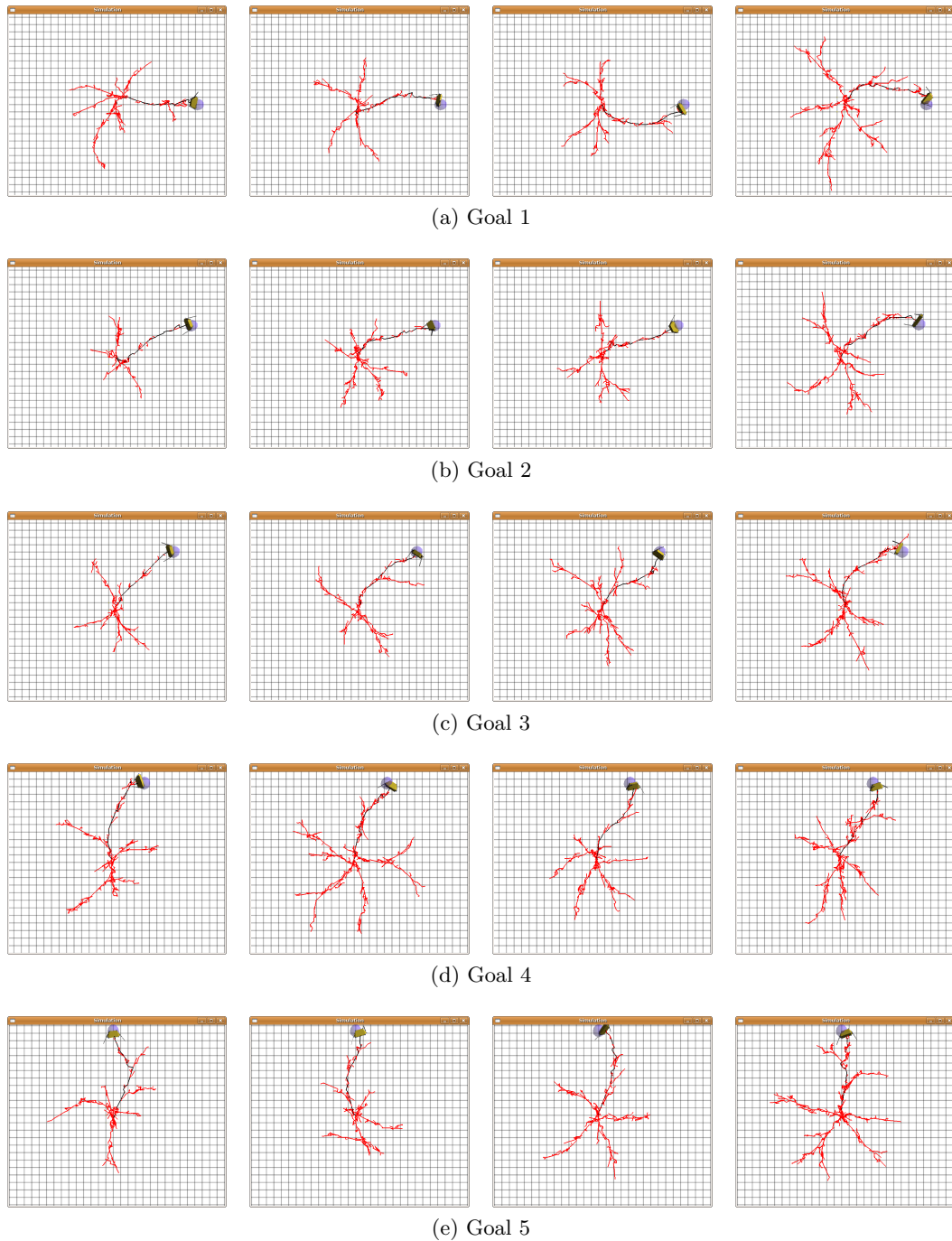


Figure E.4: Isochronal pseudo-metric $d_{\text{iso}0r448}$ example RRTs for $r = 1.5$ m.